

***STUDY OF BREAKUP/FUSION OF LOOSELY BOUND
STABLE PROJECTILES WITH SOME NUCLEI***

A THESIS SUBMITTED TO
THE MAHARAJA SAYAJIRAO UNIVERSITY OF BARODA

FOR THE DEGREE OF
DOCTOR OF PHILOSOPHY

IN
PHYSICS

BY
PRASANTA KUMAR RATH

UNDER THE SUPERVISION OF

PROF. N. L. SINGH



DEPARTMENT OF PHYSICS, FACULTY OF SCIENCE

THE MAHARAJA SAYAJIRAO UNIVERSITY OF BARODA

VADODARA-390 002, INDIA

NOVEMBER-2012

Dedicated to my

BELOVED PARENTS

DECLARATION BY THE CANDIDATE

I hereby declare that the work embodied in the present thesis entitled “**Study of Breakup/Fusion of loosely bound stable projectiles with some Nuclei**” is my own work carried out under the guidance of Prof. N. L. Singh at Department of Physics, Faculty of Science, The Maharaja Sayajirao University of Baroda, India, approved by Council of Post-Graduate Studies and Research. I have put in research work for requisite number of terms as required by the university.

I further declare that to the best of my knowledge, the thesis does not contain any part or any work, which has been submitted for the award of any degree either in this University or in other University/Institute without, proper citation.

Date:.....

Prasanta Kumar Rath
CSIR-SRF,
Physics Department,
Faculty of Science,
The M.S. University of Baroda.



The Maharaja Sayajirao University of Baroda

Department of Physics, Faculty of Science

Vadodara- 390 002, Gujarat, India.

Ph no. - +91-0265-2795339

CERTIFICATE

This is to certify that the work entitled “**Study of Breakup/Fusion of loosely bound stable projectiles with some Nuclei**” is a piece of research work done by Mr. Prasanta Kumar Rath, under my supervision and guidance for the degree of Doctor of Philosophy in Physics at The Maharaja Sayajirao University of Baroda, India. To the best of my knowledge and belief the thesis

1. embodies the work of the candidate himself,
2. has duly been completed
3. fulfils the requirements of the ordinance relating to the Ph. D. degree of the University and
4. is up to the standard both in respect of content and language for being referred to examiner.

Forwarded through:

(Prof. N. L. Singh)

Thesis Supervisor
Department of Physics

Faculty of Science

The Maharaja Sayajirao University of Baroda,
Vadodara-390002, Gujarat

ACKNOWLEDGEMENTS

I express my sincere gratitude to my supervisor Prof. N. L. Singh for his valuable guidance, motivation and encouragement. I am fortunate enough to avail all resources of his genial inspiration and enthusiastic encouragement throughout the course of my research work. I always will admire the training given by him which has helped me to achieve my goal. My special thanks to my co-supervisor Dr. S. Santra (BARC) for his guidance starting from the experimental plan to data analysis. I am indebted to him not only for introducing the objective of this work but also his support and guidance in the completion of work. My thesis work would not have been possible without their constant support, helpful discussion and valuable comments.

I am truly grateful to Dr. B. K. Nayak, Dr. K. Mahata, Dr. V. V. Parkar from BARC for their logical, analytical, moral support and fruitful discussion. My thanks to Dr. R. Tripathi, (BARC) for his help in target preparation, experimental set up and analysis.

My special thanks to Dr. S. Kailas (Director Physics Group, BARC) and Dr. R. K. Choudhury (Ex Head Nuclear Physics Division, BARC) for their technical discussion during the experimental plane and the data interpretation using different calculation procedure.

I am very much great full to Dr. R. Palit (TIFR) and Dr. Suresh Kumar (DU) for their technical support during experimental setup and data analysis.

My sincere thanks to Dr. S. Appannababu, N. N. Deshmukh, A. Parihari, Asim Pal, Sushil Sharma, D. Patel for providing their help during experiment time at TIFR, Of course I will

never forget S.V. L. S. Rao, P. Jain, Dr. R. G. Thomas and my room partner for their moral and financial support during these long days.

I never forget the help of operators specially V. Ramlal, P. Surendran, N. G. Ninaway, Ramjilal, M. L. Yadav, J.P. Nair, S. Hilari, R. N. Lokre and all pelletron staff for their kind cooperation and successful operation of Pelletron Accelerator.

In addition I will never forget my friends Chaitali, Sajel di, Sangeeta, Dolly di, Satishbahi, Devangbhai, Naveen, Dharmendra, Nishantbhai, C.S. Palshetkar, C. Yadav, Birubhai, Devubhai and NPD seniors R. Kujur, P. V. Patale, N.B.V. Subrahmanyam, Dr. A. Mitra, Dr. E.T. Mirgule, Dr. P.C. Rout, Dr. V. Jha, Dr. K. Ramachandran, S. Pandit for their kind moral support, Of course R.T. Kawale, P.J. Rout, Ben D. Suza, K.D. Waghmare, M. A. Chougale, S.S. Poul, J.P. Bhat, Bagdare, Narawade for their help and encouragement. I have no words to express my heartiest thanks to them.

I would like to thank Prof. C. F. Desai (Ex-Head) and Prof. A. C. Sharma, Head Physics Department for providing me an opportunity to work in the Department.

In addition if I have missed some name hope they excuse me, I am very much great full to all of them for their help with deepest and gratitude and express my indebtedness to all of them. I also appreciate, the love and affection shown by my brother and sisters for their ceaseless support and patience towards completion of my work. Last but not least, I express my sincere gratitude to my friends who letter me and can, made me cheerful all through these days.

I gratefully acknowledge the financial support by DAE-BRNS, Mumbai and CSIR, New Delhi.

I appreciate whole heartedly the encouragement given to me by my parents throughout my academic carrier and deep sense of affection of my brother and sister. Without their several sacrifices, it would not have been possible for me to accomplish whatever I have achieved in my life so far, I dedicate my entire thesis to my parents.

Prasanta Kumar Rath

PREFACE

The study of fusion involving loosely bound projectiles is of continued interest because of its application to nuclear astrophysics. For unstable nuclei the fusion process is affected by their low binding energy, which can cause them to break up before reaching the fusion barrier. This may reduce the complete fusion cross sections, making it difficult to make the super-heavy nuclei. Alternately, the extended structure of the loosely bound nuclei could in principle induce a large enhancement of fusion. Although sub barrier fusion involving strongly bound stable nuclei is well understood, but there are contradictory results and predictions about the enhancement or suppression of the fusion cross section (σ^{fus}) over the predictions of the single barrier penetration model calculations around the Coulomb barrier, when one of the collision partners is a weakly bound nuclei. To explain the experimental data new models are coming up with more complex logic based on the paradoxical theory of quantum mechanics. Experimental investigations of the fusion process have been made with stable weakly bound ${}^6\text{Li}$ and ${}^9\text{Be}$ nuclei; however, they have different conclusions about fusion enhancement/suppression, when compared with strongly bound stable isotopes and/or coupled-channel calculations. There are theoretical calculations that predict either suppression of the complete fusion (CF) cross sections due to breakup of loosely bound nucleus or enhancement of the same due to coupling of the relative motion of the colliding nuclei to the breakup channel. Hagino *et al.* performed an improved coupled-channel calculation that predicts the enhancement of fusion at sub-barrier energies and reduction at above barrier energies. An understanding of breakup and fusion is directly relevant for producing nuclei near the drip line and possibly super-heavy

nuclei. Experimentally such studies are limited because of the low intensities of unstable beams currently available. Light nuclei such as ${}^6\text{Li}$ (${}^7\text{Li}$), which breaks up into $\alpha + d$ ($\alpha + t$) with a breakup threshold of only 1.48 (2.47) MeV, has a large breakup probability. Fusion with such a nucleus is ideal for the quantitative testing of theoretical models and for use as a comparator for fusion measurements with other unstable beams. To differentiate the effect of projectile breakup one should choose a system where the effect of other channels (target excitations or projectile bound state excitations) on fusion is minimum. So, one can start with a spherical target with first excited state above the projectile breakup threshold and ${}^6\text{Li}$ projectile having no bound excited state. In the next step, it would be interesting to find out the effect of target deformation in addition to the effect of projectile breakup on fusion where one should choose a deformed target in place of a spherical target. Here it requires systematic experimental data with good precision at low bombarding energies, where penetrability effects are important. Also, the barrier distribution extracted from these fusion excitation functions can provide an additional information on the structure of the target/projectile. The effect of target deformation on fusion cross section is expected to differ depending on whether it is static or dynamically induced. When averaged over all orientations of a deformed nucleus, the fusion cross section becomes larger compared to a spherical nucleus. However, the dynamical effects such as excitation of the vibrational states or the rotation of the deformed nucleus during the collision can sometimes lead to reduction in fusion cross section. The static deformation effects could be very important and they may show up partly through absorption below the barrier. There are reports that the fusion cross sections involving a much deformed ${}^{154}\text{Sm}$ target nucleus are considerably larger than a less deformed ${}^{148}\text{Sm}$ nucleus with strongly bound projectile ${}^{16}\text{O}$ at sub-barrier

energies. Similar effects are also observed for two more projectiles ^{32}S and ^{40}Ar . While most of the studies on the effect of target deformation on fusion cross section involve strongly bound projectiles such as ^{16}O , ^{32}S etc., the studies involving loosely bound nuclei (^6Li , ^7Li , ^9Be) with deformed targets are scarce. Fusion reactions involving loosely bound projectiles would be more revealing towards the dominance of the effects of projectile breakup or target deformation, especially at sub-barrier energies. It would be interesting to see if the sub-barrier fusion enhancement due to deformation gets further magnified with the breakup coupling or it is neutralized by the suppression of fusion cross section due to loss of incident flux caused by projectile breakup. It has also been observed that although the effect of couplings of the target inelastic states (e.g., 2^+ , 3^- vibrational states of ^{208}Pb) on elastic scattering or fusion in the systems involving tightly bound projectiles ($^{12}\text{C}+^{208}\text{Pb}$, ^{209}Bi) are significant, it is negligible for the systems involving weakly bound projectiles ($^{6,7}\text{Li}+^{208}\text{Pb}$, ^{209}Bi), where the effect of projectile breakup is dominated. So, it would be interesting to investigate whether similar scenario is observed for a system with a target (^{152}Sm) having rotational inelastic states. Ultimately one needs to understand the effect of both projectile as well as target dependences on the fusion for which we propose to make the fusion measurements for several systems with different projectile breakup threshold and different target deformations. With these motivations, four different systems involving two weakly bound projectiles ($^{6,7}\text{Li}$) and two isotopes of Sm as targets i.e., $^{6,7}\text{Li}+^{144,152}\text{Sm}$ were chosen whose fusion cross sections were measured and analyzed. The present work is organized into the following chapters; An introduction to the problem and motivation of the present work will be given in Chapter 1. The statistical model and coupled-channels calculations are presented in Chapter 2. The experimental details and the

data analysis are described in Chapter 3. The comparison of the experimental results with the theoretical predictions as well as previous results analysis is discussed in Chapters 4, 5 and 6. Finally the summary and conclusions of the results of the investigation performed in the present work and future perspectives are mentioned in Chapter 7.

List of Publications

A. Publications in International Journals:

1. Fusion reaction studies for the ${}^6\text{Li} + {}^{90}\text{Zr}$ system at near-barrier energies
H. Kumawat, V. Jha, V. V. Parkar, B. J. Roy, S. K. Pandit, R. Palit, **P. K. Rath**, C. S. Palshetkar, Sushil K. Sharma, Shital Thakur, A. K. Mohanty, A. Chatterjee, S. Kailas
Phys.Rev. C 86, 024607 (2012).
2. Fusion of ${}^6\text{Li}$ with ${}^{152}\text{Sm}$: Role of projectile breakup versus target deformation
P.K.Rath, S.Santra, N.L.Singh, K.Mahata, R.Palit, B.K.Nayak, K.Ramachandran, V.V.Parkar,R.Tripathi, S.K.Pandit, S.Appannababu, N.N.Deshmukh, R.K.Choudhury, S.Kailas
Nucl.Phys.A874, 14 (2012).
3. Disentangling reaction mechanisms for α production in the ${}^6\text{Li} + {}^{209}\text{Bi}$ reaction
S.Santra, S.Kailas, V.V.Parkar, K.Ramachandran, V.Jha, A.Chatterjee, **P.K.Rath**, A.Parihari
Phys.Rev. C 85, 014612 (2012).
4. Fission fragment mass distributions in reactions forming the ${}^{213}\text{Fr}$ compound nucleus
S.Appannababu, S.Mukherjee, B.K.Nayak, R.G.Thomas, P.Sugathan, A.Jhingan, E.Prasad, D.Negi, N.N.Deshmukh, **P.K.Rath**, N.L.Singh, R.K.Choudhury
Phys.Rev. C 83, 034605 (2011).
5. Fission fragment angular distributions in the ${}^9\text{Be} + {}^{232}\text{Th}$ reaction
S.Appannababu, R.G.Thomas, L.S.Danu, **P.K.Rath**, Y.K.Gupta, B.V.John, B.K.Nayak, D.C.Biswas, A.Saxena, S.Mukherjee, R.K.Choudhury

Phys.Rev. C 83, 067601 (2011); Pub Note Phys.Rev. C 83, 069902 (2011).

6. Breakup threshold anomaly in the near-barrier elastic scattering of ${}^6\text{Li} + {}^{116,112}\text{Sn}$
N.N.Deshmukh, S.Mukherjee, D.Patel, N.L.Singh, **P.K.Rath**, B.K.Nayak,
D.C.Biswas, S.Santra, E.T.Mirgule, L.S.Danu, Y.K.Gupta, A.Saxena,
R.K.Choudhury, R.Kumar, J.Lubian, C.C.Lopes, E.N.Cardozo, P.R.S.Gomes
Phys.Rev. C 83, 024607 (2011).
7. Complete and incomplete fusion in ${}^9\text{Be} + {}^{124}\text{Sn}$ system
V.V.Parkar, R.Palit, S.K.Sharma, B.S.Naidu, P.K.Joshi, S.Santra, **P.K.Rath**,
K.Ramachandran, K.Mahata, T.Trivedi, A.Raghav
Radiochim.ActaSupp 1, Proc.in Radiochemistry 131 (2011).
8. Fusion cross sections for the ${}^9\text{Be} + {}^{124}\text{Sn}$ reaction at energies near the Coulomb
barrier
V.V.Parkar, R.Palit, SushilK.Sharma, B.S.Naidu, S.Santra, P.K.Joshi, **P.K.Rath**,
K.Mahata, K.Ramachandran, T.Trivedi, A.Raghav
Phys.Rev. C 82, 054601 (2010).
9. Absence of entrance channel effects in fission fragment anisotropies of the ${}^{215}\text{Fr}$
compound nucleus
S.Appannababu, S.Mukherjee, N.L.Singh, **P.K.Rath**, G.Kiran Kumar,
R.G.Thomas, S.Santra, B.K.Nayak, A.Saxena, R.K.Choudhury, K.S.Golda,
A.Jhingan, R.Kumar, P.Sugathan, H.Singh
Phys.Rev. C 80, 024603 (2009).
10. Suppression of complete fusion in the ${}^6\text{Li} + {}^{144}\text{Sm}$ reaction
P.K.Rath, S.Santra, N.L.Singh, R.Tripathi, V.V.Parkar, B.K.Nayak, K.Mahata,
R.Palit, Suresh Kumar, S.Mukherjee, S.Appannababu, R.K.Choudhury
Phys.Rev. C 79, (2009) 051601 (R).

11. Complete fusion in ${}^7\text{Li}+{}^{144,152}\text{Sm}$ reactions

P. K. Rath, S. Santra, N. L. Singh, K. Mahata, R. Palit, K. Ramachandran, S. K. Pandit, A. Parihari, S. Appannababu, D. Patel, Sushil K. Sharma, B. K. Nayak, and S. Kailas

Going to communicate in PRC

In national/International Symposium/Conference:

1. Fission fragment anisotropies for ${}^{6,7}\text{Li}+{}^{235,238}\text{U}$

Parihari, S. Santra, N. L. Singh, K. Mahata, **P. K. Rath**, K. Ramachandran, B. K. Nayak, S. Kailas

Proceedings of the DAE Symp. on Nucl. Phys. 57 (2012) 398

2. A simultaneous study of elastic scattering and fusion in ${}^7\text{Li}+{}^{27}\text{Al}$ reaction

D. Patel, S. Santra, S. Mukherjee, B. K. Nayak, **P. K. Rath**, V. V. Parkar, R. K. Choudhury

Proceedings of the DAE Symp. on Nucl. Phys. 57 (2012) 416

3. Fusion using proximity potentials and effect of projectile breakup

P. K. Rath, S. Santra, N. L. Singh, K. Mahata, R. Palit, S. K. Pandit, A. Parihari, S. Appannababu, D. Patel, B. K. Nayak, S. Kailas

Proceedings of the DAE Symp. on Nucl. Phys. 57 (2012) 518

4. Performance of Integrated δE -E Silicon Detector Telescope with Light Charged Particles and Fission Fragments

Arvind Singh, S. Santra, Anita Topkar, K. Mahata, **P. K. Rath**, A. Parihari, P. K. Mukhopadhyay, A. Chatterjee, C. K. Pithawa

Proceedings of the DAE Symp. on Nucl. Phys. 57 (2012) 862

5. Study of fission fragment mass distributions for the reaction ${}^{18}\text{O} + {}^{197}\text{Au}$

- S. Appannababu, B. K. Nayak, A. Jhingan, P. Sugathan, E. Prasad, R. G. Thomas, D. Negi, **P. K. Rath**, K. S. Golda, J. Gehlot, S. Mukherjee, and R. K. Choudhury
 Proceedings of the DAE Symp.onNucl. Phys. 56 (2011) 468
6. Projectile and target dependences on complete fusion in $^{6,7}\text{Li}+^{144,152}\text{Sm}$ reactions
P.K. Rath, S. Santra, N. L. Singh, K. Mahata, R. Palit, K. Ramachandran, S.K. Pandit, A. Parihari, S. Appannababu, D. Patel, B. K. Nayak, S. Kailas
 Proceedings of the DAE Symp.onNucl. Phys. 56 (2011) 544
7. Fission fragment mass distribution in $^{6,7}\text{Li}+^{238}\text{U}$ reaction
 S Santra, **P. K. Rath**, N. L. Singh, B. R. Behera, B. K. Nayak, A. Parihari, A. Jhingan, P. Sugathan, K. S. Golda, S. Sodaye, S. Appannababu, E. Prasad, Amit Kumar, and D. Patel
 Proceedings of the DAE Symp.onNucl. Phys. 56 (2011) 612
8. Fission cross sections for $^{6,7}\text{Li}+^{235}\text{U}$
 A. Parihar, S. Santra, N. L. Singh, K. Mahata, **P.K. Rath**, K. Ramachandran, Sushil K. Sharma, B. K. Nayak, S. Kailas
 Proceedings of the DAE Symp.onNucl. Phys. 56 (2011) 618
9. Study of fusion barrier distributions from quasi-elastic scattering for $^{6,7}\text{Li}+^{209}\text{Bi}$ Systems
 D. Patel, B. K. Nayak, S. Mukherjee, D. C. Biswas, E.T. Mirgule, V. John, Y. K. Gupta, S. Mukhopadhyay, G. Prajapati, L.S. Danu, **P. K. Rath**, V. Desai, N. N. Deshmukh, Saxena
 Proceedings of the DAE Symp.onNucl. Phys. 56 (2011) 624
10. Elastic scattering of $^7\text{Li}+^{27}\text{Al}$ system at near barrier energies,
 Patel, **P. K. Rath**, S. Mukherjee, S. Santra, Pratap Roy, B. K. Nayak, R. K. Choudhury
 Proc. DAE-BRNS Symp.onNucl. Phys. 288 (2010) B32

11. Fusion of ${}^7\text{Li}$ with ${}^{124}\text{Sn}$ at around Coulomb barrier energies;
Sushil K. Sharma, R. Palit, V. V. Parkar, T. Trivedi, J. Sethi, S. Saha, B. S. Naidu, **P. K. Rath**, S. Santra, K. Mahata, K. Ramachandran,
Proc. DAE-BRNS Symp.onNucl. Phys. 55 (2010) 296
12. Complete fusion of weakly bound ${}^7\text{Li}$ with ${}^{144}\text{Sm}$,
P. K. Rath, S. Santra, N. L. Singh, R. Palit, K. Mahata, K. Ramachandran, SushilK. Sharma, S. K. Pandit, A. Parihari, S. Appannababu, D. Patel, B. K. Nayak, R. K. Choudhury
Proc. DAE-BRNS Symp.onNucl. Phys. B38 (2010)300
13. Effect of projectile breakup on fission in ${}^{6,7}\text{Li}+{}^{238}\text{U}$
S. Santra, **P. K. Rath**, N. L. Singh, B. R. Behera, B. K. Nayak, R. K. Choudhury, A. Jhingan, P. Sugathan, Golda K. S., S. Sodaye, S. Appannababu, E. Prasad, Amit Kumar, D. Patel
Proc. DAE-BRNS Symp.onNucl. Phys. B39(2010) 302
14. Fabrication of Isotopic Ba Target,
P. K. Rath, S. R. Abhilash, S. Santra, D. Kabiraj
Proc. DAE-BRNS Symp.onNucl. Phys. H46(2010) 742
15. A time zero MWPC detector for fission TOF experiments,
Jhingan, P. Sugathan, Golda K. S., E. Prasad, **P. K. Rath**, S. Appanababu, B. R. Behera, B. K. Nayak, S. Santra, A. Saxena
Proc. DAE-BRNS Symp.onNucl. Phys. H11(2010)672
16. Fusion of ${}^9\text{Be}$ with ${}^{124}\text{Sn}$;
V. V. Parkar, R. Palit, Sushil K. Sharma, B. S. Naidu, S. Santra, P. K. Joshi, **P. K. Rath**, K. Mahata, K. Ramachandran, T. Trivedi, A. Raghav,
Zakopane Conference in Nuclear physics, Zakopane, Poland (2010)

17. Complete versus incomplete fusion in ${}^6\text{Li}+{}^{144}\text{Sm}$ reaction;
P. K. Rath, S. Santra, K. Mahata, R. Tripathi, V. V. Parkar, R. Palit, B. K. Nayak, N. L. Singh,
Proceedings of the International Symposium in Nucl. Phys. 54 (2009) 310
18. Effect of target deformation and projectile breakup in complete fusion of ${}^6\text{Li}+{}^{152}\text{Sm}$;
P. K. Rath, S. Santra, N. L. Singh, K. Mahata, R. Palit, V. V. Parkar, B. K. Nayak, R. Tripathi, S. Appannababu, N.N. Deshmukh,
Proceedings of the International Symposium in Nucl. Phys. 54 (2009) 312
19. Complete and incomplete fusion cross-sections in ${}^9\text{Be}+{}^{124}\text{Sn}$ system and its implications in horizontal spectroscopy;
V. V. Parkar, R. Palit, S. Sharma, B.S. Naidu, S. Santra, P.K. Joshi, **P.K. Rath**, K. Mahata, K. Ramachandran, T. Trivedi, A. Raghav,
Proceedings of the International Symposium in Nucl. Phys. 54 (2009) 320
20. Study of fission fragment angular distribution for ${}^9\text{Be}+{}^{232}\text{Th}$
S.Appannababu, R.G.Thomas, L.S.Danu, **P.K.Rath**, Y.K.Gupta, B.V.John, B.K.Nayak, D.C.Biswas, A.Saxena, S.Mukherjee, R.K.Choudhury
International Symposium in Nucl. Phys. 54 (2009) 340
21. Fission mass widths in ${}^{213}\text{Fr}$ compound nucleus
S.Appannababu,S.Mukherjee,B.K.Nayak,R.G.Thomas,P.Sugathan, A.Jhingan,E.Prasad,D.Negi,N.N.Deshmukh,**P.K.Rath**,N.L.Singh, R.K.Choudhury
International Symposium in Nucl. Phys. 54 (2009) 352
22. Incomplete fusion in ${}^6\text{Li}+{}^{144}\text{Sm}$;
P. K. Rath, S. Santra, N. L. Singh, R. Tripathi, V. V. Parkar, B. K. Nayak, K. Mahata, R. Palit, Suresh Kumar, S. Mukherjee, S. Appannababu, R. K.

Choudhury,

Nucleus-Nucleus collision 2009 (NN2009), Beijing, China (Aug 2009)

[Poster Presentation]

23. Suppression of complete fusion in ${}^6\text{Li}+{}^{144}\text{Sm}$;

P. K. Rath, S. Santra, N. L. Singh, R. Tripathi, V. V. Parkar, B. K. Nayak,
K. Mahata, R. Palit, Suresh Kumar, S. Mukherjee, S. Appannababu, R. K.
Choudhury,

Proc. DAE-BRNS Symp.onNucl.Phys. 53 (2008) 385.

24. Breakup fusion in ${}^6\text{Li}+{}^{144}\text{Sm}$;

P. K. Rath, S.Santra, N.L.Singh, R.Tripathi, V. V. Parkar, B.K.Nayak,
K.Mahata, R.Palit, Suresh Kumar, S.Mukherjee, S.Appannababu,
R.K.Choudhury,

Proc. DAE-BRNS Symp.onNucl.Phys. 53 (2008) 477.

25. Study of entrance channel effects in ${}^{215}\text{Fr}$.

S.Appannababu,S.Mukherjee,B.K.Nayak,R.G.Thomas,P.Sugathan,

A.Jhingan,E.Prasad, D.Negi, N.N.Deshmukh, **P.K.Rath**, N.L.Singh, .K.Choudhury

Proc. DAE-BRNS Symp.onNucl. Phys. 53 (2008) 389

Contents

Chapter 1

1.1	Introduction	1
1.2	Heavy Ion Reaction	1
1.2.1	Complete Fusion	6
1.2.2	Incomplete Fusion	7
1.3	Reaction with weakly/loosely bound system	9
1.4	General motivation of the thesis	13
	References	19

Chapter 2

2.1	Formation of Compound nucleus	21
2.2	Decay of compound nucleus (CN)	24
2.2.1	Statistical model	24
2.2.2	Level density	25
2.2.3	Total decay	29
2.2.4	PACE	30
2.3	Fusion cross section and barrier distribution	31
2.3.1	Fusion by parabolic approximation	32
2.3.2	Comparison with experimental data	34
2.3.3	Barrier distribution	35
2.4	Derivation of fusion from experimental data	36
2.4.1	Equilibrium	39
2.4.2	Estimation of fusion cross section from off line γ measurement	40
2.5	Coupled-channels formalism for heavy ion fusion	44
2.5.1	Coupled-channels equation	44
2.5.2	Vibrational coupling	47

2.5.3 Rotational coupling	49
References	52

Chapter 3

3.1 Radioactive sources	54
3.2 Detectors	58
3.2.1 Semiconductor detector	59
3.2.2 Silicon surface barrier detector	62
3.2.3 High purity germanium detector (HPGe)	63
3.3 Electronics and data accumulation	66
3.3.1 Preamplifier	66
3.3.1.i Detector bias supply	66
3.3.1.ii Pulse counting system	68
3.3.1.iii Multichannel analyzer (MCA)	68
3.3.1.iv Counter and timer	69
3.3.2 Shaping (spectroscopy) Amplifier	69
3.3.3 Analog to digital converter	70
3.4 Target Preparation	70
3.5 Accelerator facilities	73
3.5.1 The Pelletron Accelerator at TIFR	73
3.5.2 Folded Tandem Ion Accelerator (FOTIA)	77
3.6 Target thickness measurement and Irradiation	79
3.6.1 Target thickness measurement	79
3.6.2 Irradiation	82
3.6.2.i Irradiation of ${}^6\text{Li}+{}^{144}\text{Sm}$	83
3.6.2.ii Irradiation of ${}^6\text{Li}+{}^{152}\text{Sm}$	86
3.6.2.iii Irradiation of ${}^7\text{Li}+{}^{144,152}\text{Sm}$	89
References	93

Chapter 4

4.1 Complete Fusion Suppression in ${}^6\text{Li} + {}^{144}\text{Sm}$ system.	95
--	----

4.1.1 Introduction	95
4.1.2 Analysis of Experimental results	96
4.1.3 Coupled-channel (CC) calculation	99
4.1.4 Summary	105
References	106

Chapter 5

5.1 Complete fusion in ${}^6\text{Li} + {}^{152}\text{Sm}$: Role of target deformation versus projectile breakup.	107
5.1.1 Introduction	107
5.1.2 Analysis of Experimental results	108
5.1.3 Coupled-channel (CC) calculation	114
5.1.4 Fusion using proximity potential	118
5.1.5 Incomplete fusion	122
5.1.6 Summary	124
References	126

Chapter 6

6.1 Effect of Projectile breakup threshold in the complete fusion of ${}^{6,7}\text{Li} + {}^{144,152}\text{Sm}$.	128
6.1.1 Introduction	128
6.1.2 Analysis of experimental results	130
6.1.3 Statistical model analysis	132
6.1.4 Barrier distribution and CC analysis	137
6.1.5 Fusion cross sections using proximity potential	139
6.1.6 Systematics on suppression factor	140
6.1.7 Summary	143
References	145

Chapter 7

A	Summary and Conclusions	146
	(i) Complete fusion suppression involving loosely bound projectile	146
	(ii) Effect of target deformation in the presence of projectile breakup	147
	(iii) Effect of projectile breakup threshold in complete fusion	149
B	Future perspectives	150

List of Figures

Fig 1.1:	<i>Energy spectra of the emitted particles from different reaction process.</i>	2
Fig 1.2:	<i>A Schematic diagram of different type of heavy ion reactions as a function of impact parameter 'b'.</i>	4
Fig 1.3:	<i>A qualitative picture of different reaction as a function of input angular momentum l. Compound nucleus formation (σ_{CN}), deep inelastic collision (σ_{DIC}), direct reactions (σ_D), elastic scattering (σ_{el}) and Coulomb excitation (σ_{CE}).</i>	6
Fig 1.4:	<i>Schematic representation of CN formation and its decay via CF-process. The accelerated projectile nucleus collides and fuses with target nucleus lead to excited compound nucleus (CN^*). The CN^* first cools by evaporation of neutrons, protons and/or α-particles. Eventually, it may lose the rest of its excitation energy and almost all of its initial angular momentum by emission of γ-rays.</i>	8
Fig 1.5:	<i>Schematic representation of ICF process. As shown, one of the fragments fuses with target nucleus called participant leading to the formation of ICF system, while the remnant moves in forward cone as spectator, with almost projectile velocity. The IFC de-excites in the similar fashion as the CN decay in CF. Schematic representation of ICF process. As shown, one of the fragments fuses with target nucleus called participant leading to the formation of ICF system, while the remnant moves in forward cone as spectator, with almost projectile velocity. The IFC de-excites in the similar fashion as the CN decay in CF.</i>	8
Fig 1.6:	<i>Schematic representation of the fusion and breakup processes that can take place in the collision of a weakly bound projectile.</i>	10
Fig 1.7:	<i>Schematic representation of the barrier (V_B) height, R_B the barrier radius for different values of L(orbital angular momentum).</i>	13
Fig 1.8:	<i>[a] The single barrier penetration model calculation for different projectile targets ($^{12}C, ^{27}Al, ^{29}Si$) fits the expt. data very nicely.[b] Wong model fitted for $^{16}O+^{64}Zn$ system quite well.</i>	14
Fig 1.9:	<i>Enhancement of the fusion cross section bellow the Coulomb barrier compared to the single barrier penetration model calculations for $^{16}O+^A Sm$ and $^A Ni+^A Ni$.</i>	15

Fig 1.10:	<i>The dotted line corresponding to the single barrier penetration model (BPM, SBPM) calculation. Solid line is the calculation by using coupling to the rotational levels of the target which fitted the data very nicely. The dotted line corresponding to the single barrier penetration model (BPM, SBPM) calculation. Solid line is the calculation by using coupling to the rotational levels of the target which fitted the data very nicely.</i>	15
Fig 1.11:	<i>A schematic representation of the rotational coupling of the target for ^{154}Sm. Indicating the shifting of barrier positions depending on the orientation of the projectile and target.</i>	16
Fig 1.12:	<i>Complete fusion cross section for $^{6,7}\text{Li}+^{209}\text{Bi}$. The dotted line is the single BPM calculation; the dash line is the calculation by using the coupled channel (CC) and the solid line is multiplying the factor 0.66, 0.74 with the CC calculation to explain the data.</i>	17
Fig 2.1:	<i>Fusion process with relative distance between the target and projectile (i.e. time snap-shoot) are shown. Which clearly shows the pocket for fusion (shaded region). The barrier height and barrier radius has also been shown in red (dashed) and violet (dotted) line.</i>	22
Fig 2.2:	<i>A typical potential barrier for the s-wave ($l=0$) scattering as a function of the relative distance between the projectile and target. The dotted and the dashed lines are the nuclear and the Coulomb potential, respectively. The total potential is denoted by the solid line. Also shown by arrow is the touching radius where the projectile and the target nuclei begin to overlap.</i>	23
Fig 2.3:	<i>Statistical decay of a CN populated at a given E_x and over a broad window of J through particle (neutron (n), proton (p) and alpha (α-particle)) and gamma (γ-ray) emission</i>	25
Fig 2.4:	<i>Schematic illustration of formation of Compound Nucleus and its decay</i>	29
Fig 2.5:	<i>An output of Statistical model calculation using the code (PACE) to understand the different channel contribution.</i>	30
Fig 2.6:	<i>Comparison between the Coulomb barrier ($V_B(r)$) for the $^{58}\text{Ni} + ^{58}\text{Ni}$ reaction (the solid line) and a parabolic potential (the dashed line). The woods-Saxon form of potential is assumed for the nuclear interaction.</i>	33
Fig 2.7:	<i>Fusion cross section using the exact solutions and the parabolic approximation is remarkably same except at very low energy.</i>	34

Fig 2.8:	<i>Comparison of experimental fusion cross section for several systems with predictions of the parabolic potential model (the solid lines).</i>	34
Fig 2.9:	<i>The upper panel: comparison of the first derivative of $E\sigma_{fus}$ (the solid line) with the s-wave penetrability (the dotted line). The lower panel: comparison between the second derivative of $E\sigma$ (the solid line) of the s-wave penetrability which is scaled by πR_B^2.</i>	36
Fig 2.10:	<i>A plot of the number of radioactive ^{51}Cu atoms in a Ni target at various times during and after bombardment with deuteron in cyclotron</i>	40
Fig 2.11:	<i>An example of formation of a CN in a reaction $A+B$ and its decay by evaporation of different light particles.</i>	40
Fig 2.12:	<i>The effect of branching of gamma the more dense line indicates the most preferable path than the less dense line indicates the less preference path to reach to ground state from an excited state.</i>	44
Fig 2.13:	<i>Experimental fusion excitation functions for $^{16}\text{O} + ^{144,148,154}\text{Sm}$ reactions [29]. They are given as a function of normalized energy and cross section. The solid line is a prediction of the potential model.</i>	45
Fig 2.14:	<i>CCFULL [20] input and OUTPUT for $^{16}\text{O} + ^{144}\text{Sm}$ system has shown.</i>	52
Fig 3.1:	<i>Different energetic gamma rays emitted from ^{152}Eu Source.</i>	56
Fig 3.2:	<i>The efficiency (ϵ) curve of HPGe detector used for off-beam γ activity counting at different distances from the detector.</i>	56
Fig 3.3:	<i>The different energetic gamma rays emitted from ^{133}Ba Source</i>	57
Fig 3.4:	<i>The efficiency (ϵ) curve of HPGe detector used for off-beam γ activity counting using ^{133}Ba and ^{153}Eu sources.</i>	58
Fig 3.5:	<i>Schematic diagram of an n-p junction with different charge carriers.</i>	61
Fig 3.6:	<i>Typical solid state detector used in nuclear physics experiments</i>	63
Fig 3.7:	<i>Schematic diagram showing $\Delta E - E$ telescope setup</i>	63

Fig 3.8:	<i>Typical ΔE vs E_{tot} plot for ${}^7\text{Li}+{}^{12}\text{C}$ experiment. There are different bands corresponding to different particles. As from the figure one can see ${}^7\text{Li}$, ${}^4\text{He}$, ${}^3\text{H}$ are clearly separated</i>	64
Fig 3.9:	<i>Schematic representation of the HPGe detector with Ge crystal, cooling line and cryogenic. Different types of configuration are available.</i>	65
Fig 3.10:	<i>${}^{60}\text{Co}$ gamma ray spectrum detected by HPGe detector</i>	65
Fig 3.11:	<i>Typical RC feedback charge sensitive preamplifier</i>	67
Fig 3.12:	<i>Signal pattern of a resistive feedback charge sensitive preamplifier</i>	67
Fig 3.13:	<i>Detector bias voltage is applied through the resistor R_b. The bypass capacitor C_b serves to shunt any external interference coming through the bias supply line to ground. For AC signals this capacitor connects the “far end” of the bias resistor to ground, so that R_b appears to be in parallel with the detector</i>	67
Fig 3.14:	<i>Schematic representation of output of a MCA for different alpha energy of ${}^{226}\text{Ra}$ nuclei.</i>	69
Fig 3.15:	<i>Schematic of circuit diagram for CR and RC circuit</i>	71
Fig 3.16:	<i>[A] CR, RC and CR-RC time domain response for a single step function. [B] Absolute value of the frequency domain transfer function for CR, RC and CR-RC.</i>	71
Fig 3.17:	<i>[A] Simple CR discriminator. [B] Pole zero cancelation circuit</i>	71
Fig 3.18:	<i>Schematic representation of the target preparation by electro deposition</i>	72
Fig 3.19:	<i>Pelletron accelerator situated at TIFR with different parts shown in red letter. At the top SNICS ion source is present. Red strips in center are the 14 number of modules assembly having withstanding voltage of each up to 1MV.</i>	74
Fig 3.20:	<i>Different beam lines after the 90° bending magnet and switching magnet, the right side of the 90° bending magnet leads to the LINAC beam, hall which has been developed recently and shown in Fig 3.20b.</i>	75
Fig 3.21:	<i>Schematic diagram of the irradiation chamber (30° N) for irradiation of targets.</i>	76

Fig 3.22:	<i>Schematic diagram of the scattering chamber to study the Rutherford back scattering for target thickness measurement</i>	76
Fig 3.23:	<i>Schematic diagram of the 6 MV folded tandem Ion accelerator</i>	77
Fig 3.24:	<i>SNICS source using in FOTIA facility for beam ion extraction</i>	78
Fig 3.25:	<i>sketch of different beam line present at FOTIA facility</i>	78
Fig 3.26:	<i>Schematic representation of the thickness measurement set up. M1, M2 are the two SSB detectors placed at the forward for beam normalization. Another SSB placed at 170° to identify the scattered particle from ^ASm and Al. FC is the faraday cup from which the beam flux was calculated</i>	79
Fig 3.27:	<i>Schematic representation of the electronics diagram for the target thickness measurement. M1, M2 are the two SSB placed at the forward angle for beam normalization. Another SSB placed at 170° to identify the scattered particle. PA, AMP, TFA, CFD are the preamplifier, amplifier, time filter amplifier, constant fraction discriminator and ADC is the analog to digital converter. DAQ is the data acquisition system</i>	80
Fig 3.28:	<i>A typical raw-spectrum for the target thickness measurement at 6MeV of proton (p) beam</i>	81
Fig 3.29:	<i>Schematic representation of the target and catcher</i>	82
Fig 3.30:	<i>The different decay channels for $^6\text{Li}+^{144}\text{Sm}$ system with different ER and half-life. We have detected only the CF channel (i.e. 2n, 3n ER channel)</i>	84
Fig 3.31:	<i>Schematic diagram of the detection process</i>	84
Fig 3.32:	<i>A typical γ-ray spectrum showing gamma lines of different ERs populated via CF in the $^6\text{Li}+^{144}\text{Sm}$ reactions at projectile energy of 40 MeV</i>	85
Fig 3.33:	<i>The different decay channels for $^6\text{Li}+^{152}\text{Sm}$ system with different ER and half-life. We have detected only the CF channel (i.e. 2n, 3n, 4n, 5n ER channel)</i>	87
Fig 3.34:	<i>Typical γ-ray spectrum showing gamma lines of different ERs populated via CF in the $^6\text{Li}+^{152}\text{Sm}$ reaction at projectile energy = 34 MeV. Different ER channels are shown in different symbol</i>	88

Fig 3.35:	<i>Typical γ-rays spectrum showing gamma lines of different ERs populated in ${}^7\text{Li}+{}^{144}\text{Sm}$ reactions at projectile energy 28 MeV</i>	90
Fig 3.36:	<i>Typical γ-rays spectrum showing gamma lines of different ERs populated in ${}^7\text{Li}+{}^{152}\text{Sm}$ reactions at 30 MeV</i>	90
Fig 3.37:	<i>The different decay channels of ERs through CF and ICF for ${}^7\text{Li}+{}^{144}\text{Sm}$ system</i>	91
Fig 3.38:	<i>The different types of ERs through CF and ICF for ${}^7\text{Li}+{}^{152}\text{Sm}$ system</i>	91
Fig 4.1:	Fig 4.1: <i>ER cross sections for ground state (filled triangles) and metastable state (filled circles) of (a) ${}^{148}\text{Tb}$ nucleus at different E_{lab}. Total ER (g.s.+m.s.) for the 2n channel are represented by open circles. (b) Same as (a), but for the ${}^{147}\text{Tb}$ nucleus, i.e. 3n ER channel. (c) Ratio of σ_{3n} to σ_{2n}.</i>	98
Fig 4.2:	<i>(a) Complete fusion cross section (filled circles) and (b) corresponding normalized barrier distribution (filled circles) for ${}^6\text{Li} + {}^{144}\text{Sm}$ compared with coupled (dashed lines) and uncoupled (dotted lines) results from CCFULL [18] calculations. Solid lines are obtained by multiplying the coupled results by a factor of 0.68.</i>	100
Fig 4.3:	<i>Reduced cross sections ($\sigma_{\text{fus}}/\pi R_B^2$) as a function of $E_{c.m.}/V_B$ for the present system (filled circles) along with two other reactions ${}^{12}\text{C} + {}^{141}\text{Pr}$ (filled diamonds [19], filled squares [20]) and ${}^{20}\text{Ne} + {}^{133}\text{Cs}$ (filled triangles [20]). Dashed line is the result of coupled-channel calculation. Solid line is obtained by multiplying the coupled results by a factor of 0.68.</i>	101
Fig 4.4:	<i>Reduced cross sections ($\sigma_{\text{fus}}/\pi R_B^2$) as a function of $E_{c.m.}/V_B$ for (a) ${}^7\text{Li} + {}^{165}\text{Ho}$ (filled circles [3]) along with ${}^{12}\text{C} + {}^{160}\text{Gd}$ (filled diamonds [21]) and (b) ${}^7\text{Li} + {}^{159}\text{Tb}$ (filled circles [16]) along with ${}^4\text{He} + {}^{161}\text{Dy}$ (filled diamonds [15]). Dashed lines are the result of coupled-channel calculation. Solid lines are obtained by multiplying the coupled results by a factor of (a) 0.82 and (b) 0.74.</i>	103
Fig 5.1:	<i>Total cross sections for 4n evaporation (filled circles) are obtained from the sum of ${}^{154}\text{Tb}^g$ (hollow diamonds), ${}^{154}\text{Tb}^{m1}$ (hollow squares) and ${}^{154}\text{Tb}^{m2}$ (hollow triangles).</i>	109
Fig 5.2:	<i>Measured ER cross sections for ${}^{156}\text{Tb}$ — 2n-channel (triangles), ${}^{155}\text{Tb}$ — 3n-channel (stars), ${}^{154}\text{Tb}(g+m)$ — 4n-channel (diamonds) and ${}^{153}\text{Tb}$ — 5n-channel (squares). Results of SM calculations</i>	112

corresponding to the level densities of $a = A/9\text{MeV}^{-1}$, $A/10\text{MeV}^{-1}$ and $A/11\text{MeV}^{-1}$ are shown as dash-dot-dot, medium-dashed and solid lines respectively for each of the above channels. Open circles represent the experimental fusion cross sections data. (b) Comparison of the ratio of σ_{4n} to σ_{3n} obtained from PACE using different level densities with the experimental data. (c) Normalized ER cross sections from the measurement and SM calculations (with different level densities) showing the percentage contribution to CF cross section.

- Fig 5.3:** (a) Reduced fusion cross section data and calculations versus normalized energy for present system (${}^6\text{Li} + {}^{152}\text{Sm}$) compared with those for ${}^6\text{Li} + {}^{144}\text{Sm}$ [3]; (b) Ratio of the above cross sections versus normalized energy showing the target dependence; (c) Barrier distributions derived from the fusion cross sections of (a). 116
- Fig 5.4:** (a) Complete fusion cross section (filled circles) and (b) corresponding barrier distribution (filled circles) for ${}^6\text{Li} + {}^{152}\text{Sm}$ compared with no couplings (dotted lines), only target couplings (dash-dot lines), projectile + target couplings (dashed lines) results from CCFULL [46] calculations. Solid lines are obtained by multiplying the CCFULL results with full couplings by a factor of 0.72. 117
- Fig 5.5:** Fusion cross sections predicted by Wong's model using proximity potentials version 1977, 1988 and 2000 are represented by short-dashed, dotted and long dashed lines respectively. Dash-dot, solid and dash-dot-dot lines are obtained by multiplying the above results by 0.74, 0.68 and 0.72 respectively. Filled circles correspond to the measured CF data for ${}^6\text{Li} + {}^{152}\text{Sm}$ reaction 119
- Fig 5.6:** Reduced fusion cross section as a function of reduced energy for the present system (filled circles) along with two other reactions forming the same compound nucleus i.e., ${}^{12}\text{C} + {}^{141}\text{Pr}$ [19] (filled triangles) and ${}^{20}\text{Ne} + {}^{133}\text{Cs}$ [48] (hollow squares). The dashed line represents the CC results and the solid line corresponds to the CC results multiplied by a factor of 0.72 120
- Fig 5.7:** Shows the results of FRESCO calculations for the fusion cross sections obtained by cumulative absorption and barrier penetration with and without breakup coupling. 122

- Fig 5.8:** ICF cross sections (filled circles) contributed by d-capture which are estimated from the formation cross section of $^{152}\text{Eu}^{m2}$ i.e., meta stable state of 2n-ER channel (hollow diamonds). 123
- Fig.6.1:** ER cross sections for ^{148}Tb ($t_{1/2} \sim 60$ min) obtained from two different gamma lines i.e., 489.0 and 784.4 keV coming from same nuclei at 26 MeV. From the figure it is clear that in both the cases the ER cross section is same indicating the stability of analysis procedure. 130
- Fig.6.2:** Half-life fitting of the ER cross sections for ^{148}Tb (3n channel) from two different gamma lines 489.0 & 784.4 keV coming from same nuclei. The $t_{1/2}$ for 3n channel in $^7\text{Li} + ^{144}\text{Sm}$ reaction is 60 min. Dotted line is the fitted line, dashed line is the actual half-life and the solid line is the fitting with varying A_0 (activity) by keeping $t_{1/2} \sim 60$ min fix 131
- Fig.6.3:** ER cross sections for (a) ^{149}Tb (hollow circles) and ^{148}Tb (solid circles) produced in $^7\text{Li} + ^{144}\text{Sm}$ reaction and (b) ^{156}Tb (hollow stars) and ^{155}Tb (solid stars) produced in $^7\text{Li} + ^{152}\text{Sm}$ reaction. Ratio of two dominant ER channels i.e. σ_{3n} to σ_{2n} (solid squares) in 1st reaction and σ_{4n} to σ_{3n} (hollow squares) in 2nd reaction at different beam energies are shown in (c) and (d) respectively. Lines are calculations from Statistical model (see text for details). 132
- Fig.6.4:** (a) Measured complete fusion cross sections for $^7\text{Li} + ^{144}\text{Sm}$ (filled circles) and $^7\text{Li} + ^{152}\text{Sm}$ (open circles). (b) Comparison of CF cross sections involving different projectiles i.e., ^6Li (filled stars) and ^7Li (filled circles) but same target (^{144}Sm), showing the effect of projectile breakup threshold. (c) Same as (b) but involving a different target (^{152}Sm). 136
- Fig.6.5:** (a,b) Measured complete fusion cross-sections for $^7\text{Li} + ^{144}\text{Sm}$ (filled circles) and $^7\text{Li} + ^{152}\text{Sm}$ (open circles) and (c,d) their corresponding barrier distributions. Dash-dot-dot and dashed lines represent the results of coupled-channels calculations for no-coupling case and with full couplings respectively. Solid lines are obtained by normalizing the coupled results by 0.75 and 0.76 for $^7\text{Li} + ^{144,152}\text{Sm}$ reactions respectively. 138
- Fig.6.6:** Fusion cross sections calculated for (a) $^7\text{Li} + ^{144}\text{Sm}$ and (b) $^7\text{Li} + ^{152}\text{Sm}$ reactions by wong's model using proximity potentials "Proximity 2000" are represented by dashed lines. The above cross sections multiplied by a factor of 0.78 and are represented by solid lines. Filled and hollow circles correspond to the measured CF data for $^7\text{Li} + ^{144,152}\text{Sm}$ reactions respectively. 141

Fig.6.7: *Suppression factor ($1-F_{CF}$) as a function of (a) the product of the charges of projectile and target (b) projectile breakup threshold for several reactions involving ${}^6,7\text{Li}$, ${}^9\text{Be}$, ${}^{10,11}\text{B}$ projectiles including the present data. Dashed line is a guide to the eye.* 142

List of Tables

Table 3.1:	<i>Energy and branching ratio of some predominant γ-rays from standard ^{152}Eu source</i>	55
Table 3.2:	<i>The energy and branching ratio of some predominant γ-rays from Standard ^{133}Ba source</i>	57
Table 3.3:	<i>Energy required for different element to produce electron-hole pair.</i>	60
Table 3.4:	<i>The thickness of the different ^ASm samples using Proton beam and ^{16}O beam from FOTIA and TIFR Pelletron respectively</i>	81
Table 3.5:	<i>Reactions investigated and decay characteristics of evaporation residues in the $^6\text{Li} + ^{144}\text{Sm}$ system for ground state (g) and meta stable state (m).</i>	86
Table 3.6:	<i>Reactions investigated and decay characteristics of evaporation residues in the $^6\text{Li} + ^{152}\text{Sm}$ system.</i>	88
Table 3.7:	<i>Reactions investigated and the characteristics of evaporation residues in the $^7\text{Li} + ^{144,152}\text{Sm}$ system</i>	92
Table 4.1:	<i>Experimental cross sections for 2n-ER, 3n-ER, and total fusion with R_σ^{theory} from PACE2 calculations.</i>	97
Table 4.2:	<i>Parameters for AW and CC potential, along with V_B, R_B and $\hbar\omega$.</i>	101
Table 4.3:	<i>Fusion suppression factor for different systems</i>	104
Table 5.1:	<i>Complete fusion data are included in the 5th column of this table as a result of a combination of experimental data —4th column — a sum of ER cross sections for 2n, 3n, 4n and 5n evaporation channels, and the ratio R_σ from PACE calculations included in the 3rd column.</i>	111
Table 6.1:	<i>different ER cross sections (2n channel ^{149}Tb, 3n channel ^{148}Tb) for $^7\text{Li} + ^{144}\text{Sm}$ reaction</i>	134
Table 6.2:	<i>different ER cross sections (3n channel ^{156}Tb, 4n channel ^{155}Tb) for $^7\text{Li} + ^{152}\text{Sm}$ reaction</i>	134
Table 6.3:	<i>Measured complete fusion cross sections for $^7\text{Li} + ^{144}\text{Sm}$ & $^7\text{Li} + ^{152}\text{Sm}$ systems.</i>	135

Table 6.4:	<i>Parameters for CC potential used in CCFULL Calculations along with barrier parameters V_B, R_B and $\hbar\omega$</i>	139
Table 6.5:	<i>Fusion barrier parameters V_B, R_B and $\hbar\omega$ obtained from Proximity potential.</i>	140

Chapter 1

1.1 Introduction

Ever since the discovery of the nucleus by Rutherford in 1911[1] and soon after the establishment of the presence of neutron inside the nucleus, efforts are continued to have a better understanding of atomic nucleus and its properties. From time to time various types of models are predicted [2-5] to understand the nature of the nuclear forces that bound proton and neutron together in the nucleus. Even after more than 100 years of its discovery, the detail knowledge of nuclear forces is far from its complete understanding. This indicates the complicated nature of the nuclear forces. The nuclear physicists have been concerned with the investigation of various kinds of nuclear reaction and nuclear structure of the nucleus using high energy ion beam. The development of the accelerators [6] in addition with the fast electronics, sophisticated detector system, high computing power [7] helped a lot to understand the field of nuclear physics. It has an important phenomenon of paramount importance in the laboratory for the production of artificial nuclei, generation of energy in stellar interior through nucleosynthesis, as well as in the quest for super heavy elements with charges and masses significantly larger than the actinide nuclei [8-12]. Particularly the heavy ion fusion reaction is of interest because of the possibilities to produce super heavy nuclei by fusion reaction. It is well established that the fusion of two many body system can be described to a great degree of precision by model involving just the relative distance between the two objects. The fundamental quantum mechanical tunneling phenomenon is supposed to operate in full-fledged fashion allowing a quantitative description of the fusion of the two nuclei. The fusion of nuclei has received a great degree of attention over last five decades or so owing to the availability of heavy ion accelerators.

1.2 Heavy Ion Reaction

The nuclear reactions are classified into two categories in term of reactions times [13, 14, 15]. The fast “direct reaction” process, where the time interval between the incident

particle and particle emission is close to the time required for a nucleon to cross the nucleus, i.e. 10^{-22} s. On the other hand, the slow “compound nuclear reaction” the time scale is $\sim 10^{-19}$ to 10^{-16} s. The two types of reaction can be distinguished by various experimental features, such as shape of the excitation function, emitted particle spectra and angular distribution etc. Although these times of interactions cannot be measured experimentally but there are indirect experimental evidence for different types of reactions. For example, a familiar bell shape of the excitation function reveals compound nuclear mechanism. The cross section for a particular channel first increases with increasing energy and then decreases with further increase in energy due to competition from other reaction channels, which become energetically possible. In direct reaction, excitation function depends sensitively upon the level structure of the residual nucleus. The outgoing particles from compound nuclear reaction show a continuous Maxwellian distribution in their energies whereas those emitted in direct reaction have discrete energies characteristics of the residual nucleus as shown in Fig. 1.1.

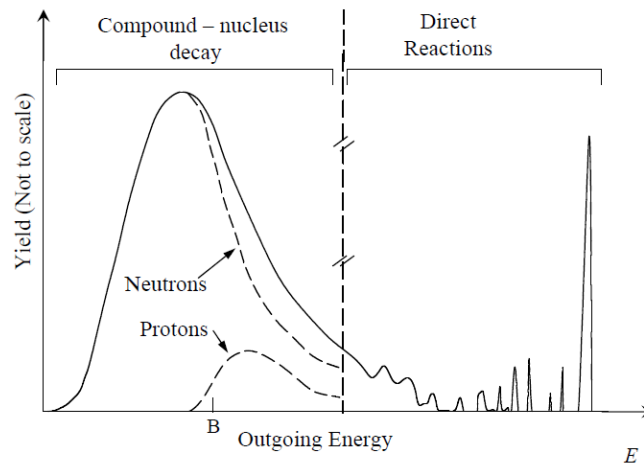


Fig 1.1: Energy spectra of the emitted particles from different reaction processes.

In direct reaction, the emitted particles are partially polarized whereas they are completely unpolarized in compound nuclear reaction. An important distinction lies in the angular distribution of the emitted particles of compound nucleus reaction is characterized by fore and aft symmetry (symmetry around 90°) whereas it is predominantly forward peaked in direct reaction. In low energy studies, the bulk of the particle emission can be attributed to one of these processes. As the isochronous

Cyclotron came into wide usage in the 1960's and higher projectile energies became available for nuclear reaction studies, several new experimental features emerged from systematic investigations of fusion cross-section measurement, elastic scattering, fission fragment mass distribution and many more. There has been an increasing evidence to point out that some reaction takes place within intermediate time between the two extremes. They manifest them self in the high energy tail of excitation function. A gradually changing pattern of angular distribution from forward peaked to fore- and aft symmetry occurs depending on the reaction process. These new experimental features were neither consistence with the compound nucleus model [16,17] nor with the direct reaction model [18].

The main feature of the heavy ion (HI) induced reaction includes (i) large excitation energy transfer (ii) large angular momentum transfer (iii) exchange of large number of nucleons and (iv) special type of interactions, such as multi Coulomb excitation, short range interactions etc. Due to these special features, it is possible to study the properties of the nucleus under unusual conditions, which are not normally meet with light ion studies. Thus, nuclear matter with unusual high density (super dense nuclei) rotating at extremely high speed (due to high angular momentum) and decaying with extremely short radioactive half lives (due to being highly proton-rich and hence far away from the stability line) can be studied in these types of experiments. In addition, super heavy (in the far transuranic region) and super charged (nuclear molecules) nuclei can also be studied.

The study of HI induced reactions is quite intricate due to the involvement of many nucleons in the interaction procedure and interaction partners having large Coulomb barrier (V_B). Therefore, a certain amount of projectile energy $E > V_B$ is required to initiate a heavy ion (HI) reaction. Further, the de-Broglie wavelength (λ) involved in HI- induce reaction is very small. Since, the associated de-Broglie wave length (λ) of the HI's is very small, therefore, the HI induce reactions can be described using semi-classical approach. In semi- classical approach, one consider relative motion of ions classically and angular motion in central force filled. The semi- classical nature of HI-induced reactions makes it possible to give general description of their classical characteristics, particularly their relative motion along with quit well defined orbits in term of distance of closet approach between interacting nuclei (r_{min}) which is related to the impact parameter 'b'[18,19] and may be expressed as ;

$$r_{min} = \frac{b}{\sqrt{\left[1 - \frac{V(r_{min})}{E_{CM}}\right]}}$$

Where, $V(r_{min})$ is the nuclear potential acting between the interacting nuclei and $E_{c.m.}$, is the center of mass energy of the interacting system.

The classical trajectories of projectiles leading to the different modes of reactions may be classified on the basis of impact parameter, as schematically represented in Fig.1.2.

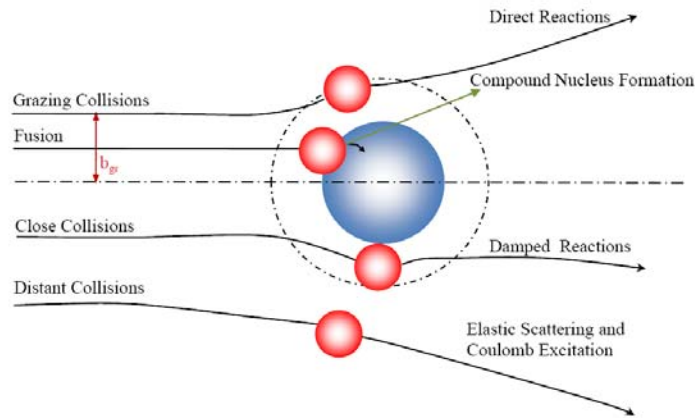


Fig 1.2: A Schematic diagram of different type of heavy ion reactions as a function of impact parameter 'b'.

As can be seen from the Fig.1.2, [1, 56] at projectile energies deep below the fusion barrier (V_B or V_{fus}), the projectile does not touch the target nucleus and is assumed to be elastically scattered through the Coulomb field with a large values of impact parameter, leading to the 'distant collision'. In this 'distant collision' no mass is transfer from projectile to target and/or vice-versa. However, when the projectile and the target nucleus come into close contact then the nuclear reaction will set in, i.e., if the impact parameter is comparable to the sum of the radii of the interacting partners, 'grazing collision' takes place and the projectile can be elastically or in elastically scattered, in which the projectile smoothly graze along the outer surface of the target nucleus. In this process, the system keeps its original asymmetry in kinetic energy, mass, etc. Moreover, when the projectile interacts with the targets nucleus at smaller values of impact parameter with relatively high bombarding energies (just enough to enter in the nuclear field range of target nucleus) then 'deep inelastic collision' (DIC) dominates, in which

the projectile interacts strongly with the target nucleus. In such a case, the nuclear density rise very rapidly in the surface region of target nucleus, and a few nucleons may get transferred from projectile to target nucleus, which is also called as ‘massive transfer reaction’. Further, if the projectile interacts with the target nucleus very strongly at still smaller values of impact parameters, the projectile fuses with target nucleus to form a compound nucleus (CN). The different processes are summarized bellow associated with impact parameter and energy.

(a) Elastic (Rutherford) scattering of Coulomb excitation ($r_{\min} > R_N$)

(b) Transfer reaction or peripheral collision ($r_{\min} = R_N$)

(c) Deep inelastic scattering and incomplete fusion ($r_{\min} \leq R_N$)

(d) Fusion reaction ($r_{\min} \ll R_N$)

Where, $R_N = R_1 + R_2$ is the sum of radii of interacting partners, $b =$ impact parameter.

It has already been mentioned, in HI- induced reactions, when the center of mass energy of the interacting partners is greater than the V_{fus} , they overcome the Coulomb barrier may lose some of the relative energy through nuclear friction to get trapped in the pocket of the potential and ultimately lead to the CN formation. In general, the angular momentum dependent partial reaction cross-section $\sigma^R_l(E)$ at a given energy for these reactions may be given as,

$$\sigma^R_l(E) = \pi \lambda^2 (2l+1) T_l(E)$$

Where, $T_l(E)$ is the transmission coefficient for a particular l -wave.

In the simplest form, one may assume a nuclear potential which depends on the relative separation (r) of two nuclei. In nuclear reactions, emphasis is laid on the interaction between the incident particle and the target nucleus, the nuclear scattering processes are more sensitive to the potential on the nuclear surface region. The $v_{\text{eff}}(r)$ as a function of distance consists of the sum of Coulomb, centrifugal and nuclear potentials and may be given as

$$V_{\text{eff}}(r) = V_{\text{coul}}(r) + V_{\text{nucl}}(r) + V_{\text{cent}}(r)$$

Where; $V_{\text{coul}}(r)$ is the repulsive Coulomb potential, $V_{\text{cent}}(r)$ is the repulsive centrifugal potential and $V_{\text{nucl}}(r)$ is the attractive nuclear potential.

The dependence of the reaction probability for different types of collision on the impact parameter ‘ b ’, can be converted into a dependence on the driving input angular momentum, using the relation $l = m_p v_p b$. In this expression $m_p v_p$ denotes the asymptotic initial momentum of the projectile nucleus relative to the target nucleus. A qualitative

picture of the reaction probability (σ_l) as a function of entrance channel angular momentum (l) is given in Fig 1.3. The area below the solid curve gives the reaction cross section for CN formation (σ_{CN}), deep inelastic collision (σ_{DIC}), direct reaction (σ_D). As indicated in the figure, different regions are overlapping in different l -values. At present it is not clear how large the overlapping regions are for an individual mode of reaction. More over the different modes of reactions can also be understood on the basis of contact duration of projectile and target nuclei, depending upon the relative velocity of projectile. For sufficiently large time of contact corresponding to the small relative velocity, CN formation is more likely to take place. However at high relative velocity where the time of contact is suppose to be very small other reactions like DIC, direct reaction etc. follows. It is now well established that, in HI-induced reactions at energies near and above the Coulomb barrier the most dominating fusion process are: i) complete fusion and ii) incomplete fusion.

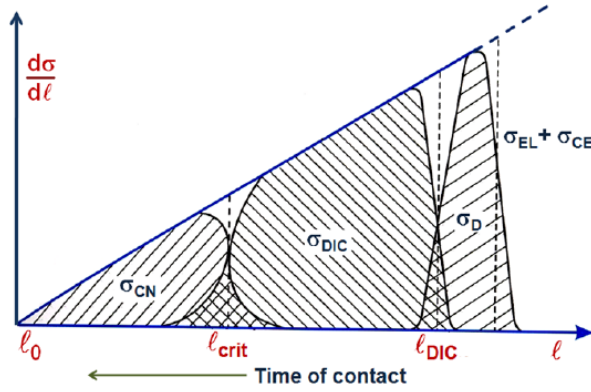


Fig 1.3: A qualitative picture of different reaction as a function of input angular momentum l . Compound nucleus formation (σ_{CN}), deep inelastic collision (σ_{DIC}), direct reactions (σ_D), elastic scattering (σ_e) and Coulomb excitation (σ_{CE}).

1.2.1 Complete fusion

In this process a composite system is formed due to intimate contact and complete amalgamation of projectile and target nucleus leading to the formation of fully equilibrated compound nucleus (CN). Following condition must be satisfied;

- i) The projectile energy must be sufficiently enough to overcome the fusion barrier

$$(V_B = \frac{1.44 Z_P Z_T}{r_0(A_P^{1/3} + A_T^{1/3})}) \text{ of the projectile-target system.}$$

Where, Z_P , Z_T & $A_P A_T$ are atomic number and mass number of incident projectile and target respectively.

- ii) The projectile and target should have maximum overlap for amalgamation to occur.
- iii) The CN cannot be formed, if the entrance channel introduces more input angular momentum than the composite system can sustain.

A schematic representation of CN reaction dynamics is shown in Fig 1.4. The CN reaction is said to occur probably at zero/small values of impact parameter. The kinetic energy of projectile in the centre of mass frame is converted into the excitation energy of the CN. All the kinetic energy which is allowed by energy and momentum conservation is distributed statistically among all internal degrees of freedom. The CN thus formed de-excites by the evaporation of the light nuclear particles from a characteristic equilibrated system but only with small amount of angular momentum. The angular distribution of the emitted light particles from the CN provides different types of reaction process. The evaporation residues (ER) are expected to be concentrated in forward cone due to recoil when the light particle will emit from it. Further, it has been experimentally observed that the CF cross section (σ_{CF}) is smaller than the calculated fusion cross section using single barrier penetration model calculation (SBPM) involving loosely bound projectiles (${}^6,7\text{Li}$, ${}^9\text{Be}$..). [13, 14, 20, 21].

1.2.2 Incomplete fusion

Incomplete fusion (ICF) corresponds to the reaction dynamics where a hot metastable incompletely fused composite system is formed as a result of partial linear momentum transfer (PLMT) from projectile to target nucleus. Here one of the fragment of the projectile will fuse with the target and the other fragment will fly with the beam velocity. A schematic representation of ICF dynamics is shown in Fig.1.5. At relatively higher projectile energies and at a finite values of impact parameters, CF gradually gives way to ICF, where the centrifugal potential (V_{cent}) increases due to projectile-target interaction. Under the influence of centrifugal force field, the driving angular momenta exceed its critical limit (l_{crit}) for CF, as such the attractive nuclear potential (V_{nuc}) is no more strong enough to capture entire projectile. . Fusion of heavy ions is a subject that has been extensively studied in the last few decades. At energies around the Coulomb barrier, the study of fusion mechanism is particularly interesting due to its dependence on the nuclear structure of the colliding nuclei and its strong couplings with

elastic, inelastic and transfer channels. As the bombarding energy increases, the competition with the other reaction mechanisms decreases and corresponding to the

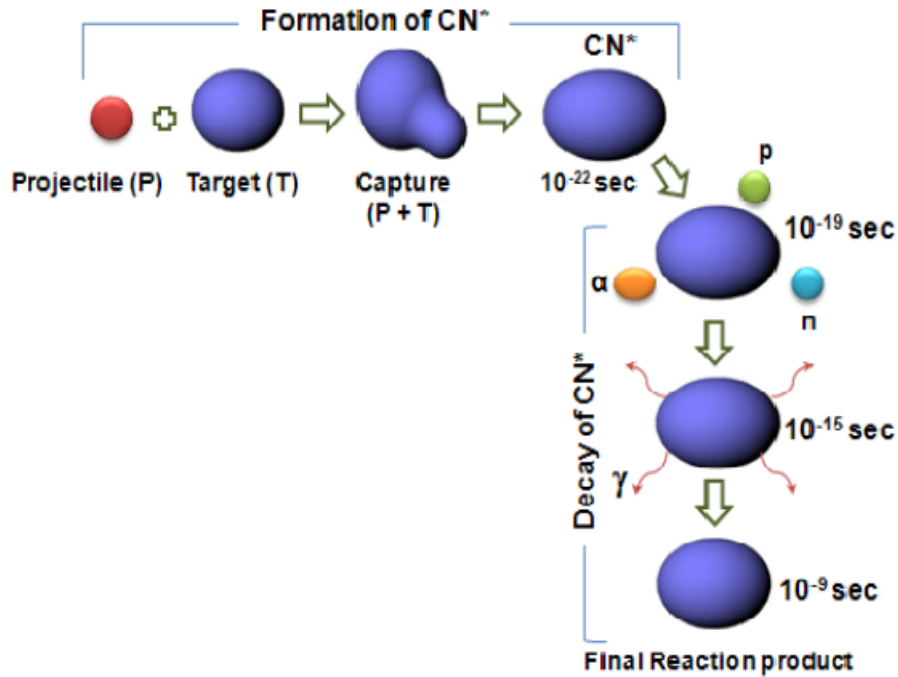


Fig 1.4: Schematic representation of CN formation and its decay via CF-process. The accelerated projectile nucleus collides and fuses with target nucleus lead to excited compound nucleus (CN^*). The CN^* first cools by evaporation of neutrons, protons and/or α -particles. Eventually, it may lose the rest of its excitation energy and almost all of its initial angular momentum by emission of γ -rays.

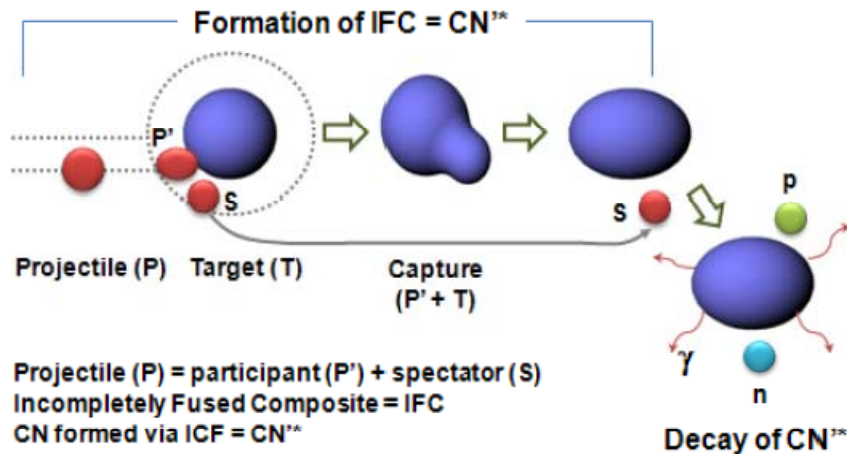


Fig 1.5: Schematic representation of ICF process. As shown, one of the fragments fuses with target nucleus called participant leading to the formation of ICF system, while the remnant moves in forward cone as spectator, with almost projectile velocity. The IFC de-excites in the similar fashion as the CN decay in CF.

fusion cross section. At present, the studies of fusion process are reasonably understood, and their most remarkable effect is the enhancement of the fusion cross section at the sub-barrier energies regime, relative to the predictions of one dimensional barrier penetration models.

1.3 Reaction with weakly/ loosely bound systems

In recent years great theoretical and experimental efforts have been made to investigate breakup process in collision of weakly/loosely bound systems, as well as their effects on the fusion cross section [14]. The fusion of weakly bound nuclei differs in a fundamental way from that of tightly bound ones in so far as the influence of the breakup channel is concerned. Whereas this channel does play an important role in reducing the fusion cross-section of the latter well above the Coulomb barrier, the effect in the former is felt in the vicinity of the Coulomb barrier, owing to the small Q -value involved. What accompanies breakup is the occurrence of ICF or breakup fusion where a part of the mass of the broken projectile is captured by a target while one or more fragments are fly away from the interaction region. Such process competes with the CF, where the whole projectile is absorbed by the target. From the experimental point of view distinguishing of these two processes is a very difficult task, which can only be carried out for some particular projectile target combinations. For this reason, operational definition the CF and ICF are usually adopted. CF is defined as the process in which the total projectile charge fuse with the target while ICF occurs when some charged fragments survive the fusion process. In fact other processes are also contributed as shown in Fig. 1.6 [14]. The different contributions are depicted in a varying degree of complexity. The direct complete fusion (DCF) involves the capture of whole projectile by the target without explicitly going through the breakup channel. The sequential complete fusion is a process (SCF) when breakup does occur followed by the successive capture of the two fragments. From the experimental point of view SCF cannot be distinguish from direct projectile target fusion (DCF), which is not preceded by breakup. Only complete fusion, CF cross section ($CF=SCF+DCF$) can be measured. Further only for a few systems it is possible to measure ICF and CF separately. Most experiments give the total fusion (TF) cross section, corresponding to the sum of $CF+ICF$. It is also very hard to distinguish experimentally ICF from direct stripping

transfer process leading to the same target like nucleus. In this way the TF cross section usually included contribution from the CF, ICF and from some charged particle stripping transfer.

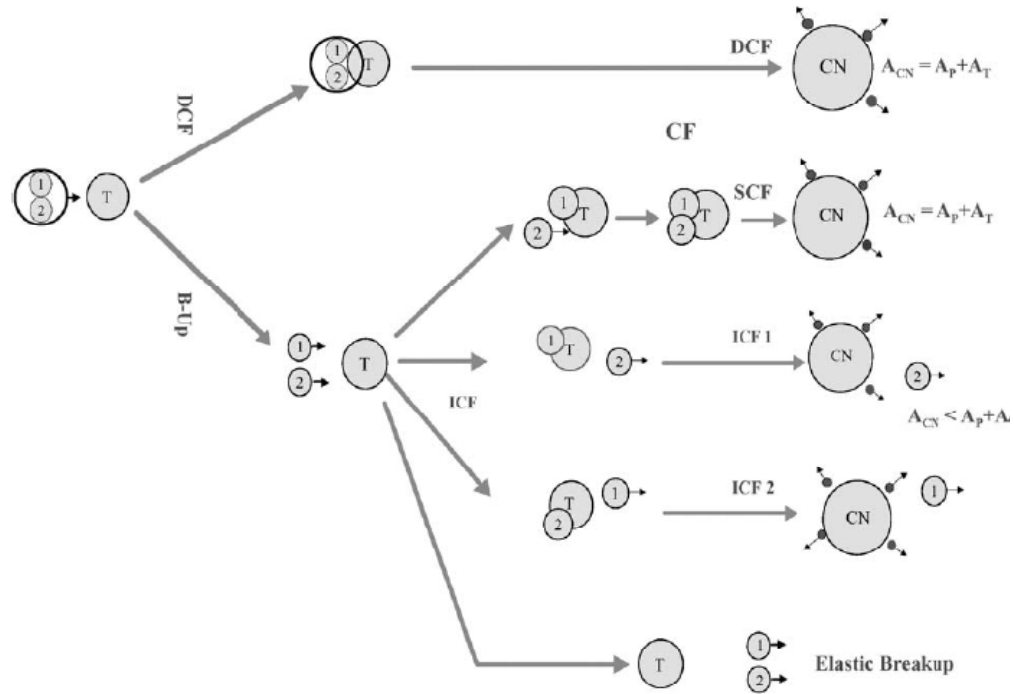


Fig. 1.6: Schematic representation of the fusion and breakup processes that can take place in the collision of a weakly bound projectile.

There is a special interest on this subject due to the recently available radioactive beam of very weakly bound nuclei. Reactions with these nuclei are important in process of astrophysical interest, as well as in the search of mechanisms that produce super heavy elements. The full understanding of reactions induced by the highly intense beam of stable weakly bound nuclei is a key for the study of the reactions induced by low intensity radioactive beams [14].

The most suitable stable nuclei for this type of investigations are ${}^9\text{Be}$, ${}^6\text{Li}$, ${}^7\text{Li}$, due to their small separation energies that should favor the break-up process. It is important to study the role of the breakup (nuclear and Coulomb breakup) of these projectiles on the fusion cross section of different target masses. Also it is important to span the energy

region from sub-barrier to two or three times the barrier energy, because there are evidence that the role of the breakup on the fusion depends on the energy regime.

The studies presented in the literature can roughly be divided in three different domains; light, medium and heavy nuclei. The recent measurement carried out for reactions with heavy targets, namely ${}^9\text{Be}+{}^{208}\text{Pb}$ [21], ${}^9\text{Be}+{}^{209}\text{Bi}$ [22], ${}^{6,7}\text{Li}+{}^{209}\text{Bi}$ [23], ${}^{6,7}\text{Li}+{}^{208}\text{Pb}$ [24] and ${}^{6,7}\text{Li}+{}^{165}\text{Ho}$ [25] etc., show a substantial suppression of complete fusion (CF) cross section above the barrier with respect to SBPM calculations. For reactions with medium mass targets such as ${}^9\text{Be}+{}^{64}\text{Zn}$ [26], ${}^{6,7}\text{Li}+{}^{64}\text{Zn}$ [27], ${}^{6,7}\text{Li}+{}^{60}\text{Co}$ [28], no suppression of total fusion cross section can be seen at energies near the barrier. For reaction with the light mass nuclei though fusion cross section measurements have been reported for various system, like ${}^{6,7}\text{Li}+{}^9\text{Be}$ [29], ${}^{6,7}\text{Li}+{}^{12,13}\text{C}$ [30-33], ${}^{6,7}\text{Li}+{}^{16}\text{O}$ [32, 34-37], ${}^7\text{Li}+{}^{11}\text{B}$ [38], ${}^9\text{Be}+{}^9\text{Be}$ [38], ${}^9\text{Be}+{}^{13}\text{C}$ [39], ${}^9\text{Be}+{}^{27}\text{Al}$ [40], ${}^6\text{Li}+{}^{90}\text{Zr}$ [41], ${}^{6,7}\text{Li}+{}^{27}\text{Al}$ [27] etc.. there exists large experimental disagreements between measurements done using different techniques.

The fusion cross section measured for systems, ${}^{6,7}\text{Li}+{}^{12,13}\text{C}$ [30-33], ${}^{6,7}\text{Li}+{}^{16}\text{O}$ [34-36], ${}^9\text{Be}+{}^9\text{Be}$ [38] by detecting the γ - ray emitted from the evaporation residue (ERs) show the fusion cross section for these systems to be close to the total reaction cross sections at energies bellow (E_{cm})~8 MeV around the respective Coulomb barrier. The reaction cross sections were calculated using optical model with parameters obtained from fitting of the elastic scattering data, in the energy region of fusion cross sections measurements. On the other hand, the cross section measured for ${}^{6,7}\text{Li}+{}^9\text{Be}$ and ${}^{6,7}\text{Li}+{}^{12,13}\text{C}$ [29,31] by the direct reaction of evaporation residues, show a strong suppression of fusion cross section, particularly at low energies. This has been interpreted by Takahashi *et. al.*[29] that the result of breakup is due to the small separation energies of the ${}^{6,7}\text{Li}$ nuclei. This interpretation is in conflict with the Mukherjee *et.al.*[36,37] when it has been argued from the measurements of ${}^{6,7}\text{Li}+{}^{16}\text{O}$ that the large gamma ray cross section observed do not support breakup of ${}^{6,7}\text{Li}$ prior to fusion. For the systems ${}^{6,7}\text{Li}+{}^{12,13}\text{C}$ show the large discrepancies in the overlapping energy region.

The discrepancy has been resolved experimentally by measuring the fusion cross section for ${}^7\text{Li}+{}^{12}\text{C}$, with ${}^{12}\text{C}$ beam of energies 10.5 and 22 MeV from 14UD pelletron accelerators at the Australian National University. This measurement employed the direct detection of evaporation residues formed following the fusion of ${}^7\text{Li}$ with ${}^{12}\text{C}$. Direct detection of ERs for this system poses experimental difficulties due to low

kinetic energy of the ERs, particularly when ${}^7\text{Li}$ used as the projectile. In the above work the higher momentum of ${}^{12}\text{C}$ projectile produced ERs with kinetic energy nearly twice to those using conventional kinematics [42]. It needs to be mention here that contributions of the ERs bellow 4MeV could not be detected owing to the experimental limitations. It was found from PACE [43] calculations that this missing contribution was $\sim 20\%$ at $E=10.5$ MeV, but was negligible at $E=22$ MeV. The 10.5 MeV data when corrected for this missing contribution agree well with the gamma ray measurement. This reveals that the direct detection measurements [29] were underestimated in the energy region $E\sim 8$ MeV. Besides in these cases, the total fusion cross sections are very close to the total reaction cross sections, barely leaving any room for breakup to contribute in the region of measurement.

Total fusion cross sections have also been measured for ${}^{6,7}\text{Li}+{}^{27}\text{Al}$ [27] above the barrier and compared with the existing data of ${}^9\text{Be}+{}^{27}\text{Al}$ [40], ${}^{11}\text{B}+{}^{27}\text{Al}$ [43] and ${}^{16}\text{O}+{}^{27}\text{Al}$ [44]. The works show that the fusion excitation functions for all these systems are quite similar, regardless of the projectile separation energy, there by indicating no signature of fusion hindrance, when compared with fusion cross sections of the strongly bound nuclei ${}^{12}\text{C}$ and ${}^{16}\text{O}$. It has been conjectured by Padron *et al.*[27] the direct breakup cross section for the three weakly bound nuclei may be large and quite different for each of these projectiles and they may increase the reaction cross section, but they do not affect the total fusion cross section(CF+ICF), at least within the limits of experimental uncertainties.

The interaction at Coulomb barrier originated by the loosely bound nuclei is a relevant research topic because new nuclear physics phenomena are expected to occur. Theses nuclei are bigger than the stable ones since they have a RMS radius considerably larger than that deduced from the $r_0A^{1/3}$ systematic. This implies a considerable lowering of Coulomb barrier, 1-3 MeV, $\sim 5\%$ and then a strong increase in the sub barrier fusion cross section, since it depends more or less exponentially on the barrier height. These nuclei are less bound than stable ones. The binding energy per nucleon is in the range of 0.1 to 1.0 MeV compared to ~ 8 MeV of the stable nuclei. This means that all breakup related phenomena are expected to be stronger in particular the coupling of the continuum via suitable excitation mode to the magnitude of the fusion cross section. Practically speaking the breakup arguments can be and it has effectively been utilized to make opposite conclusion, namely that fusion cross sections around the barrier can be enhanced or hindered. The effect of the breakup of weakly bound nuclei on the fusion

cross section is a subject of major interest. The understanding of this is important for the production of the nuclei near neutron drip line and super heavy nuclei.

1.4 General motivation of the thesis

The aim of the present thesis is to understand the effect of breakup of loosely bound projectile on fusion process. Fusion, the word itself tells the amalgamation of two nuclei to form a single equilibrated CN. As we know both (projectiles/target) made up of protons (p) and neutrons (n), there must be a Coulomb repulsion between them. So in order to fuse with the target, the projectile must overcome the Coulomb barrier energy (V_B). Classically, if the energy of the projectile is less than the V_B fusion will not take place but according to quantum mechanics there are certain probabilities that the projectile can fuse with the target by passing through the barrier even if the incident energy $E < V_B$ by quantum tunneling. The heavy ion fusion barrier arises due to the combined effect of Coulomb (repulsive) + nuclear (attractive) + centrifugal (repulsive) potentials, assuming the projectile have the head on collision with the target (i.e. $L=0$) and with the increasing value of L is shown in Fig.1.7 [45]. The process by which some of the incident projectile pass through the V_B and fuse with the target to form an equilibrated compound nucleus is called as barrier penetration and the transmission probability depends on the height of the barrier, width of the barrier and the energy of the incident projectile. So for a given set of projectile and target we should have one

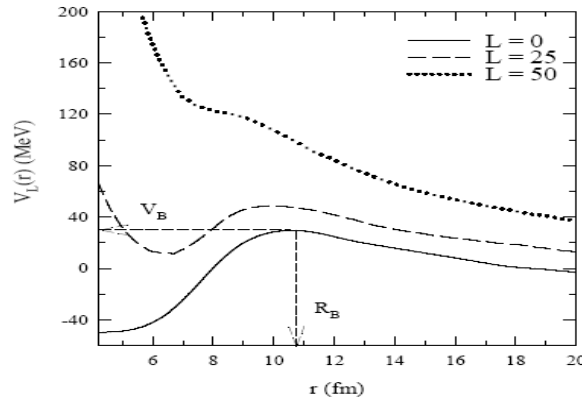


Fig.1.7: Schematic representation of the barrier (V_B) height, R_B the barrier radius for different values of L (orbital angular momentum).

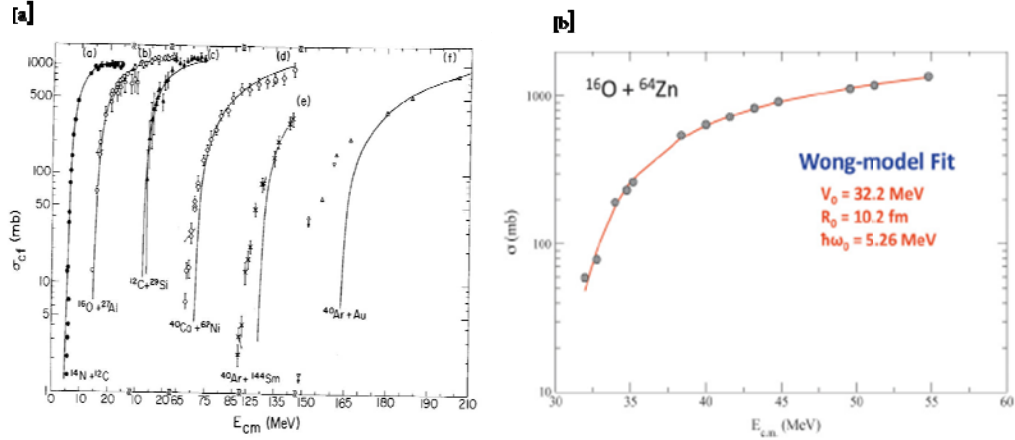


Fig.1.8: [a] The single barrier penetration model calculation for different projectile targets (^{12}C , ^{27}Al , ^{29}Si) fits the expt. data very nicely. [b] Wong model fitted for $^{16}\text{O}+^{64}\text{Zn}$ system quite well.

value for V_B and R_B for head on collision. The barrier penetration model (BPM) fits the experimental data very well. Some of the examples are shown in Fig.1.8 for some systems ($^{16}\text{O}+^{27}\text{Al}$, $^{14}\text{N}+^{12}\text{C}$, $^{40}\text{Ar}+^{144}\text{Sm}$, $^{40}\text{Co}+^{64}\text{Ni}$ etc.) and also for $^{16}\text{O}+^{64}\text{Zn}$ [46]. When a heavy target was used, the experimental results for fusion cross section were found much higher than the calculated ones using BPM model. Some examples are shown in Fig.1.9 which reveals that specially at lower energy say at $E < V_B$, the fusion cross section was found to be much more large compared to what was expected from BPM model. It was also found that the fusion cross section at below barrier ($E < V_B$) increased with the increasing mass of the target with same projectile, but the fusion cross sections are same at above barrier. This is again more surprising. Investigations are carried out to resolve this problem by introducing deformation and vibration in the calculation [47] and also coupling [30] of different inelastic states, transfer channels, breakup channels to the incident channel and they reproduce the experimental data quite successfully as shown in Fig.1.10.

Some of the models which were being used for couplings are CDCC, FRESKO, CCFULL, CCFUS etc. It will also be clear, if we think of a classical picture, if the target will be deformed one then depending on which side, the projectile interact with target. The separation distance will change and that leads to the change of V_B and R_B , which was earlier single valued. In a reaction, all orientation are possible and for each orientation there will be one V_B , R_B and for each V_B and R_B one transmission coefficient will arise. Practically all orientations will be possible and the sum over all

gives rise to the enhanced fusion cross section compared to the prediction by the single barrier calculation (BPM). A schematic representation is shown in Fig.1.11. The effect of breakup of loosely bound stable (${}^6,7\text{Li}$, ${}^9\text{Be}$) or radioactive nuclei on fusion process is a subject of current experimental and theoretical interest [48,49] because in this case the

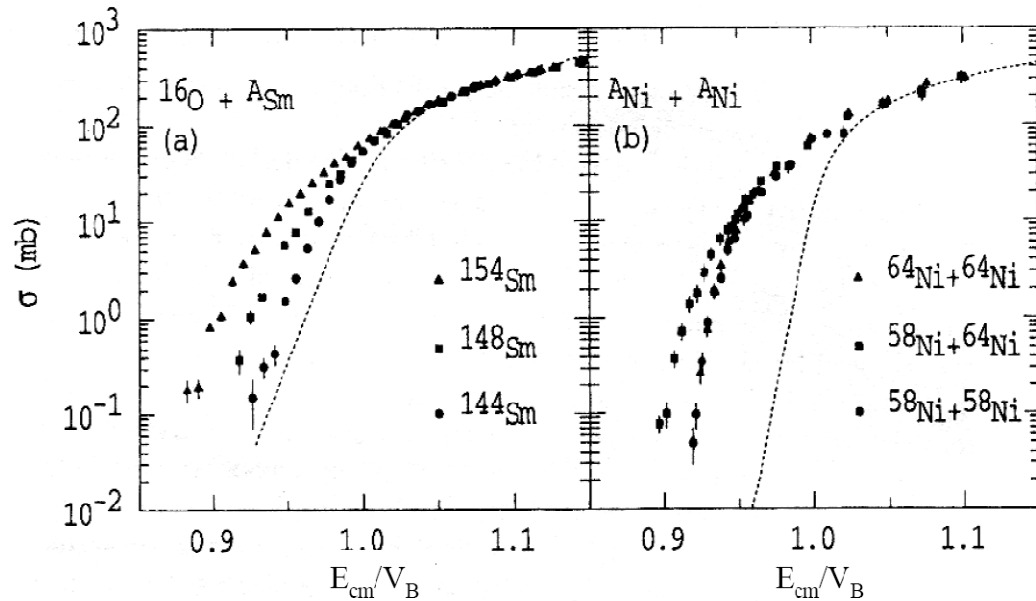


Fig.1.9: Enhancement of the fusion cross section below the Coulomb barrier compared to the single barrier penetration model calculations for ${}^{16}\text{O} + A_{\text{Sm}}$ and $A_{\text{Ni}} + A_{\text{Ni}}$.

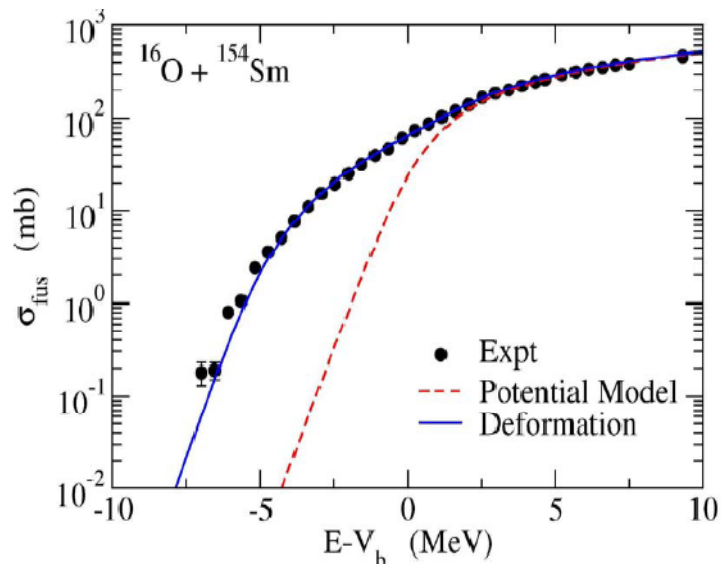


Fig 1.10: Fusion cross section for ${}^{16}\text{O} + {}^{154}\text{Sm}$. The dotted line corresponding to the single barrier penetration model (BPM, SBPM) calculation. Solid line is the calculation by using coupling to the rotational levels of the target which fitted the data very nicely.

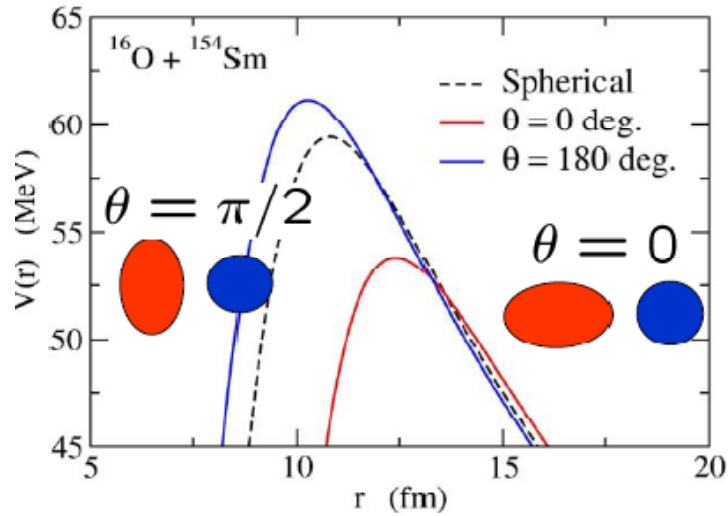


Fig 1.11: A schematic representation of the rotational coupling of the target for ^{154}Sm . Indicating the shifting of barrier positions depending on the orientation of the projectile and target.

binding energy per nucleon is less than 1 MeV compared to the stable nuclei ~ 7 to 8 MeV. Although sub-barrier fusion involving stable nuclei is well understood, there are contradictory results and predictions about enhancement or suppression of fusion cross-section (σ_{fus}) over predictions for single fusion barrier, around the Coulomb barrier when one of the collision partners is a loosely bound nucleus. One of the examples is shown in Fig. 1.12. It is shown that the experimental data for fusion cross section is more/less at below/above barrier energies compared to the single barrier penetration model (SBPM) predictions are enhanced/suppressed. Investigations of the fusion process have been made with stable loosely bound $^6,7\text{Li}$ [29,28,23-25,27-38] and ^9Be [21,22,26,38] however with different conclusions about fusion enhancement/suppression, when compared with stable isotopes and/or coupled channel calculations [50,51]. There are theoretical works which predict either suppression of the complete fusion cross sections [52,53] due to breakup of loosely bound nucleus or enhancement [54] of the same due to coupling of the relative motion of the colliding nuclei to the breakup channel. Also, the large radii of such loosely bound nuclei and the coupling to low lying resonant states should tend to enhance the fusion cross-section. Hagino *et al.* [55] performed an improved coupled channel calculation which predicts

the enhancement of fusion at sub-barrier energies and reduction at above barrier energies. An understanding of breakup and fusion is directly relevant to produce nuclei

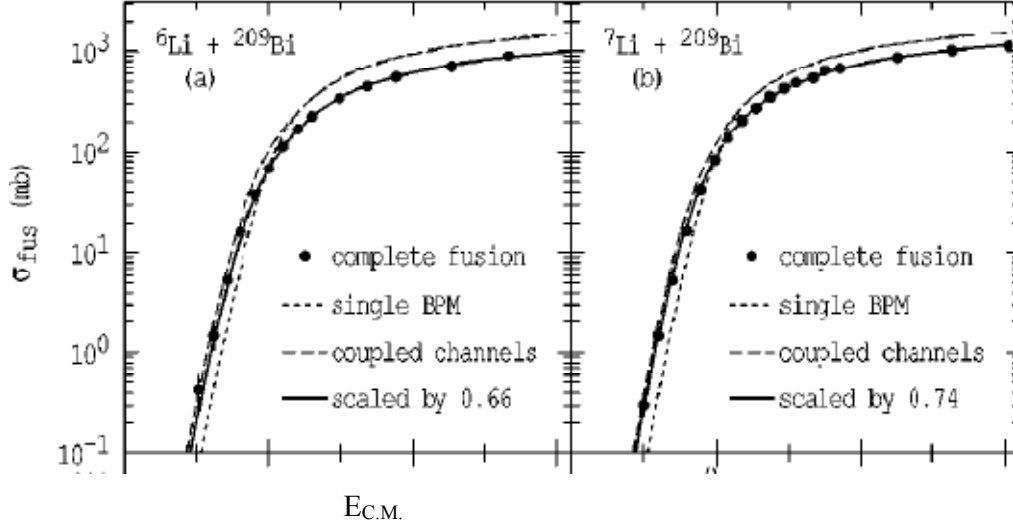


Fig 1.12: Complete fusion cross section for $^{6,7}\text{Li}+^{209}\text{Bi}$. The dotted line is the single BPM calculation; the dash line is the calculation by using the coupled channel (CC) and the solid line is multiplying the factor 0.66, 0.74 with the CC calculation to explain the data [57].

near the drip line and possibly super heavy nuclei. But experimentally such studies are limited due to low intensities of unstable beam currently available. A light nucleus such as ^6Li , which breaks up into $^4\text{He} + ^2\text{H}$ with breakup threshold of only 1.48 MeV, has a large breakup probability. Fusion with such a nucleus is ideal for the quantitative test of theoretical models, which is also useful as comparators for fusion measurements with other unstable beams. The study of the effect of the breakup process on the fusion cross section has become a very interesting subject of investigation and in the present situation it is still very far from being fully understood. At present there are quite a few controversial experimental observations. From the theoretical side, there are models that predict the fusion cross section enhancement, when compared with the fusion induced by strongly bound nuclei, due to additional breakup channel. This enhancement should be particularly important at sub barrier energy where the coupling effects on the fusion may be strong. On the other hand some models suggest the hindrance of the complete fusion, due to lose of incident flux in this channel, caused by the breakup. There are

Chapter 1: Introduction

predictions of fusion cross section enhancement at sub barrier energies and fusion hindrance above barrier energies, both effects originated from the break up process.

In the present thesis we have studied the fusion for ${}^{6,7}\text{Li}+{}^{144,152}\text{Sm}$ systems. We have used the activation technique and gamma ray counting method. There is no data available for this system and as it is medium mass region so this will act as a bridge between the light mass region and the heavy mass region. We have adopted the simple experimental set up (Activation technique) to separate out the complete fusion (CF) and the incomplete fusion (ICF) part. In addition, the effect of target deformation on the fusion cross section has also studied using ${}^{152}\text{Sm}$ as it is a deformed target. Comparing the experimental data of ${}^{6,7}\text{Li} + {}^{144}\text{Sm}$, we have studied the effect of projectile breakup threshold on fusion cross section as ${}^7\text{Li}$ has more break up threshold (2.47MeV) than the ${}^6\text{Li}$ (1.47 MeV). We have compared the present data with the previous data available in literature and found some systematic also. This has given a clear picture of the projectile breakup effect on fusion cross section in addition with the effect of target deformation on fusion cross section.

This thesis consists of seven chapters. Chapter 1 deals with the general introduction about complete and incomplete fusion reaction, literature survey and the motivation for present work. Chapter 2 contains an outline of statistical model and coupled channels calculations. Chapter 3 devoted to the experimental details and data analysis. Chapters 4, 5 and 6 describe the results and discussion on various systems, comparison of the experimental results with the theoretical predictions and investigation out come. Finally the summary and conclusion of the investigation carried out in the present thesis along with future perspective are presented in chapter 7.

References:

- [1] E. Rutherford, “Scattering of α & β Particles by matters & the structure of the atom”, Philos. Mag. Vol. 6, PP. 21(1911).
- [2] A. Gavron, Phys. Rev. C 21, 230 (1980).
- [3] K. Hagino *et al.*, Comput. Phys. Commun. 123, 143(1999)
- [4] Krane Kenneth S., “Introductory nuclear physics”, Jhonwiley& son, PP. 68(1988).
- [5] Mottelson B. ,Physica script, 1125 (2006)
- [6] Article, “Van-de-graaff generator” in electrical engineering hand book, CRC , Press, Florida, USA (1993)
- [7] Hoffman. Allan *et al.*, super computer: direction in technology & applications. National academics, PP. 35-47(1990)
- [8] D. J. Hind *et al.*, EPJ web of conference 17, 04001(2011)
- [9] M. F. Itkis *et al.*, Nucl. Phys. A 787,150c (2007)
- [10] R. du Rietz *et al.*, Phys. Rev. Lett. 106, 052701(2011)
- [11] E. M. Kozulin *et al.*, Phys. Lett. B 686,227(2010)
- [12] Y. Aritomo *et al.*, Nucl. Phys. A 734,180(2004)
- [13] C.H. Dasso *et al.*, NPA 405, 381(1983), Phys. Lett.B 183, 141(1987).
- [14] L. F. Canto *et al.*, Phys. Rep. 424,1(2006)
- [15] P. E. Hodgson, E.Gadioli and E.Gadioli-Erba, Introductory Nuclear Physics, Clarendon press Oxford (1997)
- [16] N. Bhor, Nature137,344 (1936)
- [17] S. N. Ghosal, Phy. Rev. 80,1939(1950)
- [18] N. Austern, Direct nuclear Reaction Theory, Wiley Inter Science, New York (1956)
- [19] J. Wilczynski *et al.*,Nucl. Phys. A. 373,109(1982)
- [20] A.C. Berriman *et al.*, Nature, 413,144(2001)
- [21] M. Dasgupta *et al.*, Annu. Rev. Nucl. Part. Sci 48 (1998) 401
- [22] C. Signorini *et al.*, Eur. Phys. J. A5,7(1999)
- [23] M. Dasgupta *et al.*, Phys. Rev. C 66, R041602 (2002)
- [24] Y. W. Wu *et al.*, Phys. reV. C 68, 0444605(2003)
- [25] V. Tripathi , *et al.*, Phys. Rev. Lett. 88 (2002) 172701
- [26] S. B. Moraeset. *et al.*,. Phys. Rev. C 61, 064608(2000)
- [27] I. Padron *et al.*,. Phys. Rev. C 66, 044608(2008)

Chapter 1: Introduction

- [28] C. Beck, *et al.*, Phys. Rev. C 67 054602,(2003)
- [29] J. Takahashi, *et al.*, Phys. Rev. Lett 78, 30(1997)
- [30] A. Mukherjee *et al.*, Nucl. Phys. A. 596,299(1996)
- [31] L.C. Dennis *et al.*, Phys. Rev. C 26,981(1982)
- [32] J. F. Mateja *et al.*, Phys. Rev. C 30,134(1984)
- [33] A. Mukherjee *et al.*, Nucl. Phys. A. 635,205(1998)
- [34] C.J.S.Scholz *et al.*, Z. Phys. A 325,203(1986)
- [35] K. Glasner *et al.*, Nucl.Phys. A 452,150(1986)
- [36] A. Mukherjee *et al.*, Nucl.Phys. A 645, 13(1999)
- [37] .Muhherjee and B. Dasmahapatra, Phys. Rev C 63, 017604(2000)
- [38] Muhherjee and B. Dasmahapatra, Nucl. Phys. A 614,238(1997)
- [39] B. Cujec *et al.*, Nucl. Phys. A. 453,505(1986)
- [40] R.M. Anjos *et al.*, Phys. Lett. B 534,45(2002)
- [41] H. Kumawat, *et al.*, Phys.Rev. C 86, 024607 (2012)
- [42] A. Mukherjee *et al.*, Phys. Lett. B 526,295 (2002)
- [43] R. M. Anjos *et al.*, Phys. Rev.C 42, 044607(2003)
- [44] B. B. Back et. al. Phys. Rev C 68,044607(2003)
- [45] N. Keeley *et al.*, Prog. Part. Nucl. Phys. 59, 879(2008)
- [46] L.C. Vaz *et a.*, Phys. Rep. 69,373(1981)
- [47] C.H. Dasso *et al.*, NPA 405, 381(1983), Phys. Lett.B 183, 141(1987).
- [48] L. f. Canto *et al.*, Phys. Rep. 424,1(2006)
- [49] N. Keley , *et al.*, Prog. Part. Nucl. Phys. 59, 879 (2008)
- [50] V. tripathi *et al.*, Phys. Rev. Lett. 88 ,172701 (2002)
- [51] C. Beck *et al.*, Phys. Rev. C 67, 054602 (2003)
- [52] A. Diaz-Torres *et al.*, Phys. Rev. C 65, 0024606 (2002)
- [53] A. Diaz-Torres *et al.*, Phys. Rev. C 68, 044607 (2003)
- [54] M. S. Hussein *et al.*, Phys. Rev. C 46 ,2377 (1999)
- [55] K. Hagino *et al.*, Phys. Rev. C 61, 037602 (2000),
<http://www.nucl.phys.tohoku.ac.jp/~hagino>
- [56] J. Toke and W.U. Schroder, Ann. Rev. Nucl. Science 42,401(1992)
- [57] M. Dasgupta *et al.*, Phys. Rev. C 66, 041602 (R)(2002)

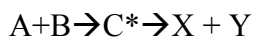
Chapter 2

Theoretical models

To analyze the experimental data (fusion cross section, fission fragment angular distribution, elastic angular distribution...) observed using loosely bound nuclei (${}^6\text{Li}$, ${}^7\text{Li}$, ${}^9\text{Be}$...) and to understand the underlying physics different theoretical models have been used. Broadly, there are two category of models that are used to understand i) the compound nucleus formation and decay products by statistical model and ii) the effect of coupling on fusion cross section by coupled -channels model. A successful model must satisfy two criteria: (1) it must reasonably well account for previously measured nuclear properties and (2) it must predict additional properties that can be measured in new experiments. Therefore models are inevitable for making predictions and interpretation of experimental results. In this chapter we will discuss about the relevant theoretical models.

2.1 Formation of compound nucleus

When two nuclei collides with each other they form a composite system called compound nucleus (CN) and this process is called complete fusion (CF), where the whole projectile will fuse with the target. Then the composite system equilibrates in all degrees of freedom (e.g. energy, angular momentum, mass, shape) with time and forgets everything about the entrance channel. Symbolically,



Where 'C' is the CN, A is the incident particle (projectile), B is the target nucleus and X, Y are the emitted particle and corresponding evaporation residue respectively. These two entrances and exit channels are treated independent of each other. Study of the formation as well as decay of such excited compound nucleus provides a wealth of information about the dynamics of the processes and influence of nuclear structure of the participant on reaction dynamics. When the incident energy of the projectile is not so large, the reaction process is

predominantly governed by quantum tunneling over the Coulomb barrier (VB) created by the combination of repulsive Coulomb interaction, the attractive nuclear interaction and repulsive centrifugal force. Extensive experimental as well as theoretical studies have revealed that the fusion reactions at energies near and below the Coulomb barrier are strongly influenced by couplings of the relative motion of the colliding nuclei to several nuclear intrinsic motions. In a simple conceptual picture if the system (projectile+target) enters in to the pocket created by the addition of all potential (Coulomb, nuclear and centrifugal) as shown in Fig 2.1 for $^{64}\text{Ni}+^{64}\text{Ni}$ [1] it leads to fusion. Theoretically, the simplest approach to heavy-ion fusion

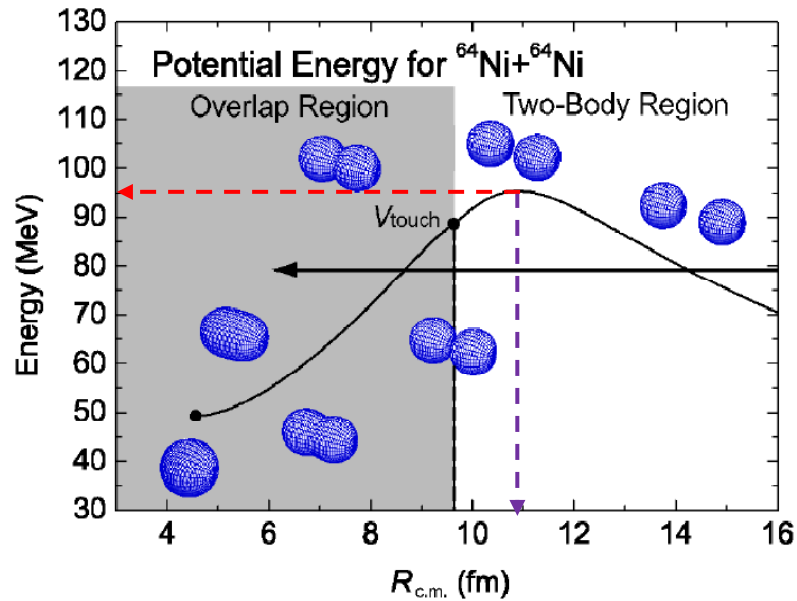


Fig 2.1: Fusion process with relative distance between the target and projectile (i.e. time snap-soft) are shown. Which clearly shows the pocket for fusion (shaded region). The barrier height and barrier radius has also been shown in red (dashed) and violet (dotted) line.

reactions is to use the one dimensional potential model where both the projectile and the target are assumed to be structure less. The potential between the projectile and the target is given as a function of the relative distance ‘r’ between them. It consists of three parts: $V_0(r) = V_N(r) + V_C(r) + V_L(r)$. $V_N(r)$ is the nuclear potential, $V_C(r)$ is the Coulomb potential given by $V_C(r) = \frac{Z_p Z_T e^2}{r}$ in the outside region where the projectile and the target do not overlap

with each other, and $V_L(r)$ is the centrifugal potential. A typical potential $V_0(r)$ for the s -wave ($l=0$) scattering is shown in Fig 2.2. One can find that a potential barrier appears due to a strong cancellation between the short-ranged attractive nuclear interaction and the long-ranged repulsive Coulomb force. The addition of both the Coulomb and the nuclear potentials generates a barrier referred as the Coulomb barrier $V_B(r)$ and has to be overcome by the incident projectile for fusion reactions to take place for $l=0$ i.e., for an head on collision. The arrow in Fig. 2.2 is the touching radius, where the projectile and the target nucleus begin to overlap. This is a characteristic feature for systems where the charge product $Z_P Z_T$ is not so large. Akyuz-Winther parameterized Woods-Saxon form of nuclear potential is given as

$$V_N(r) = -\frac{V_0}{1+\exp\left(\frac{r-R_0}{a}\right)}, \text{ Where, } V_0=16\pi\gamma\check{R}a, R_0=R_p+R_T+0.29,$$

$$R_i=1.233A^{1/3}-0.98A^{-1/3} \text{ (i=P, T), } \check{R}=R_p R_T / (R_p+R_T), \gamma = \gamma_0 \left[1-1.8 \left(\frac{N_P-Z_P}{A_P}\right)\left(\frac{N_T-Z_T}{A_T}\right)\right],$$

where $a=0.63$ fm, and $\gamma_0=0.95$ MeV fm⁻²

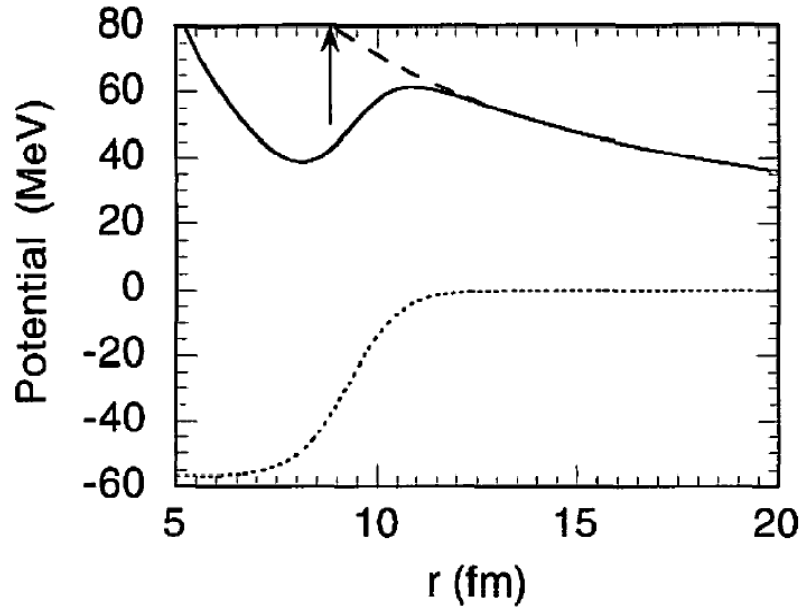


Fig 2.2: A typical potential barrier for the s -wave ($l=0$) scattering as a function of the relative distance between the projectile and target. The dotted and the dashed lines are the nuclear and the Coulomb potential, respectively. The total potential is denoted by the solid line. Also shown by arrow is the touching radius where the projectile and the target nuclei begin to overlap.

2.2 Decay of compound nucleus (CN)

2.2.1 Statistical model

As we know in a typical nucleus the number of nucleons are much less than the Avogadro's number ($\sim 6.023 \times 10^{23}$) and they follow quantum mechanics. Hence, the statistical approach taken for understanding various phenomena is questionable. However, when the projectile interacts with the target nucleus it form an intermediate state called compound nucleus (CN) with a very high excitation energy ($E_x = E_{c.m.} + Q$) and very high angular momentum with a broad spreading (J^π), which give rise to a rapidly increasing number of discrete level [2,3]. In a typical medium mass nuclei of $A \sim 100$, the density of level may be more than a million/MeV at $E_x = 10$ MeV. So due to a large number of nucleons in the CN and large number of levels with spreading angular momentum (J), A statistical approach has been considered to deal with the situation and to explain different properties of the nuclei. The subsequent emission of charge particle and neutron (n) are called as the evaporated particle and the remaining CN is called evaporation residue (ER). During dealing with CN with high E_x and high spin (j^π) with wide spreading an important quantity is called nuclear temperature (T), which is a useful parameter to discuss various types of reaction. Essentially this temperature (T) is not our classical temperature, it is linked with E_x and the density of levels in the CN. A more pioneering work has been done on this by Bethe [4] and Weisskopf [5] to understand thermodynamic concept in nuclear physics. The CN lives long enough for a complete statistical equilibrium to be established. Particles are emitted from the CN by a statistical process similar to the evaporation of the molecule from the liquid drop when it was heated up. The statistical model assumes the decay of the CN which is thermally equilibrated in all degrees of freedom (mass, energy, spin).

Whenever an incident particle (incident particle or projectile) will interact with the target nucleus, a CN will form over a wide range of E_x and J . A schematic representation of the angular momentum J vs E_x is shown in Fig. 2.3 For a given target projectile combination once the CN equilibrates, it de-excites by losing bulk of its energy through the emission of particle say ($n, p, \alpha \dots$). Once the nucleus lands below the particle threshold (~ 8 MeV) called yrast line, it is energetically forbidden to emit particles and then it emits characteristic gamma (γ) ray to approach the ground state ($J = J_{g.s.}, E_x = 0$). Statistical model is the model

which describes the decay of a thermally equilibrated CN. The main assumption which goes under the calculation is that all possibilities of CN decay are intrinsically equally likely and are governed by the factor such as the density of the final residual state and the barrier penetration factor. The important ingredients which decide the decay of the CN are the level density and the transmission coefficient for inverse reaction.

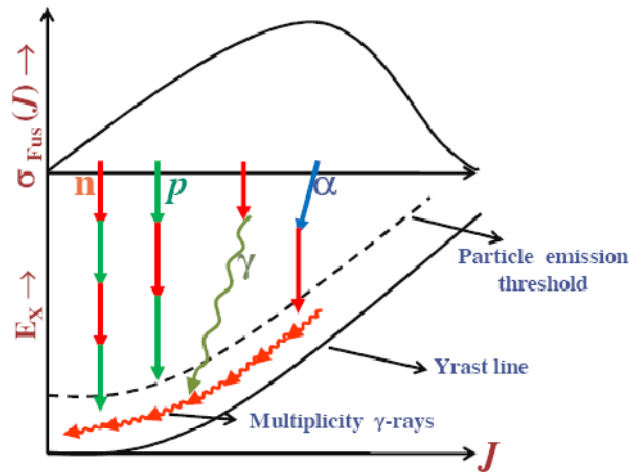


Fig 2.3: Statistical decay of a CN populated at a given E_x and over a broad window of J through particle (neutron (n), proton (p) and alpha (α -particle)) and gamma (γ -ray) emission.

2.2.2 Level density

The level densities are the key ingredients in a Statistical model calculation. Simple analytical expression for level density of a nucleus with a given excitation energy E_x and angular momentum J was obtained by Bethe [4] on the basis of Fermi gas model [6,7] as.

$$\rho(u) = \frac{\sqrt{\pi}}{12 \cdot a^4 \cdot u^4} * \exp(2\sqrt{au}) \dots \dots \dots (1)$$

$$\rho(u, J) = \frac{(2j+1)}{2\sqrt{2\pi\sigma^3}} * \rho(u) * \exp\left(\frac{-(J+\frac{1}{2})^2}{2\sigma^2}\right) \dots \dots \dots (2)$$

Where $a = \pi^2 g/6$, is the level density parameter, proportional to single particle state density ‘g’ near the Fermi surface and σ^2 is the spin cut off factor. U is defined as the $U = E_x - E_{rot}(J)$. where, $E_{rot}(J)$ is the rotational energy. The underlying physical assumptions in Fermi gas model are not sufficiently sophisticated to take into account some of the observed variation of the level density (shell effect, pairing effect, collective effects). More rigorous model that takes into account all of these are very laborious to run which limits their application to

Chapter 2: Theoretical models

analyze the experimental data. Hence, a phenomenological prescription of level density based on certain experimental data is performed in Statistical Model analysis. The effective excitation energy is given as

$$U^* = U - \{\delta_Z + \delta_N, \delta_Z, \delta_N, 0 \text{ for even-even, even Z, even N, odd-odd} \} \text{ nuclei}$$

Where, $\delta_X \rightarrow$ is the corresponding phenomenological correction for odd-even difference of nucleus binding energies and generally taken to be $\delta_N = \frac{12}{\sqrt{A}}$ to reproduce the average behavior. The observed energy dependence of the cumulative number of low lying levels can be described by the function of

$$N(u) = \exp\left(\frac{(u_0 - u)}{T}\right) \dots \dots \dots (3)$$

Where, $N(u)$ is the number of discrete levels and hence the level density

$$\rho(u) = \frac{dN}{du} = -\frac{1}{T} * \exp\left(\frac{(u_0 - u)}{T}\right) \dots \dots \dots (4)$$

Where u_0 and T are the free parameters determined by fitting the experimental data. A description of the level density for whole range of E_x is generally obtained by combining constant temperature formula at low energy with the Fermi gas model (ρ_{fg}) for higher energies. The link between the parameters of the two prescriptions is $U_x = U_0 + T * \ln(\rho_{fg})$

$$\text{and } \frac{1}{T} = \sqrt{\frac{a}{u_x}} - \frac{3}{2u_x} \dots \dots \dots (5)$$

which is obtained by matching the level density and its first derivative at some matching energy. Under the phenomenological approach the experimental data has been analyzed by Gilbert and Camron [8] and they provide a simple systematics for level density. But one of the most important parameters of the systematics discussed above is the energy independent level density parameter. In order to account for the damping of shell effect, the level density parameter [9] (a) showed to be energy dependent as approximated as

$$\rho(u) = \tilde{a} \left(1 + \frac{A}{U} (1 - e^{-\gamma u})\right) \dots \dots \dots (6)$$

where $\tilde{a} \rightarrow$ is the asymptotic level density parameter, $\gamma, A \rightarrow$ the shell correction and the damping factor respectively.

The decay of an equilibrated CN is successfully described in terms of the Statistical Model. The number of possible configuration having energy between E and $E+\Delta E$ increases exponentially with the increase in excitation energy. A nucleus even at lowest bombarding energy at which nuclear reaction can be initiated with any charge particle there are many states available for the CN and often there are many ways in which it can decay. The probability of decay of CN to a particular channel or a group of ‘n’ channels out of ‘N’ number of open channels is given by just $1/N$ or n/N respectively.

The various decay channels of the CN are as follows:

- a) Compound nuclear decay by charged particle and neutron emission.
- b) Compound nuclear decay by gamma (γ) ray emission.
- c) Compound nuclear decay by fission.

a) Compound nuclear decay by charged particle and neutron emission.

Let us consider an ensemble of nucleus in an equilibrium with energy E_i & E_i+dE_i and angular momentum J_i , that emits a particle μ with kinetic energy ϵ , spin ‘s’ and angular momentum ‘J’ and leaving the residual nucleus in a final state of excitation energy E_f & E_f+dE_f , spin ‘ s_f ’, angular momentum ‘ J_f ’[10]. The average rate of emission, summed over orbital angular momentum is

$$R_{\mu}(E_i, J_i; E_f, J_f, s) = \frac{1}{h} \sum_{s=J_f-s}^{J_f+s} \sum_{l=J_i-s}^{J_i+s} T_l(\epsilon) \frac{\rho(E_f, J_f)}{\rho(E_i, J_i)} \dots \dots \dots (7)$$

Where s is the channel spin, $E_i = E_f + S_{\mu} + \epsilon_i$, where S_{μ} is the separation energy for the particular type of particle ‘ μ ’. $T_l(\epsilon) \rightarrow$ the transmission coefficient for inverse reaction. the total evaporation probability (R_{ev}) obtained by integration over the all allowed energy and summing over particle type and average angular momentum is given by equation

$$R_{ev} = \sum_{\mu} \sum_{j_f, s} \int_{\epsilon=0}^{E_i - S_{\mu}} R_{\mu}(E_i, J_i; E_i - S_{\mu} - \epsilon, J_f, s) d\epsilon \dots \dots \dots (8)$$

b) Compound nuclear decay by gamma (γ) ray emission.

In case of gamma (γ) - ray emission the transmission coefficient is replaced by the gamma-ray strength function. The rate of gamma ray emission is given by equation

$$R_{\lambda}(E_i, J_i; E_f, J_f) = C_{\lambda}(\epsilon_{\gamma}) \epsilon_{\gamma}^{2\lambda+1} \frac{\rho(E_f, J_f)}{\rho(E_i, J_i)} \dots \dots \dots (9)$$

Where $\epsilon_{\gamma} \rightarrow$ energy of the emitted gamma ray

$C_{\lambda} \rightarrow$ average squared intrinsic matrix elements

$\rho(E_i, J_i) \rightarrow$ level density at initially excitation energy (E_x).

$\rho(E_f, J_f) \rightarrow$ level density at final excitation energy (E_x).

The gamma decay process itself becomes important towards the later stage of decay which helps the CN in the removal of its angular momentum, when particle decay is energetically forbidden. The total width summed over all is given as

$$R_{\lambda} = \sum_{\lambda} \sum_{J_f} \int_{\epsilon=0}^{E_i} R_{\lambda}(E_i, J_i; E_i - \epsilon, J_f) d\epsilon \dots \dots \dots (10)$$

c) Compound nuclear decay by fission.

In this process there is no residual nucleus. The fission decay is sensitive to the transition states of the CN. This is the point (saddle point) where the nucleus becomes committed to fission and the fission rates is given by the following equation

$$R_f(E_i, J_i; E_f, J_f) = \frac{2J_i+1}{h} \frac{\rho(E_f, J_f)}{\rho(E_i, J_i)} \dots \dots \dots (11)$$

where $\rho(E_f, J_f) \rightarrow$ level density at the transition state $E_f = E_i - E_f(j_i)$

$E_B(j_i) \rightarrow$ The fission barrier or saddle point energy, which depends on the angular momentum J_i . The total fission width (R_{fis}) can be obtained by integrating over allowed energy range and summing over J_f and is given by following equation.

$$R_{fis} = \sum_{J_f} \int_0^{E_i - E_B(J_i)} R_f(E_i, J_i; E_i - E_B(J_i), J_f) d\epsilon \dots \dots \dots (12)$$

The schematic diagram of fission and evaporation is shown in Fig 2.4.

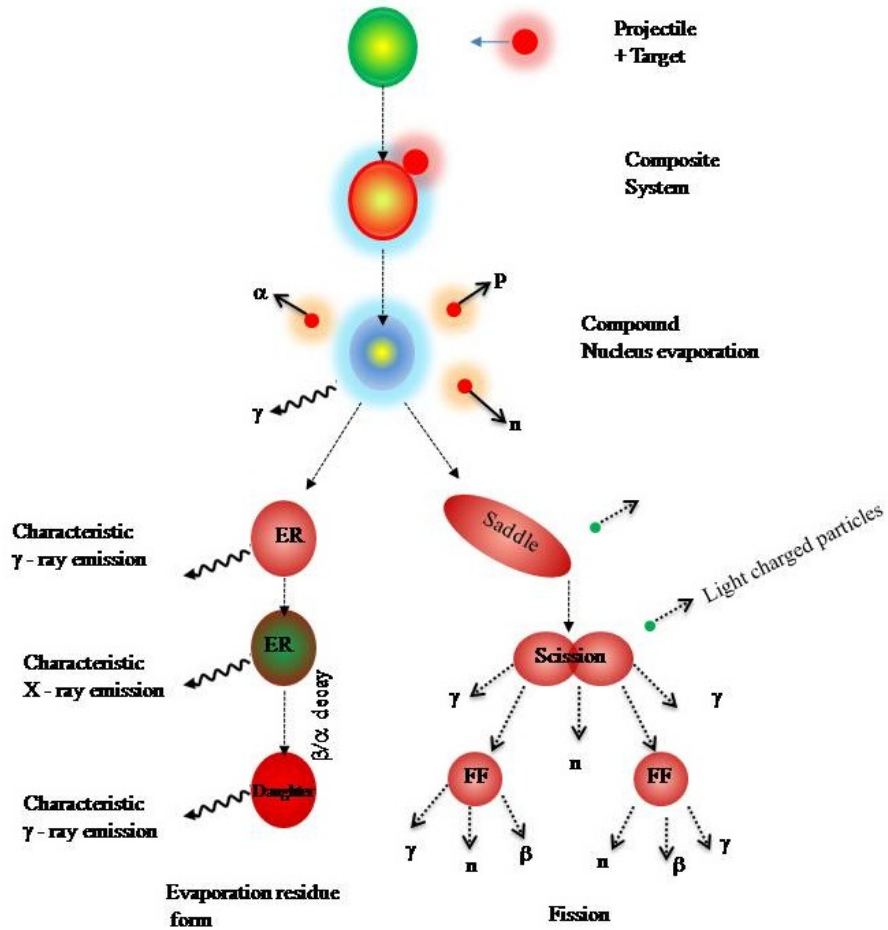


Fig 2.4: Schematic illustration of formation of Compound Nucleus and its decay

2.2.3 Total decay

Total width of CN decay can be obtained by simply adding all decay widths

$$R(E_i, J_i) = R_{ev} + R_{fis} + R_\gamma \dots \dots \dots (13)$$

The probability that any given channel, x, will be populated is just

$$P(E_i, J_i ; x) = \frac{R(E_i, J_i ; x)}{R(E_i, J_i)}$$

thus the cross section for the population of a given channel can be

written as in the following equation

$$\sigma(x) = \sum_{J_i} \sigma(E_i, J_i) P(E_i, J_i ; x) \dots \dots \dots (14)$$

Where $\sigma(E_i, J_i)$ is the production cross section of equilibrated nucleus with excitation energy and angular momentum E_i and J_i respectively.

2.2.4 PACE: A Statistical model code

For our calculations we have used the Statistical model code called PACE2 (Projected Angular momentum Coupled Evaporation, version 2) developed by Gaveron [11]. It uses a Monte Carlo procedure to determine the decay sequence of an excited state of CN using the Hauser- Feshbach [12] formalism. The advantage of the Monte Carlo method is that it can predict energy spectrum, angular distribution and multi particle co- relation in a laboratory frame. Typical results of PACE calculations for different outgoing channels in ${}^7\text{Li}+{}^{144}\text{Sm}$ reaction are shown in Fig. 2.5. The main input is the level density parameter which we have discussed earlier. It essentially controls the excitation energy of the CN. In addition to this, there are other input parameters like charge, mass and spin of both projectile and target, beam energy, etc. There is a provision to put the fusion cross section as an input to the PACE and obtain the individual channel cross sections. There is also an option of feeding the external l - distribution to get the prediction of the cross sections for different outgoing channels. The PACE code provides facility to have an event by event trace back of the entire decay sequence for a given CN to any excited channel. Through the calculations using PACE for ${}^7\text{Li}+{}^{144}\text{Sm}$ reaction, we have been able to estimate the cross sections of undetected channels (which is $\sim 3\text{-}5\%$ of the total fusion cross section) after matching the calculated cross sections with the measured ones for the individual channels.

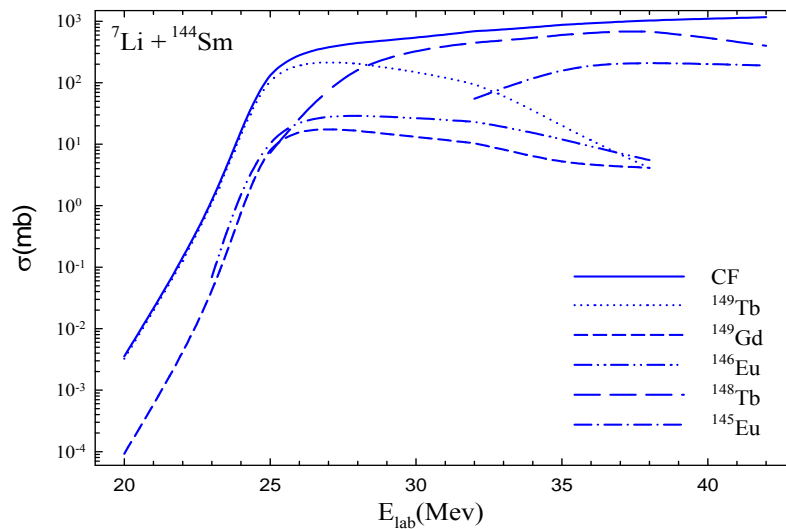


Fig 2.5: An output of Statistical model calculation using the code (PACE) to understand the different channel contribution.

2.3 Fusion cross section and barrier distribution

Here we will derive the basic formula to calculate the fusion cross section. The Schrodinger equation in three dimensions with a potential given by $V_0(r)$ can be written as

$$\left[-\frac{\hbar^2}{2\mu} \nabla^2 + V_0(r) - E \right] \psi(r) = 0 \dots \dots \dots (15).$$

Where μ is the reduced mass of the system. In the absence of the potential $V_0(r)$, this equation can be explicitly solved in a form $\psi(r) = e^{(ik.r)}$, k being the wave number vector

whose magnitude is given by $k = \sqrt{\frac{2\mu E}{\hbar^2}}$. This solution has an asymptotic form as

$$\psi(r) = e^{ik.r} \rightarrow \frac{i}{2k} \sum_{l=0}^{\infty} (2l+1) i^l \left(\frac{e^{-i(kr-\frac{l\pi}{2})}}{r} - \frac{e^{i(kr-\frac{l\pi}{2})}}{r} \right) P_l(\cos\theta), \quad r \rightarrow \infty \dots (16)$$

Where, θ is the angle between r and k , and P_l are the Legendre polynomials. In the presence of the potential, the behavior of the wave function will be modified, as the potential goes to zero at infinity. When the interaction potential is complex as treated in optical model calculation, the reaction is due to the absorption of the incident flux, which can be taken care by the complex part of the potential. Expanding the wave function $\psi(r)$ by the spherical harmonics we have

$$\psi(r) = \sum_{l=0}^{\infty} \sum_{m=-l}^l A_{lm} \left(\frac{u_l(r)}{r} Y_{lm}(r) \right) \dots \dots \dots (17)$$

A_{lm} being expansion coefficients, the Schrödinger equation which, $u_l(r)$ obeys reads

$$\left[-\frac{\hbar^2}{2\mu} \nabla^2 + V_0(r) + \frac{l(l+1)\hbar^2}{2\mu r^2} - E \right] u_l(r) = 0 \dots \dots \dots (18)$$

This equation can be solved under the boundary condition

$$u_l(r) \sim r^{l+1}, \quad r \rightarrow 0 \dots \dots \dots (19)$$

In heavy-ion fusion reactions, instead of imposing the regular boundary condition at the origin, Eqⁿ(19), the so called incoming wave boundary condition (IWBC) is often applied with keeping the potential real [13,14]. Under the incoming wave boundary condition, the wave function has a form

$$u_l(r) = T_l \exp \left(-i \int_{r_{abs}}^r k_l(r') dr' \right), \quad r \leq r_{abs} \dots \dots \dots (20)$$

at the distance smaller than the absorption radius r_{abs} , which is taken to be inside the Coulomb barrier. $k_l(r)$ is the local wave number for the l -th partial wave, which is defined

by $k_l(r) = \sqrt{\frac{2\mu}{\hbar^2} (E - V_0(r) - \frac{l(l+1)\hbar^2}{2\mu r^2})}$. The incoming wave boundary condition

corresponds to the case where there is a strong absorption in the inner region such that the incoming flux does not return back. For heavy-ion fusion reactions, the final result does not depend so much on the choice of the absorption radius ‘ r_{abs} ’, and it is often taken to be at the minimum position of the potential (see Fig. 2.2). In the incoming wave boundary condition, T_l in Eqⁿ(20) is interpreted as the transmission coefficient and hence after some few mathematical steps, we will get the fusion cross section as follow

$$\sigma(E) = \frac{\pi}{k^2} \sum_l (2l + 1) P_l(E) \dots \dots \dots (21)$$

Where, $P_l(E)$ is the penetrability for the l _{th}-wave scattering defined as

$$P_l(E) = \frac{k_l(r_{abs})}{k} |T_l|^2 \dots \dots \dots (22)$$

And the averaged angular momentum of the compound nucleus is evaluated in a similar way as $\langle l \rangle (E) = (\frac{\pi}{k^2} \sum_l l(2l + 1) P_l(E)) / (\frac{\pi}{k^2} \sum_l (2l + 1) P_l(E)) \dots \dots \dots (23)$

2.3.1 Fusion by parabolic approximation

If the Coulomb barrier is approximated by a parabola, penetrability in Eqⁿ (22) can be analytically evaluated. In Fig. 2.6, the Coulomb barrier for the s-wave scattering is compared with the parabolic potential. Akyuz-Winter potential is used for the nuclear potential. Because of the long ranged Coulomb interaction, the Coulomb barrier is asymmetric, and thus the parabolic potential has less width compared to the realistic situation. However, the parabolic approximation works more than what would be expected from Fig. 2.7. The agreement between the exact solutions and the parabolic approximation is remarkable, especially at energies above the Coulomb barrier. Using the parabolic approximation Wong has derived an analytic expression of fusion cross sections [15]. He assumed that (i) the curvature of the Coulomb barrier is independent of the angular momentum ‘ l ’, and (ii) the dependence of the penetrability on the angular momentum can be well approximated by the shift of the incident energy as

$$P_l(E) = P_0 \left(E - \frac{l(l+1)\hbar^2}{2\mu r_B^2} \right) \dots \dots \dots (24)$$

where $r_B \sim$ is the position of Coulomb barrier for the s-wave scattering. If many partial waves contribute to fusion cross section, the sum in Eqⁿ (21) can be replaced by an integral.

$$\sigma(E) = \frac{\pi}{k^2} \int_0^\infty (2l + 1) P_l(E) dl \dots \dots \dots (25)$$

Changing the variable from l to $l(l + 1)$, the integration can be explicitly carried out, leading to the so called Wong formula as

$$\sigma(E) = \frac{\hbar\omega}{2E} r_B^2 \log \left[1 + \exp \left(\frac{2\pi}{\hbar\omega} (E - V_B) \right) \right] \dots \dots \dots (26)$$

Where, $\hbar\omega$, V_B are the curvature and the height of the Coulomb barrier for the s-wave and E is the energy of the incident particle in center-of-mass system respectively. At energies well above the Coulomb barrier, this formula gives the classical expression of fusion cross section as

$$\sigma(E) = \pi r_B^2 \left[1 - \frac{V_B}{E} \right] (E \gg V_B) \dots \dots \dots (27)$$

One can observe from the Fig 2.7, that the Wong formula works very well except well below the Coulomb barrier, where the parabolic approximation breaks down.

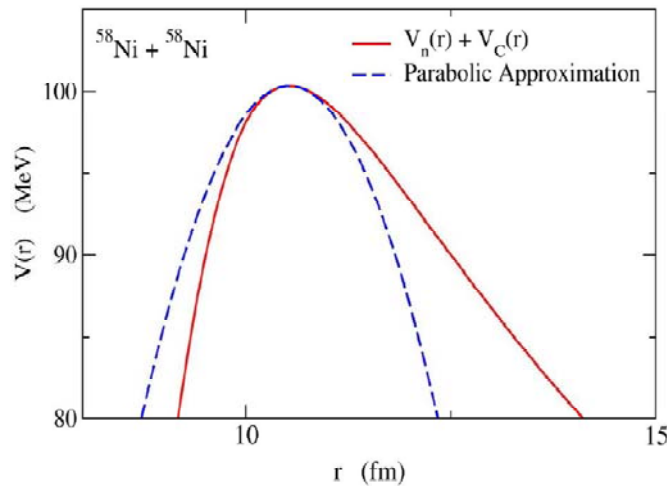


Fig 2.6: Comparison between the Coulomb barrier ($V_B(r)$) for the $^{58}\text{Ni} + ^{58}\text{Ni}$ reaction (the solid line) and a parabolic potential (the dashed line). The woods-Saxon form of potential is assumed for the nuclear interaction.

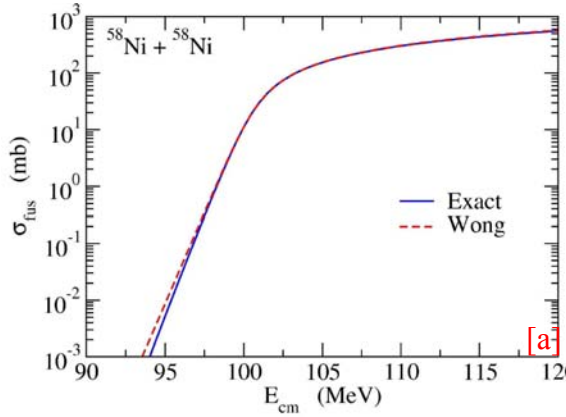


Fig 2.7: Fusion cross section using the exact solutions and the parabolic approximation is remarkably same except at very low energy.

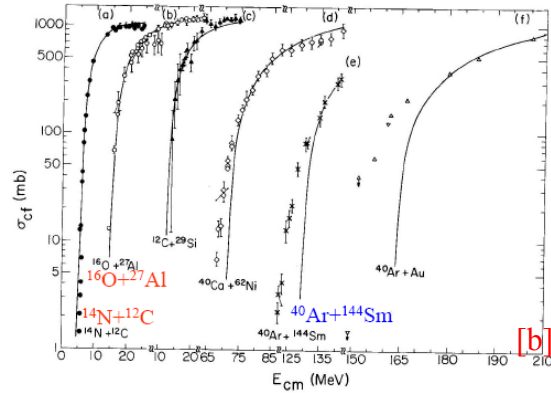


Fig 2.8: Comparison of experimental fusion cross section for several systems with predictions of the parabolic potential model (the solid lines).

2.3.2 Comparison with experimental data

We now compare the one dimensional potential model for heavy-ion fusion reaction with experimental data. Fig 2.7 shows the experimental excitation functions of fusion cross section for several systems. The solid lines are predictions of the potential model obtained by using the parabolic approximation [16]. One can find that the potential model reproduces the experimental data very well. Slight deviations at low energies can be attributed to the inadequacy of the parabolic approximation discussed in the previous section. The situation is, however, very different for the heavier systems. The potential model systematically underestimates fusion cross sections, suggesting that it is too simple to describe the realistic situation. Fig 2.13 shows the experimental fusion excitation functions for the $^{16}\text{O}+^{144,148,154}\text{Sm}$ reactions [17] and comparisons with the potential model (the solid line) calculation. These are plotted as functions of normalized energy and normalized fusion cross section. The barrier height and the result of the potential model are obtained by using the Akyuz-Winther potential. From the Fig 2.7 and Fig. 2.8 it is clear that the one dimensional potential model calculation reproduced the experimental fusion cross section at high energy ($E > V_B$) nicely. We again observe that the experimental fusion cross sections drastically enhance compared to the prediction of the potential model at low energy ($E < V_B$). The enhancement for the $^{16}\text{O}+^{154}\text{Sm}$ system is order of magnitude, while

that for the $^{16}\text{O}+^{144}\text{Sm}$ system is about factor of four at energies below the Coulomb barrier.

2.3.3 Barrier distributions

Rowley *et. al.*[18] suggested that the quantity $d^2(\sigma E)/dE^2$ can be used as the distribution of barriers. To elaborate let us consider penetration probabilities for different partial waves of a one-dimensional system neglecting coupling to internal structure). The l - dependence of the transmission probability at a given energy can be approximated by simply shifting the energy [19,20]. $T_l \approx T_0(E - \frac{l(l+1)\hbar^2}{2\mu R^2} R(E))$ (28)

In the problem of heavy-ion fusion reaction, the experimental observable is not penetrability, but fusion cross section, and thus if one intends to discuss the effects of channel-coupling on fusion in terms of the first derivative of penetrability, one has to convert fusion cross sections to penetrability of the s-wave scattering. The Wong formula given by Eqⁿ (26) suggests one prescription for this, i.e. it was suggested that the first derivative of the product of fusion cross section and the center of mass energy E with respect to the energy, $d(E\sigma)/dE$, is proportional to the penetrability of the s-wave scattering.

$$\frac{d(\sigma E)}{dE} = \frac{\pi R_B^2}{1 + \exp(\frac{2\pi}{\hbar\omega}(E - V_B))} = \pi R_B^2 p_0(E) \dots \dots \dots (29)$$

This equation immediately leads to a relation between the first derivative of the penetrability and the fusion cross section [21].

$$\frac{d^2(\sigma E)}{dE^2} = \pi R_B^2 \frac{p_0(E)}{dE} \dots \dots \dots (30)$$

This quantity, which is conventionally called fusion barrier distribution, is peaked at the height of the Coulomb barrier for the s-wave scattering V_B , with the height and the full width half maximum (FWHM) respectively. In order to enquire how well the first derivative of $E\sigma$ describes the s-wave penetrability, the upper panel of Fig. 2.9 compares the first derivative $d(E\sigma)/dE$ obtained by numerically solving the Schrodinger equation without using the Wong formula, with the numerical solution of the s-wave penetrability scaled by πR_B^2 .

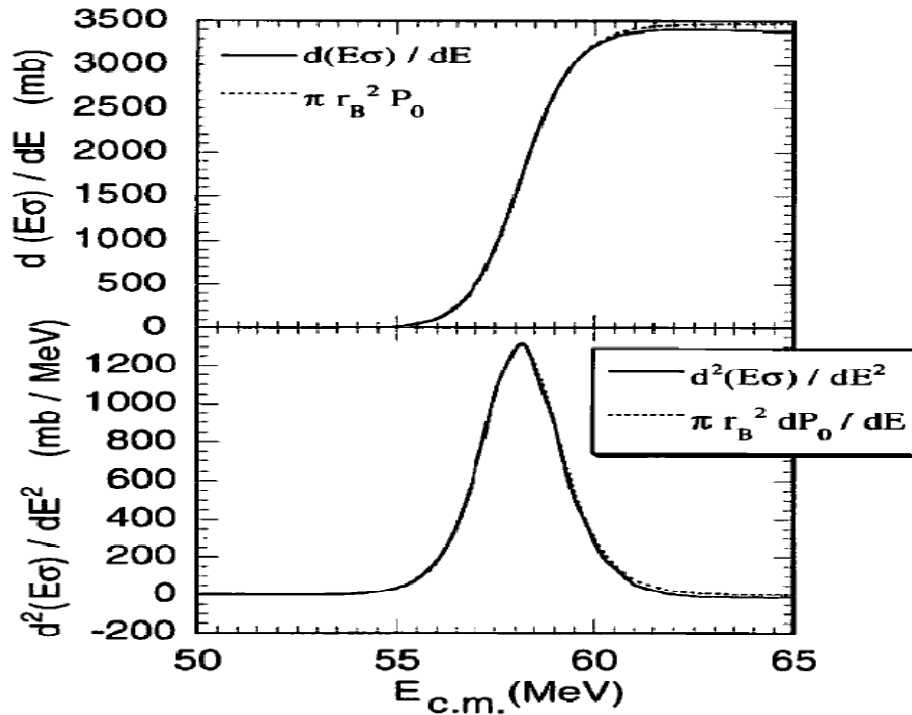


Fig 2.9: The upper panel: comparison of the first derivative of $E\sigma_{fus}$ (the solid line) with the s -wave penetrability (the dotted line). The lower panel: comparison between the second derivative of $E\sigma$ (the solid line) of the s -wave penetrability which is scaled by πR_B^2 .

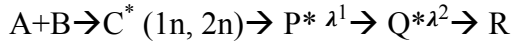
2.4 Derivation of fusion from experimental data

Let us put a thin target (B) in an experimental chamber and produce some radioactive nuclei by interaction of the nuclei B with the projectile A. So the production rate (R) of the CN will depends on the incident energy of projectile, number of incident particle (N_A), the number of target nuclei (N_B) and the fusion cross section σ . So the CN rate (R) is given by [22,23]

$$R = N_A * N_B * \sigma \dots \dots \dots (31)$$

Where $\rightarrow N_A$ is the incident flux and it will be estimated from the total current integrator. Number of target nuclei (N_B) will be calculated by using the Avogadro's number where one use mass thickness in unit mg/cm^2 . Let us consider a reaction where the projectile (A)

interact with the target nucleus (B) and form a CN (C). Once a CN (C) forms it will have excitation energy and angular momentum. It emits particles say 1n or 2n and go to another nuclide called ER (P) and if P is a radioactive nuclei then it will again decay to another nuclei called Q with decay constant say λ_1 and again Q is also a radioactive nuclei it will decay to another nuclei called (R) with decay constant λ_2 . The radioactive nuclei will decay by emitting characteristic gamma ray or x- ray as shown in the following sketch.



Our main aim is to get the total number of CN (C). We get it by counting the number of ‘P’ nuclei, if all the CN will go to ‘P’ just after emitting the particle. The number of ‘Q’ atoms form per sec is of course the number of ‘P’ atoms disintegrates per second. Let at any time t, P has N_1 number of atoms. Now we can write the rate of disintegration of ‘P’ atoms as

$$\frac{dN_1}{dt} = -\lambda_1 N_1 \dots \dots \dots (32)$$

at the same time Q is formed, so the production rate of Q will depend on the decay rate of P with the decay constant λ_1 and at the same time as Q is forming it is also going under decay to R with decay constant λ_2 . So the rate of disintegration of P is shown in Eqⁿ (32) which is the production rate of the Q. If N_2 is the number of Q nuclei at any time ‘t’ then the rate of disintegration of Q is also given by the same Eqⁿ (32) with decay constant λ_2 (the –ve sign indicates it is decaying). So the rate of change of number of Q atoms at any instant of time ‘t’ is given by following Eqⁿ (33).

$$\frac{dN_2}{dt} = \lambda_1 N_1 - \lambda_2 N_2 \dots \dots \dots (33)$$

To solve the above equation let us write, $N_2 = f(t) \times e^{-\lambda_2 t} \dots \dots \dots (33.a)$

Differentiating Eqⁿ (33.a) with respect to time, we have

$$\frac{dN_2}{dt} = \frac{df}{dt} * \exp(\lambda_2 t) - f(t) * \lambda_2 * \exp(-\lambda_2 t) \dots \dots \dots (34)$$

$$\frac{dN_2}{dt} = \left[\frac{df}{dt} - f(t) * \lambda_2 \right] * \exp(-\lambda_2 t) \dots \dots \dots (35)$$

Putting this in the Eqⁿ (33), we have

$$\left[\frac{df}{dt} - f(t) * \lambda_2 \right] * \exp(-\lambda_2 N_2) = \lambda_1 N_1 - \lambda_2 N_2 \dots \dots \dots (36)$$

$$\left[\frac{df}{dt} - f(t) * \lambda_2 \right] * \exp(-\lambda_2 t) = \lambda_1 * N_{10} \exp(-\lambda_1 t) - \lambda_2 * f * \exp(-\lambda_1 t) \dots \dots (37)$$

$$\left[\frac{df}{dt} - f(t) * \lambda_2 \right] * \exp(-\lambda_2 t) = \lambda_1 * N_{10} \exp(-\lambda_1 t) - \lambda_2 * f * \exp(-\lambda_1 t) \dots \dots \dots (38)$$

$$\left[\frac{df}{dt} = \frac{f * \lambda_2 * \exp(-\lambda_2 t) + \lambda_1 N_{10} * \exp(-\lambda_1 t) - \lambda_2 * f * \exp(-\lambda_2 t)}{\exp(-\lambda_2 t)} \right]$$

$$\frac{df}{dt} = \lambda_1 * N_{10} * \exp(\lambda_2 - \lambda_1) t \dots \dots \dots (39)$$

Integrating both sides with time we have

$$\int df = \int \lambda_1 * N_{10} * \exp(\lambda_2 - \lambda_1) t * dt \dots \dots \dots (40)$$

$$f(t) = \frac{\lambda_1 * N_{10}}{\lambda_2 - \lambda_1} [\exp(\lambda_2 - \lambda_1) * t] + C \dots \dots \dots (41)$$

Where, ‘c’ is a constant of integration which can be obtained by the initial condition. At time t=0, there is no Q atoms, so N₂=0. Therefore,

$$C = \frac{\lambda_1 * N_{10}}{\lambda_2 - \lambda_1}$$

Putting all in Eqⁿ (41), we have

$$f(t) = \frac{-\lambda_1 * N_{10}}{\lambda_1 - \lambda_2} [\exp(\lambda_2 - \lambda_1) * t] + \frac{\lambda_1 * N_{10}}{\lambda_1 - \lambda_2}$$

$$f(t) = \frac{\lambda_1 * N_{10}}{\lambda_1 - \lambda_2} [1 - \exp(\lambda_2 - \lambda_1) * t] \dots \dots \dots (42)$$

Putting this into Eqⁿ [33.a] for N₂, we have

$$N_2 = \frac{\lambda_1 * N_{10}}{\lambda_1 - \lambda_2} [1 - \exp(\lambda_2 - \lambda_1) * t] * \exp(-\lambda_2 t)$$

$$N_2 = \frac{\lambda_1 * N_{10}}{\lambda_1 - \lambda_2} [\exp(-\lambda_2 t) - \exp(-\lambda_1 t)]$$

$$N_2 = \frac{\lambda_1 * N_{10}}{\lambda_1 - \lambda_2} [1 - \exp(-\lambda_2 t)] \dots \dots \dots (43)$$

This gives the variation of number of Q atoms with time.

From the above equation, we see that at time $t=0$, $N_2=0$. (i.e. the Q atom is zero, as no P atom has undergone disintegration at that time i.e, $t=0$). N_2 will start from zero at time $t=0$ and then attains a maximum value at certain time say t_{max} . Which can be obtained by taking the derivative of the above equation w.r.t. time.

$$\left[\frac{dy}{dx}\right]_{t_{max}} = \frac{\lambda_1 * N_{10}}{\lambda_1 - \lambda_2} [-\lambda_2 * \exp(-\lambda_2 t) + \lambda_1 * \exp(-\lambda_1 t)]_{t_{max}} \dots \dots \dots (44)$$

2.4.1 Equilibrium

The decay constant λ of different radioactive substance are usually different as shown in Fig 2.10. The variation of N_0 , N_2 w.r.t. time for two cases $\lambda_1 > \lambda_2$ and $\lambda_1 < \lambda_2$. In both the cases N_2 increases with time starting from $t = 0$ to $t = t_{max}$. When the $t_{1/2}$ of the parent is long compared to daughter, it is known as the secular equilibrium. So in this cases the half-life of the parent element is so long during the time $t \ll t_{1/2}$. So the decrease in the number of Parent nuclei atom is very less and the term $\lambda_1 t \sim 1$ in the above equation. And the equation becomes

$$N_2 = \frac{\lambda_1 * N_{10}}{\lambda_1 - \lambda_2} [\exp(-\lambda_2 t) - \exp(-\lambda_1 t)].$$

$$N_2 = \frac{\lambda_1 * N_{10}}{\lambda_1} [1 - \exp(-\lambda_1 t)] \dots \dots \dots (45)$$

This shows that the number of daughter nuclei increases exponentially with time and this was observed by Crookes in his experiment. At different times, the expected counts are given as.

$$N_2 = \frac{\lambda_1 * N_{10}}{\lambda_1} [1 - \exp(-\lambda_1 t)] \dots \dots \dots (46)$$

Let, $Y = \frac{\lambda_1 * N_{10}}{\lambda_1}$, so $N_2 = Y * [1 - \exp(-\lambda_1 t)] \dots \dots \dots (47)$

If we observe for two $t_{1/2}$ ($t=2*t_{1/2}$), three $t_{1/2}$ ($t=3*t_{1/2}$), four $t_{1/2}$ ($t=4*t_{1/2}$) and so on. Then we will obtain the following values of N_2 :

- $N_2 (t=2*t_{1/2}) = Y * 0.75$
- $N_2 (t=3*t_{1/2}) = Y * .87$
- $N_2 (t=4*t_{1/2}) = Y * .93$

$$N_2(t=7*t_{1/2})=Y*.99$$

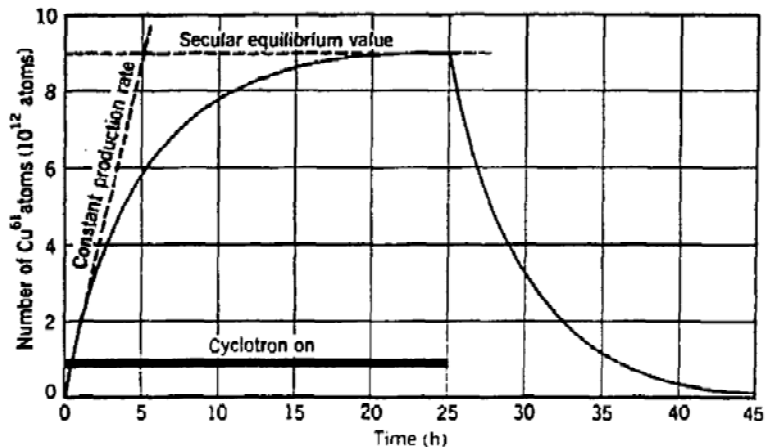


Fig 2.10: A plot of the number of radioactive ^{51}Cu atoms in a Ni target at various times during and after bombardment with deuteron in cyclotron.

From the above values, we observed that for a long time observation say $t_{\text{obs}}=7t_{1/2}$ or $8t_{1/2}$ we will get no more advantage. Whereas, the looking of N_2 for first $3t_{1/2}$ or $4t_{1/2}$ is important as we are able to cover 93% of the total $N_2(Q)$. That is why in our measurements described in this thesis we have counted the offline gammas (γ) for at least $3t_{1/2}$. i.e., If $t_{1/2}$ is 3hr, then at least we have to count (record the spectrum) for 9hr.

2.4.2 Estimation of fusion cross section from offline gamma measurement

In a typical experiment for the fusion measurement, normally a thin target has been irradiated by energetic projectiles. A large number of CN are formed which first de-excite by emitting p, n or alpha (α) particles and then by emitting characteristic gamma rays which is measured by offline procedure. By detecting these gamma rays of different energies we can identify the ERs and their corresponding cross sections.

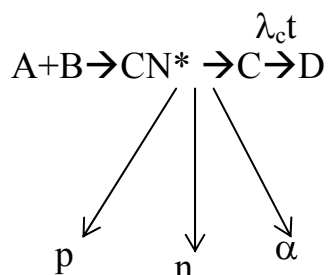


Fig 2.11: An example of formation of a CN in a reaction $A+B$ and its decay by evaporation of different light particles.

From the schematic figure given above (Fig. 2.11), we can see that the evaporation residue ‘C’ (which is formed after particle evaporation) undergoes a radioactive decay to form D by emitting characteristic gamma or X-rays. So, using Eqⁿ (31) one can obtain the net production rate of C during the irradiation. It depends on two factors: formation and decay.

(a) The formation rate is given by

$$R_c = \sigma_c * N_t * N_i \dots \dots \dots (48)$$

Where, $\sigma_c \rightarrow$ The probability of formation of CN

$N_t \rightarrow$ number of target nucleon per cm²

$N_i \rightarrow$ number of incident projectile

(b) Decay of ‘C’ will be given by decay constant (λ_c)

$$\frac{dN_c}{dt} = R_c - \lambda_c N_c \dots \dots \dots (49)$$

Using previous equation of N_2 (Eqⁿ45) we have

$$N_2 = \frac{\lambda_1 * N_{10}}{\lambda_1 - \lambda_2} [\exp(-\lambda_2 t) - \exp(-\lambda_1 t)] \dots \dots \dots (50)$$

In the above practical situation we have $\lambda_2 = 0$ and $\lambda_1 = \lambda_c$ hence

$N_2 = N_c$, so the above equation becomes $\lambda_2 = 0$. Then (Eqⁿ 50) becomes

$$N_2 = \frac{\lambda_1 * N_{10}}{\lambda_1 - \lambda_2} [1 - \exp(-\lambda_1 t)] \dots \dots \dots (51)$$

$$N_c = \frac{R_c}{\lambda_c} [1 - \exp(-\lambda_c t)] \dots \dots \dots (52)$$

Here, the daughter nuclei Q is not undergoing radioactive decay, so we have from Eqⁿ (52)

$$\lambda_c N_c = \sigma * N_t * N_i [1 - \exp(-\lambda_c t)]$$

$$N_c = \frac{\sigma * N_t * N_i}{\lambda_c} [1 - \exp(-\lambda_c t)] \dots \dots \dots (53)$$

Now if the irradiation is stopped after a time $t = t_{irr}$ then we have

$$N_{irr}^C = \frac{\sigma * N_t * N_i}{\lambda_c} [1 - \exp(-\lambda_c t_{irr})] \dots \dots \dots (54)$$

After irradiation is stopped there will be no formation of 'C' and only decay will occur. So the rate of decay of C at any time is

$$\frac{dN}{dt} = -\lambda_c N_C = -\lambda_c N_{irr}^C \exp(-\lambda_c t) \dots \dots \dots (55)$$

But we can count the decay for certain time say from time t_1 to t_2 . So to get the number of decay 'N_c' in time t_1 to t_2 , we integrate the above equation with respect to time from t_1 to t_2

$$\int_{t=t_1}^{t=t_2} \frac{dN_C}{N_{irr}^C} = \int_{t=t_1}^{t=t_2} -\lambda_c * \exp(-\lambda_c t) dt \dots \dots \dots (56)$$

$$N_C = \frac{-\lambda_c}{-\lambda_c} [N_{irr}^C * \exp(-\lambda_c t_1) - \exp(-\lambda_c t_2)] \dots \dots \dots (57)$$

In the above equation 'N_c' is the number of particle decay to 'D' from C i.e. these are the number of particle which we have observed between the time t_1 to t_2 and we will call it as yield 'Y'. Then the above equation becomes

$$Y_C = [N_{irr}^C * \exp(-\lambda_c t_1) - \exp(-\lambda_c t_2)] \dots \dots \dots (58)$$

Putting the value of 'N_{irr}^C' from Eqⁿ(54) into Eqⁿ(58) we have

$$Y_C = \frac{\sigma * N_t * N_i}{\lambda_c} [1 - \exp(-\lambda_c t_{irr})] [\exp(-\lambda_c t_1) - \exp(-\lambda_c t_2)] \dots \dots \dots (59)$$

Again another important factor is that after the irradiation was stop and before the counting starts there will be a small time gap due to offline experimental set up. But during that time there will be some decay which we are not counting. We will call this as cooling time (t_{cool}). Putting this factor in the above equation we have

$$Y_C = \frac{\sigma * N_t * N_i}{\lambda_c} [1 - \exp(-\lambda_c t_{irr})] * [\exp(-\lambda_c t_1) - \exp(-\lambda_c t_2)] * \exp(-\lambda_c t_{cool})$$

From the above equation the fusion cross section can now be expressed as

$$\sigma_C = \frac{\lambda_c * Y_C}{N_t * N_p * \text{eff} * (\text{br}\%) * [1 - \exp(-\lambda_c t_{irr})] * [\exp(-\lambda_c t_1) - \exp(-\lambda_c t_2)] * \exp(-\lambda_c t_{cool})} \dots \dots (60)$$

Where 'eff' in the above expression is the efficiency of the detector for the required characteristic gamma line, the efficiency decreases with increasing energy. 'br' is the branching ratio of that gamma i.e., the probability that a given gamma will come from a nuclei which has been shown in Fig.2.12. The more dense black indicates the more probability of that gamma. By using any one gamma line corresponding to the same ER one should obtain the desired fusion cross section provided the care is taken for proper

efficiency and branching ratio of that gamma line. Thus one can verify the fusion cross section determination by using different gamma lines emitted from the same ER.

The expression (Eqⁿ(60) is valid when the beam current is fixed i.e. there is no fluctuation in the incident beam current. Experimentally it is very difficult to maintain a constant current. So, correction for such beam current fluctuation is necessary. If N_A has the fluctuation as a function of time but it is constant within a small interval of time t_{step} then the current can be recorded at time less than or equal to t_{step} during the irradiation. The total irradiation time t_{irr} can be considered to be made of up 'n' such intervals of size t_{step} ($t_{irr}=n*t_{step}$). When the irradiation is stopped after the n^{th} interval, then the activity due to the number of nuclei N_{Cn} produced during the n^{th} interval at any time t after the beam is stop

$$\frac{dN_{Cn}}{dt} = -\lambda_c N_{Cn} = -\lambda N_{Cn}^{t_{step}} e^{-\lambda_c t} \dots\dots\dots (61)$$

For nuclei produced in the $(n-1)^{th}$ interval time t when counting is started is shifted by t_{step} giving the start and stop time for counting the activity, t_1+t_{step} and t_2+t_{step} respectively.

The number of C nuclei decay during this interval is

$$Y_{C_{n-1}} = \frac{\sigma_C N_B N_{A_{n-1}}}{\lambda_c} (1 - e^{-\lambda_c t_{step}}) (e^{-\lambda_c(t_1+t_{step})} - e^{-\lambda_c(t_2+t_{step})})$$

We discretized the irradiation time as $t_{irr} = n*t_{step}$ and the incident beam, where n is the number of step. So after doing some simple mathematical steps, we have

$$1 - \exp(-\lambda * t_{irr}) = \sum_{n=0}^n 1 - \exp(-\lambda * t_{step})$$

$$= \sum 1 - \exp(\lambda t_1) + 1 - \exp(\lambda t_2) + 1 - \exp(\lambda t_3)$$

$$+ \dots \dots \dots \dots \dots \dots \dots + 1 - \exp(\lambda t_n)$$

$$\sigma_C = \frac{\lambda_c Y_C}{N_t * Br \% * eff * e^{-\lambda_c t_0} \sum_i I_{Ai} e^{\lambda_c \sum_{j \leq i} \Delta t_j} (1 - e^{-\lambda_c \Delta t_i}) (e^{-\lambda_c t_1} - e^{-\lambda_c t_2})} \dots\dots\dots (62)$$

We use the above formula to extract the fusion cross section. For online measurement, it is very simple as we are able to get all the information at time $t=0$, so all time dependent factors will go. And the cross section formula is given as follow.

$$\sigma_C = \frac{\lambda_c Y_C(A_0, \text{at } t=0)}{N_t * N_i * \text{eff} * \text{br} \% * (1 - e^{-\lambda_c t_{\text{irr}}})} \dots\dots\dots (63)$$

we have used Eqⁿ (62) for our offline analysis in all the experiments and cross checked by Eqⁿ (63) using activity A_0 at time $t=0$, which we got from the activity half life fitting plot.

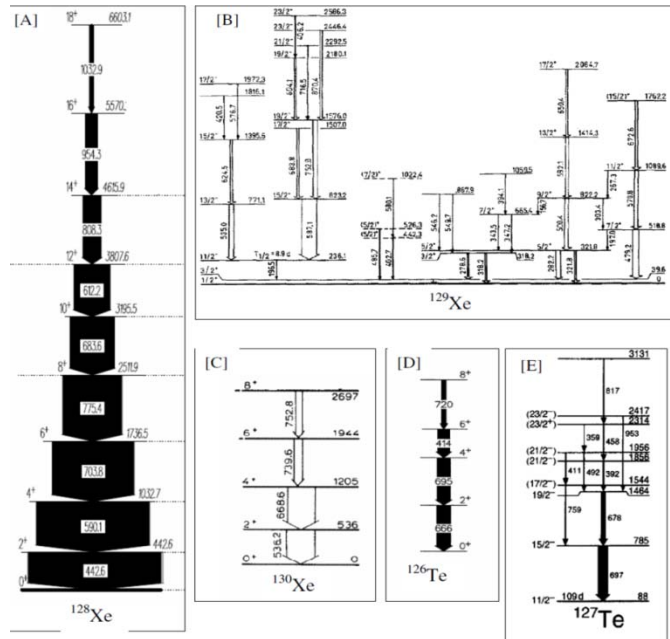


Fig 2.12: The effect of branching of gamma the more dense line indicates the most preferable path than the less dense line indicates the less preference path to reach to ground state from an excited state.

2.5 Coupled-channels formalism for heavy-ion fusion

2.5.1 Coupled-channels equation

Extensive experimental and theoretical studies have revealed the inadequacy of the potential model. The large enhancements of fusion cross section against predictions of the

potential model can be attributed to the effects of couplings of the relative motion between the colliding nuclei to several nuclear intrinsic motions [24-28]. Among possible intrinsic excitations of a nucleus, single particle states couple so weakly to the ground state that they do not affect heavy-ion fusion reactions. Also, their excitation energy is in general much larger than the curvature of the Coulomb barrier between the colliding nuclei

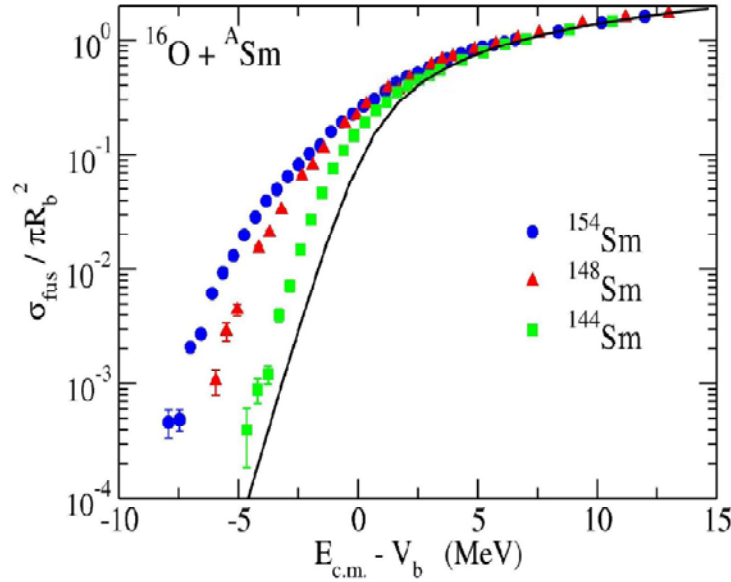


Fig 2.13: experimental fusion excitation functions for $^{16}\text{O} + ^{144,148,154}\text{Sm}$ reactions [29]. They are given as a function of normalized energy and cross section. The solid line is a prediction of the potential model.

Therefore, the most relevant nuclear intrinsic motions to heavy-ion fusion reactions are low-lying collective motions, e.g. low-lying vibrational excitations with several multi-polarities or rotational motions of deformed nuclei. In this section, we formulate the coupled-channels framework by taking into account the finite multi-polarity of nuclear intrinsic motion and discuss the effects of the couplings on heavy-ion fusion reactions. Consider a collision between two nuclei in the presence of the coupling of the relative motion between the centers of mass of the colliding nuclei, $r = (r, \check{r})$, to a nuclear intrinsic motion ξ . We assume the following Hamiltonian for this system

$$H(r, \xi) = -\frac{\hbar^2}{2\mu} \nabla^2 + V_0(r) + H_0(\xi) + V_{coup}(r, \xi) \dots \dots \dots (64)$$

where, $H_0(\xi)$ and $V_{coup}(r, \xi)$ are the internal and the coupling Hamiltonians, respectively.

In general, the internal degree of freedom has a finite spin. We therefore expand the coupling Hamiltonian in multipoles as $V_{\text{coup}}(r, \xi) = \sum_{\lambda \gg 0} f_{\lambda}(r) Y_{\lambda}(\check{r}) \cdot T_{\lambda}(\xi)$. Here $Y_{\lambda}(\check{r})$ are the spherical harmonics and $T_{\lambda}(\xi)$ are spherical tensors constructed from the internal coordinate. The dot indicates a scalar product. The sum is taken over all values of λ except for $\lambda = 0$, which is already included in $V_0(r)$. For a fixed total angular momentum J or I and its z component M , the expansion basis of the coupled-channels equations are defined as

$$H_0(\xi) \varphi_{nI m_I}(\xi) = \epsilon_{nI} \varphi_{nI m_I}(\xi) \dots \dots \dots (65)$$

And the coupled channel equations for $u_{nI}^j(r)$ read as

$$\left[-\frac{\hbar^2}{2\mu} \frac{d^2}{dr^2} + \frac{l(l+1)\hbar^2}{2\mu r^2} + V_0(r) - E + \epsilon_{nI} \right] u_{nI}^j(r) + \sum_{n'l'I'} V_{nI; n'l'I'}^j(r) u_{n'l'I'}^j(r) = 0 \dots (66)$$

These coupled-channels equations are solved with the incoming boundary conditions

$$u_{nI}^j \sim T_{nI}^j \exp(-i \int_{r_{abs}}^r k_{nI}(r') dr'), \quad r \leq r_{abs} \dots \dots \dots (67)$$

$$\text{Where, } k_{nI}(r) = \sqrt{\frac{2\mu}{\hbar^2} (E - \epsilon_{nI} - V_0(r) - \frac{l(l+1)\hbar^2}{2\mu r^2} - V_{nI; nI}^j(r))}$$

Once the transmission coefficients T_{nI}^j are obtained, the penetration probability through the Coulomb potential barrier is given by

$$P_{l_i I_i}^j(E) = \sum_{nI} \frac{k_{nI}(r_{abs})}{k} |T_{nI}^j|^2 \dots \dots \dots (68)$$

Where, $k = k_{n_i I_i}$ is the wave number for the entrance channel. The fusion cross section for an unpolarized target is then given by

$$\sigma(E) = \frac{\pi}{k^2} \sum_j l_i \frac{2j+1}{2I_i+1} P_{l_i I_i}^j(E) \dots \dots \dots (69)$$

If the initial intrinsic spin I_i is zero, the initial orbital angular momentum l_i is j . Suppressing the indices l_i and I_i in the penetrability, Eqⁿ(69) becomes

$$\sigma(E) = \frac{\pi}{k^2} \sum_j (2j + 1) P^j(E) \dots \dots \dots (70)$$

Which is similar to Eqⁿ(21) except that the penetrability $P^j(E)$ are influenced by the channel couplings.

2.5.2 Vibrational coupling

Let us now discuss the explicit form of the coupling Hamiltonian (V_{coup}) in the problem of heavy-ion fusion reactions. We first consider couplings of the relative motion to the 2^λ -pole surface vibration of a target nucleus. In the geometrical model of Bohr and Mottelson, the radius of the vibrating target is parameterized as

$$R(\theta, \Phi) = R_T(1 + \sum_{\mu} \alpha_{\lambda\mu} Y_{\lambda\mu}^*(\theta, \Phi)) \dots \dots \dots (71)$$

Where R_T is the equivalent sharp surface radius and $\alpha_{\lambda\mu}$, is the surface co-ordinate of the target nucleus. To the lowest order, the surface oscillations are approximated by a harmonic oscillator and the Hamiltonian for the intrinsic motion is given by

$$H_0 = \hbar\omega \left(\sum_{\mu} a_{\lambda\mu}^{\dagger} a_{\lambda\mu} + \frac{2\lambda+1}{2} \right) \dots \dots \dots (72)$$

Here $\hbar\omega$ is the oscillator quanta and $a_{\lambda\mu}^{\dagger}$ and $a_{\lambda\mu}$ are the phonon creation and annihilation operators, respectively. The surface co-ordinate $\alpha_{\lambda\mu}$, is related to the phonon creation and annihilation operators by

$$\alpha_{\lambda\mu} = \alpha_0 (a_{\lambda\mu}^{\dagger} + (-)^{\mu} a_{\lambda\mu}) \dots \dots \dots (73)$$

where α_0 is the amplitude of the zero point motion. It is related to the deformation parameter by $\alpha_0 = \frac{\beta_{\lambda}}{\sqrt{2\lambda+1}}$ [30] and can be estimated from the experimental transition probability as

$$\alpha_0 = \frac{1}{\sqrt{2\lambda+1}} \frac{4\pi}{3Z_T R_T^{\lambda}} \sqrt{\frac{B(E\lambda)_{\uparrow}}{e^2}} \dots \dots \dots (74)$$

The surface vibration modifies both the nuclear and the Coulomb interactions between the colliding nuclei. In the collective model, the nuclear interaction is assumed to be a function of the separation distance between the vibrating surfaces of the colliding nuclei.

It is conventionally taken as

$$V^{(N)}(\mathbf{r}, \alpha_{\lambda\mu}) = V_N(\mathbf{r} - R_T \sum_{\mu} \alpha_{\lambda\mu} Y_{\lambda\mu}^*(\check{\mathbf{r}})) \dots \dots \dots (75)$$

If the amplitude of the zero point motion of the vibration is small, one can expand this equation in terms of $\alpha_{\lambda\mu}$ and keep only the linear term:

$$V^{(N)}(\mathbf{r}, \alpha_{\lambda\mu}) = V_N(\mathbf{r}) - R_T \frac{dV_N(\mathbf{r})}{dr} \sum_{\mu} \alpha_{\lambda\mu} Y_{\lambda\mu}^*(\check{\mathbf{r}}) \dots \dots \dots (76)$$

This approximation is called the linear coupling approximation, which has often been used in coupled-channels calculations. The first term of the r.h.s. of Eqⁿ (76) is the bare nuclear potential, i.e. the nuclear potential in the absence of the coupling, while the second term is the nuclear component of the coupling Hamiltonian. The Coulomb component of the coupling Hamiltonian is evaluated as follows. The Coulomb potential between the spherical projectile and the vibrating target is given by

$$V_C(r) = \frac{Z_P Z_T e^2}{r} + \sum_{\lambda' \neq 0} \sum_{\mu'} \frac{4\pi Z_P e}{2\lambda'+1} Q_{\lambda'\mu'} Y_{\lambda'\mu'}^*(r) \frac{1}{r^{\lambda'+1}} \dots \dots \dots (77)$$

Where, ρ_T is the charge density of the target nucleus and $Q_{\lambda'\mu'}$ the electric multipole operator defined by

$$Q_{\lambda'\mu'} = \int dr Z_T e \rho_T(r) r^{\lambda'} Y_{\lambda'\mu'}(\check{r}) \dots \dots \dots (78)$$

The first term of the r.h.s. of Eqⁿ (77) is the bare Coulomb interaction, and the second term is the Coulomb component of the coupling Hamiltonian. If we assume a sharp matter distribution for the target nucleus, the electric multipole operator is given by

$$Q_{\lambda'\mu'} = \frac{3e}{4\pi} Z_T R_T^{\lambda'} \alpha_{\lambda\mu} \delta_{\lambda\lambda'} \delta_{\mu\mu'}(\check{r}) \dots \dots \dots (79)$$

by combining Eqⁿ (76), Eqⁿ (77) and Eqⁿ (79), the coupling Hamiltonian is expressed by

$$V_{coup}(r, \alpha_\lambda) = f_\lambda(r) \sum_\mu \alpha_{\lambda\mu} Y_{\lambda\mu}^*(\check{r}) \dots \dots \dots (80)$$

up to the first order of $\alpha_{\lambda\mu}$. $f_\lambda(r)$ is the coupling form factor, which is given by

$$f_\lambda(r) = -R_T \frac{dV_N}{dr} + \frac{3}{2\lambda+3} Z_P Z_T e^2 \frac{R_T^\lambda}{r^{\lambda+1}} \dots \dots \dots (81)$$

Where, the first and the second terms are the nuclear and the Coulomb coupling form factors respectively. The coupling form factor $f_\lambda(r)$ has the value at the position of the bare Coulomb barrier r_B .

$$f_\lambda(r_B) = \frac{Z_P Z_T e^2}{r_B} \left(\frac{3}{2\lambda+3} \frac{R_T^\lambda}{r_B^\lambda} - \frac{R_T}{r_B} \right) \dots \dots \dots (82)$$

Transforming to the rotating frame, the coupling Hamiltonian used in the no-Coriolis Approximation is then given by

$$V_{coup}(r, \alpha_{\lambda 0}) = \sqrt{\frac{2\lambda+1}{4\pi}} f_\lambda(r) \alpha_{\lambda 0} = \frac{\beta_\lambda}{\sqrt{4\pi}} f_\lambda(r) (\alpha_{\lambda 0}^+ + \alpha_{\lambda 0}) \dots \dots \dots (83)$$

The no-Coriolis approximation drastically reduces the dimension of the coupled-channels equations. A further reduction can be achieved by introducing the n-phonon channels [31, 32]. In general, the multi-phonon state of the vibrator has several levels and they are distinguished from each other by the angular momentum and the seniority [33]. For example, for the quadruple surface vibrations, the two phonon state has three levels (0+, 2+, 4+). In the harmonic limit, these two-phonon triplets are degenerate in the excitation energy.

2.5.3 Rotational coupling

We next consider couplings to the ground rotational band of a deformed target. In discussing them, it is convenient to transform to the body fixed frame where the z axis is along the orientation of the deformed target. The surface coordinate $\alpha_{\lambda\mu}$ is then transformed to

$$\alpha_{\lambda\mu} = \sum_{\mu'} D_{\mu\mu'}^{\lambda}(\Phi_d, \theta_d, \chi_d) \alpha_{\lambda\mu'} \dots \dots \dots (84)$$

Where, Φ_d, θ_d and χ_d are the Euler angles which specify the orientation of the target. If we are particularly interested in the quadruple deformation ($\lambda=2$), the surface coordinates in the body fixed frame are expressed as

$$a_{20} = \beta_2 \cos \gamma$$

$$a_{22} = a_{2-2} = \frac{1}{\sqrt{2}} \beta_2 \sin \gamma$$

If we further assume that the deformation is axial symmetric ($\gamma = 0$) the coupling Hamiltonian for the rotational coupling becomes,

$$V_{coup}(r, \Phi_d, \theta_d) = f_2(r) \sum_{\mu} \beta_2 \sqrt{\frac{4\pi}{5}} Y_{2\mu}(\Phi_d, \theta_d) Y_{2\mu}^*(\check{r}) \dots \dots \dots (85)$$

In obtaining Eqⁿ. (85), we use the identity

$$D_{M0}^L(\theta, \Phi, \chi) = \sqrt{\frac{4\pi}{2L+1}} Y_{LM}^*(\theta, \Phi) \dots \dots \dots (86)$$

The coupling Hamiltonian in the rotating frame is thus given by

$$V_{coup}(r, \theta) = f_2(r) \beta_2 Y_{20}(\theta) \dots \dots \dots (87)$$

Where, θ is the angle between (Φ_d, θ_d) and \check{r} , i.e. the direction of the orientation of the target measured in the rotating frame. Since the wave function for the $|I0\rangle$ state in the ground rotational band is given by $|I0\rangle = Y_{I0}$, the corresponding coupling matrix is given by

$$V_{coup} = \begin{pmatrix} 0 & F(r) \\ F(r) & \epsilon_2 + 2\sqrt{5}F(r)/7 \end{pmatrix} \dots \dots \dots (88)$$

when it is truncated at the first 2+ state. In Eqⁿ (88), ϵ_2 is the excitation energy of the first 2+ state, and $F(r)$ is defined as $\beta_2 f_2(r)/\sqrt{4\pi}$. The matrix elements in Eqⁿ (88) are calculated by using

$$\int Y_{l_1 m_1}(\Omega) Y_{l_2 m_2}(\Omega) Y_{l_3 m_3}(\Omega) d\Omega = \sqrt{\frac{(2l_1+1)(2l_2+1)(2l_3+1)}{4\pi}} \times$$

$$\begin{pmatrix} l_1 & l_2 & l_3 \\ 0 & 0 & 0 \end{pmatrix} \begin{pmatrix} l_1 & l_2 & l_3 \\ m_1 & m_2 & m_3 \end{pmatrix} \dots \dots \dots (89)$$

One of the main differences between the vibrational and the rotational Eqⁿ (88) Couplings is that the latter has a diagonal component which is proportional to the deformation parameter β_2 . This is referred to as the 'reorientation effect' and has been used in the Coulomb excitation technique to determine the sign of the deformation parameter [34]. The effects of the γ deformation on sub-barrier fusion were studied in Ref. [35]. If there is a finite γ deformation, the coupling Hamiltonian in the rotating frame becomes

$$V_{coup}(r, \theta, \Phi) = f_2(r) \left(\beta_2 \cos\gamma Y_{20}(\theta) + \frac{1}{\sqrt{2}} \beta_2 \sin\gamma (Y_{22}(\theta, \Phi) + Y_{2-2}(\theta, \Phi)) \right) \dots \dots \dots (90)$$

Higher order deformations can be also taken into account in a similar way as described above. For example, if there is an axial symmetric hexa-decapole deformation in addition to an axial symmetric quadruple deformation, the coupling Hamiltonian reads

$$V_{coup}(r, \theta) = f_2(r) \beta_2 Y_{20}(\theta) + f_4(r) \beta_4 Y_{40}(\theta) \dots \dots \dots (91)$$

Where, β_4 is the hexa-decapole deformation parameter.

References:

- [1] Takatoshi Ichikawa *et al.*, Phys. Rev. C 75,057603 (2007)
- [2] N. Bohr Nature 137,344(1936)
- [3] V.C. Weisskopf “theoretical physics” wiley N.Y.1952
- [4] H. A. Bethe, Rev, Mod. Phys, 9, 69, (1937)
- [5] V. Weisskopf, Phy. Rev. 52,295(1937)
- [6] D. J. Morrissey *et al.*, Annu. Rev. Nuclei Sci 4427(1994)
- [7] H. A. Bethe *et al.*, Phys. Rev. 50,332(1936)
- [8] A. Gilbert *et al.*, Can. J. phys. 43, 1446(1965)
- [9] <http://www.nds.iaea.org/RIPL-2>
- [10] “Heavy Ion Science” , (Plenum New York)1985
- [11] A. Gavron, Phys. Rev. C 21,230(1980)
- [12] Walter Hauser *et al.*, Phys. Rev. 87,366(1952)
- [13] S. landowner, Nucl. Phy. A 405,381(1983)
- [14] C. H. Dasso, Phys. Rev. C 29, 1352(1984)
- [15] C. Y. Wong, Phys. Rev. Lett. 31,766(1973)
- [16] Louis C. Vaz *et al.*, Phys. Rep. 69,373(1981)
- [17] Morton *et al.*, Phys. Rev. Lett. 72, 4074 (1994)
- [18] N. Rowley *et al.*, phys. Lett. B 254, 25(1991)
- [19] A. B. Balantekin *et al.*,Phys. Rev. C 28,1565(1983)
- [20] A. B. Balantekin *et al.*, Phys. Rev. C 33,379(1986)
- [21] S. N. Ghoshal “Nuclear Physics, ISBN 81-219-0413-7
- [22] K.S. Krane “Introductory Nuclear Physics”
- [23] A. Balantekin, Phys. Rev. C 28, 1565(1983)
- [24] M. Beckerman, Rep. Prog Phys 51, 1047 (1988)
- [25] M. Beckerman, Phys. Rep 129,145,1351 (1985)
- [26] S. G. Steadman *et al.*, Ann. Rev. Nucl. Part. Sci 36,649(1986)
- [27] W. Reisdorf , J. Phys. G: Nucl. Part. Phys. 20, 1297(1994)
- [28] J. R. Leigh *et al.*, Phys. Rev. C 52, 3151(1995)
- [29] Nuclear Structure (Benjamin, New York, 1975,vol 2)

Chapter 2: Theoretical models

[30] N. Takigawa and K. Ikeda, in Proceedings of the Symposium on Many Facets of “Heavy Ion Fusion Reactions”, edited by W. Henning et al. (Argonne National Laboratory, Report No. ANL-PHY-87-1), 1986, p.613.

[31] A.T. Kruppa *et al.*, Nucl. Phys. A560, 845(1993).

[32] A. Bohr and B. Mottelson” Nuclear Structure” (Benjamin, New York, 1975), vol. 2.

[33] “Advance in Nuclear physics”, (Plenum, New York 1968) vol-1

[34] C. H. Dasso *et al.*, Phys. Rev. C 55, 2112(1997)

[35] K. Hagino *et al.*, Comp. Phys. Comm 123,143(1999)

[36] <http://www.nuclphys.tohokuac.jp/hagino/ccfull>

Chapter 3

Instruments, Detection techniques and Analyses

Detectors, signal processing electronics, thin targets, radioactive sources and accelerators are the essential components for the study of experimental nuclear physics. The study of nuclear physics demands beam of energetic particles to induce nuclear reactions with target nuclei [1]. It was from this need, the accelerators were developed. Experimental data are an important tool for the nuclear physics community to test the various theoretical models to explain the nuclear properties and also for applied research [2-4]. The radiation detector is a device used to detect, track, and/or identify the particles produced in nuclear reaction. With the increasing technology of detecting systems and accelerator facilities more and more accurate results are published which are playing a very important role to understand the properties of nuclei. There are many types of accelerators such as DC accelerator [5,6] (Pelletron, Van-de-Graff etc.) and AC accelerators [7,8] (Cyclotron, Synchrotron) to deliver high energy particles from light to heavy elements. In the present thesis work, the detectors used with their characteristics are discussed briefly in the present chapter. A brief description about target preparation techniques, different radioactive sources used and reactions shielded are also presented.

3.1 Radioactive sources

The radioactive sources with the known parameters such as the half life, energy and branching ratio of the emitted radiation, etc. play an important role in the study of experimental nuclear physics. Particularly, the characterization and calibration of the different detectors are performed using various radioactive sources. A brief description about the sources used is as follows;

(i) ^{152}Eu a multi gamma ray source: ^{152}Eu is a radioactive element which emits gamma radiation with different energies spread over the energy region ~ 122 to 1500 keV.

Efficiency and calibration of the γ -detector are performed by using this source of radio nuclides. The details of this nuclide have been widely published are listed in Table 3.1.

Table 3.1: Energy and branching ratio of some predominant γ -rays from standard ^{152}Eu source.

γ ray energy (keV)	Branching ratio (%)
121.7	28.58
244.7	7.583
344.3	26.50
411.1	2.234
443.9	2.821
678.6	0.471
688.7	0.857
778.9	12.94
867.4	4.245
964.1	14.60
1085.8	10.21
1089.7	1.727
1112.0	13.64
1212.9	1.422
1299.1	1.623
1408.0	21.005

The prominent γ -rays of the standard ^{152}Eu source have been used and a typical spectrum is shown in Fig 3.1. The following equation has been used for efficiency calculation, $\varepsilon=A_t/(A_0 \times \text{Br})$. Where, A_t is the activity of the standard γ -source at the time of measurement, A_0 is the activity at the time of manufacture of the source and 'Br' is the branching ratio of the characteristic γ -ray. Fig 3.2 shows an efficiency plot using ^{152}Eu source at different distances from the detector. We have also used ^{133}Ba for low energy gamma ray. Table 3.2 shows different gamma ray energies of ^{133}Ba source with their

branching ratios. A typical spectrum of ^{133}Ba is shown in Fig 3.3. Fig. 3.4 shows the efficiency of the detector using ^{133}Ba and ^{152}Eu sources.

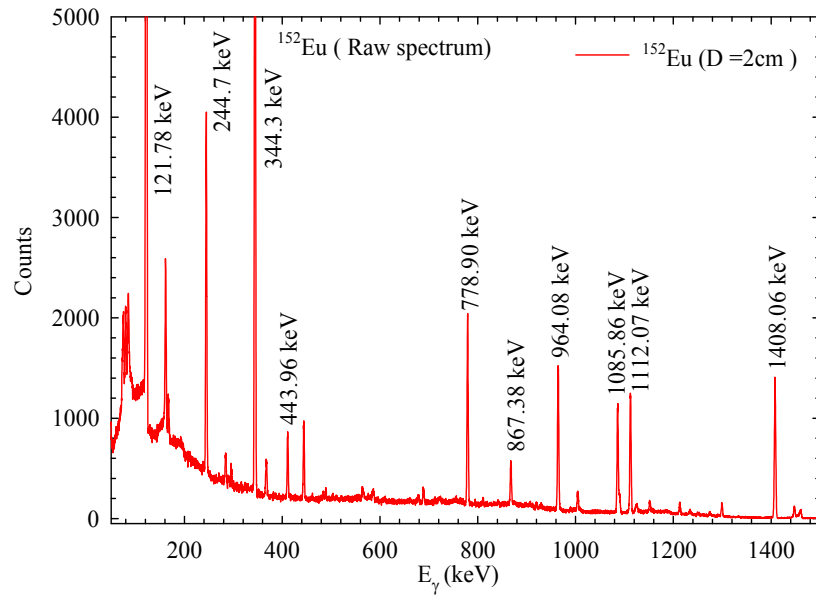


Fig 3.1: Different energetic gamma rays emitted from ^{152}Eu Source.

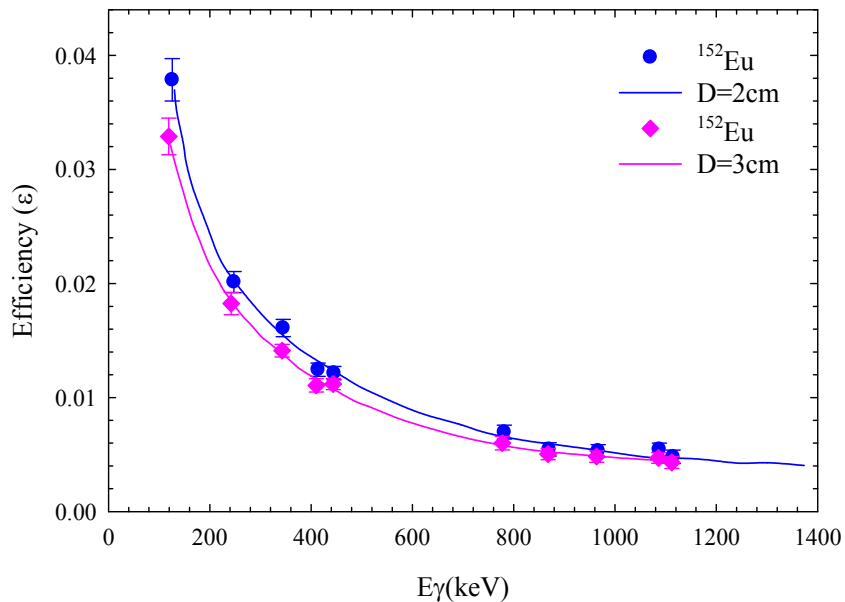
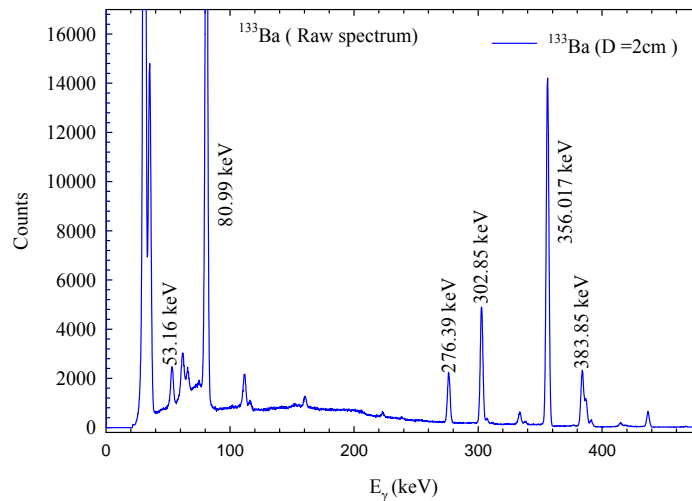


Fig 3.2: The efficiency (ϵ) curve of HPGe detector used for off-beam γ activity counting at different distances from the detector.

Table 3.2: The energy and branching ratio of some predominant γ -rays from Standard ^{133}Ba source.

γ ray energy (keV)	Branching ratio (%)
53.161	2.199
80.997	34.06
160.613	0.645
223.234	0.450
276.398	7.164
302.853	18.33
356.017	62.05
383.851	8.94

**Fig 3.3:** The different energetic gamma rays emitted from ^{133}Ba Source.

(ii) ^{241}Am - ^{239}Pu for α - particles: Many unstable heavy nuclei attains the stability by alpha-decay where certain amount of energy is released depending on mass difference of the parent and daughter nuclei. The alpha decay can lead to any of the excited state (E_x) of the daughter nucleus and accordingly the alpha particle kinetic energy is observed to be

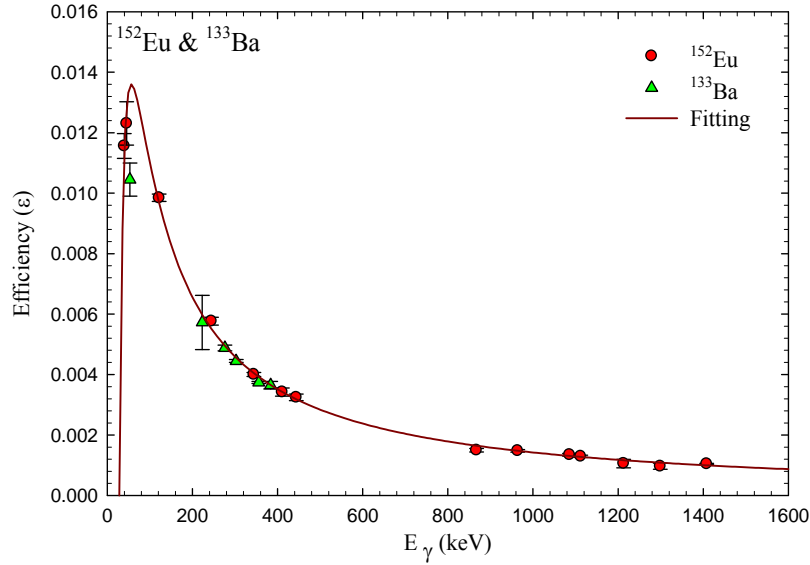


Fig 3. 4: The efficiency (ϵ) curve of HPGe detector used for off-beam γ activity counting using ^{133}Ba and ^{152}Eu sources .

$E_\alpha = Q_{\text{eff}}[1 - 4.0/A]$, where $Q_{\text{eff}} = Q - E_x$ and A is the mass number of the parent nucleus. Both ^{241}Am as well as ^{239}Pu emits α - particles of various discrete energies but only few of them are dominant. In case of ^{241}Am , the dominant energies are 5.486 MeV (~85%) and 5.443 (~13%), where as in the case of ^{239}Pu , the energies are 5.155 MeV (~71%), 5.144 MeV(~17%) and 5.105 MeV (~12%) [26]. The half lives of ^{241}Am and ^{239}Pu are 432.6 years and 24110 years, respectively. In the present work, we have used ^{241}Am - ^{239}Pu for α -source and ^{152}Eu , ^{133}Ba for gamma source to characterize and calibrate the SSB and HPGe detector respectively.

3.2 Detectors

Detectors are always considered as an eye and ear of an experimentalist in any branches of physics. The field of radiation detector has gone through the tremendous advances since the primitive stage of photographic emulsion and simple gas detector like Geiger Muller (GM) counter [14]. With the advances of the nuclear and particle physics, the scientific community has shown zeal to develop a many complex detector system characterized by

the fast timing, high energy resolution, better stability, resistivity against radiation damage and most important the cost effectiveness. All these demands have led to the experiment with the novel material using cutting edge technology and this field is highlighted when scientists like Donald Glaser, Luis Alvarez and G. Charpalu received Nobel Prize. Here we discuss briefly the working principle of various types of detectors used in the present study. In most of the nuclear physics experiments, the fundamental parameters are i) the nature of the emitted particle (charge and mass), ii) The kinetic energy of the emitted particles and iii) the angular distribution of the emitted particles. Various techniques such as ΔE -E counter telescope, time of flight measurement, electric/magnetic field based technique etc. are available for the detection of these three parameters. In the present work we have employed (1) Si-surface barrier and (2) HPGe detectors. A brief description about these detectors is presented here along with some simplified electronics. Detailed characteristics of the detectors have been documented in various reference books [14, 27].

3.2.1 Semiconductor detector

Semiconductor detectors [13] are most commonly used when best energy resolution for the emitted particle is required. In semiconductor detector, the carriers are the electron and the hole pairs created by the radiation when pass through the material along its path. Of the available semiconductor material, silicon is mainly used for the detection of the charge particle and soft x-ray, while germanium is used widely for gamma rays detection [1,13]. These detectors are characterized by the fast response, particle identification capability and compact size. Semiconductors are special types of materials which have two distinct bands, valence band and conduction band. The same bands are also present in the conductor and insulator. In all cases the valence band is filled with electrons whereas the conduction band is empty. The only difference between them is the band gap, for insulator it is $> 5\text{eV}$, for semiconductor it is $\sim 2\text{eV}$ and for conductor there is no band gap. The probability per unit time that an electron hole pair is thermally generated is $P(T) = CT^{3/2} e^{-(E_g/2kT)}$, where T is absolute temperature, E_g is the band gap, k is the Boltzmann constant and 'C' is the proportionality constant of the material. Thermal excitation in a semiconductor strongly depends on the temperature. A pure semiconductor at absolute zero temperature acts like an

insulator. There are two types of semiconductors; intrinsic and extrinsic (doped). The intrinsic semiconductors like Silicon (Si), Germanium (Ge) are pure semiconductors, where the entire electrons in the conduction band and entire holes in the valence band are due to the thermal excitation. However intrinsic semiconductors are extremely difficult to achieve in practical because even a very low level of impurities can affect the electrical property of the semiconductor. The extrinsic semiconductors are again classified into two group, p-type and n-type. In p-type, the majority charge carrier is the holes and this can be created when a tetravalent atom like 'Si' is doped by a trivalent atom (group-III) of the periodic table. The n-type can be produced when a pentavalent atom (group-V) is doped in the tetravalent atom (group-IV) and the electrons are in majority charge carrier. The fundamental information associated with the interaction between the semiconductor and the radiation is contained in the number of electron-hole pair generated in the path of the detector material when radiation passes through it. The number of electron-hole pair is governed by the average energy spent by the charge particle to produce a single pair of electron- hole. Table 3.3 shows the energy required for Si and Ge to produce an electron-hole pair at different temperature (temp) [13, 14]. ($0^{\circ}\text{C} = 273\text{K}$).

Table 3.3: Energy required for different element to produce electron-hole pair.

Element	Si			Ge		
	0K	77K	300K	0K	77K	300K
Band Gap	1.16eV	-	1.11eV	0.74eV	-	0.67eV
Energy per electron - hole pair	-	3.76 eV	3.62eV	-	2.96eV	-

The dominant level in p-type or n-type semiconductor is usually low and the radiation interaction with these impurities element can be neglected. Therefore p- or n-type silicon (Si) of equal thickness will show same interaction pattern with radiation. The semiconductor detectors operate in the reverse bias condition to create a depleted region of free charge carriers. whenever a radiation falls on this depleted region, it creates electron-hole pairs which will move to the opposite direction and give rise a pulse. To collect charge

carriers (electron-hole pairs) in a semiconductor detector produced through radiation interaction, an electric field must exist as in the case of gas-filled detectors. The applied high voltage varies depending on the detector size and is typically hundreds or thousands of volts. This high voltage induces leakage current even in the absence of radiation because the semiconductor material itself has a finite conductivity. However, the current level produced by radiation interaction is very small ($\sim\mu\text{A}$), which is significantly lower than the leakage current. Therefore an active method, a p-n junction, is required to reduce the leakage current to pick up the signal corresponding to the radiation interaction. In other word, semiconductor detectors are a “sandwich” of p- and n-type materials; the detector is a semiconductor diode. The standard process of making a junction is to modify the impurity concentration on one side of the material so that both sides can have opposite configurations. Depending on the type of the initial material, two different configurations are possible as shown in Fig. 3.5.

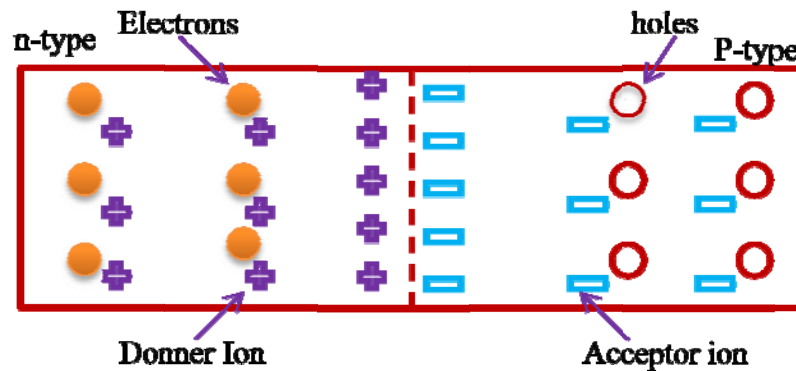


Fig. 3.5: Schematic diagram of a n-p junction with different charge carriers.

If the initial material is p-type, the majority of carriers is holes, and this is called p-type detector. Similarly, the majority of carriers is electrons in second case, hence called n-type detector. The semiconductor detector operates much better as a radiation detector if an external voltage is applied across the junction in the reverse biased direction. The semiconductor junction or semiconductor detector is really a large diode. The junction is reverse-biased when the p-side of the junction is made negative with respect to the n-side. The natural potential difference that arises upon contact of the two sides of the junction is greatly enhanced. The minority carriers are attracted across the junction, but because their

concentration is low, the reverse current across the junction is pretty small. The p-n junction acts as a rectifying element i.e. it allows relatively free flow of current in one direction, while representing a large resistance to current flow in the other direction. Reverse biasing a junction increases the thickness of the depletion region because the potential difference across the junction is enhanced. The size of the depletion region depends on both bias voltage and the initial impurity concentration by the following relation $d = \left(\frac{2\varepsilon V_0}{eN}\right)^{1/2}$. Where, N represents the net impurity concentration on the initial semiconductor material. d is the depletion depth, ε is the dielectric constant. The depletion region behaves as a capacitor since the charges are built up on either side of the p-n junction. The capacitance per unit area is $C = \frac{\varepsilon}{d} = \left(\frac{2\varepsilon N}{2V_0}\right)^{1/2}$. Thus, as the reverse bias voltage increases, the depletion region grows and the capacitance decreases and a small capacitance is preferred for a good energy resolution. From the width of the depletion region, the active volume of the detector can be estimated.

3.2.2 Silicon surface barrier detector

One of the two types of semiconductor detector used in our experiments is silicon surface barrier detector (SSB). Generally a thin layer of high concentration p-type material is formed on top of n-type (Si) to form a p-n junction. The n-type Si is etched with acid on one side and oxidized in air to form a p-type material and coated with a thin gold layer to form electrical contact. Slight oxidization before evaporation of gold layer plays an important role in resulting properties of the surface barrier. This is called surface barrier detector (SSB) [15]. The other side of the crystal coated with the Al for electrical contact. The depletion depth depends on the resistivity of the material and the applied voltage. Due to the relatively wide band gap of Si, the Si diode detectors can be operated at room temperature. A typical solid state detectors used in nuclear physics experiments are shown in Fig 3.6. These detectors are light sensitive and as ΔE is very thin crystal and photon passes through the crystal will reach to the active region and produce noise. These detectors are sensitive to temperature also. Trapping and recombination centers lead

partial charge carrier loss and degradation in energy resolution. The principle based on which it identifies particles of different energy, charge, mass is very simple. A schematic representation of a telescope (ΔE - E) is shown in Fig 3.7. The identification of the charge particle depends on the facts that different charge particles of same energy will lose energy at different rate on passing through the material. The rate of energy loss of an ion passing through a medium is described by well known Bethe-Block formula. For a non-relativistic particle it can be approximated as $dE/dx \propto AZ^2/E$, where A , Z , E are the mass, charge and energy of the incident particle which will fall on the detector. The same energy particle with different masses or same mass with different charges or same masses and energy having different charges will be separated clearly [16,17]. A 2D picture for this type of separation is shown in Fig 3.8 for ${}^7\text{Li}+{}^{12}\text{C}$ [18] reaction .



Fig 3.6: Typical solid state detector used in nuclear physics experiments

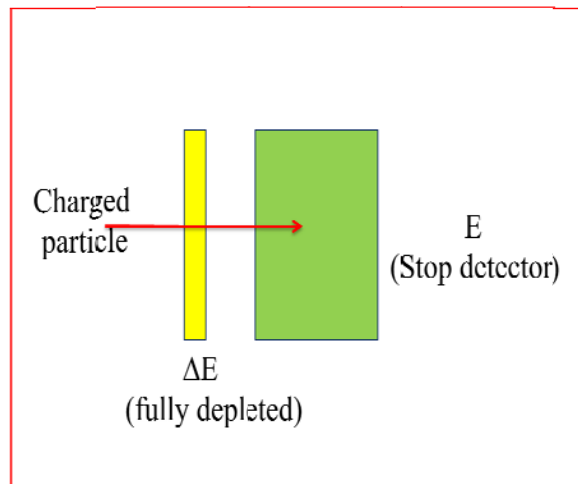


Fig 3.7: Schematic diagram showing $\Delta E - E$ telescope setup.

3.2.3 High purity germanium detector

This is another semiconductor detector which we have used in our experiments. High-purity Germanium (HPGe) detector is regularly used for experimental study of complex gamma ray spectra involving many discrete peaks [13]. Using the technique of Zone

refining method, the highly purified Germanium (HPGe) is produced. This detector is used mainly for gamma ray spectroscopy. Due to low atomic number of Ge compared to Iodine (I) or Bismuth (Bi), the photo peak efficiency is low compared to scintillation detector, but the energy resolution of the HPGe detector is excellent. An important technological development has been the production of large size Germanium

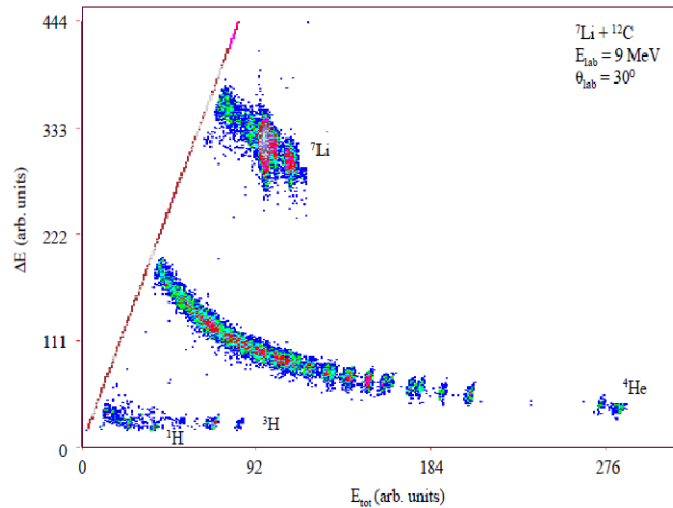


Fig 3.8: Typical ΔE vs E_{tot} plot for ${}^7\text{Li} + {}^{12}\text{C}$ experiment. There are different bands corresponding to different particles. As from the figure one can see ${}^7\text{Li}$, ${}^4\text{He}$, ${}^3\text{H}$ are clearly separated

crystals with a very high degree of purity (p-type impurity levels only in the range 5×10^9 to 10^{11} atoms per CC). This material can be used directly for manufacturing of detectors without using the Li-ion drift process, which is only needed to compensate for the much higher p-type of impurity levels in the more standard quality of Ge. An important consequence is that these HPGe detectors do not have to be maintained permanently at liquid nitrogen temperatures after fabrication. In the case of Li-doped . i.e., Ge(Li) detectors, it is necessary to keep the detectors always cooled, to avoid redistribution of Li by diffusion process, which could eventually lead to incomplete and in adequate compensation. This is operated at the liquid nitrogen temperature. Room temperature operation of any Ge detector of any type is impossible due to its low band gap ($\sim 0.67\text{eV}$) leading to a large thermally induce leakage current. Hence, they are cooled to liquid nitrogen (77K) through the use of insulated dewar in which a reservoir of liquid nitrogen

is kept in thermal contact with the detector. The detector must be housed in a vacuum - tight cryostat to inhibit thermal conductivity between the crystal and the surrounding air. The cryostat is normally evacuated and sealed by manufacturer. A thin end window is usually located near the crystal to minimize attenuation of gamma rays before they enter the germanium. The preamplifier is normally incorporated as a part of the cryostat package in modern HPGe systems. The input stage of the preamplifier normally is also cooled along with the detector to reduce electronic noise. [13]. A picture of HPGe detector with crystal is shown in Fig 3.9. A typical gamma ray spectrum of ^{60}Co source using HPGe detector is shown in Fig 3.10.

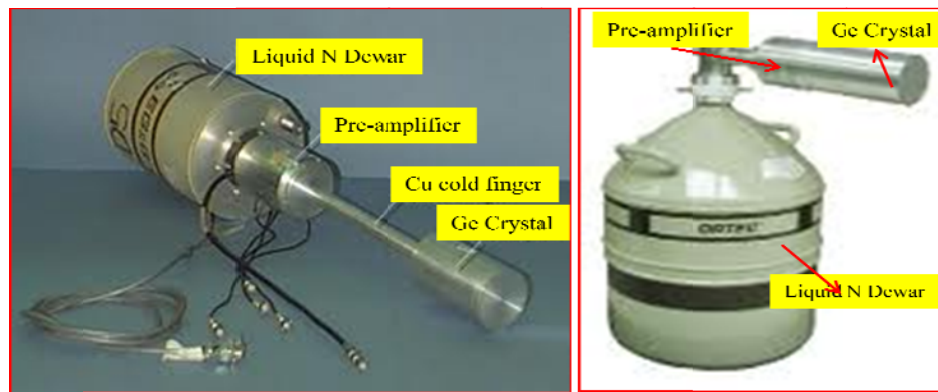


Fig 3.9: Schematic representation of the HPGe detector with Ge crystal, cooling line and cryogenic. Different types of configuration are available.

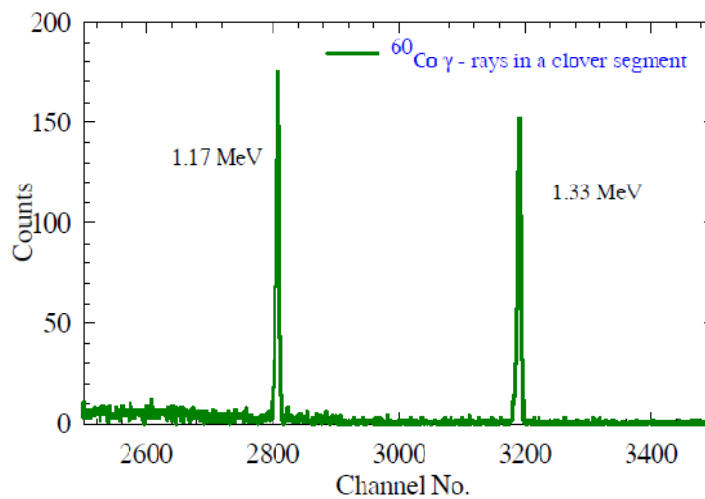


Fig 3.10: ^{60}Co gamma ray spectrum detected by HPGe detector.

3.3 Electronics and data accumulation

Most of the radiation detector requires signal (pulse) processing electronics so that the energy or the timing information involved with the radiation interaction can be properly extracted. There are two types of signal (pulse) in radiation measurement, i.e Linear and logic pulse. A linear pulse is signal carrying information through its amplitude and shape. A logic pulse is a signal which carries information only by its presence or by its absence. Generally linear pulses are produced in any radiation interaction and then they are converted to logic pulse. Measurements were carried out at 0° and 30° N (irradiation chamber) beam line for target thickness measurement and irradiation of the targets respectively. The details of the experiments have been discussed in the successive sections. For each radiation detector, the corresponding electronics circuit, the basic components are described below depending on the data accumulation system.

3.3.1 Preamplifier

This is the first component in the signal processing chain of radiation detector. The Preamplifier (preamp) acts like an interface between the detector and the pulse processing unit. The main function of the preamp is to extract the signal from the detector without significantly degrading the signal to noise ratio. Therefore, it is located as close as possible to the detector and the input circuit is designed to match the input characteristics of the detector. A schematic of the RC feedback charge sensitive preamplifier is shown in Fig 3.11. The detector high voltage power supply is fed through the preamplifier. The output pulse height of preamp is in proportions with the energy deposited by the radiation interaction with the detector. The output pulse of a preamp is shown in Fig 3.12. The output pulse shape is characterized by a short rise time determined by the charge collection.

3.3.1. i Detector bias supply

The important characteristics of the detector bias supplies are:

- (1) The maximum voltage level and its polarity

- (2) The maximum current availed from the supply
- (3) The degree of regulation against long term drifts due to change in temperature or line voltages
- (4) The degree of filtrating to eliminate ripples at power line frequency or other source.

Such that the output pulse of the detector has a fast rise time and a long decay time (~100 μ s) as shown in Fig 3.13.

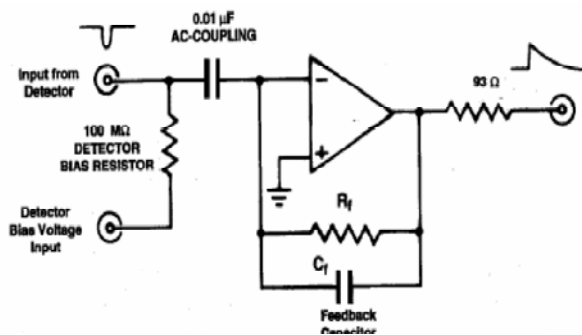


Fig 3.11: Typical RC feedback charge sensitive preamplifier.

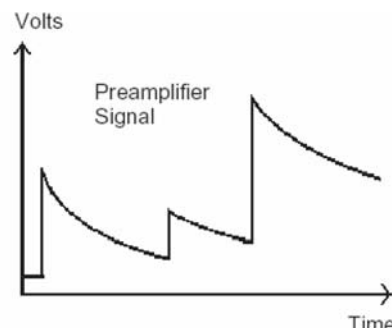


Fig 3.12: Signal pattern of a resistive feedback charge sensitive preamplifier.

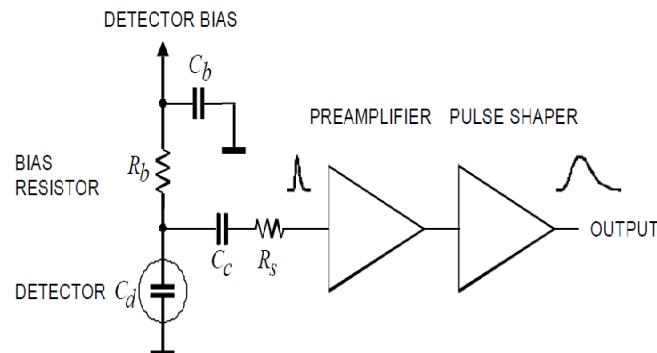


Fig 3.13: Detector bias voltage is applied through the resistor R_b . The bypass capacitor C_b serves to shunt any external interference coming through the bias supply line to ground. For AC signals this capacitor connects the “far end” of the bias resistor to ground, so that R_b appears to be in parallel with the detector

3.3.1.ii Pulse counting system

In order to count pulse reliably, the preamp output signal must be shaped and amplified by a shaping amplifier and then the shaped linear pulse must be converted to a logic pulse. The integral discriminator is the simplest unit that does this operation and consist of a device that produce a logic output pulse only when the linear input pulse height exceed a threshold i.e. the linear pulses cross the discrimination level. Integral discriminator are designed to accept shaped linear pulses in 0~10 V range.

3.3.1.iii Multi channel analyzer (MCA)

A multichannel analyzer is a succession of single channel analyzers (SCA) whose windows are all the same width and are arranged sequentially, in order of increasing energy. Thus by plotting the count rate of each SCA versus its mean energy window setting, a spectrum of count rate versus energy will result. In an actual MCA, the single channel analyzers are replaced by a single device called an analog to digital converter (ADC). The ADC measures the height of each pulse as it comes in and determines to which SCA window the pulse corresponds. The SCA windows are replaced by a histogram memory that stores the number of counts in each energy window in sequential channels. As well as the counts in each channel the MCA also records elapsed time so that the count rate can be determined. The MCA provides manipulation of the spectrum display often with expand/contract/logarithmic display modes and calculation capabilities such as energy scale (x-axis) calibrations, peak finding, and area extraction. In the MCA, the ADC, histogram memory and controlling micro processor are built into a device called a multichannel buffer (MCB). The combination of MCB and software provides the MCA functions. MCAs are available which can provide anything from 1000 channels of memory upward. The 0 to 10V amplifier output may be divided into 1000 or up to 8000 separate channels. There are numerous powerful data processing capabilities available in MCA. However the main features that will be helpful for experiments includes determination of area under peak, centroid position, multiple region of interest, automatic energy calibration, spectrum and transfer to another segment of the memory Fig. 3.14 shows a MCA output of different energetic alpha particle emitting from ^{226}Ra .

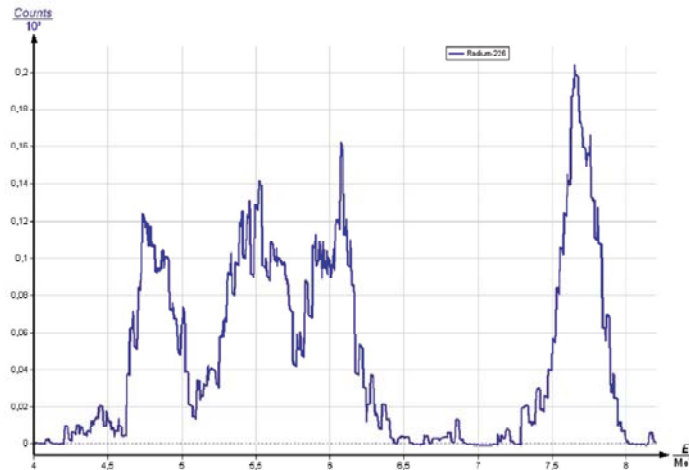


Fig 3.14: Schematic representation of output of a MCA for different alpha energy of ^{226}Ra nuclei.

3.3.1. iv Counter and timer

As the final step in a counting system, the logic pulse must be accumulated and their number recorded over a period of time. A counter is used for this purpose and increments one count each time a logic pulse is presented to its input. These are operated in two modes, one is preset time mode or preset count mode. The function of a timer is simply to start and stop the accumulation period for an electronic counter or other recording device.

3.3.2 Shaping (spectroscopy) Amplifier

For pulse height or energy spectroscopy, the linear pulse shaping amplifier performs several essential functions. Its primary role is to magnify the amplitude of the preamplifier output pulse from mV range to 0.1 to 10 V range. This makes possible accurate pulse height measurement with a peak sensing analog to digital converter (ADC) or SCA. In addition, the amplifier shapes the pulse to optimize the resolution and minimize the risk of overlap between the successive pulses. The linear pulse shaping amplifier must accept the output pulse shapes provided by the preamplifier and change them into pulse shape suitable for optimum energy spectroscopy. Much higher counting rates can be tolerated before the pulse pile up occurs. The simplest concept for the pulse shaping is the use of the CR circuit

followed by a RC circuit. In this shaping the preamp signal first passes through CR shaper and then RC shaper. Fig 3.15 shows the circuit diagram. The CR circuit acts like high pass filter and the RC circuit acts like as low pass filter and their combination give a shaped pulse as shown in Fig 3.16. Most of the shaping amplifier includes a pole zero cancellation circuit to eliminate the under shoot/over shoot pulses. The benefits of the pole zero cancelation is to improved the peak shape and resolution in the energy spectrum at high counting rates. Fig 3.17 illustrates the pole zero cancelation circuit and its effect. If single CR high pass filter is followed by several stages of RC integration the output pulse shape become close to Gaussian. Amplifier shaping in this way is called semi-Gaussian shaping amplifier [19].

3.3.3 Analog to digital converter

A peak sensing analog to digital converter (ADC) measures the height of an analog pulse and convert that value to a digital number. The digital output is proportional representation of the analog pulse height at the ADC input. For sequentially arriving pulses, the digital output from the ADC are fed to a dedicated memory or a computer and shorted in to a histogram. This histogram represents the spectrum of the input pulse height. The dynamic range of the ADC operation is consistent with the range of the spectroscopy amplifier output (i.e 0-10V), even if the peak sensing ADC is mainly used for the energy spectroscopy, it can be used for the timing spectroscopy as well. When the output of a time to amplitude converter (TAC) is connected to the ADC input, the histogram represents the time spectrum measured by the time to amplitude converter. We have measured first the thickness of the target by the energy information of the scattered particle, ^{16}O . We have used the Rutherford back scattering (RBS) method and used the simple spectroscopy amplifier, normal ADC to record the spectrum [14]. The detail experimental methods are discussed in the next section.

3.4 Target Preparation

Target material has an important role for the success of any nuclear physics experiments because all the practical observable are directly proportional to the number of target nuclei

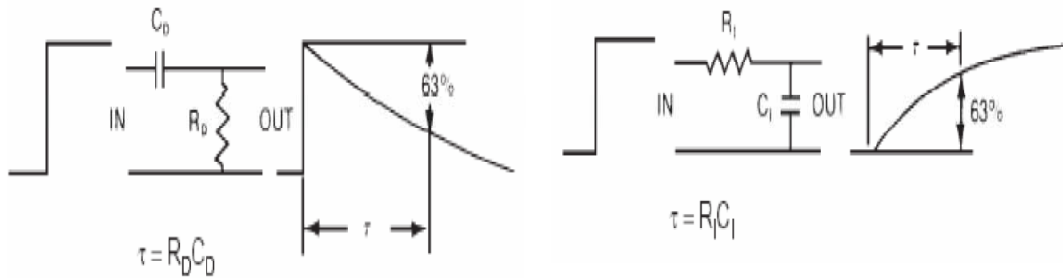


Fig 3.15: Schematic of circuit diagram for CR and RC circuit.

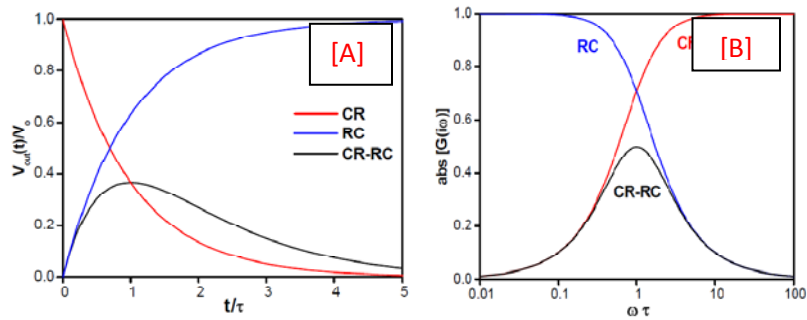


Fig 3.16: [A] CR, RC and CR-RC time domain response for a single step function. [B] Absolute value of the frequency domain transfer function for CR, RC and CR-RC.

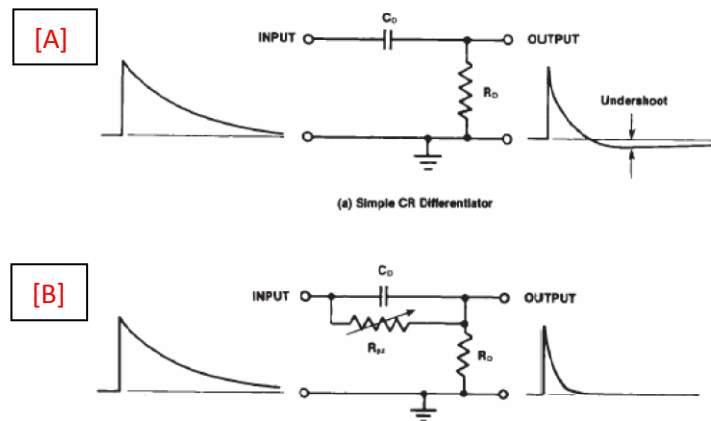


Fig 3.17: [A] Simple CR discriminator. [B] Pole zero cancellation circuit.

present in the sample. So the target preparation is as much important as to get the incident beam of precise energy and intensity. For good results, the target must be checked from the point of view of its purity, composition, thickness, homogeneity etc. The study of heavy ion

induced reaction say fission fragments angular distribution and the fusion excitation function measurements at bellow barrier energy requires thickness of the order of $<1\text{mg}/\text{cm}^2$. This is because the incident beam will lose the energy in the target and there will be no meaning of precise energy available for the reaction. The cross section falls very fast exponentially bellow the Coulomb barrier energy, which require a precise definition of the energy which depends on target thickness also. There are many methods to prepare targets, mainly three methods, i.e chemical, Mechanical and physical. Chemical method normally includes electro deposition, electro polishing, electric discharge etc. Mechanical technique includes compacting, rolling etc. Physical technique includes direct deposition using isotope separation, electro spraying, sputtering, vacuum deposition etc. In many cases target nucleus heavily cost and they are not available independently naturally and also they have low melting point so for those types of targets, electro deposition method is used. In our experiment, we have used the electro deposition method to prepare all targets at the Radiochemistry division, BARC. But in electro deposition [12] a backing material is required and for our case it was Al (thickness $\sim 2\text{mg}/\text{cm}^2$). This is fine because we have measured the offline gamma rays coming out from the evaporation residue (ER). It is necessary that ER should not cross the target plus backing, otherwise this will reduce the ER and hence fusion cross section measurement. Normally pure targets of very thin thickness are required to avoid the absorption of fission fragments, as they should come out from the thin targets. A schematic representation of target preparation by electro deposition method is shown in Fig 3.18.

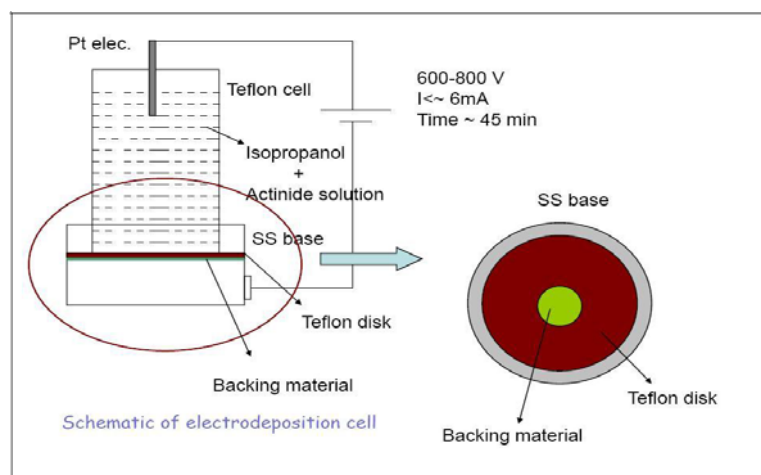


Fig 3.18: Schematic representation of the target preparation by electro deposition

3.5 Accelerator facilities

One of the most essential components of heavy ion (HI) induced studies is the accelerator facilities that deliver energetic nuclear species in the form of beam (incident particles or projectile). When the projectile interacts with the target nuclei, it produces many new particles of interest at desired excitation energy (E_x) and angular momentum (J). The experimental investigations were carried out by carried out using 14UD BARC-TIFR Pelletron accelerator facility at TIFR, Mumbai, India [9] and 6MV FOTIA facility at BARC, Mumbai [6]. Brief descriptions about these facilities are given bellow.

3.5.1 The Pelletron Accelerator at TIFR

The Pelletron Accelerator of 14 million volts was installed in 1988 under a joint collaboration project of BARC and TIFR and the facility housed at TIFR campus, Mumbai. The layout of the accelerator facility is shown in Fig3.19. The source for the charge particles is located at the top of the accelerator tower. A cesium sputter ion source (SNICS) generates [10] negative ion which are initially accelerated to low energies (150-250 keV) in a short horizontal section. The low energy negative ions are then bent through 90° using an injector magnet into the vertical accelerating column. In the first stage, the acceleration results from the electrostatic attraction of the negative ions by the positively charged high voltage terminal situated at the center of the column. The high electric potential at the terminal is achieved by a continuous transfer of charge to the terminal by means of chain of steel pellets and hence gained the name Pelletron Accelerator. The main component of the machine is the accelerating tube, which is made up of eighty-four short sections and housed in an insulating column. The column itself consists of fourteen modules, each capable of withstanding a high voltage up to 1 MV. The whole assembly of the column and tube is located inside a large pressure tank. The pressure throughout the accelerating tube is maintained at an extremely low value, down to $\sim 10^{-10}$ Torr, with the help of the highly insulating sulfur hexafluoride (SF_6) gas at a high pressure of about 6-7 bar. This is necessary to prevent electrical discharge of the high voltage terminal. Inside the terminal, the ions pass through thin carbon foils or a small volume of a gas, where they lose electrons

and become positively charged. The average charge on the ions depends upon the type of ion and the terminal voltage. The resulting positive ions now enter the second or high energy stage of acceleration where the positive voltage of the terminal acts repulsively on the positive ions, in this way the final energy of the ion that has acquired a positive charge

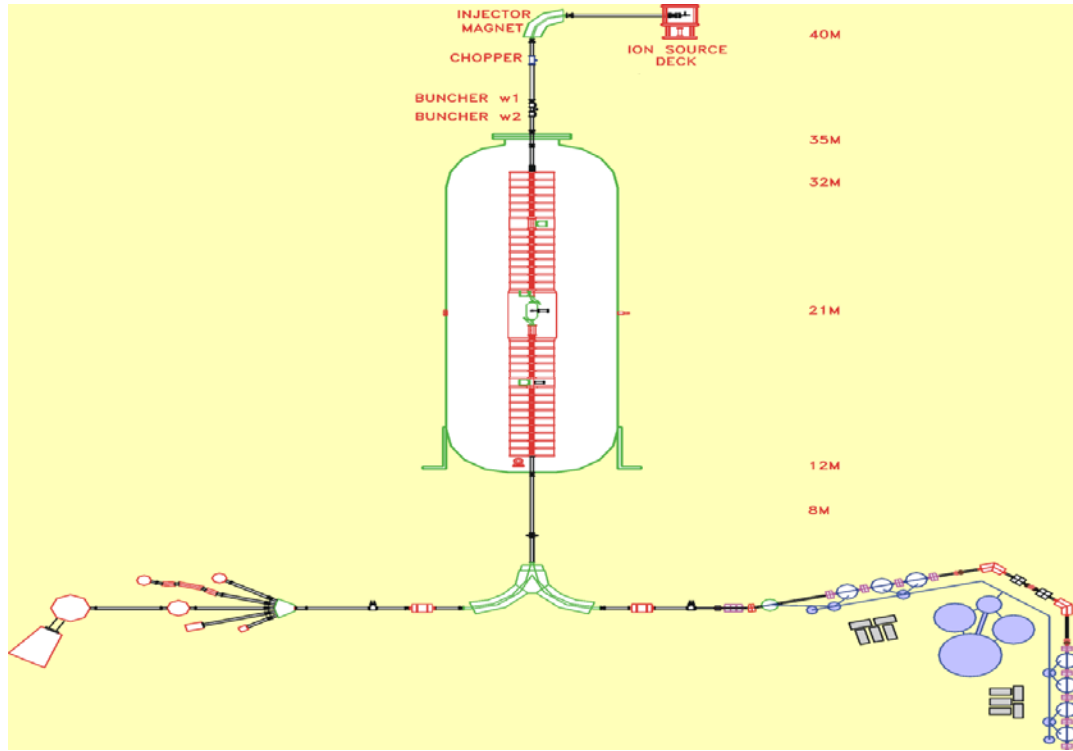


Fig 3.19: Pelletron accelerator situated at TIFR with different parts shown in red letter. At the top SNICS ion source is present. Red strips in center are the 14 number of modules assembly having withstanding voltage of each up to 1MV.

with (+n) unit will be $(n+1)V$, where V is the terminal voltage (maximum 14 MV). Different parts of the accelerator are shown in Fig3.19. Finally at the bottom of the machine, the beam is bent again through 90° and led to the experimental area with the help of another magnet which acts also as an analyzer. The magnet selects and delivers the desired accelerated ions with a particular charge state and energy for the purpose of experiments. The energy (MeV) of the analyzed ions of mass A and charge state q, neglecting relativistic effects, is related to the magnetic field (B is in Gauss) of the analyzing magnet by the relation [11] $B = \frac{720.76\sqrt{AE}}{q}$.

The analyzed beam of ion with high energy resolution ($\Delta E \sim 2$ keV) is then switched to various experimental beam lines and transported to the experimental set up area (where experiments are performed) using a switching magnet. There are five beam lines (along with the types of experiments being done) in the pelletron accelerator facility and is shown in Fig 3.20a. The 0^0 beam line consists of a general purpose scattering chamber (used for

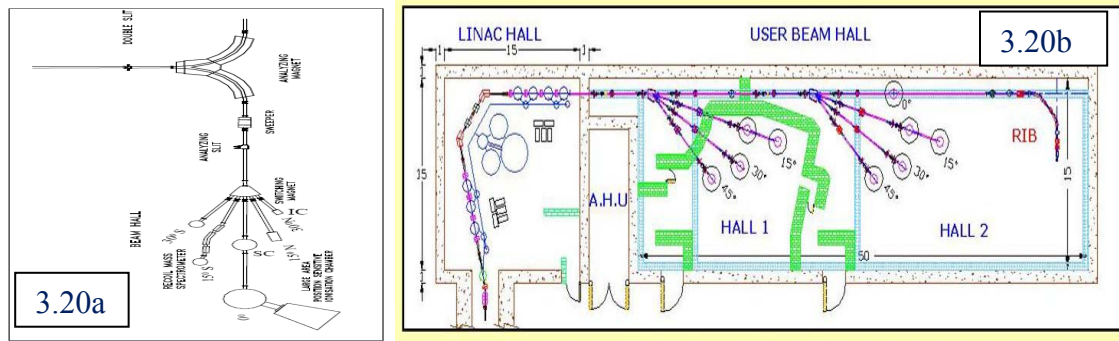


Fig 3.20a: Different beam lines after the 90^0 bending magnet and switching magnet, the right side of the 90^0 bending magnet leads to the LINAC beam, hall which has been developed recently and shown in **Fig 3.20b**.

angular distribution, cross section measurement and various types of nuclear reaction measurements). The 30^0 north beam line is used for irradiation of targets and other samples that are used for the study of material science, radiation biology, etc. The 15^0 north beam line is dedicated for gamma and charge particles spectrum measurements. 15^0 south beam line is dedicated for recoil mass spectrometer. 30^0 south beam line used for γ - rays, charge particles and also atomic physics experiments. In Fig 3.20b new LINAC beam hall is shown. Measurements presented in this thesis are carried out in 0^0 degree (general purpose Scattering chamber) for target thickness measurement and 30^0 north beam line for irradiation of targets. The schematic diagram of the online irradiation chamber is shown in Fig 3.21. Different beam lines are shown in Fig 3.20 with a schematic representation of the beam line which was used during experiments (general purpose scattering chamber (0^0 is shown in Fig 3.22). Each elements of the beam line required careful alignment by means of Theodolite to minimize the non-intentional beam hitting that would result unnecessary neutron, gammas in the back ground. The coupling between the various components was

leak proof and they were cleaned prior to obtain a good vacuum inside the scattering chamber.

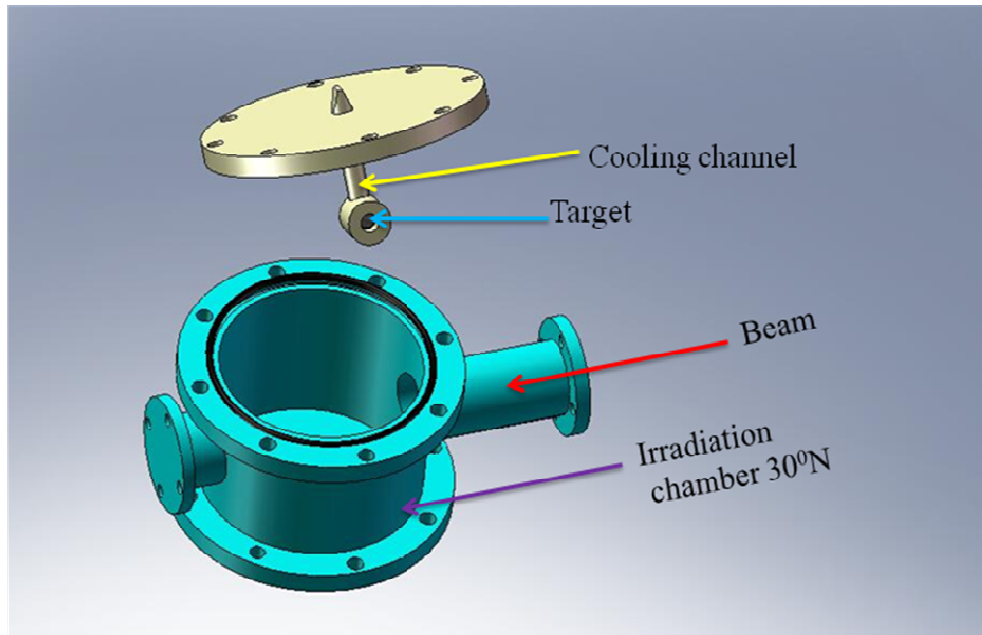


Fig 3.21: Schematic diagram of the irradiation chamber (30° N) for irradiation of targets.

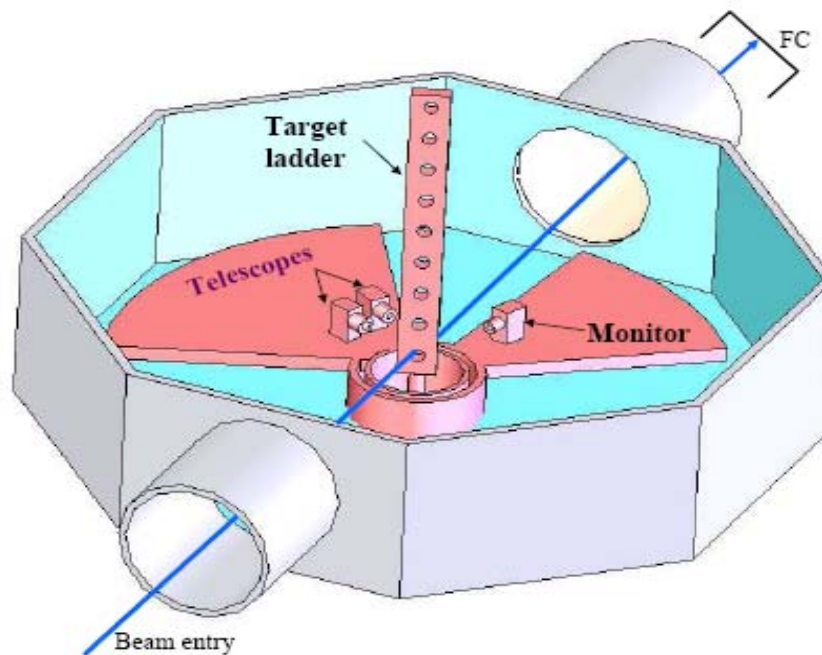


Fig 3.22: Schematic diagram of the scattering chamber to study the Rutherford back scattering for target thickness measurement.

3.5.2 Folded Tandem Ion Accelerator (FOTIA)

The working principle of this accelerator is same as the pelletron. This has been originated from a Van-de-Graff accelerator. Out of a large number of Van-de-Graff accelerators, few of them has been converted to folded tandem accelerator, this is one of them. Initially, it was a single stage 5.5 MV Van-de-Graff generators and converted to a 6 MV folded tandem ion accelerator (FOTIA) by Nuclear Physics Division (NPD) at BARC. The layout of FOTIA is shown in Fig 3.23. It consists of various parts. Several important components are dipole magnets, high voltage generator, electric and magnetic focusing lens, steering devices, vacuum system, SF₆ gas handling and computer controlled systems. Here the negative ion beam extracted from SNICS source is shown in Fig 3.24 and is accelerated up to 150 keV. The negative ion of the desired mass is selected using 70° dipole magnet

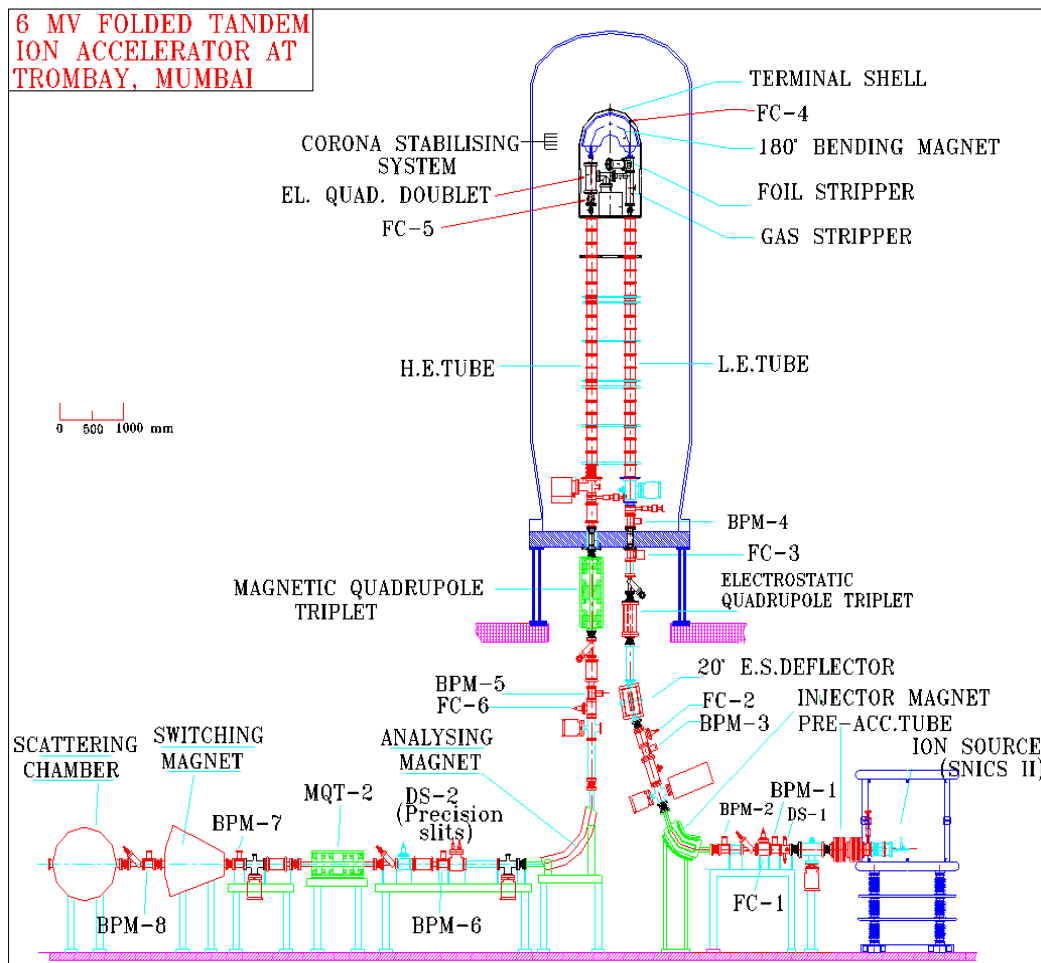


Fig 3.23: Schematic diagram of the 6 MV folded tandem Ion accelerator.

for injection into the low energy accelerating section. An electrostatic quadruple triplet and an einzel lens are used to focus and match the beam parameter to the acceptance of the low energy tube. The electrons of the negative ion then get stripped off at the stripper and a desired charge state of positive ion thus produced is selected through 180° magnet inside the high voltage terminal before being bent after which it enters into the high energy acceleration tube, where further acceleration occurs. A quadruple doublet has been used to focus the diverse beam of 180° magnet at the exit of magnet to enter the high energy tube and then the desired beam has been bent by 90° bending magnet as shown in Fig 3.23 and transported to different beam lines through the switching magnet. There are five beam lines available for different experiments. Different beam lines are shown in Fig 3.25. We have measured the thickness of the targets ($^{144,152}\text{Sm}$) by Rutherford back scattering (RBS) method using proton beam from FOTIA in the 0° beam line (general purpose scattering chamber) and found that the results are consistent with the ones measured by RBS method using ^{16}O beam from TIFR Pelletron Accelerator.



Fig 3.24: SNICS source using in FOTIA facility for beam ion extraction.

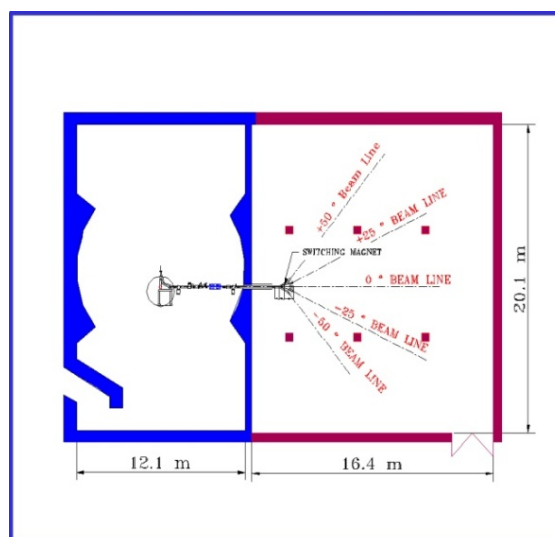


Fig 3.25: sketch of different beam line present at FOTIA facility.

3.6 Target thickness measurement and Irradiation

We measured the thickness of the targets which was prepared at RCD laboratory, BARC by electro deposition method.

3.6.1 Target Thickness measurement

The schematic representation of the thickness measurement set up is shown in Fig 3.26. Three surface barrier (SSB) detectors have been used. One at the back angle (i.e. 170°) and another two SSB at forward angle (i.e. 30°) for beam normalization and is shown in Fig 3.26.

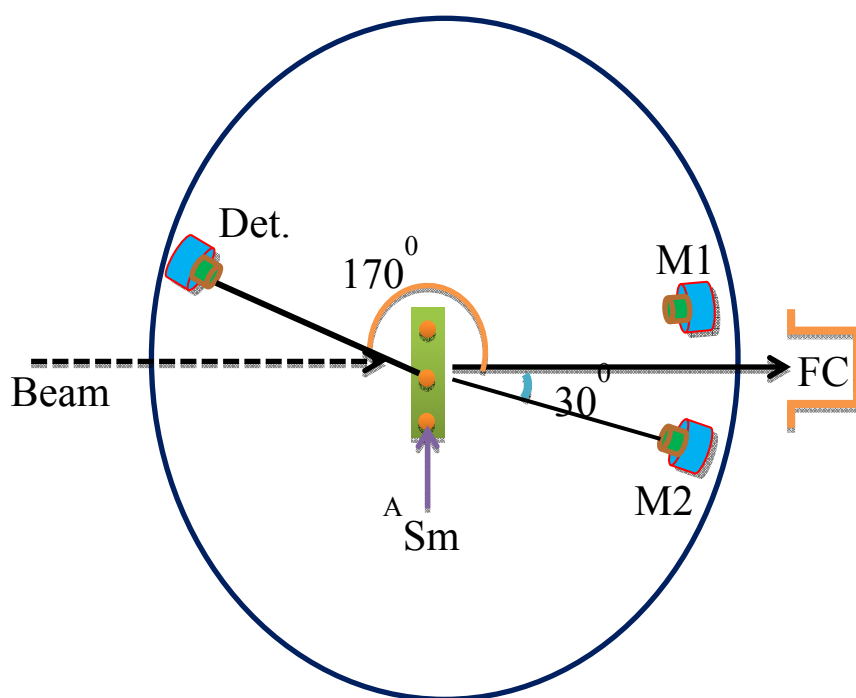


Fig 3.26: Schematic representation of the thickness measurement set up. M1, M2 are the two SSB detectors placed at the forward for beam normalization. Another SSB placed at 170° to identify the scattered particle from ^ASm and Al. FC is the faraday cup from which the beam flux was calculated.

The detector thickness was $300\ \mu\text{m}$ such that the scattered beam will stop in the detector and deposited all its energies. The targets were mounted at the center of the chamber and a beam of ^{16}O of 40MeV [20] from TIFR Pelletron and proton (p) of 4MeV from FOTIA facility was used [20], ($V_B \sim 10\ \text{MeV}$ and $\sim 64\ \text{MeV}$ for $p^{144,152}\text{Sm}$ and $^{16}\text{O}^{144,152}\text{Sm}$ system respectively). The schematic of the electronic circuit diagram for the target thickness measurement is shown in Fig 3.27. We found the consistency in the thickness measurement using proton and oxygen beams. We kept our detector in the backward angle

(i.e. 170°) to protect the detectors from huge background of elastic in forward direction. A typical raw spectrum acquired in RBS measurement for target thickness is shown in Fig 3.28 from the detected spectrum; we have extracted the thickness of the target by using the following formula

$Y = N_t N_p (d\sigma/d\Omega) d\Omega$. [1]. Y is the yield under the ^{A}Sm peak as shown in Fig 3.28, N_p is the number of incident projectile, which has been calculated from the current integrator (CI) as follows, $N_p = \text{CI} (\text{nC}) / (Z_p \times 1.6 \times 10^{-19} \text{ C})$, Z_p is the charge state of the incident particle (projectile) and it was assumed that almost all the electrons will strip out after passing through the stripper foil. $d\Omega$ is the solid angle subtended by the detector. $d\sigma/d\Omega$ is the partial Rutherford cross section at that scattering angle.

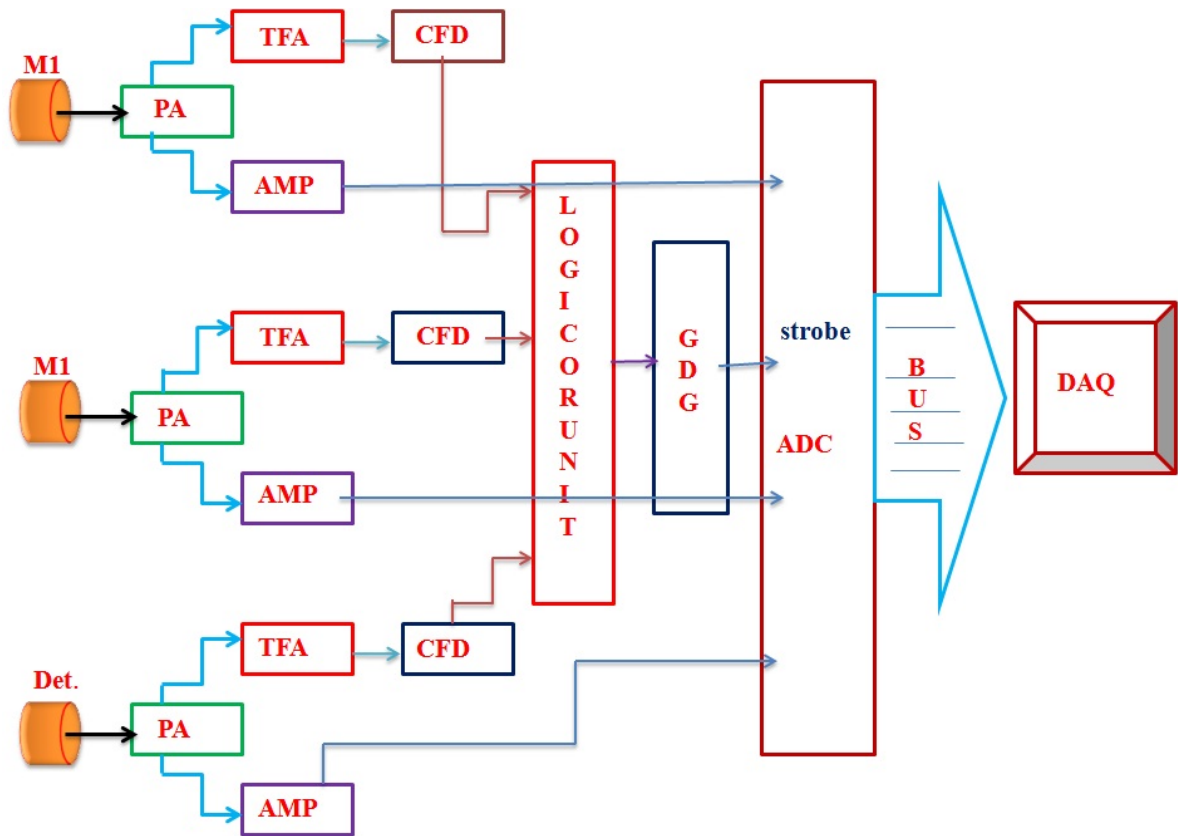


Fig 3.27: Schematic representation of the electronics diagram for the target thickness measurement. $M1$, $M2$ are the two SSB placed at the forward angle for beam normalization. Another SSB placed at 170° to identify the scattered particle. PA, AMP, TFA, CFD are the preamplifier, amplifier, time filter amplifier, constant fraction discriminator and ADC is the analog to digital converter. DAQ is the data acquisition system.

Using all the above values we have determined the thickness of the target as,

$N_t = Y / (N_p (d\sigma/d\Omega) d\Omega)$ in cm, by divide the N_t with the density (ρ) of the material we will get mass thickness of the target. Table3.2 shows the thickness (mass thickness) of the different ^ASm samples which was used for irradiation . Using Proton beam and ^{16}O beam, the thickness of the samples is consistent with each other.

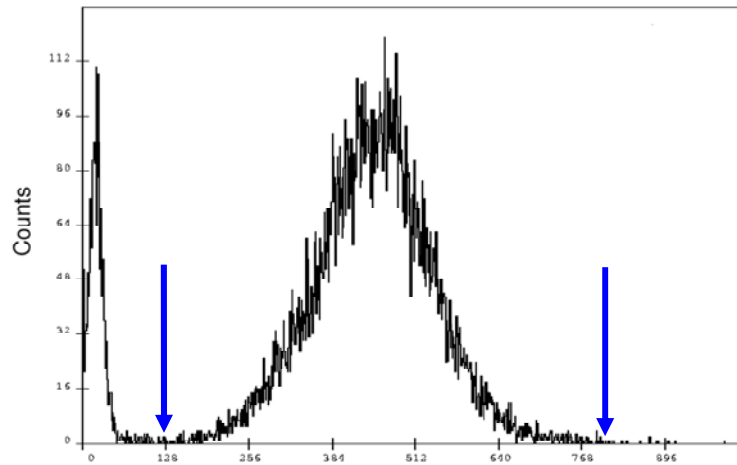


Fig 3.28: A typical raw-spectrum for the target thickness measurement at 6MeV of proton (*p*) beam.

Table 3.4: The thickness of the different ^ASm samples using Proton beam and ^{16}O beam from FOTIA and TIFR pelletron respectively.

Sample number.	60 Mev ^{16}O in unit ($\mu\text{g}/\text{cm}^2$) (TIFR)		6MeV proton in unit ($\mu\text{g}/\text{cm}^2$) (FOTIA)	
	^{144}Sm	^{152}Sm	^{144}Sm	^{152}Sm
Sm-1	614.37	603.3	608.5	551.2
Sm-2	442.45	527.6	451.3	466.4
Sm-3	585.47	577.2	578.3	552.6
Sm-4	678.53	480.8	665.2	467.8
Sm-5	596.96	591.5	576.2	514.2
Sm-6	563.32	450.3	553.5	449.8
Sm-7	477.64	486.9	475.3	508.5

Sm-8	666.40	479.4	650.4	479.7
Sm-9	565.47	523.6	572.6	577.8
Sm-10	540.91	499.9	545.2	494.9
Sm-11	449.64	497.7	441.3	445.4
Sm-12	540.91	519.4	551.8	477.5
Sm-13	478.644	585.5	465.9	595.8

3.6.2 Irradiation

The sample ($^{144,152}\text{Sm}$) was loaded on the target holder in the irradiation chamber shown previously in Fig 3.21. The target material faced the incident beam and the Al backing act as the catcher. When Li ion interacts with Sm target giving away all its energy in collision with the nucleons of the target nucleus. Once this has happened, the incident particle loses its identity and becomes a part of the target nucleus. The nucleus thus formed is called the compound nucleus (CN) Terbium which is in a highly excited state (Tb^*) [20,21]. The excited Tb^* decays mostly by neutron emission and the evaporation residue (ER) goes to Gd^* isotope through electron capture and then decay by gamma emission. We have observed the emitted gamma by off line gamma measurement procedure. The CN will

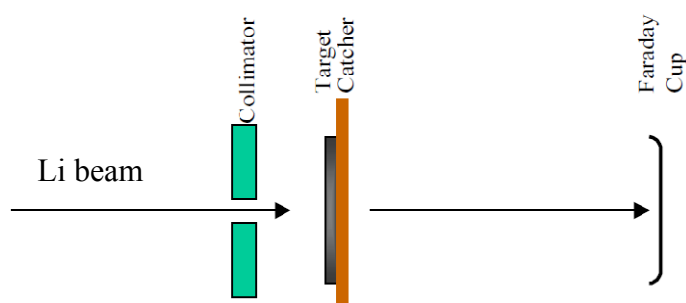


Fig 3.29: Schematic representation of the target and catcher.

decay by the emission of either particle or gamma and try to cool down. In most of the cases the neutron emission is more favorable as it will not see any barrier. The thickness of the Al or catcher is such that ER will stop in the Al backing. There are two types of off-line gamma spectroscopy, i) Thick target irradiation, where the CN formed due to different channels will stop in the target itself and the emitted gamma rays from the ER will be

counted off line. The identification is quite complex as many gamma rays will coming from different nuclei. ii) Thin target irradiation, where after the formation of the CN due to the recoil velocity, the CN will come out from the target and stop in very thin Al catcher foil placed behind it, which is called the recoil range distribution (RRD) method and then same off-line counting is to be done for different catcher.

The concept of RRD based on the momentum transfer to the target by the incident particle. When we use a light particle ${}^6,7\text{Li}$ (say) and do the RRD measurements for different channels, the difference in the momentum transfer to the target from one channel to the other will be very small. Hence in the case of light particles, we have to use very very thin catcher at very close precise distance and measure RRD. This leads to more uncertainty in the results. For energy bellow the barrier there will be no fusion classically but only due to quantum tunneling then it will be difficult to measure using RRD method. The prominent γ -rays of the standard ${}^{152}\text{Eu}$ source have been used in the present measurements. Fig 3.2 shows a typical efficiency plot using ${}^{152}\text{Eu}$ & ${}^{133}\text{Ba}$ at different distance from the source.

3. 6. 2. i Irradiation of ${}^6\text{Li}+{}^{144}\text{Sm}$ [20].

We have used Samarium (${}^{144}\text{Sm}$) targets of isotopic abundance of 94% (enriched) having thickness in the range of 450-678 $\mu\text{g}/\text{cm}^2$. For the fusion measurement, the target was mounted with an additional Al backing downstream. The thickness of the Al backing was sufficient to completely stop all the evaporation residues (ERs) produced during irradiation. According to the half- life, each target was irradiated for 4–5 h by the ${}^6\text{Li}$ beam with energy $E_{\text{lab}}= 20\text{--}40$ MeV, in steps of 2 MeV. The beam current was ~ 60 nA, and the beam flux was calculated by the total charge collected in the Faraday cup placed behind the target using a precision current integrator device. The reaction products, which were stopped in the target and Al backing, were identified by their characteristic γ rays and half life by off-line counting using a high-purity Ge detector coupled to a multichannel analyzer as mentioned in Table 3.5. A ${}^{152}\text{Eu}$ source was used for the energy calibration as well as for the efficiency measurement. The standard γ source and the irradiated samples were counted in the same geometry. The spectroscopic detail of ${}^6\text{Li}$ tells that there is no bound excited state of ${}^6\text{Li}$ as the breakup threshold is 1.47 MeV for (α +d) channel. Fig 3.30 shows

different reaction channels. In one case, the ${}^6\text{Li}$ has completely fused with the target called complete fusion (CF) and in other case, the ${}^6\text{Li}$ has breakup and a part of the projectile has fused (either α or d) with the target called incomplete fusion (ICF) or breakup fusion.

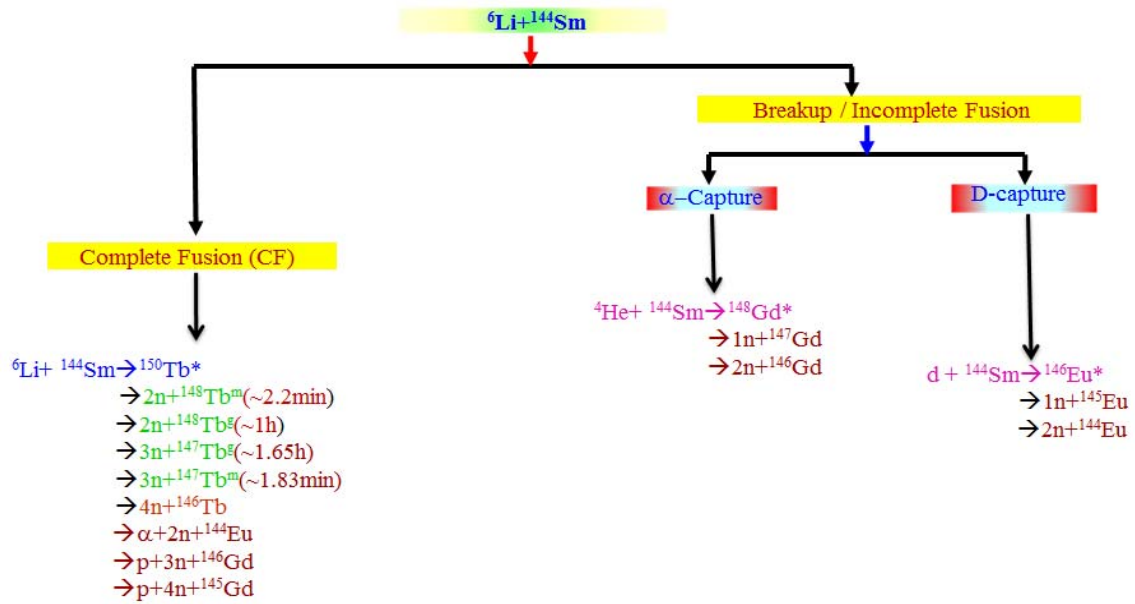


Fig 3.30: The different decay channels for ${}^6\text{Li} + {}^{144}\text{Sm}$ system with different ER and half-life. We have detected only the CF channel (i.e. 2n, 3n ER channel)

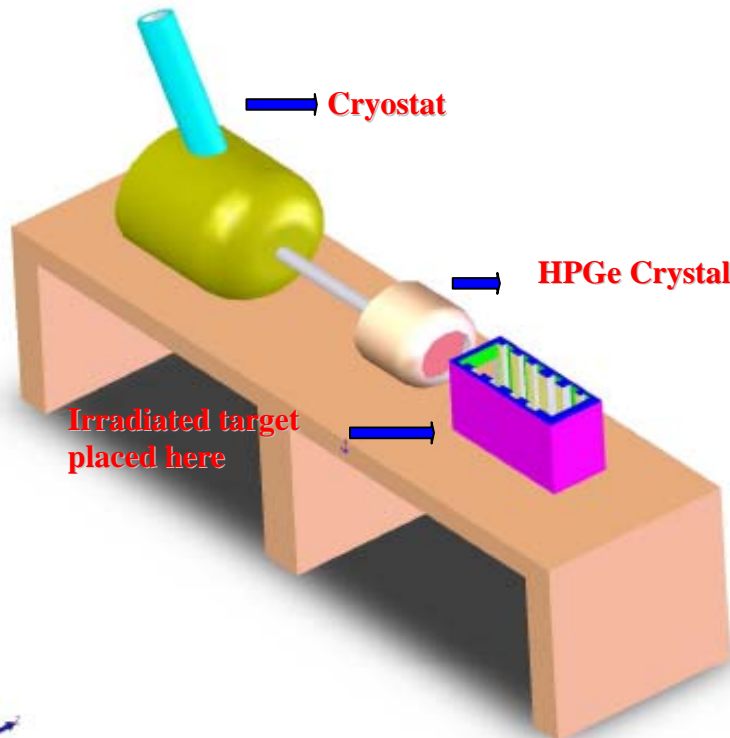


Fig 3.31: Schematic diagram of the detection process.



A schematic diagram of the detection process is shown in Fig 3.31. After irradiation, the sample was kept in front of HPGe detector for measuring γ activity at a appropriate distance to avoid high dead time of the detector, normally dead time was kept bellow 5% , during data acquisition. The cryocan was filled with liquid Nitrogen (77K) to reduce thermal noise. At regular interval of time the performance of the detector was verified. A typical recorded gamma (γ) ray spectrum for ${}^6\text{Li}+{}^{144}\text{Sm}$ at 40 MeV is shown in Fig3.32.

After detection of different gamma rays emitted from the different ER channels we have done the half-life fitting. Corresponding nuclear data, such as half-lives ($T_{1/2}$), γ -ray energies (E_γ), and branching ratios (I_γ), etc., were taken from the Table of Isotope and Nuclear Wallet card [69] and are listed in Table 3.5 . The intense γ lines were chosen to evaluate the cross sections. The ER cross section has been extracted from the raw data using the formula as shown in Eqⁿ (62) discussed in chapter2. To check the consistency we have compared the cross section using different gamma rays coming from the same ER with different branching ratio and efficiency and giving the same results. To see the effect of the breakup of loosely bound projectile ${}^6\text{Li}$ on fusion cross sections, the present data

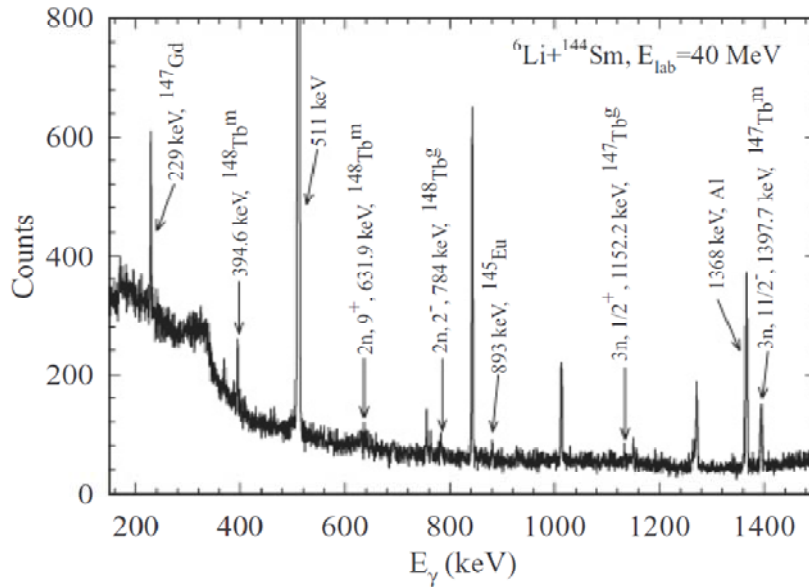


Fig 3.32: A typical γ -ray spectrum showing gamma lines of different ERs populated via CF in the ${}^6\text{Li}+{}^{144}\text{Sm}$ reactions at projectile energy of 40 MeV

Table 3.5: Reactions investigated and decay characteristics of evaporation residues in the ${}^6\text{Li} + {}^{144}\text{Sm}$ system for ground state (g) and meta stable state (m).

Reaction	ER	E_γ (keV)	$T_{1/2}$	J^π	I_γ (%)
${}^{144}\text{Sm}({}^6\text{Li},3n)$	${}^{147}\text{Tb}^m$	1397.7 (m)	1.83 min	$11/2^-$	83.2
${}^{144}\text{Sm}({}^6\text{Li},3n)$	${}^{147}\text{Tb}^g$	1152.2 (g)	1.65h	$1/2^+$	72.5
${}^{144}\text{Sm}({}^6\text{Li},2n)$	${}^{148}\text{Tb}^m$	631.9 (m)	2.2 min	9^+	95
${}^{144}\text{Sm}({}^6\text{Li},3n)$	${}^{148}\text{Tb}^g$	784 (g)	1.0h	2^-	100

were compared with the data for other systems forming similar compound nuclei but involving strongly bound projectiles ${}^{12}\text{C} + {}^{141}\text{Pr}$ [22,23] and ${}^{20}\text{Ne} + {}^{133}\text{Cs}$ [24] forming the compound nucleus ${}^{153}\text{Tb}$. The CF cross section has been compared and found that the CF induced by ${}^6\text{Li}$ reaction is more suppressed than the other systems mentioned above, their by indicating the effect of break up. The detail analysis using statistical model and the coupled channel calculations will be discussed in chapter-4.

3. 6. 2. ii Irradiation of ${}^6\text{Li} + {}^{152}\text{Sm}$ [21].

We have used Samarium (${}^{152}\text{Sm}$) targets of isotopic abundance of 98% (enriched) having the thickness in the range of 450-580 mg/cm². The targets were prepared by electro deposition method on Al backing of thickness ~ 2 mg/cm². The thickness of the targets was measured by Rutherford back scattering (RBS). Using 60 MeV ${}^{16}\text{O}$ beam as well as 6 MeV proton beam. The targets with the Al backings were placed normal to the beam direction so that the recoiling nuclei, which are formed during the interaction of the projectile and the target nucleus are stopped in target + Al backing assembly. Each target was irradiated for 6–8 hours by ${}^6\text{Li}$ beam with energy $E_{lab} = 20\text{--}40$ MeV in steps of 0.5–2.0 MeV. The beam current was $\sim 40\text{--}100$ nA and the beam flux was calculated by the total charge collected in the Faraday cup placed behind the target. The reaction products stopped in the target and Al backing were identified by their characteristic gamma rays and half life mentioned in Table 3.6 by off-line counting using HPGe detector coupled to a multichannel analyzer. The radioactive sources viz., ${}^{152}\text{Eu}$ and ${}^{133}\text{Ba}$ has been used for efficiency measurement and

calibration of the detector (HPGe). The energy resolution of the HPGe detector was ~ 2.7 keV for $E_\gamma = 778$ keV and ~ 3 keV for $E_\gamma = 1408$ keV of the ^{152}Eu source. Time to time the calibration and the efficiency spectrum was recorded to confirm the consistence performance of the detector. In Fig3.33 shows different reaction channels, in one case, the ^6Li has completely fused with the target called complete fusion (CF) and in other case, the ^6Li has breakup and a part of the projectile has fused (either α or d) with the target called incomplete fusion (ICF) or break up fusion. After irradiation we kept the sample in front of HPGe detector and a typical gamma (γ) ray spectrum was recorded for $^6\text{Li}+^{152}\text{Sm}$ system at $E_{\text{lab}} = 34$ MeV and is shown in Fig3.34. 2n,3n,4n and 5n evaporation forming the residual nuclei ^{156}Tb , ^{155}Tb , ^{154}Tb and ^{153}Tb either in ground state (g.s) or in metastable state (m.s), which then decay to Gd isotopes by electron capture. Corresponding nuclear data, such as half-lives ($T_{1/2}$), γ -ray energies (E_γ), and branching ratios (I_γ), etc., are listed in Table 3.6 The intense γ lines were chosen to evaluate the cross sections

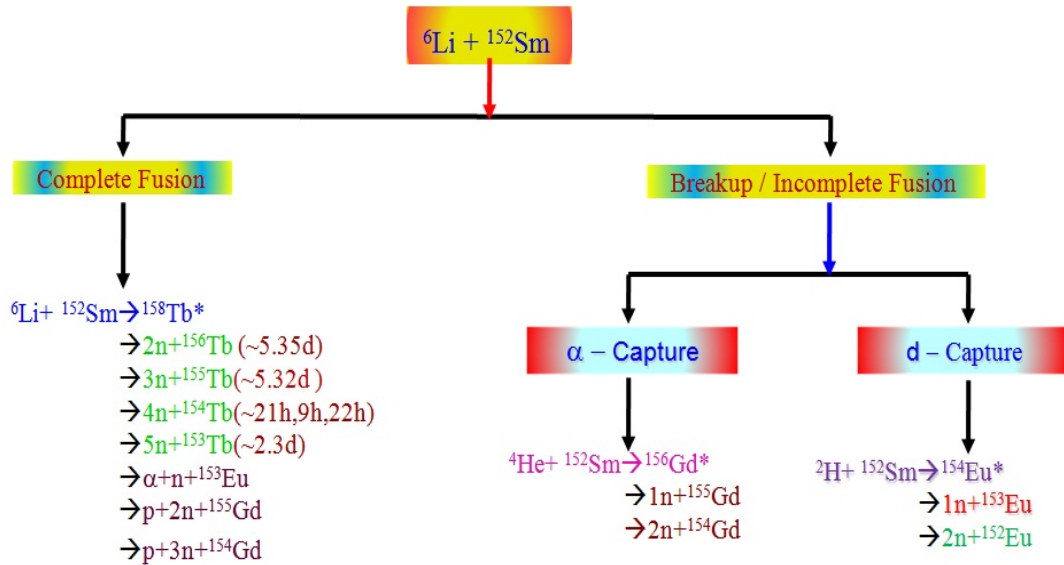


Fig 3.33: The different decay channels for $^6\text{Li}+^{152}\text{Sm}$ system with different ER and half-life. We have detected only the CF channel (i.e. 2n, 3n,4n,5n ER channel)

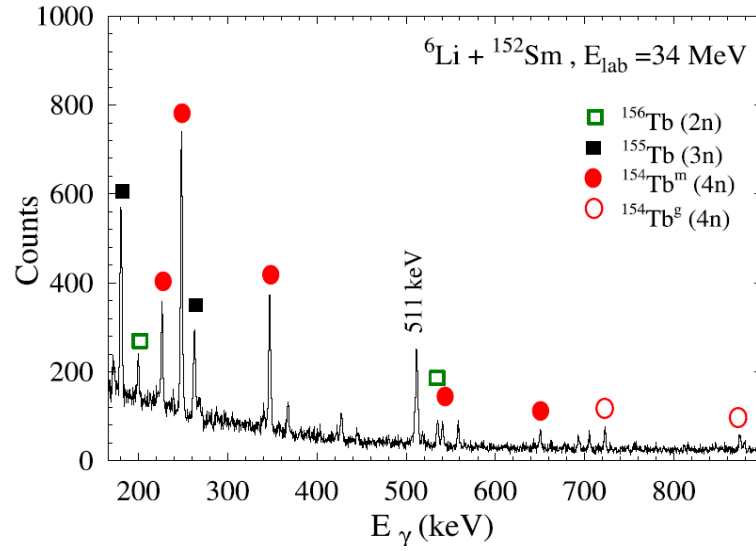


Fig 3.34: Typical γ -ray spectrum showing gamma lines of different ERs populated via CF in the ${}^6\text{Li} + {}^{152}\text{Sm}$ reaction at projectile energy = 34 MeV. Different ER channels are shown in different symbol.

Table 3.6: Reactions investigated and decay characteristics of evaporation residues in the ${}^6\text{Li} + {}^{152}\text{Sm}$ system.

Reaction	ER	E_γ (keV)	$T_{1/2}$	I_γ (%)
${}^{152}\text{Sm}({}^6\text{Li}, 2n)$	${}^{156}\text{Tb}$	534.3	5.35d	66.34
${}^{152}\text{Sm}({}^6\text{Li}, 3n)$	${}^{155}\text{Tb}$	180.1	5.32d	7.45
		262.3	5.32d	5.3
${}^{152}\text{Sm}({}^6\text{Li}, 4n)$	${}^{154}\text{Tb}^g$	1274.4	21.5h	10.5
		722.1	21.5h	7.7
${}^{152}\text{Sm}({}^6\text{Li}, 4n)$	${}^{154}\text{Tb}^{m1}$	540.2	9.4h	20.0
		649.6	9.4h	10.9
${}^{152}\text{Sm}({}^6\text{Li}, 4n)$	${}^{154}\text{Tb}^{m2}$	346.7	22.7h	69.2
		1419.8	22.7h	46.0
		225.9	22.7h	26.8
${}^{152}\text{Sm}({}^6\text{Li}, 5n)$	${}^{153}\text{Tb}$	212	2.34d	31.0
		170.5	2.34d	6.3
${}^{152}\text{Sm}(d, 3n)$	${}^{152}\text{Eu}^{m1}$	841.6	9.274h	14.2
		963.4	9.274h	11.67

The extraction of the cross section for different ER channels has been done using the same formula as discussed in chapter 2 and used for ${}^6\text{Li}+{}^{144}\text{Sm}$ system. The CF cross section has extracted using the cumulative cross section of all the channels with the help of theoretical ratio R_{σ}^{theory} and the analysis using theoretical calculations are discussed in chapter-4.

3. 6. 2. iii Irradiation of ${}^7\text{Li}+{}^{144,152}\text{Sm}$ [25].

We have used ${}^7\text{Li}$ beam as incident particles and ${}^{144}\text{Sm}$ (94% enriched) and ${}^{152}\text{Sm}$ (98%enriched) as the targets. Targets were prepared by electro deposition method on Al backing of thickness $2.2\text{mg}/\text{cm}^2$. The thickness of the targets was measured by the Rutherford backscattering method and found in the range of $450 - 680 \mu\text{g}/\text{cm}^2$. For the fusion measurement, the target was mounted with additional Al backing down stream of the beam. The thickness of the Al backing was sufficient to completely stop all the evaporation residues (ERs) that are produced during irradiation. According to the half life of the ERs that were expected to be formed in significant abundance and their total cross sections, each target was irradiated for 4 to 8 hours by ${}^7\text{Li}$ beam with energy $E_{lab}= 22$ to 40 MeV, in steps of $1 - 2$ MeV. The beam current was $\sim 25-60$ nA and the beam flux was calculated by the total charge collected in the Faraday cup, placed behind the target using a precision current integrator device. The reaction products, which were stopped in the target and Al backing, were identified by their characteristic γ -rays by off-line counting using HPGe detector coupled to a multichannel analyzer.

${}^{152}\text{Eu}$ source was used for the energy calibration as well as for the efficiency measurement.. A typical gamma (γ) ray spectrum is recorded for ${}^7\text{Li}+{}^{144}\text{Sm}$ and ${}^7\text{Li}+{}^{152}\text{Sm}$ at 28, 30 MeV and is shown in Fig3.35. When ${}^7\text{Li}$ fuses with the target nucleus, ${}^{144}\text{Sm}$, it will produce the excited compound nucleus ${}^{151}\text{Tb}^*$. After 2n evaporation, it produces the evaporation residue (ER) ${}^{149}\text{Tb}^*$ (g.s.) with the half-life ($t_{1/2}$) of 4.118h and ${}^{149}\text{Tb}^*$ (m.s.) with $t_{1/2}\sim 4.16\text{m}$. In case of 3n evaporation it produces the residues ${}^{148}\text{Tb}^*$ having meta stable state (${}^{148}\text{Tb}^*\text{m}$, $t_{1/2}\sim 2.2\text{m}$) and ground state (${}^{148}\text{Tb}^*(\text{g.s.})$, $t_{1/2}\sim 60.0\text{m}$), which decay to Gd nuclei after electron capture. Similarly, for ${}^7\text{Li}+{}^{152}\text{Sm}$ reaction, the compound nucleus ${}^{159}\text{Tb}^*$ decays by 3n and 4n evaporation followed by electron capture to ${}^{156}\text{Gd}$ and

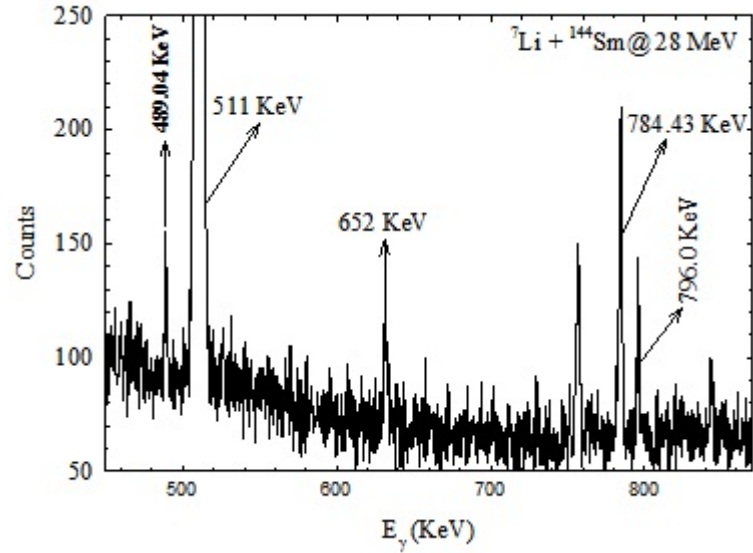


Fig 3.35: Typical γ -rays spectrum showing gamma lines of different ERs populated in ${}^7\text{Li} + {}^{144}\text{Sm}$ reactions at projectile energy 28 MeV.

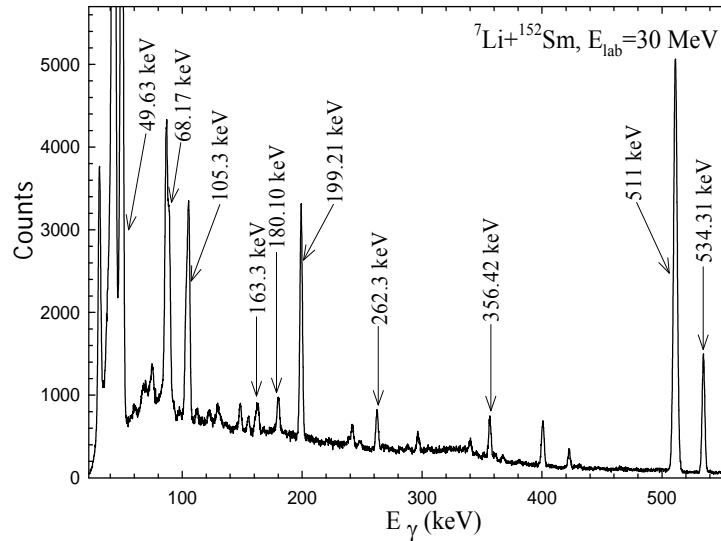


Fig 3.36: Typical γ -rays spectrum showing gamma lines of different ERs populated in ${}^7\text{Li} + {}^{152}\text{Sm}$ reactions at 30 MeV.

${}^{155}\text{Gd}$ nuclei with $t_{1/2} = 5.35$ d and 5.32 d respectively. Corresponding nuclear data, such as half-lives ($T_{1/2}$), γ -ray energies (E_γ), and branching ratios (I_γ), for different channel etc. are listed in Table 3.7[69]. Fig3.38 shows different reaction channels populated via complete

fusion and breakup fusion of ${}^7\text{Li}+{}^{152}\text{Sm}$. In one case the ${}^7\text{Li}$ has completely fused with the target and in other case, the ${}^7\text{Li}$ has breakup (into α & t) and a part of the projectile has fused (either α or t) with the target. Intensities of the gamma lines with proper branching ratio corresponding to both ground and meta stable states of different ERs together give the cross sections for different ER channels. The intense gamma lines were chosen to evaluate the cross sections. The other gamma lines corresponding to the same ERs were also used to cross check the measured cross sections.

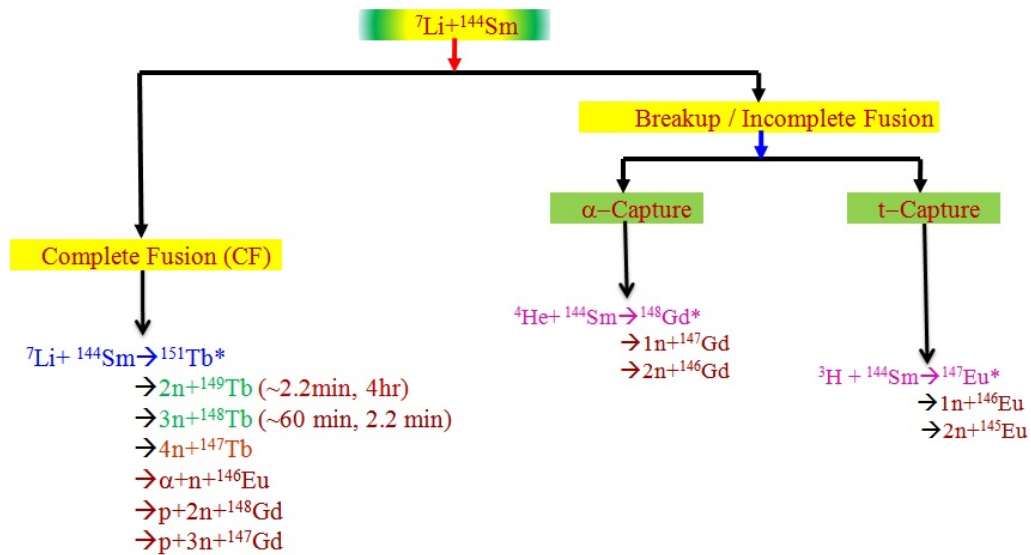


Fig 3.37: The different decay channels of ERs through CF and ICF for ${}^7\text{Li}+{}^{144}\text{Sm}$ system

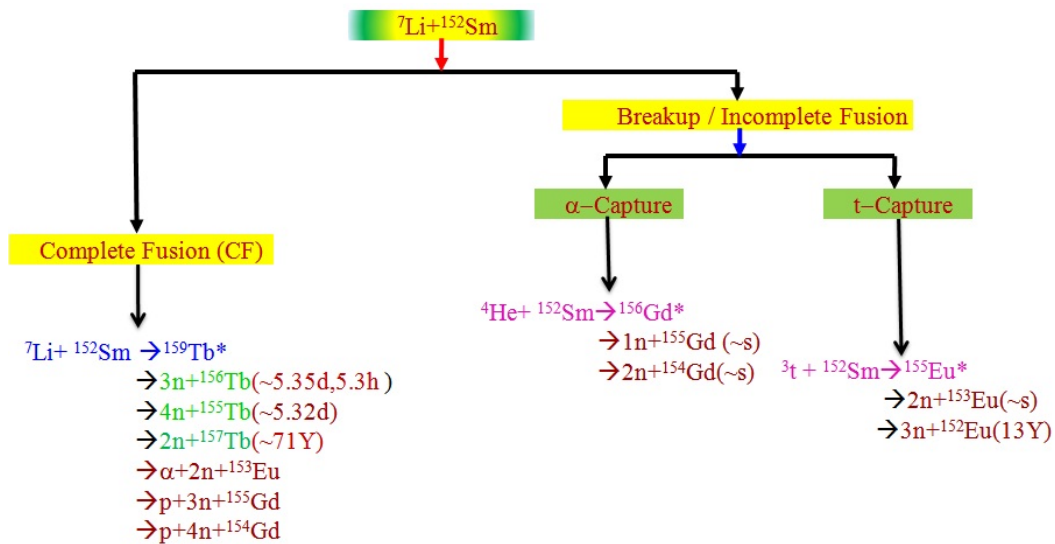


Fig 3.38: The different types of ERs through CF and ICF for ${}^7\text{Li}+{}^{152}\text{Sm}$ system

Table 3.7: Reactions investigated and the characteristics of evaporation residues in the ${}^7\text{Li}+{}^{144,152}\text{Sm}$ systems.

Reaction	ER	E_γ (keV)	$T_{1/2}$	J^π	I_γ (%)
${}^7\text{Li}+{}^{144}\text{Sm}$					
${}^{144}\text{Sm}({}^7\text{Li},2n)$	${}^{149}\text{Tb}^m$	796.0	4.16 m	$11/2^-$	90
${}^{144}\text{Sm}({}^7\text{Li},2n)$	${}^{149}\text{Tb}^g$	352.2	4.118h	$1/2^+$	29.3
${}^{144}\text{Sm}({}^7\text{Li},2n)$	${}^{149}\text{Tb}^g$	853.4	4.118h	$1/2^+$	15.4
${}^{144}\text{Sm}({}^7\text{Li},3n)$	${}^{148}\text{Tb}^m$	394.5	2.2 m	9^+	86
${}^{144}\text{Sm}({}^7\text{Li},3n)$	${}^{148}\text{Tb}^m$	784.5	2.2m	9^+	100
${}^{144}\text{Sm}({}^7\text{Li},3n)$	${}^{148}\text{Tb}^g$	489.0	60m	2^-	19.74
${}^{144}\text{Sm}({}^7\text{Li},3n)$	148Tbg	784.4	60m	2^-	84
${}^7\text{Li}+{}^{152}\text{Sm}$					
${}^{152}\text{Sm}({}^7\text{Li},3n)$	${}^{156}\text{Tb}^g$	199.2	5.35d	3^-	40.9
${}^{152}\text{Sm}({}^7\text{Li},3n)$	${}^{156}\text{Tb}^g$	356.4	5.35d h	3^-	13.61
${}^{152}\text{Sm}({}^7\text{Li},3n)$	${}^{156}\text{Tb}^g$	534.3	5.35d	3^-	66.6
${}^{152}\text{Sm}({}^7\text{Li},4n)$	${}^{155}\text{Tb}^g$	163.3	5.32d	$3/2^+$	4.44
${}^{152}\text{Sm}({}^7\text{Li},4n)$	${}^{155}\text{Tb}^g$	180.1	5.32d	$3/2^+$	7.45
${}^{152}\text{Sm}({}^7\text{Li},4n)$	${}^{155}\text{Tb}^g$	262.3	5.32d	$3/2^+$	5.29

References:

- [1] S. N. Ghoshal, “ Nuclear Physics” ISBN: 81-219-0413-7, (2004)
- [2] S. Santra *et al.*, Nucl. Instr. & Meth. A 496, 44–50 (2003)
- [3] Luong *et al.*, Phys. Lett. B 695, 105 (2011)
- [4] K. Kalita Phys. Rev. C 73, 024609 (2006)
- [5] S. S. Kapoor *et al.*, Indian Jour. of pure & applied phys., 27 623 (1989)
- [6] P. P. Singh *et al.*, Pramana 57 639 (2001)
- [7] (USA) Patent 1948384, Ernest O. Lawrence “method & apparatus for the acceleration of ions”.
- [8] Alonso M., Finn, E. (1996) Phys. addit. Wesley
- [9] <http://www.tifr.res.in/~pell/>
- [10] X. M. Wang, “Nucl. Instr. methods. Phys. Res .B 241, 885 (2006)
- [11] C. Olmer *et al.* , phys. Rev. Lett. 476 (1977)
- [12] Dufour.jim (2006), “an introduction to metallurgy 5th Cameron
- [13] K. S. Krane, “ Introductory Nuclear Physics” , Jhonwiley & sons,ISBN 0-471-85914-1
- [14] G. F. Knoll, “ Radiation Detection &Measurement”,
- [15] M. S. Livingston and H. A. Bethe : Rev. mod. phys. 9, 245 (1937)
- [16] F. S. Goalding, in treastise on “heavy ion science” , edited by D.A. bromley (plenum prss, N. Y., Vol 7, P-227, (1985)
- [17] S. Kailas & A. shrivastava in “reaction detection and measurements”
(IANCAS Bulletin), vol 111, P-225 (July 2004)
- [18] V. V. Parkar *et al.*, Nucl. Phys. A 794, 187-20, (2007)
- [19] Electroics & Med. Phys. 4 R06/6R03 “radioisotope and radiation methelogy” p-6
- [20] P. K. Rath *et al.*, Phys. Rev. Phy. C 79, 051601 (R) (2009)

Chapter 3: Instruments, Detection techniques...

- [21] P. K. Rath *et al.*, Nul. Phys. A 874 , 14 (2012)
- [22] P. P. singh *et al.*, Int. J. Modrn Phys. E 17, No-9,549(2008)
- [23] F. Plasil *et al.*, Phys. Rev. Lett. **45**, 333 (1980).
- [24] R. Kossakowski *et al.*, Phys. Rev. C **32**, 1612 (1985).
- [25] P. K. Rath *et al.*, going to communicate to PRC (2012)
- [26] National Nuclear data Center (NNDC). Brookhaven National Laboratory Upton,
New York 11973-5000(2012), URL <http://www.nndc.bnl.gov/>
- [27] W. R. Leo, “Techniques for Nuclear and Particle Physics Experiments”
(Springer Verlag Berline Heidelberg, 1995 2nd ed.)

Chapter 4

4.1 Complete Fusion Suppression in ${}^6\text{Li} + {}^{144}\text{Sm}$ system.

4.1.1 Introduction

The effect of the breakup of weakly bound (stable or radioactive) nuclei on the fusion process is a subject of current experimental and theoretical interest [1,2]. Although sub-barrier fusion involving strongly bound stable nuclei is well understood, there are contradictory results and predictions about the enhancement or suppression of the fusion cross section σ_{fus} , over predictions of the single fusion barrier around the Coulomb barrier, when one of the collision partners is a weakly bound nucleus. Experimental investigations of the fusion process have been made with stable weakly bound ${}^6,7\text{Li}$ [3, 4] and ${}^9\text{Be}$ [5, 6] nuclei, however, they have different conclusions about fusion enhancement/suppression, when compared with strongly bound stable isotopes [7] and/or coupled-channel calculations [8,9]. There are theoretical calculations that predict either suppression of the complete fusion (CF) cross sections [10, 11] due to breakup of loosely bound nucleus or enhancement [12,13] of the same due to coupling of the relative motion of the colliding nuclei to the breakup channel. Hagino *et al.* [14] performed an improved coupled-channel calculation that predicts the enhancement of fusion at sub-barrier energies and reduction at above barrier energies. An understanding of breakup and fusion is directly relevant for producing nuclei near the drip line and possibly super heavy nuclei. Experimentally such studies are limited because of the low intensities of unstable beams currently available. Light nuclei such as ${}^6\text{Li}$, which breaks up into $\alpha + d$ with a breakup threshold of only 1.48 MeV, has a large breakup probability. Fusion with such a nucleus is ideal for the quantitative testing of theoretical models and for use as a comparator for fusion measurements with other unstable beams. In this section we present precise excitation

function measurements for the complete fusion of ${}^6\text{Li}$ with ${}^{144}\text{Sm}$ by activation method, at energies ranging from 20 to 40 MeV in steps of 2 MeV, i.e., 0.75 to 1.5 times the Coulomb barrier ($V_B \approx 26.2$ MeV). The target nucleus ${}^{144}\text{Sm}$ ($Z = 62$, $N = 82$) was chosen because it is a spherical nucleus, which minimizes the target effect on fusion, and that makes the effect of projectile breakup more evident. Coupled-channel calculations are presented to find the influence of breakup on fusion cross sections. The present data have been compared with those involving strongly bound projectiles (${}^{12}\text{C} + {}^{141}\text{Pr}$ and ${}^{20}\text{Ne} + {}^{133}\text{Cs}$) forming similar compound nuclei [25]. The existing data from the literature [3, 15,16] for two more systems (${}^7\text{Li} + {}^{165}\text{Ho}$ and ${}^7\text{Li} + {}^{159}\text{Tb}$) involving loosely bound projectiles have also been reanalyzed to look for any systematic behavior on the suppression of fusion cross sections.

4.1.2 Analysis of experimental results

The experimental detail has been given in Chapter-3 with some experimental gamma spectrum. Here only the analysis and the physics output will be discussed. The intense γ -lines were chosen to evaluate the cross sections. After $2n$ evaporation of the compound nucleus, the residue nucleus ${}^{148}\text{Tb}$ can be populated either in the ground state (g.s.) or the metastable state (m.s.) and then decay into ${}^{148}\text{Gd}$ by electron capture with half-lives of 60 min and 2.2 min, respectively. Similarly for $3n$ evaporation, ${}^{147}\text{Tb}$ decays to ${}^{147}\text{Gd}$ with half-lives of 1.7 h (g.s.) and 1.83 min (m.s.). Intensities of the γ lines with proper branching ratios corresponding to both ground and metastable states of ${}^{148}\text{Tb}$ (${}^{147}\text{Tb}$) together give the cross sections of the $2n$ ($3n$) channel. The excitation functions for individual ER channels are shown in Fig 4.1. Statistical model (SM) calculations were performed using the code PACE2 [17] with default potential parameters. For energies below the Coulomb barrier, the SM calculations were carried out by feeding the l -distribution obtained from external coupled-channel calculations. The results of PACE2 calculations for the ratio of σ_{3n} to σ_{2n} with level density (ρ) equal to $A/10$ (solid line) are shown in Fig 4.1(c), which provides a good description of the present experimental data. The value of σ_{3n}/σ_{2n} was found to be less sensitive to the level density parameter (for $\rho = A/10$, $A/9$ and $A/8$). Calculated cross

sections for $2n$ and $3n$ channels are plotted as solid lines in Fig 4.1(a) and 4.1(b). The ratio, $R_{\sigma}^{\text{theory}} = (\sigma_{2n} + \sigma_{3n}) / \sigma_{\text{F}}$, of the combined cross section has been used to extract the complete fusion (σ_{CF}) calculated at each energy using the same parameters in PACE2 in the entire energy range (20–40 MeV) of our measurement which is shown in Fig 4.1(c). The complete fusion $\sigma_{\text{fus}}^{\text{expt}}$ was determined by dividing the cumulative cross sections of the two measured channels ($2n$ & $3n$) by the ratio $R_{\sigma}^{\text{theory}}$ and listed in Table 4.1. Further, to check the consistency in SM results for different channels, $\sigma_{\text{fus}}^{\text{expt}}$ was given as

Table 4.1: Experimental cross sections for $2n$ -ER, $3n$ -ER, and total fusion with $R_{\sigma}^{\text{theory}}$ from PACE2 calculations.

E_{lab} (MeV)	$\sigma_{2n}^{\text{expt}} + \sigma_{3n}^{\text{expt}}$ (mb)	$R_{\sigma}^{\text{theory}}$	$\sigma_{\text{fus}}^{\text{expt}}$ (mb)
20	0.034±0.01	0.8571	0.04±0.01
22	0.54±0.06	0.9211	0.59±0.08
24	8.2±0.8	0.8979	9.13±1.10
26	49±4.9	0.8302	59.0±6.0
28	116±12	0.8263	140±15
30	192±12	0.8152	236±15
32	270±13	0.8055	335±18
34	331±16	0.7933	417±27
36	378±19	0.7530	502±30
38	407±21	0.6709	607±31
40	374±20	0.5551	674±33

input to PACE2 and its output for σ_{2n} , σ_{3n} and their ratio are plotted as dashed lines in Fig 4.1, which are found to be reasonably close to the experimental data. The errors in $\sigma_{\text{fus}}^{\text{expt}}$ include the errors in ERs as well as the uncertainty in the SM calculations. The measured

excitation function for complete fusion and the corresponding barrier distribution are shown in Fig 4.2.

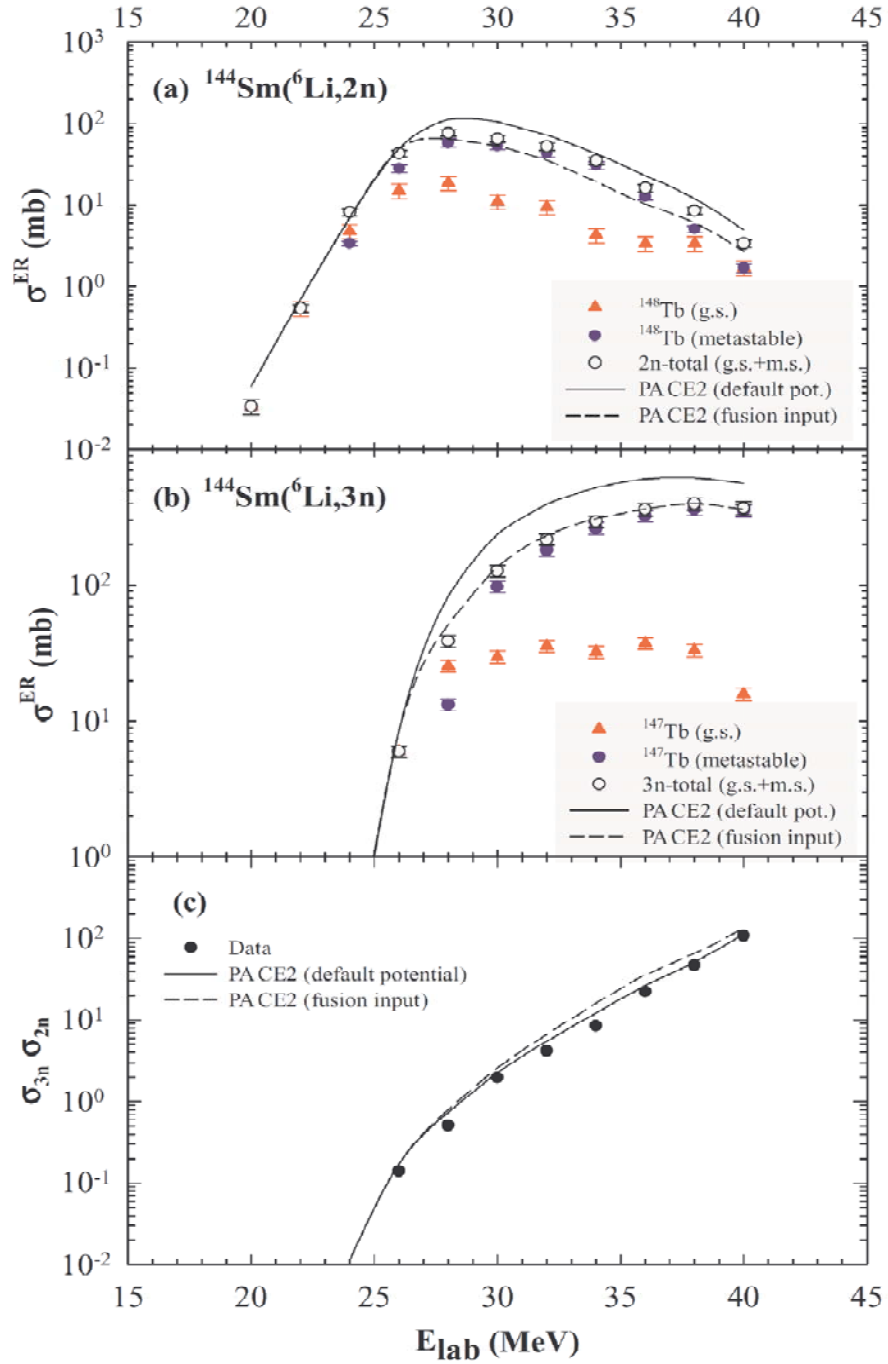


Fig 4.1: ER cross sections for ground state (filled triangles) and metastable state (filled circles) of (a) ${}^{148}\text{Tb}$ nucleus at different E_{lab} . Total ER (g.s.+m.s.) for the 2n channel are represented by open circles. (b) Same as (a), but for the ${}^{147}\text{Tb}$ nucleus, i.e. 3n ER channel. (c) Ratio of σ_{3n} to σ_{2n} .

The distribution of fusion barriers $D(B)$ was calculated by $[d^2(\sigma_{\text{fus}}^{\text{expt}}(E_{\text{c.m.}})/dE^2)]$ using the measured $\sigma_{\text{fus}}^{\text{expt}}$ which is shown in Fig 4.2(b). In the problem of heavy-ion fusion reaction, the experimental observable is not penetrability, but fusion cross section, and thus if one intends to discuss the effects of channel-coupling on fusion in terms of the first derivative of penetrability, one has to convert fusion cross sections to penetrability of the s-wave scattering. The Wong formula given in chapter 2, suggests one prescription for this, i.e. it suggests that the first derivative of the product of fusion cross section σ and the center of mass energy E with respect to the energy, $d(E\sigma)/dE$, is proportional to the penetrability of the s-wave scattering

4.1.3 Coupled-Channel (CC) calculations

Coupled-channel calculations using the CCFULL code [18] are performed with the potential parameters that reproduce the average fusion barrier ($V_B = 25.1 \pm 0.3$ MeV) of the experimental $D(B)$. The value of V_B was obtained following the procedure adopted in Ref. [7]. Parameters for the Akyuz-Winther (AW) potential and modified potential used for coupled-channel (CC) calculations, and the corresponding uncoupled barrier heights V_B and radii R_B and curvatures $\hbar\omega$, derived for the present system as well as several other systems, are given in Table 4.2. The projectile ground state (1^+) with spectroscopic quadrupole moment, $Q = -0.082$ fm², and the unbound first excited state (3^+ , 2.186 MeV) are coupled. A value of $(BE_2, 1^+ \rightarrow 3^+) = 21.8$ e² fm⁴ is used for the 3^+ rotational excitation [4]. The target excitation state (3^- , 1.81 MeV) is coupled as a vibrational state. Coupling of the breakup channel is not considered. The results of the coupled-channel calculations are shown in Fig 4. 2. It can be seen from Fig 4. 2(a) that at energies below the barrier, there is a large enhancement of fusion cross section with coupling (dashed line) compared to the uncoupled values (dotted lines). But the coupled results over predict the measured fusion data over the entire energy range. However, it was interesting to see that the measured fusion cross section agrees very well with the calculated ones when multiplied by a factor of 0.68 (solid line) over the entire energy range. This implies that there is an overall

suppression of $\sim 32\%$ of the fusion cross section in the entire energy range compared to the ones predicted by CCFULL. An uncertainty of $\pm 5\%$ in suppression factor is estimated from the uncertainties in V_B and σ_F . The normalized barrier distribution obtained from the calculated fusion cross sections. Fig 4. 2(b) shows that the experimental $D(B)$ agrees reasonably well with the coupled (solid line) one, which is very different from the uncoupled (dotted line) distribution. To see the effect of the breakup of loosely bound projectile ${}^6\text{Li}$ on fusion cross sections, the present data were compared with the data for other systems forming similar compound nuclei but involving strongly bound projectiles [19,20]. Fig 4.3 shows the comparison of the reduced cross

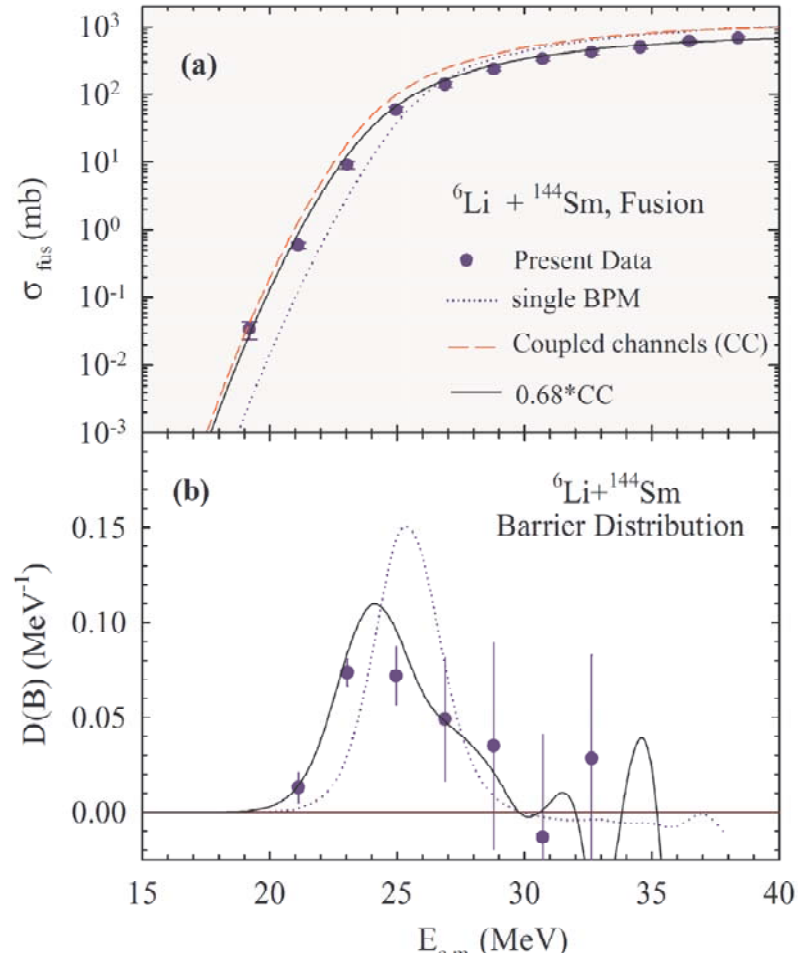


Fig 4.2: (a) Complete fusion cross section (filled circles) and (b) corresponding normalized barrier distribution (filled circles) for ${}^6\text{Li} + {}^{144}\text{Sm}$ compared with coupled (dashed lines) and uncoupled (dotted lines) results from CCFULL [18] calculations. Solid lines are obtained by multiplying the coupled results by a factor of 0.68.

Table 4.2: Parameters for AW and CC potential, along with V_B , R_B and $\hbar\omega$.

System	Potential	V_0 (MeV)	r_0 (fm)	a (fm)	V_B (MeV)	R_B (fm)	$\hbar\omega$ (MeV)
${}^6\text{Li} + {}^{144}\text{Sm}$	AW	42.33	1.158	0.63	24.65	10.2	4.85
	CC	47.00	1.100	0.63	25.55	9.78	5.04
${}^{12}\text{C} + {}^{141}\text{Pr}$	AW	54.71	1.177	0.63	45.07	10.6	4.55
${}^{20}\text{Ne} + {}^{133}\text{Cs}$	AW	63.40	1.187	0.63	68.20	10.9	4.33
${}^7\text{Li} + {}^{165}\text{Ho}$	AW	45.61	1.160	0.63	25.44	10.7	4.50
	CC	170.00	0.950	0.95	23.78	11.12	3.50
${}^{12}\text{C} + {}^{160}\text{Gd}$	AW	55.38	1.180	0.63	47.75	10.9	4.61
${}^7\text{Li} + {}^{159}\text{Tb}$	AW	45.48	1.165	0.63	24.84	10.6	4.45
	CC	132.00	0.980	0.85	24.17	10.68	3.81
${}^4\text{He} + {}^{162}\text{Dy}$	AW	35.18	1.470	0.63	17.48	10.2	4.11

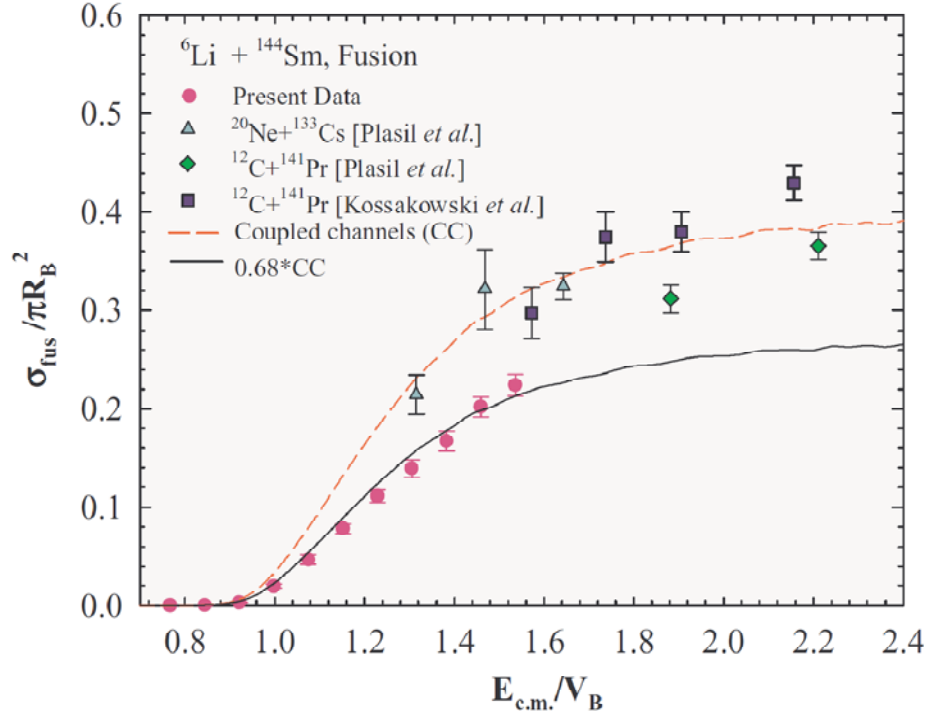


Fig 4.3: Reduced cross sections ($\sigma_{\text{fus}}/\pi R_B^2$) as a function of $E_{c.m.}/V_B$ for the present system (filled circles) along with two other reactions ${}^{12}\text{C} + {}^{141}\text{Pr}$ (filled diamonds [19], filled squares [20]) and ${}^{20}\text{Ne} + {}^{133}\text{Cs}$ (filled triangles [20]). Dashed line is the result of coupled-channel calculation. Solid line is obtained by multiplying the coupled results by a factor of 0.68.

sections ($\sigma_{\text{fus}}/\pi R_B^2$) as a function of $E_{\text{c.m.}}/V_B$ for the present system along with two other systems ${}^{12}\text{C} + {}^{141}\text{Pr}$ [19,20] and ${}^{20}\text{Ne} + {}^{133}\text{Cs}$ [20] forming the compound nucleus ${}^{153}\text{Tb}$. It is interesting to see that the reduced fusion cross sections involving strongly bound projectiles (${}^{12}\text{C} + {}^{141}\text{Pr}$ and ${}^{20}\text{Ne} + {}^{133}\text{Cs}$) are much larger than those for the present system, and they agree very well with the results of coupled-channel calculations using CCFULL without any suppression factor. This confirms that the complete fusion for ${}^6\text{Li} + {}^{144}\text{Sm}$ is suppressed by $32 \pm 5\%$ compared to those with the stable projectiles as well as those predicted by the fusion model adopted in CCFULL. Any model dependence on calculated fusion at sub-barrier energies, where couplings are important, can be singled out by having more fusion data for the systems involving tightly bound projectiles. The suppression in fusion cross section may be a direct consequence of the loss of incident flux due to the projectile breakup, which seems to be independent of energy over the measured energy range. The above observation on fusion suppression is quite different from what Tripathi *et al.* [3] concluded for ${}^7\text{Li} + {}^{165}\text{Ho}$, ${}^7\text{Li} + {}^{159}\text{Tb}$ [15], and ${}^9\text{Be} + {}^{208}\text{Pb}$ [5] systems. To find whether their conclusions remain valid, the data for ${}^7\text{Li} + {}^{165}\text{Ho}$ and ${}^7\text{Li} + {}^{159}\text{Tb}$ [15,16] were reanalyzed in the same line as above. The advantages and/or differences in the present analysis compared with the earlier one are (i) comparison of the fusion data with a system involving tightly bound projectile forming the same compound nucleus, (ii) use of an improved version of the coupled-channel code to take care of nonlinear couplings of all orders, and (iii) comparison of fusion data with coupled results (instead of uncoupled ones) to estimate the suppression. The reduced fusion cross sections for the above two systems have been compared with those of ${}^{12}\text{C} + {}^{160}\text{Gd}$ [21] and ${}^4\text{He} + {}^{162}\text{Dy}$ [15], respectively, forming the same compound nuclei, as shown in Fig. 4.4. The parameters for the potential barrier used in CC calculations for these systems are given in Table 4.2. CC potentials are chosen to reproduce the average fusion barrier of the barrier distribution derived from the fusion data. For ${}^7\text{Li} + {}^{165}\text{Ho}$, the effect of deformation was calculated by coupling to the ground state rotational band (with $\beta_2 = 0.285$ and $\beta_4 = 0.024$, $E_x = 0.077$ MeV) of the deformed target nucleus, following the method of Ref. [16]. Projectile deformation could not be included, as CCFULL cannot handle both the deformed target and deformed projectile. For the pair transfer coupling, the channel ${}^{165}\text{Ho} ({}^7\text{Li}, {}^4\text{He})$, with a positive Q

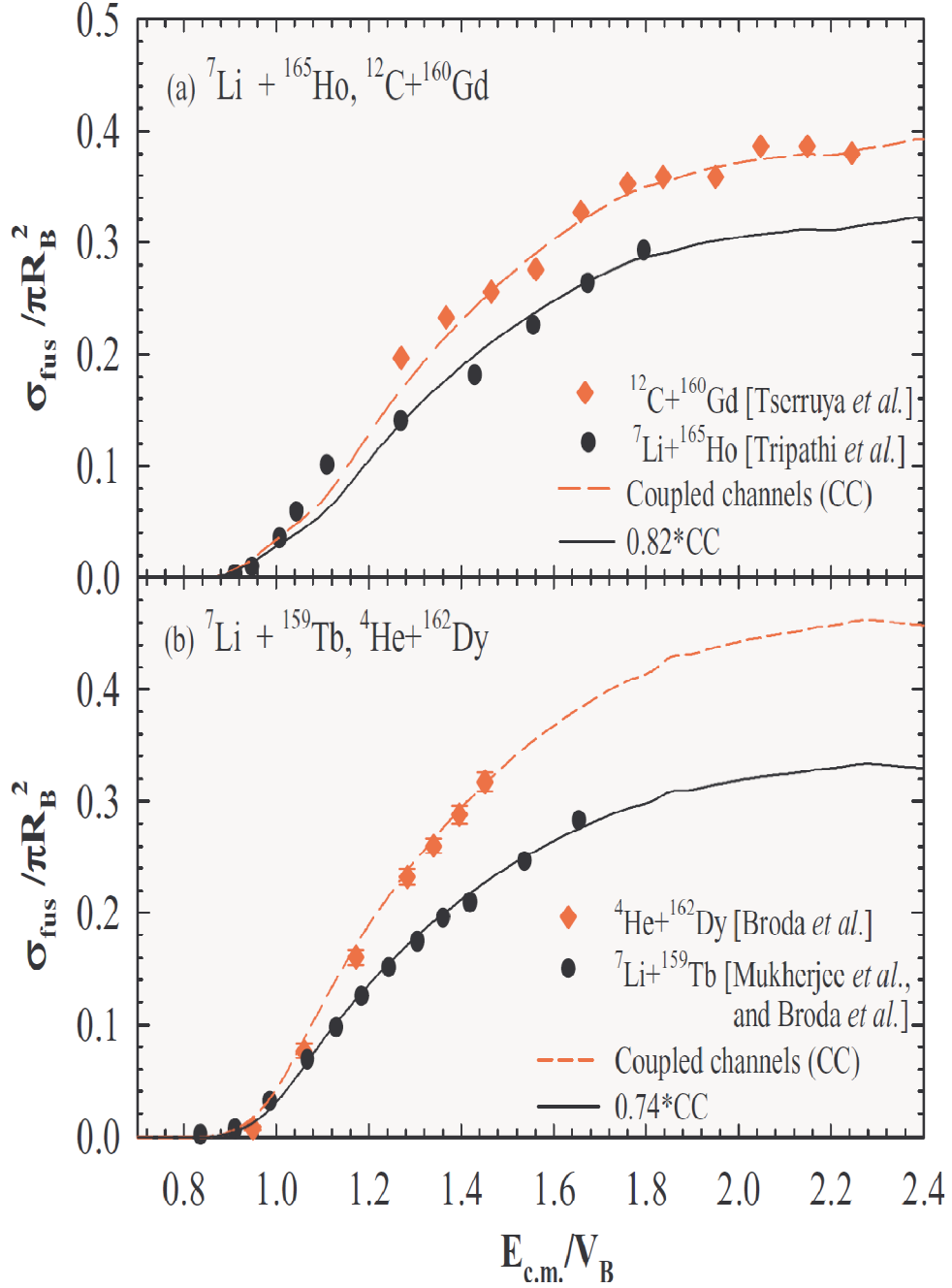


Fig 4.4: Reduced cross sections ($\sigma_{\text{fus}}/\pi R_B^2$) as a function of $E_{\text{c.m.}}/V_B$ for (a) ${}^7\text{Li} + {}^{165}\text{Ho}$ (filled circles [3]) along with ${}^{12}\text{C} + {}^{160}\text{Gd}$ (filled diamonds [21]) and (b) ${}^7\text{Li} + {}^{159}\text{Tb}$ (filled circles [16]) along with ${}^4\text{He} + {}^{161}\text{Dy}$ (filled diamonds [15]). Dashed lines are the result of coupled-channel calculation. Solid lines are obtained by multiplying the coupled results by a factor of (a) 0.82 and (b) 0.74.

value of 10.5 MeV, whose cross section was measured to be maximum [3], was included. A form factor of 0.85 was used, which reproduces the fusion data well. Coupling parameters of CCFULL calculations for ${}^7\text{Li} + {}^{159}\text{Tb}$ were same as those of Ref. [16]. It is interesting to find that the fusion for ${}^7\text{Li}$ -induced reactions is suppressed by about 18% and 26%, respectively, compared to those involving strongly bound projectiles of ${}^{12}\text{C}$ or ${}^4\text{He}$ forming the same compound nuclei. These results are quite different from the conclusions drawn in Ref. [3]. Similar suppression in complete fusion cross sections has been observed in several other reactions involving loosely bound nuclei but forming different compound nuclei. The results are summarized in Table 4.3. It is observed that the suppression has a clear dependence on two main factors, i.e., (i) breakup threshold of the projectile and (ii) charge of the target nucleus. For a particular projectile, the suppression increases with the increase in the Z of the target. Similarly, for a particular target, the suppression increases with a decrease in the breakup threshold. Thus, it indicates that the reduction in the complete fusion cross section is mainly due to the breakup of the projectile in the Coulomb field of the target nucleus.

Table 4.3: Fusion suppression factor for different systems.

Projectile	Breakup threshold (MeV)	Target	Suppression factor
${}^6\text{Li}$	$S_{\alpha d}=1.48$	${}^{209}\text{Bi}$	36%
${}^6\text{Li}$	$S_{\alpha d}=1.48$	${}^{208}\text{Pb}$	34%
${}^6\text{Li}$	$S_{\alpha d}=1.48$	${}^{144}\text{Sm}$	32%
${}^9\text{Be}$	$S_{\alpha \alpha n}=1.57$	${}^{208}\text{Pb}$	32%
${}^9\text{Be}$	$S_{\alpha \alpha n}=1.57$	${}^{144}\text{Sm}$	10%
${}^7\text{Li}$	$S_{\alpha t}=2.45$	${}^{209}\text{Bi}$	26%
${}^7\text{Li}$	$S_{\alpha t}=2.45$	${}^{165}\text{Ho}$	18%
${}^7\text{Li}$	$S_{\alpha t}=2.45$	${}^{159}\text{Tb}$	26%

4.1.4 Summary

The complete fusion excitation function for the ${}^6\text{Li} + {}^{144}\text{Sm}$ reaction has been measured at energies near and above the Coulomb barrier. An activation technique was used to determine the cross sections of $2n$ and $3n$ evaporation channels, which were the most dominating channels of decay of the compound nucleus formed by the complete fusion process in the measured energy range. Statistical model calculations were performed using PACE2 to estimate the relative contributions of other residue channels in order to determine the experimental cross sections for the complete fusion. Coupled-channel calculations using CCFULL show an enhancement in fusion at energies below the barrier compared to the predictions given by the single barrier penetration model. However, the experimental results suggest that there is an overall suppression of the fusion cross section, particularly at energies above the barrier, for the present reaction as compared to CCFULL calculations with full couplings. A comparison of the results for the present system with other systems involving strongly bound stable projectiles such as ${}^{12}\text{C} + {}^{141}\text{Pr}$ and ${}^{20}\text{Ne} + {}^{133}\text{Cs}$ forming similar compound nuclei, clearly shows that fusion cross sections for the present system are systematically lower. From these two comparisons, fusion suppression was estimated to be $32 \pm 5\%$. This suppression may be ascribed to the low breakup threshold energy of ${}^6\text{Li}$, which allows it to break up prior to fusion. A similar procedure was applied to reanalyze the fusion data from the literature for ${}^7\text{Li} + {}^{165}\text{Ho}$ and ${}^7\text{Li} + {}^{159}\text{Tb}$, and it was found that the cross sections are suppressed by about 18% and 26% compared to those with ${}^{12}\text{C} + {}^{160}\text{Gd}$ [21] and ${}^4\text{He} + {}^{162}\text{Dy}$ [15] systems, respectively, forming the same compound nuclei. Most importantly, these results are different from the earlier conclusions of Tripathi *et al.* [3]. A systematic comparison of fusion excitation functions for several reactions involving loosely bound stable projectiles shows that the suppression in fusion is a common phenomenon, and it increases with (i) the increase in the target atomic number Z_T and (ii) the decrease of the projectile breakup threshold E_{th} . To obtain an empirical expression for the suppression as a function of Z_T and E_{th} , the fusion data for a large number of reactions involving loosely bound projectiles is necessary.

References:

- [1] L. F. Canto *et al.*, Phys. Rep. 424, 1 (2006)
- [2] N. Keeley *et al.*, Prog. Part.Nucl. Phys. 59, 579 (2007)
- [3] V. Tripathi *et al.*, Phys. Rev. Lett. 88, 172701 (2002)
- [4] C. Beck *et al.*, Phys. Rev. C 67, 054602 (2003)
- [5] M. Dasgupta *et al.*, Phys. Rev. Lett. 82, 1395 (1999)
- [6] I. Padron *et al.*, Phys. Rev. C 66, 044608 (2002).
- [7] M. Dasgupta *et al.*, Phys. Rev. C 70, 024606 (2004)
- [8] A. Diaz-Torres and I. J. Thompson, Phys. Rev. C 65, 024606(2002)
- [9] A. Diaz-Torres *et al.*, Phys. Rev. C 68,044607 (2003)
- [10] M. S. Hussein *et al.*, Phys.Rev. C 46, 377 (1992)
- [11] N. Takigawa, M. Kuratani, and H. Sagawa, Phys. Rev. C 47, R2470 (1993)
- [12] C. H. Dasso *et al.*, Nucl. Phys. A405, 381(1983)
- [13] M. Dasgupta *et al.*, Annu. Rev. Nucl. Part. Sci. 48, 401(1998)
- [14] K. Hagino *et al.*, Phys. Rev.C 61, 037602 (2000)
- [15] R. Broda *et al.*, Nucl. Phys. A248, 356 (1975)
- [16] A. Mukherjee *et al.*, Phys. Lett. B636, 91 (2006)
- [17] A. Gavron, Phys. Rev. C 21, 230 (1980)
- [18] K. Hagino *et al.*, Comput. Phys. Commun. 123, 143(1999)
- [19] F. Plasil *et al.*, Phys. Rev. Lett. 45, 333 (1980)
- [20] R. Kossakowski *et al.*, Phys. Rev. C 32, 1612 (1985)
- [21] I. Tserruya *et al.*, Phys. Rev. Lett. 60, 14 (1988)
- [22] Y. W. Wu *et al.*, Phys. Rev. C 68, 044605 (2003)
- [23] D. J. Hinde *et al.*, Phys. Rev. Lett. 89, 272701 (2002)
- [24] P. R. S. Gomes *et al.*, Phys. Rev. C 73, 064606 (2006)

Chapter 5

5.1 Complete fusion in ${}^6\text{Li} + {}^{152}\text{Sm}$: Role of target deformation versus projectile breakup.

5.1.1 Introduction

In the previous chapter, we have studied the fusion measurement involving a weakly bound projectiles [1-7] and a spherical target, i.e., ${}^6\text{Li}+{}^{144}\text{Sm}$ system [3]. We have observed in the previous chapter that there is a suppression of complete fusion (CF) cross section compared to the coupled channels calculations, particularly at above barrier energies. The reduction in the CF cross section was attributed to the loss of incident flux due to the projectile breakup. The target (${}^{144}\text{Sm}$) being spherical, its static effects on fusion cross section was negligible. However, if the target is deformed it is expected to play a significant role in governing the fusion process [8-18]. To determine the effect of deformation in addition to the effect of projectile breakup on fusion requires experimental data with good precision at low bombarding energies, where penetrability effects are important. Barrier distribution extracted from these fusion excitation functions can provide additional information on the structure of the target/projectile [19,20]. The effect of target deformation on fusion cross section is expected to differ depending on whether it is static or dynamically induced [21-22]. When averaged over all orientations of a deformed nucleus [10,21], the fusion cross section becomes larger compared to a spherical nucleus. However, the dynamical effects such as excitation of the vibrational states or the rotation of the deformed nucleus during the collision can sometimes lead to reduction in fusion cross section [13,21,22]. The static deformation effects could be very important and they may show up partly through absorption below the barrier [11]. There are reports [12-14] that the fusion cross sections involving a much deformed ${}^{154}\text{Sm}$ target nucleus are considerably larger than a less deformed ${}^{148}\text{Sm}$ nucleus with strongly bound projectile ${}^{16}\text{O}$ at sub-barrier energies. Similar

effects are also observed for two more projectiles ${}^{32}\text{S}$ and ${}^{40}\text{Ar}$ [14,23]. While most of the studies on the effect of target deformation on fusion cross section involving strongly bound projectiles such as ${}^{16}\text{O}$, ${}^{32}\text{S}$ etc., the studies involving loosely bound nuclei (${}^6\text{Li}$, ${}^7\text{Li}$, ${}^9\text{Be}$) with deformed targets are scarce. Fusion reactions involving loosely bound projectiles would be more revealing towards the dominance of the effects of projectile breakup or target deformation, especially at sub-barrier energies. It would be interesting to see if the sub-barrier fusion enhancement due to deformation gets further magnified with the breakup coupling or it is neutralized by the suppression of fusion cross section due to loss of incident flux caused by projectile breakup. It has also been observed that although the effect of couplings of the target inelastic states (e.g., 2^+ , 3^- vibrational states of ${}^{208}\text{Pb}$) on elastic scattering or fusion in the systems involving tightly bound projectiles (${}^{12}\text{C} + {}^{208}\text{Pb}$, ${}^{209}\text{Bi}$) are significant [24,25], it is negligible for the systems involving weakly bound projectiles (${}^{6,7}\text{Li}+{}^{208}\text{Pb}$, ${}^{209}\text{Bi}$) [26,27], where the effect of projectile breakup is dominated. So, it would be interesting to investigate whether similar scenario is observed for a system with a target (${}^{152}\text{Sm}$) having rotational inelastic states. In this section we present excitation function measurements for complete fusion of ${}^6\text{Li}$ with ${}^{152}\text{Sm}$ (deformed) target by recoil catcher technique followed by off-line gamma-ray spectrometry around Coulomb barrier energies. Fusion cross sections are compared with our previously measured data for ${}^6\text{Li} + {}^{144}\text{Sm}$ [3] to investigate the isotopic target dependence.

5.1.2 Analysis of experimental results

The Experimental detail and a typical raw spectrum recorded by HPGe detector has been shown in previous Chapter-3 for ${}^6\text{Li}+{}^{152}\text{Sm}$ reaction. The excited compound nucleus formed by complete fusion decays predominantly by $2n$, $3n$, $4n$ and $5n$ evaporation forming the residual nuclei ${}^{156}\text{Tb}$, ${}^{155}\text{Tb}$, ${}^{154}\text{Tb}$ and ${}^{153}\text{Tb}$ either in ground state (g.s.) or in meta stable state (m.s.), which then decay to Gd isotopes by electron capture(EC). The respective half-lives of Tb isotopes are 5.35 d, 5.32 d, 21.5 h and 2.34 d respectively. The ${}^{154}\text{Tb}$ may also decay to ${}^{154}\text{Gd}$ from any of its two metastable states (m.s.) with half-lives of 9.4 h and 22.7 h. The half-lives of all the ERs of our interest are confirmed by following their

activities as a function of time. Various gamma lines corresponding to the same ER having different branching ratios, $I_\gamma(\%)$ were also used for confirmation of estimated channel cross section. The ER cross section (σ_{ER}) at a particular beam energy $E_{\text{lab}}(\text{MeV})$ was obtained by the formula which we have discussed in the Chapter-2. Since an ER can be populated either in its ground or in metastable states, the cross section of the corresponding channel is equal to the sum of the contributions from both of these states. Fig5.1 shows the ER cross sections for 4n channels. Total cross sections for 4n-ER (filled circles) were obtained from the sum of the ground state of ${}^{154}\text{Tb}^g$ (hollow diamonds), 1st meta stable state of ${}^{154}\text{Tb}^{m1}$ (hollow squares) and second metastable state of ${}^{154}\text{Tb}^{m2}$ (hollow triangles). The gamma line (534.3 keV) corresponding to 2n channel has the contamination from 5n channel (533.08 keV). At low energies, the contribution from 5n channel is expected to be negligible because of its low cross section as well as low branching ratio, but at high energies where

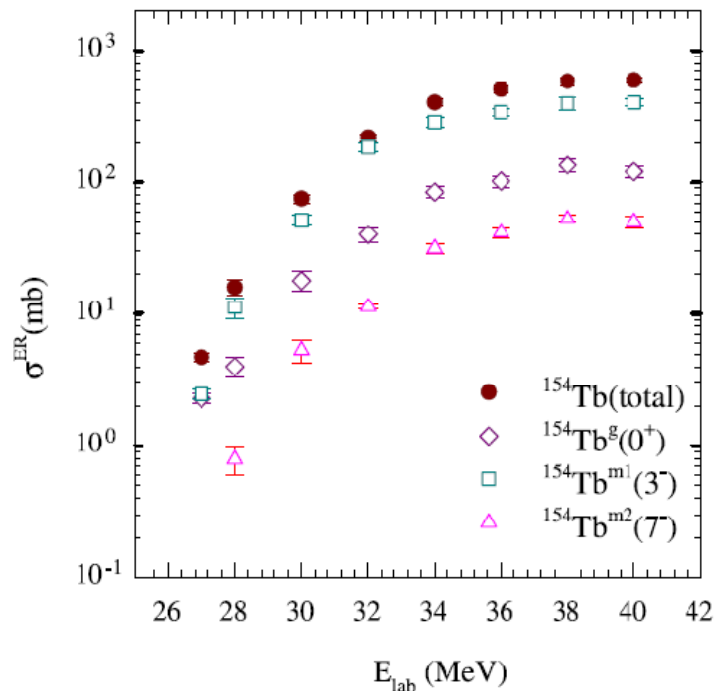


Fig 5.1: Total cross sections for 4n evaporation (filled circles) are obtained from the sum of ${}^{154}\text{Tb}^g$ (hollow diamonds), ${}^{154}\text{Tb}^{m1}$ (hollow squares) and ${}^{154}\text{Tb}^{m2}$ (hollow triangles).

the cross section for 5n channel is very high its contribution is significant and needs correction. This was done by fitting the gamma (534.3 keV) activity curve with two half-

lives (5.35 d for 2n and 2.34 d for 5n channels). Cross sections for 5n channel were obtained from independent gamma lines (212 keV and 170.5 keV) and they were used as constraints in the above fit to extract the ER cross section for the 2n channel only for few high energy data points. The measured excitation functions for individual ER channels thus obtained are shown in Fig. 5.2. The ER data for 2n, 3n, 4n and 5n channels are represented by triangles, stars, diamonds and squares respectively. To study the relative contributions of different ER channels to the CF, statistical model (SM) calculations were performed using the code PACE [28]. The optical model potentials of Perey and Perey [29] are used for neutron and proton, while that of Huizenga and Igo [30] for alpha particle emission. For sub-barrier energies, the ℓ -distributions obtained from coupled-channels calculations were used as input. Two important parameters in the statistical model calculations are (i) transmission co-efficient of the outgoing particles and (ii) level density of the residual nuclei. The transmission coefficients are calculated by Hill-Wheeler formula [31]. The level density parameter is ‘a’ = $A/K \text{ MeV}^{-1}$, where A is the mass number of the residual nucleus and K is a free parameter. The ER cross sections for 2n, 3n, 4n and 5n channels predicted by SM calculations with three different level density parameters are shown in Fig 5.2(a). The ratio of present experimental data of σ_{4n} to σ_{3n} is shown in Fig 5.2(b). The ER cross sections obtained from both theory ($\sigma_{\text{PACE}}^{\text{ER}}$) and experiment ($\sigma_{\text{expt}}^{\text{ER}}$) in terms of percentage fraction of the complete fusion cross section ($\sigma_{\text{PACE}}^{\text{CF}}$) are shown in Fig5.2(c). Results for each ER are shown by dash-dot-dot, medium dashed and solid lines corresponding to $a = A/9 \text{ MeV}^{-1}$, $A/10 \text{ MeV}^{-1}$ and $A/11 \text{ MeV}^{-1}$ respectively. It can be seen that the SM results with $K = 10 \text{ MeV}$ provide the best description of the ratio of present experimental data of σ_{4n} to σ_{3n} over the entire energy range. The dominant channels for most of the energy range were found to be 3n and 4n ERs except few points at extreme low energies where the contribution from 2n channel is significant of the order of $\leq 10\%$. From PACE calculations (with $K = 10 \text{ MeV}$), it was found that the sum of the measured ER cross sections corresponding to 2n, 3n, 4n and 5n channels (i.e., $\sigma_{2n} + \sigma_{3n} + \sigma_{4n} + \sigma_{5n}$) accounts for about 97–100% of the complete fusion (σ_{CF}) in the entire energy range of our interest. Thus the contribution from the missing channels (e.g., the charged particles like p and α evaporation

channels) that have not been measured is found to be negligible ($\leq 3\%$). The complete fusion cross sections ($\sigma_{\text{expt}}^{\text{CF}}$) are determined by dividing the cumulative

Table 5.1: Complete fusion data are included in the 5th column of this table as a result of a combination of experimental data —4th column — a sum of ER cross sections for 2n, 3n, 4n and 5n evaporation channels, and the ratio R_σ from PACE calculations included in the 3rd column.

E_{lab} (MeV)	$E_{\text{c.m.}}$ (MeV)	R_σ	$(\sigma_{2n+3n+4n+5n})^{\text{expt}}$ (mb)	$\sigma_{\text{CF}}^{\text{expt}}$ (mb)
20.0	19.2	1.00	0.26±0.05	0.26±0.05
21.0	20.2	1.00	1.07±0.22	1.07±0.22
21.5	20.7	1.00	1.77±0.34	1.77±0.34
22.0	21.2	1.00	3.57±0.45	3.57±0.45
22.5	21.6	1.00	6.74±0.65	6.74±0.65
23.0	22.1	1.00	9.62±0.80	9.64±0.80
23.5	22.6	1.00	17.3±1.5	17.3±1.5
24.0	23.1	1.00	25.7±2.1	25.8±2.1
24.5	23.6	0.99	39.4±3.2	39.7±3.2
25.0	24.1	0.99	53.4±4.3	53.7±4.3
25.5	24.5	0.99	76.2±6.1	76.8±6.1
26.0	25.0	0.99	96.4±5.7	97.0±5.7
27.0	26.0	0.99	150±7.0	151±7.0
28.0	26.9	0.99	196±9.0	198±9.0
30.0	28.9	0.99	301±10	304±10
32.0	30.8	0.99	413±12	418±12
34.0	32.7	0.99	555±15	563±15
36.0	34.6	0.98	626±16	637±16
38.0	36.6	0.97	682±18	705±19
40.0	38.5	0.93	739±18	797±20

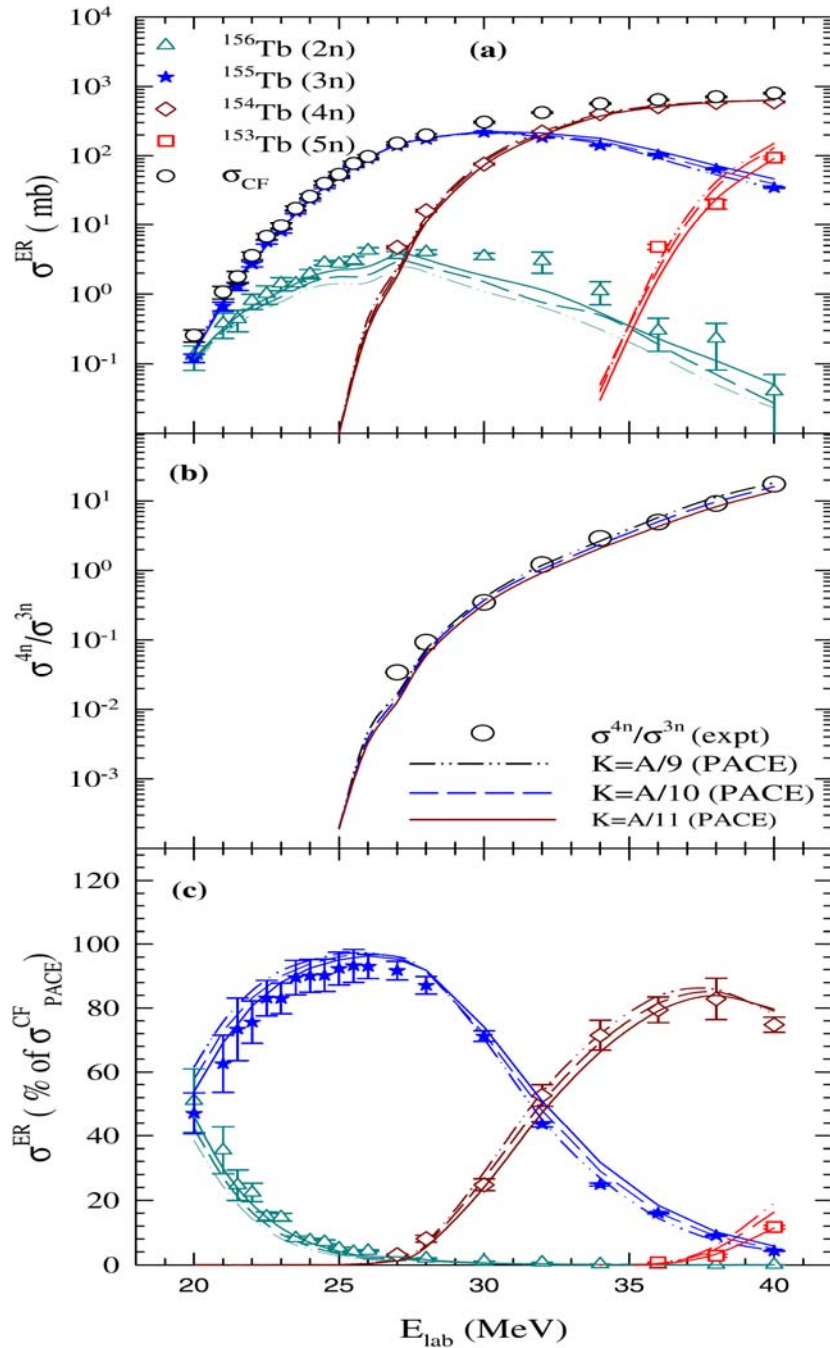


Fig 5.2: Measured ER cross sections for ${}^{156}\text{Tb}$ — 2n-channel (triangles), ${}^{155}\text{Tb}$ — 3n-channel (stars), ${}^{154}\text{Tb}$ (g+m) — 4n-channel (diamonds) and ${}^{153}\text{Tb}$ — 5n-channel (squares). Results of SM calculations corresponding to the level densities of $a = A/9\text{MeV}^{-1}$, $A/10\text{MeV}^{-1}$ and $A/11\text{MeV}^{-1}$ are shown as dash-dot-dot, medium-dashed and solid lines respectively for each of the above channels. Open circles represent the experimental fusion cross sections data. (b) Comparison of the ratio of σ_{4n} to σ_{3n} obtained from PACE using different level densities with the experimental data. (c) Normalized ER cross sections from the measurement and SM calculations (with different level densities) showing the percentage contribution to CF cross section.

experimental cross section of four channels (i.e., $\sigma_{\text{expt}}^{2n} + \sigma_{\text{expt}}^{3n} + \sigma_{\text{expt}}^{4n} + \sigma_{\text{expt}}^{5n}$) by the ratio $R_{\sigma}^{\text{theory}}$ following the procedure of Ref. [3]. The value of $\sigma_{\text{expt}}^{\text{CF}}$ are tabulated in Table 5.1 and the experimental CF cross section $\sigma_{\text{expt}}^{\text{CF}}$ plotted in Fig 5.2(a) with different ER channel. Only for the lowest three energies i.e., $E_{\text{lab}} = 20, 21$ and 21.5 MeV, directly from the errors attributed to the measured ER cross sections. It can be observed that the errors are minimum ($\sim 2.5\%$) for the highest beam energies and they increase slowly as one goes down in energy to a maximum of $\sim 20\%$ at the lowest energy. The errors are mainly due to the statistical uncertainties but having small contributions from systematic uncertainties. Since the contributions of the charged particle evaporation channels to CF are small ($\leq 3\%$ for $E_{\text{lab}} = 20-38$ MeV), the uncertainties on the estimation of these missing cross sections are negligible. Care has been taken to limit the systematic uncertainties that could arise from different sources such as (i) current integrator reading, (ii) target thickness (iii) detector efficiency, (iv) estimation of gamma yield, etc. The current integrator reading has been calibrated using standard Keithley current source. The target thicknesses have been crosschecked by two measurements using different ion beams (proton and ${}^{16}\text{O}$) for elastic scattering measurements at backward angles. The absolute energy dependent detector efficiency has been measured every ten to twelve hours during off-line gamma counting using standard radioactive sources of ${}^{152}\text{Eu}$ and ${}^{133}\text{Ba}$ and found to remain invariant with time during the whole experiment shown in Fig 3.2, Fig 3.4 in Chapter 3. However, the uncertainty ($\sim 1\%$) in the fitting parameters of the efficiency curve has been taken into account in the final error of the ERs. So, most of the errors on ER cross sections are due to the uncertainties on gamma yield extraction and gamma statistics. For lowest three beam energies, the contribution from 2nER channel to CF is substantial and the large uncertainties on σ_{2n} lead to large errors in $\sigma_{\text{expt}}^{\text{CF}}$. To see the isotopic target dependence if any, the experimental CF cross sections obtained for the present system have been compared with those of ${}^6\text{Li}+{}^{144}\text{Sm}$ [3]. The reduced fusion cross sections “ $\sigma_{\text{expt}}^{\text{CF}} / (A^{1/3}_{\text{P}} + A^{1/3}_{\text{T}})^2$ ” as a function of reduced energy “ $E_{\text{c.m.}} / [Z_{\text{P}}Z_{\text{T}} / (A^{1/3}_{\text{P}} + A^{1/3}_{\text{T}})]$ ” for the two systems are shown in Fig. 5.3(a). The above normalization was made following the prescription by Gomes et al. [32] to remove the geometrical dependence. The solid and

dashed lines correspond to the CC calculations with only target inelastic couplings for ${}^6\text{Li} + {}^{152}\text{Sm}$ and ${}^6\text{Li} + {}^{144}\text{Sm}$ systems respectively. Details of the calculations are given in the following section and Ref. [3]. To emphasize the low energy enhancement for the present system, the ratio of the CF cross sections of the present system to those for ${}^6\text{Li} + {}^{144}\text{Sm}$ is plotted in Fig 5.3(b) both experimental as well as the calculated values. The calculated ratio represented by the dash-dot line shows similar trend as that of the data. These comparisons reveal that although the CF cross sections at above-barrier energies are of similar order, they are much enhanced for the present system at sub-barrier energies as expected from the influence of the deformed ${}^{152}\text{Sm}$ target nucleus compared to that of spherical ${}^{144}\text{Sm}$ nucleus. Similar effects have also been observed for the systems involving different isotopes of Sm but with strongly bound projectiles e.g., ${}^{16}\text{O}+{}^{148,150,152,154}\text{Sm}$ [12,13], ${}^{40}\text{Ar}+{}^{144,148,154}\text{Sm}$ [14,45] and ${}^{32}\text{S} + {}^{144,154}\text{Sm}$ [23]. This implies that the qualitative effect of the target deformation on sub-barrier fusion, i.e., enhancement is independent of whether the projectile is weakly or strongly bound. The barrier distributions derived from the above experimental fusion cross sections for two systems are also compared as shown in Fig5.3(c). There is no major difference found in the main peaks of the two barrier distributions. However, the shoulder structure at high energy region looks to be more prominent for the ${}^6\text{Li} + {}^{152}\text{Sm}$ compared to the one for ${}^6\text{Li} + {}^{144}\text{Sm}$. Due to the large error bars on the barrier distribution in this energy region, no conclusion can be drawn on whether this difference is due to the effect of target deformation.

5.1.3 Coupled-channel (CC) calculations

Coupled-channels calculations were performed using the modified version of CCFULL [46] that can include the effect of projectile ground state spin and the projectile excitation. To make a sensible coupled-channel calculation it is important to choose a proper set of potential parameters. The best way to do this is to find some experimental quantity that will constrain these parameters. In the present measurement, there could be two constraints: the experimental fusion excitation function at high energies or the average experimental fusion barrier. Since the barrier distribution is more sensitive to the structure of the interacting

nuclei compared to the fusion excitation function, in the present calculations we have used the average experimental fusion barrier as the constraint. The weighted average of the experimental barrier distribution was found to be 25.1 ± 0.2 MeV. For CC calculations, the initial potential parameters chosen are obtained from the parameterization of Broglia and Winther (BW) [33] and their values in Woods–Saxon form are equal to $V_0= 42.6$ MeV, $r_0= 1.02$ fm, and $a_0= 0.65$ fm. To reproduce the experimental barrier of $V_B= 25.1$ MeV and remove the oscillatory states. The target (${}^{152}\text{Sm}$) being a deformed nucleus in its ground state, both quadrupole ($2^+, 0.122$ MeV) and hexadecapole (4^+) rotational states with behavior of fusion cross section at high energies, the depth of the real potential was increased. The final parameters that are used in the present CC calculations are: $V_0= 131$ MeV, $r_0= 1.01$ fm, and $a_0= 0.64$ fm. Once the potential parameters are fixed, one needs to find the possible channels along with their coupling parameters that are to be coupled. CC calculations were made first with only target inelastic deformation parameters $\beta_2= 0.26$ and $\beta_4= 0.05$ [34] are coupled. The results of the CC calculations with no couplings and only target couplings are shown in Fig. 5.4 (a) as dotted and dash–dot lines respectively. It can be seen that at energies below the barrier, there is a large enhancement in the fusion cross sections calculated with only target couplings compared to the uncoupled values. However, at above-barrier energies, it can be seen that the coupled results over predict the measured fusion data. The barrier distribution, $d^2(\sigma_{CF}^{\text{expt}}/E_{c.m.})/dE^2$, obtained from both the experimental and the calculated fusion cross sections are shown in Fig5.4 (b). To improve the shape of the calculated barrier distribution, the projectile couplings were also included. In addition to the reorientation of the projectile ground state (1^+) with spectroscopic quadrupole moment, $Q=-0.082$ fm², the unbound 1st excited state (3^+ , 2.186 MeV) was also included as done in Refs. [3,47]. This however is a considerable simplification and does not reflect the realistic breakup couplings. A value of $B(E_2; 1^+ \rightarrow 3^+) = 21.8$ e²fm⁴ was used for the $3^+(2.18\text{MeV})$ unbound excited state (same as in Ref. [17]). The parameters for the projectile couplings that were used in the CCFULL calculations are: β_{00} (i.e., β_2 for the ground State reorientation) $=-0.079$, β_{01} (i.e., β_2 for the transition between the ground and

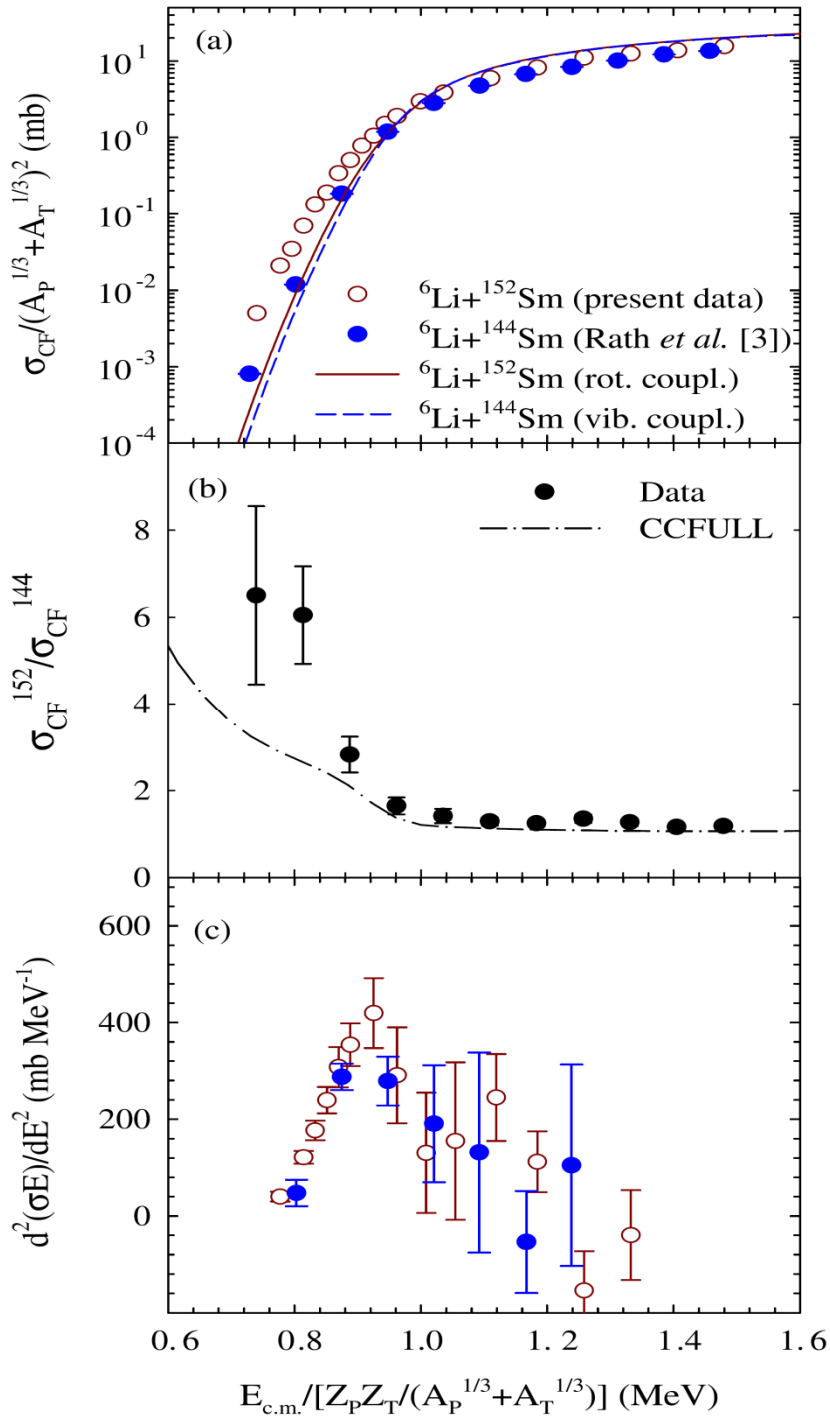


Fig 5.3: (a) Reduced fusion cross section data and calculations versus normalized energy for present system (${}^6\text{Li} + {}^{152}\text{Sm}$) compared with those for ${}^6\text{Li} + {}^{144}\text{Sm}$ [3]; (b) Ratio of the above cross sections versus normalized energy showing the target dependence; (c) Barrier distributions derived from the fusion cross sections of (a).

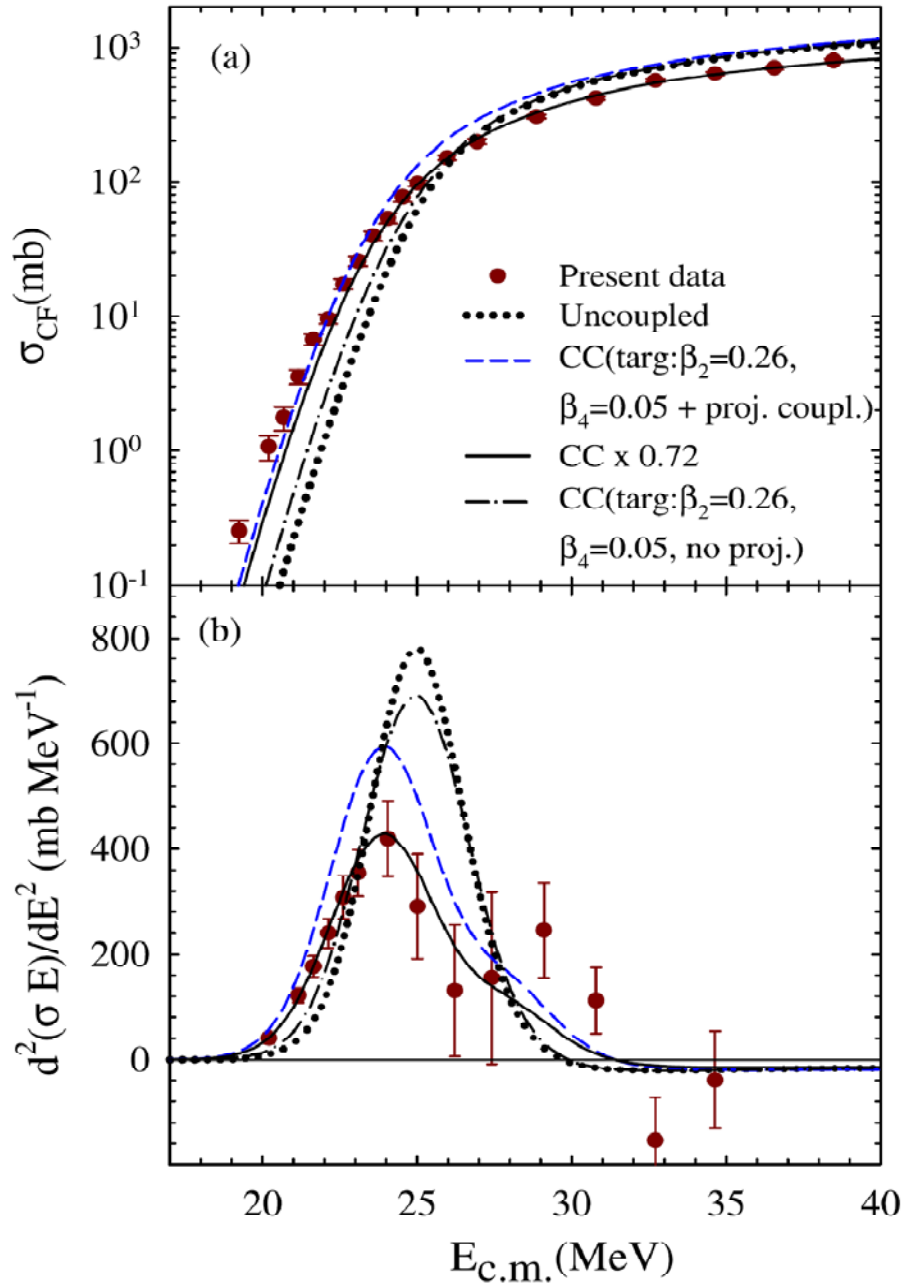


Fig 5.4: (a) Complete fusion cross section (filled circles) and (b) corresponding barrier distribution (filled circles) for ${}^6\text{Li} + {}^{152}\text{Sm}$ compared with no couplings (dotted lines), only target couplings (dash-dot lines), projectile + target couplings (dashed lines) results from CCFULL [46] calculations. Solid lines are obtained by multiplying the CCFULL results with full couplings by a factor of 0.72.

the first excited states) = 1.51 and β_{11} (i.e., β_2 for the reorientation of the 1st excited state) = 1.51. Inclusion of both target as well as projectile couplings (dashed line) further enhances the fusion cross sections at sub-barrier energies. However, the fusion cross sections at above-barrier energies were found to be insensitive to the projectile couplings. It should be emphasized that the measured fusion cross sections at above-barrier energies agree very well with the calculated ones when multiplied by a factor of 0.72 (solid line), implying that there is an overall suppression of $\sim 28\%$ of the fusion cross section in this energy range compared to the ones predicted by CCFULL. An uncertainty of $\pm 4\%$ in the suppression factor is estimated from the uncertainties in V_B and σ_{CF} . It was also interesting to find that the barrier distribution derived from the calculated fusion with full couplings when normalized by a factor of 0.72 (solid line) agrees quite well with the experimental distribution (filled circles).

5.1.4 Fusion using proximity potential

CF cross sections for the present system were compared to those predicted using the “Proximity potentials” [35,36]. These potentials are parameterized from the existing fusion data in the literature for many systems mostly with strongly bound projectiles. Fusion barrier parameters, i.e., barrier height and barrier radius, can be obtained by adding the Coulomb potential with the proximity potentials as done by Dutt *et al.* [37] and they can be used to predict the fusion cross section. The original version of this potential (Proximity 1977) was described by Blocki *et al.* [35], which was later modified and renamed as “Proximity 1988” by Reisdorf [36] to incorporate more refined mass formula of Moller and Nix [38,39]. Myers and Swiatecki [40], using their concept of droplet model, have updated the values of nuclear radii and nuclear surface tension coefficients in the latest version of the above potential and named as “Proximity 2000”. Using 1977, 1988 and 2000 forms of proximity potentials and corresponding expressions for the fusion barrier parameters, the barrier heights were calculated to be 25.0 MeV, 24.5 MeV and 24.9 MeV, and barrier radii as 9.91 fm, 10.18 fm and 9.98 fm respectively. Using the above parameters in simplified Wong’s formula, the fusion cross sections were calculated and the results are shown as

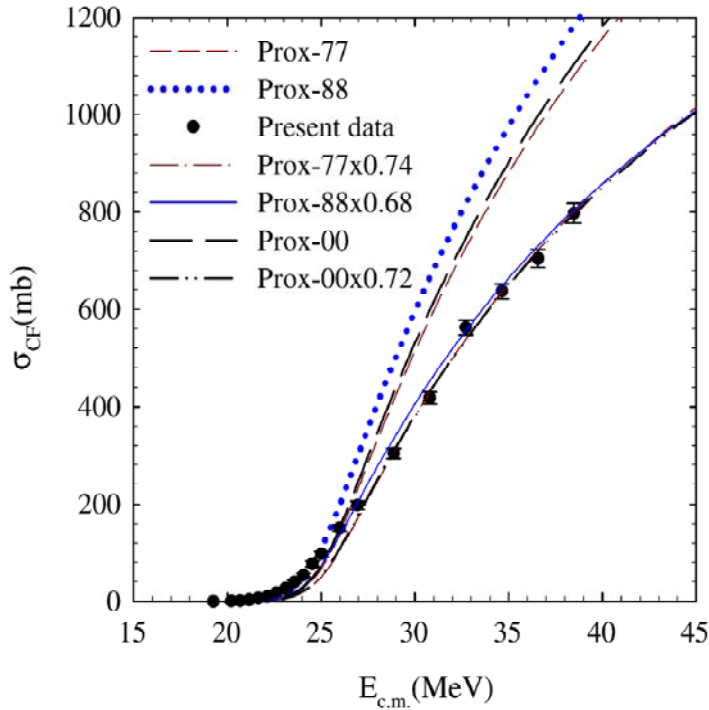


Fig 5.5: Fusion cross sections predicted by Wong's model using proximity potentials version 1977, 1988 and 2000 are represented by short-dashed, dotted and long dashed lines respectively. Dash-dot, solid and dash-dot-dot lines are obtained by multiplying the above results by 0.74, 0.68 and 0.72 respectively. Filled circles correspond to the measured CF data for ${}^6\text{Li} + {}^{152}\text{Sm}$ reaction.

Short-dashed, dotted and long dashed lines respectively in Fig 5.5. It was observed that the fusion cross sections provided by proximity potentials are required to be scaled down by factor of 0.74 (dash-dot line), 0.68 (solid line) and 0.72 (dash-dot-dot line) respectively to reproduce the experimental data (filled circles) at above barrier energies. This implies that the measured fusion cross sections at higher energies are suppressed by $\sim 26\text{--}32\%$ compared to the calculations using proximity potentials, which are consistent with our conclusions on fusion suppression that we obtained from the CC analysis. These observations indicate that projectile breakup may be playing a crucial role in reducing the flux from the entrance channel and leading to the suppression of complete fusion cross section. Comparison with tightly bound projectiles has shown in Fig 5.6, the CF cross sections for the present system are compared with those for two other systems ${}^{12}\text{C} + {}^{141}\text{Pr}$ [19] and ${}^{20}\text{Ne} + {}^{133}\text{Cs}$ [48] forming nearly same compound nucleus ${}^{153}\text{Tb}$. Since CCFULL does not have the provision to include the realistic breakup coupling in the CC calculations, one can use FRESKO [41] to understand the effect of projectile breakup on fusion. To see

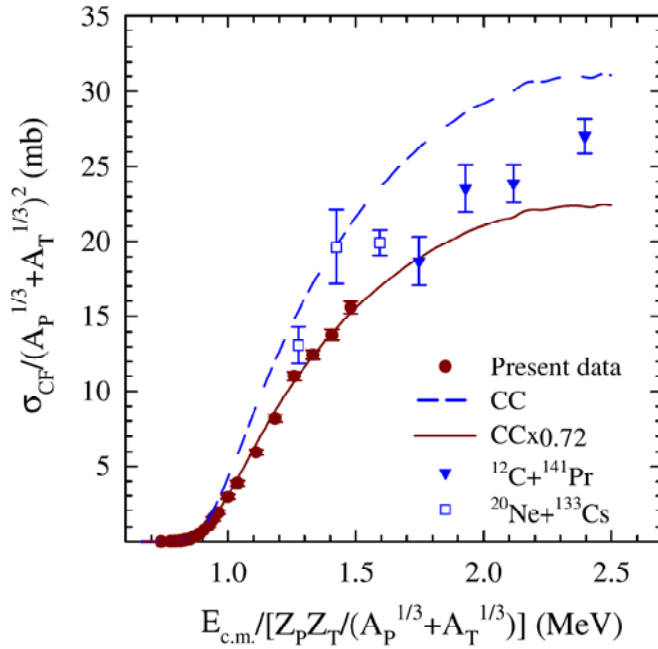


Fig 5.6: Reduced fusion cross section as a function of reduced energy for the present system (filled circles) along with two other reactions forming the same compound nucleus i.e., ${}^{12}\text{C} + {}^{141}\text{Pr}$ [19] (filled triangles) and ${}^{20}\text{Ne} + {}^{133}\text{Cs}$ [48] (hollow squares). The dashed line represents the CC results and the solid line corresponds to the CC results multiplied by a factor of 0.72.

the effect of both projectile breakup as well as target excitations together in an approximate way as done in Ref. [27], one can first calculate the polarization potential due to breakup coupling using FRESKO and then use the effective (bare+polarization) potential as an input to the FRESKO where only target excitations are coupled. Since we already know about the effect of the target deformation from the CC calculations using CCFULL, it would be interesting to see the effect of projectile breakup employing FRESKO and find whether the results qualitatively agree with the conclusion of ‘CF suppression due to projectile breakup’. However, FRESKO calculations using cluster-folded potential with long range imaginary part for the entrance channel interaction do not provide the CF cross section. Instead, the cumulative absorption cross section by the long range imaginary potential equals to the sum of the cross sections for CF, ICF, transfer and target inelastic reactions. In a second method, fusion is calculated by the barrier penetration model (BPM) as done by Rusek *et al.* [6]. But the BPM fusion too may not explain the CF data as mentioned by Keeley *et al.* [2] and also observed recently by Santra *et al.* for ${}^6\text{Li} + {}^{209}\text{Bi}$ [27]. Thus, one can obtain a reasonable cross section for CF only when the information on the cross sections for the remaining reaction channels are available. Despite these difficulties one can still perform the FRESKO calculations including only the projectile excitations in the

continuum and find the effect of breakup on fusion to see whether it is consistent with the present experimental observations. So, the continuum discretized coupled channels (CDCC) calculations are performed using FRESKO- version 2.8 to understand the effect of projectile breakup coupling on fusion. The projectile (${}^6\text{Li}$) is assumed to be a cluster of α and d with a breakup threshold of 1.48 MeV. The projectile excited states in the continuum up to 7 MeV above the breakup threshold are coupled. Each discretized state is assigned with $L=0, 1$ and 2 , where L is the relative angular momentum between the two breakup fragments (α and d). Both resonant and non-resonant states in the continuum are included. For s- and p-waves, the continuum was discretized into 14 bins of equal width in the momentum of α, d relative motion. In the presence of resonances for d-waves, the discretization of the continuum was slightly modified in order to avoid double counting. Three resonant states, with widths corresponding to 0.1MeV, 2.0 MeV and 3.0MeV, respectively, were also treated as momentum bins, but with finer steps. Reorientation coupling is also included. The target is assumed to be in the ground state. The cluster-folded potential obtained from the two fragment-target potentials ($V_{\alpha+152\text{Sm}}$ and $V_{d+152\text{Sm}}$) was used for the entrance channel interaction potential ($V_{6\text{Li}+152\text{Sm}}$). The potential parameters used for $V_{\alpha+152\text{Sm}}$ ($V_{d+152\text{Sm}}$) are taken from Ref. [42,43], and the values are $V_0=60.5$ (91.82) MeV, $r_0=1.107$ (1.013) fm, $a_0=0.607$ (0.938)fm for real part and $W=18.72$ (21.04) MeV, $r_w=1.035$ (1.116) fm, $a_w=0.735$ (0.581) fm for the imaginary part. The radius parameter used for the Coulomb term is 0.964 (1.011) fm. The $\alpha+d$ binding potentials are same as those used in Ref. [44]. Two separate potentials were used for (i) ground state and s-wave continuum and (ii) p- and d-wave continuum. These potentials were chosen as they reproduce the resonances (energies and widths) correctly [49]. The dynamic polarization potential generated due to the breakup coupling in the CDCC calculations was found to be repulsive around the nuclear surface region for all the beam energies of our interest, similar to that observed in our recent study for ${}^6\text{Li} + {}^{209}\text{Bi}$ [27]. The effective (bare + polarization) potential reduces the absorption/penetration of the flux from the entrance channel into the attractive potential well. The Fusion cross sections obtained by cumulative absorption and barrier penetration model from the CDCC calculations are shown in Fig 5.7. The uncoupled (coupled) results for the above two methods are represented by dotted and dash-dot-dotted (solid and long-dashed) lines respectively. It can be observed that the fusion cross sections

with breakup coupling obtained by both the methods are systematically lower than the uncoupled ones at energies above the Coulomb barrier. Thus, these results qualitatively agree with our earlier conclusion on the fusion suppression due to projectile breakup.

5.1.5 Incomplete fusion

Incomplete fusion cross sections due to the capture of any of the breakup fragments, i.e., α or d by the target were investigated. Since the ERs formed after α -capture, e.g. ${}^{155}\text{Gd}$ (1n-

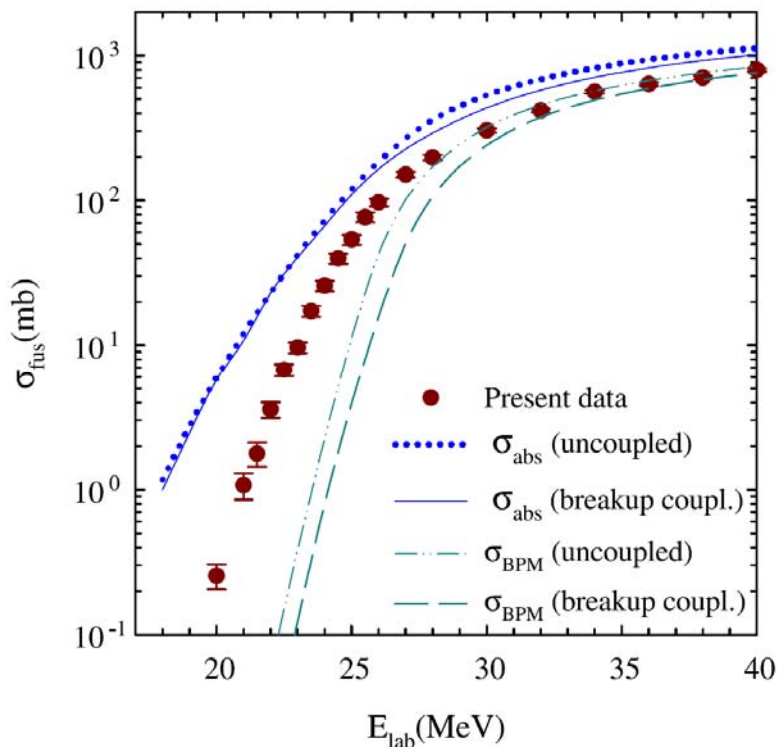


Fig 5.7: Shows the results of FRESKO calculations for the fusion cross sections obtained by cumulative absorption and barrier penetration with and without breakup coupling.

ER) and ${}^{154}\text{Gd}$ (2n-ER) are all stable, it was not possible to measure their formation cross section by offline gamma-ray spectrometry. However, for d-capture there are few ER channels with measurable half-lives. The dominant channels of d-capture are expected to be 1n and 2n ERs as per PACE predictions at deuteron energies equal to one-third of the

beam (${}^6\text{Li}$) energies. Since the residue after 1n evaporation following d-capture is stable, its cross section could not be measured. For 2n channel there could be contributions from the decay of ${}^{152}\text{Eu}^g$, ${}^{152}\text{Eu}^{m1}$ and ${}^{152}\text{Eu}^{m2}$ states with half-lives of 13.542 y, 9.274 h and 96 m respectively. Here m1 and m2 correspond to two metastable states and g corresponds to ground state of ${}^{152}\text{Eu}$. Since the half-life of ${}^{152}\text{Eu}^g$ is very large, the contributions from its meta stable states were only possible to measure. Out of the two meta stable states, only the first meta stable state with half-life of 9.274 hr has clearly been identified and the cross sections are extracted and shown as hollow diamonds in Fig. 5.8. The cross section for second meta stable state ($t_{1/2}=96\text{ m}$) could not be extracted accurately because of the contamination of its characteristic gamma line (89.85 KeV) with 88.97 keV gamma of ${}^{156}\text{Tb}$ corresponding to 2n-ER of CF. The experimental cross section for d-capture has been estimated from experimental 2n-ER (${}^{152}\text{Eu}^{m1}$) channel cross section by scaling with PACE predicted fusion for $d + {}^{152}\text{Sm}$ reaction at energies $E = E_{tab}/3$. Results are shown as filled

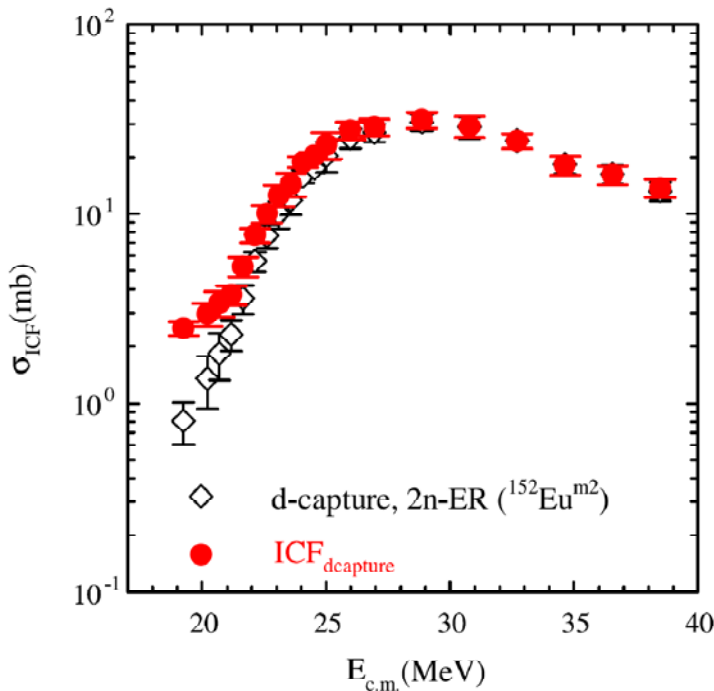


Fig 5.8: ICF cross sections (filled circles) contributed by d-capture which are estimated from the formation cross section of ${}^{152}\text{Eu}^{m2}$ i.e., meta stable state of 2n-ER channel (hollow diamonds).

circles in Fig. 5.8. Since d-capture is only part of the ICF the above cross sections are considered to be as lower limits of the ICF. The above ICF channel that we have discussed so far may also get populated via deuteron transfer i.e., ${}^{152}\text{Sm}({}^6\text{Li}, \alpha)$ reaction. It is difficult to distinguish between these two contributions from present measurement. However, one

can conclude that a significant cross section of ICF observed is probably due to breakup. Further theoretical and experimental investigations will be required to pin down this point definitively.

5.1.6 Summary

The complete fusion cross sections for ${}^6\text{Li} + {}^{152}\text{Sm}$ reaction have been measured at energies near and above the Coulomb barrier. The decay of the compound nucleus formed by the complete fusion process was dominated by neutron evaporation channels. Combined ER cross sections for 2n, 3n, 4n and 5n contribute to more than 97% of CF for most of the beam energies. ER cross sections were measured by recoil catcher technique followed by off-line gamma-ray spectrometry. Statistical model calculations were performed using PACE to quantitatively understand the ER cross sections, and estimate the contribution from the missing channels so as to obtain the experimental complete fusion cross sections. A comparison of the experimental data with ${}^6\text{Li} + {}^{144}\text{Sm}$ [3] showed that at above-barrier energies the CF cross sections are comparable but at sub-barrier energies they are largely enhanced for the present system. This implies that the effect of target deformation on sub-barrier fusion, i.e., enhancement is independent of whether the projectile is weakly- or strongly-bound. Coupled-channels calculations using CCFULL were performed to understand the measured CF data. At sub-barrier energies, the coupling of target deformation shows enhancements in CF cross sections and explains the data. However, at above barrier energies there is a suppression of $28\pm 4\%$ in the CF data compared to the CC calculations. The low energy threshold of the projectile seems to allow it to break up prior to fusion, leading to loss of flux from the entrance channel. It can therefore be concluded that the complete fusion cross section at energies above the barrier is suppressed due to projectile breakup. Thus the effects of both the target deformation as well as the projectile breakup are present, and their influence on each other seems to be negligible.

CF cross sections for the present system at above-barrier energies are found to be smaller by a factor of $\sim 28\text{--}32\%$ than those calculated by Wong's formula using proximity potential, which is consistent with the above conclusion on fusion suppression. Comparison

with the other systems involving strongly bound stable projectiles such as ${}^{12}\text{C}+{}^{141}\text{Pr}$ and ${}^{20}\text{Ne}+{}^{133}\text{Cs}$ forming similar compound nucleus also shows that CF cross sections for the present system at above-barrier energies are systematically lower compared to those with strongly bound projectiles, which further supports the above mentioned suppression and since the CF cross sections at sub-barrier energies are slightly higher than those predicted by CC calculations, it may be assumed that the net effect of breakup (i.e., suppression due to loss of flux plus enhancement due to breakup coupling) is a small enhancement in fusion at this region. CDCC calculations with projectile breakup channels reveal that the dynamic polarization potential generated due to breakup coupling is repulsive which leads to reduction in absorption cross section. Fusion cross sections obtained by both the cumulative absorption and BPM methods are found to be smaller compared to the ones with no breakup coupling, supporting the above conclusions on the effect of projectile breakup. Present experimental data provide important input to the future realistic models of fusion with weakly bound projectiles to predict both qualitative and quantitative effects of projectile breakup at energies below as well as above Coulomb barrier energies, and how these effects get modified in the presence of large target deformation specially at sub-barrier energies where the deformation plays a significant role.

References

- [1] L. F. Canto *et al.*, Phys. Rep. 424, 1 (2006)
- [2] N. Keeley *et al.*, Prog. Part.Nucl. Phys. 59, 579 (2007)
- [3] P.K. Rath *et al.*, Phys. Rev. C 79, R051601 (2009)
- [4] C.S. Palshetkar *et al.*, Phys. Rev. C 82, 044608 (2010)
- [5] V.V. Parkar *et al.*, Phys. Rev. C 82, 054601 (2010)
- [6] K. Rusek *et al.*, Phys. Rev. C 70, 014603 (2004)
- [7] K. Rusek, Eur. Phys. J. A 41, 399 (2009)
- [8] R. Beringer, Phys. Rev. Lett. 18, 1006 (1967)
- [9] C.Y. Wong, Phys. Lett. B 42, 186 (1972)
- [10] C.Y. Wong, Phys. Rev. Lett. 31, 766 (1973)
- [11] M. Hussein *et al.*, Phys. Rev. 21, 772 (1980)
- [12] R.G. Stokstad *et al.*, Phys. Rev. C. 21, 2427 (1980)
- [13] R.G. Stokstad *et al.*, Phys. Rev. Lett. 41, 465 (1978)
- [14] R.G. Stokstad *et al.*, W. Z. Phys. A 295, 269 (1980)
- [15] J.R. Leigh *et al.*, Phys. Rev. C 52, 3151 (1995)
- [16] P.R.S. Gomes *et al.*, Phys. Rev. C 49, 245 (1994)
- [17] W. Reisdorf *et al.*, Nucl. Phys. A 438, 212 (1985)
- [18] M. Trotta *et al.*, Nucl. Phys. A 734, 245 (2004)
- [19] P.N. Rowley, G.R. Satchler, Phys. Lett. B 254, 25 (1991)
- [20] M. Dasgupta *et al.*, Ann. Rev. Nucl. Part. Sc. 48, 401 (1998)
- [21] H. Holm, W. Scheid, W. Greiner, Phys. Lett. B 29, 473 (1969)
- [22] P.W. Riesenfeldt, T.D. Thomas, Phys. Rev. C 02, 711 (1970)
- [23] B.B. Back *et al.*, Phys. Rev. Lett. 45, 1230 (1980)
- [24] S. Santra *et al.*, Phys. Rev. C 64, 024602. (2001)
- [25] S. Santra *et al.*, Phys. Rev. C 60, 034611 (1999)
- [26] N. Keeley, K. Rusek, Phys. Rev. C 56, 3421 (1997)
- [27] S. Santra *et al.*, Phys. Rev. C 83, 034616 (2011)
- [28] A. Gavron, Phys. Rev. C 21, 230 (1980)
- [29] C.M. Perey, F.G. Perey, Atm. Data. Nucl. Data Tables 17, 1 (1976)

Chapter 5: Complete fusion in ${}^6\text{Li}+{}^{152}\text{Sm}$

- [30] J.R. Huizenga *et al.*, Nucl. Phys. 29, 462 (1962)
- [31] D. Hill *et al.*, Phys. Rev. C 89, 1102 (1953)
- [32] P.R.S. Gomes *et al.*, Phys. Rev. C 71, 017601 (2005)
- [33] R.A. Broglia, A. Winther, Heavy Ion Reaction Lecture Notes I, Benjamin Cummings, Redwood City, CA, 1981,p. 114.
- [34] U. Gotz *et al.*, Nucl. Phys. A 192, 1 (1997)
- [35] J. Blocki *et al.*, Ann. Phys. (NY) 105, 427 (1977)
- [36] W. Reisdorf *et al.*, Nucl. Part. Phys. 20, 1297 (1994)
- [37] I. Dutt *et al.*, Phys. Rev. C 81, 064608 (2010)
- [38] P. Moller, J.R. Nix, Nucl.Phys. A 361, 117 (1981)
- [39] P. Moller *et al.*, At. Data Nucl. Data Tables 59, 185 (1995)
- [40] W.D. Myers, W.J. Swiatecki, Phys. Rev. C 62, 044610 (2000)
- [41] I.J. Thompson, Comput. Phys. Rep. 7, 167 (1988)
- [42] P. Christensen *et al.*, Nucl. Phys. A 129, 337 (1969)
- [43] E. Obiajunwa *et al.*, Nucl. Phys. A 500, 341 (1989)
- [44] H. Nishioka *et al.*, Nucl. Phys. A 415, 230 (1984)
- [45] K. Hagino *et al.*, Phys. Rev.C61, 037602 (2000)
- [46] K. Hagino *et al.*, Comput. Phys. Commun. 123, 143(1999)
- [47] C. Beck *et al.*, Phys. Rev. C 67, 054602 (2003)
- [48] R. Kossakowski *et al.*, Phys. Rev. C 32, 1612 (1985)
- [49] A. Diaz-Torres *et al.*, Phys. Rev. C 68,044607 (2003)

Chapter 6

6.1 Effect of Projectile breakup threshold in the complete fusion of $^{6,7}\text{Li}+^{144,152}\text{Sm}$.

6.1.1 Introduction

Further we have used the same targets (i.e., $^{144,152}\text{Sm}$) but ^7Li as the projectile which has more breakup threshold of 2.45 MeV compared to ^6Li (i.e., 1.48 MeV). Different explanations exist regarding the enhancement or suppression of the fusion cross section σ_{fus} compared to single barrier fusion model, around the Coulomb barrier [1-4]. It has been observed that, at energies above the Coulomb barrier, the complete fusion (CF) cross sections for the reactions involving heavy mass or medium mass targets are suppressed by various degrees compared to the one dimensional barrier penetration model predictions. However, there was no fusion suppression observed for the reactions involving light mass and light medium mass targets e.g., $^9\text{Be}+^{64}\text{Zn}$ [5], $^{6,7}\text{Li}+^{59}\text{Co}$ [6], $^9\text{Be}+^{19}\text{F}$, ^{27}Al , ^{28}Si [7], $^7\text{Li}+^{12}\text{C}$ [8], etc. Fusion cross sections for $^6\text{Li}+^{144,152}\text{Sm}$ reactions, that we have measured recently [9,10] and discussed in chapter 4 & 5, were found to be enhanced compared to the uncoupled results at sub-barrier energies, but at above barrier energies they were suppressed by $32 \pm 4\%$ and $28 \pm 5\%$ respectively. Systematics of the fusion cross sections for the systems involving loosely bound projectiles [9] with medium mass and heavy mass targets showed that the fusion suppression factor on an average increases with the Z of the target (Z_T) and decreases with the breakup threshold of the projectile (E_{th}). With the availability of more and more fusion data involving weakly bound projectiles in the literature, several systematic studies on CF suppression factor ($1-F_{\text{CF}}$) have been made in order to find out the effect of breakup threshold of the projectile (E_{th}) on fusion cross section. , L. R. Gasques *et al.* [16] and M. Dasgupta *et al.*[11] have shown that the suppression factor is independent of target charge particularly for the reactions involving heavy targets (e.g., ^{208}Pb , ^{209}Bi) and projectiles like $^{6,7}\text{Li}$, ^9Be , $^{10,11}\text{B}$. Systematics made by

V. V. Parkar *et al.* included the results of the fusion measurements for ${}^6\text{Li}+{}^{144}\text{Sm}$ [9] and ${}^9\text{Be}+{}^{124}\text{Sn}$ [12] reactions where it was observed that the fusion suppression factors for reactions involving medium mass targets are not very different from the ones involving heavy mass targets. Later, CF cross sections were measured for a reaction involving slightly lighter mass target i.e., ${}^9\text{Be}+{}^{89}\text{Y}$ reaction by C. Palshetkar *et al.*[13] where it was observed that cross sections at above barrier energies were suppressed by $\sim 20\%$. Thus it would be great interest to measure the suppression factors for as many reactions involving different targets and study its dependence on target mass or charge starting from light to heavy targets. Similarly, the study of the suppression factor dependence on projectile breakup threshold is even more exciting. The alpha separation energies for the ${}^6,{}^7\text{Li}$ and ${}^9\text{Be}$ nuclei are $S_\alpha=1.48, 2.45$ and 1.57 MeV, respectively, and it has been shown[14] that the break-up effects on the fusion for the ${}^7\text{Li}$ induced reactions are much less important than for ${}^6\text{Li}$ and ${}^9\text{Be}$. it would be interesting to study the fusion reaction involving ${}^7\text{Li}$ as a projectile with the above two targets (i.e. ${}^{144,152}\text{Sm}$) , i.e., for ${}^7\text{Li}+{}^{144,152}\text{Sm}$ and compare with our earlier measurements to test the suppression factor dependence on breakup threshold. Since ${}^7\text{Li}$ has a higher breakup threshold than ${}^6\text{Li}$, it is expected that the complete fusion (CF) suppression factor for the above reactions would be less compared to ${}^6\text{Li}+{}^{144,152}\text{Sm}$. Secondly it would be interesting to study the role of target deformation versus projectile breakup and their dominance over each other by comparing the fusion cross sections involving two isotopes of Sm i.e., ${}^{144,152}\text{Sm}$, having different deformation parameters as studied in previous sections[10] but with a different projectile (${}^7\text{Li}$). In this chapter we present precise excitation function measurements for the complete fusion of ${}^7\text{Li}$ with ${}^{144,152}\text{Sm}$ by activation method at energies ranging from 20 to 40 MeV, i.e. from 0.75 to 1.5 times the Coulomb barrier ($V_B \sim 26$ MeV), in steps of 1-2 MeV. Fusion excitation function for present systems are compared with each other as well as with the ones previously measured by our group to find the target and projectile dependence. Coupled-channels calculations to understand the measured data and find the influence of projectile breakup and target deformation on fusion are presented. The detail experimental procedure has been discussed in Chapter-3.

6.1.2 Analysis of experimental results

When ${}^7\text{Li}$ fuses with the target nucleus (${}^{144}\text{Sm}$), it produces the excited compound nucleus ${}^{151}\text{Tb}^*$. After 2n evaporation, it produces the evaporation residue (ER) ${}^{149}\text{Tb}^*$ (g.s.) with the half-life ($t_{1/2}$) of 4.118h and ${}^{149}\text{Tb}^*$ (m.s.) with $t_{1/2} \sim 4.16\text{m}$. In case of 3n evaporation it produces the residues ${}^{148}\text{Tb}^*$ having meta stable state (${}^{148}\text{Tb}^m$, $t_{1/2} \sim 2.2\text{m}$) and ground state (${}^{148}\text{Tb}^g$, $t_{1/2} \sim 60.0\text{m}$), which decay to Gd nuclei after electron capture. Similarly, for ${}^7\text{Li}+{}^{152}\text{Sm}$ reaction, the compound nucleus ${}^{159}\text{Tb}^*$ decays by 3n and 4n evaporation followed by electron capture to ${}^{156}\text{Gd}$ and ${}^{155}\text{Gd}$ nuclei with $t_{1/2} = 5.35\text{ d}$ and 5.32 d respectively. Intensities of the γ -lines with proper branching ratios corresponding to both ground and metastable states of ERs together give the cross sections of different ER channels. The intense γ -lines were chosen to evaluate the cross sections. The other γ -lines

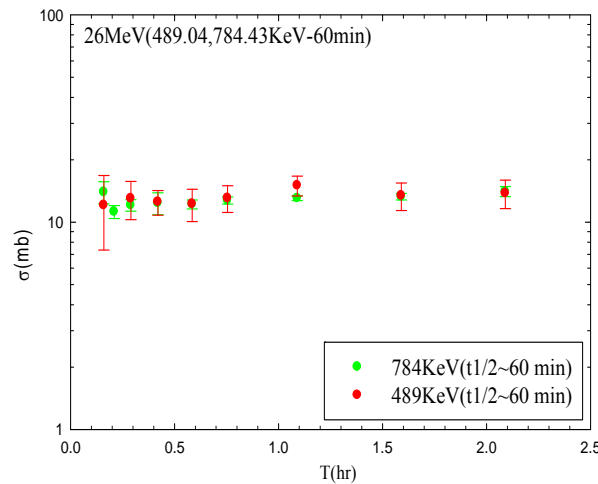


Fig 6.1: ER cross sections for ${}^{148}\text{Tb}$ ($t_{1/2} \sim 60\text{ min}$) obtained from two different gamma lines i.e., 489.0 and 784.4 keV coming from same nuclei at 26 MeV. From the figure it is clear that in both the cases the ER cross section is same indicating the stability of analysis procedure.

corresponding to the same ERs were also used to cross check the accepted cross sections in addition with the half-life fitting of the ER. One example is shown in Fig. 6.1 and Fig. 6.2. In Fig 6.1 two γ - lines having different efficiency ‘eff’, only after the correction of ‘eff’ and branching ratio ‘br’ the cross section will be the same using two independent γ rays of different energy coming from same ER. The ‘eff’ has been discussed in chapter-3. The

intense γ -lines were chosen to evaluate the cross sections. The other γ -lines corresponding to the same ERs were also used to cross check the accepted cross sections in addition with the half-life fitting of the ER and are shown in Fig 6.2. The excitation function of individual ER channels corresponding to ${}^7\text{Li}+{}^{144}\text{Sm}$ and ${}^7\text{Li}+{}^{152}\text{Sm}$ reactions is respectively shown in Fig. 6.3(a) and (b). The ratios of two dominant ER channels i.e., σ_{3n}/σ_{2n} in ${}^7\text{Li}+{}^{144}\text{Sm}$ reaction and σ_{4n}/σ_{3n} in ${}^7\text{Li}+{}^{152}\text{Sm}$ reaction are also shown in Fig. 6.3(c) and (d) respectively.

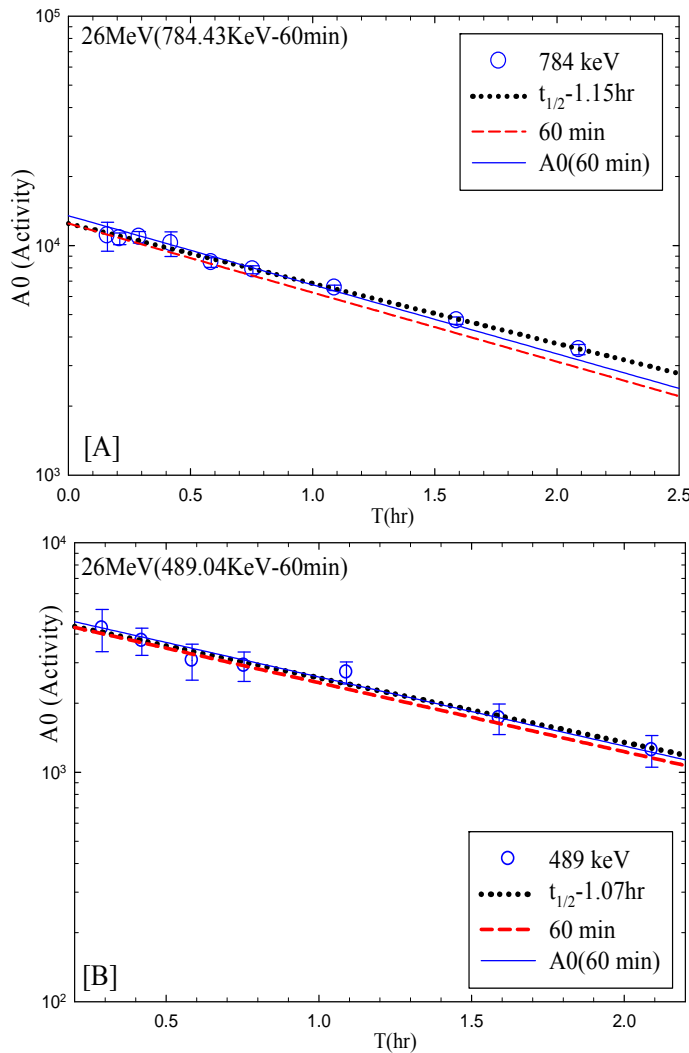


Fig 6.2: Half-life fitting of the ER cross sections for ${}^{148}\text{Tb}$ (3n channel) from two different gamma lines 489.0 & 784.4 keV coming from same nuclei. The $t_{1/2}$ for 3n channel in ${}^7\text{Li} + {}^{144}\text{Sm}$ reaction is 60 min. Dotted line is the fitted line, dashed line is the actual half-life and the solid line is the fitting with varying A_0 (activity) by keeping $t_{1/2} \sim 60$ min fix.

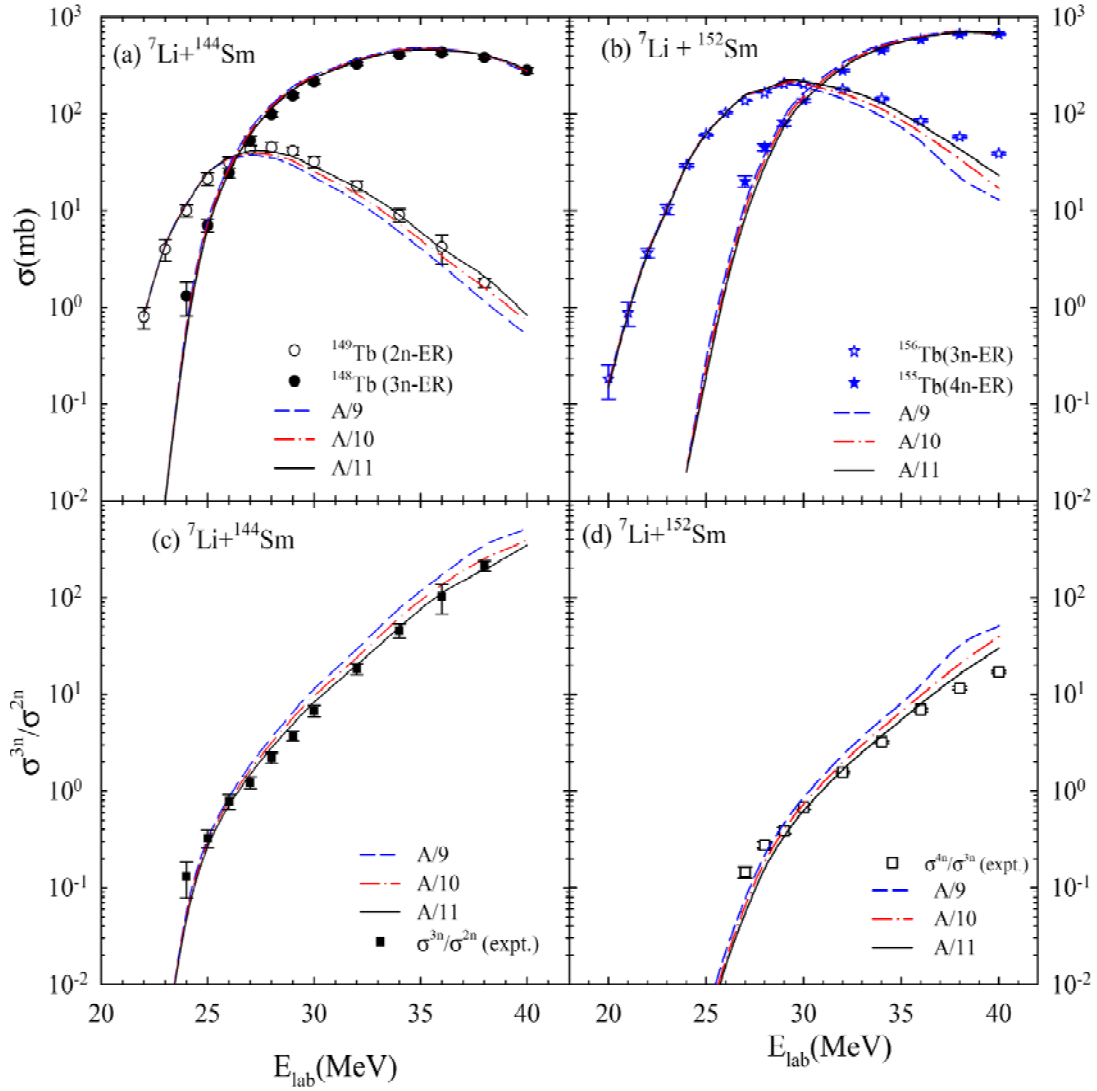


Fig 6.3: ER cross sections for (a) ^{149}Tb (hollow circles) and ^{148}Tb (solid circles) produced in $^7\text{Li}+^{144}\text{Sm}$ reaction and (b) ^{156}Tb (hollow stars) and ^{155}Tb (solid stars) produced in $^7\text{Li}+^{152}\text{Sm}$ reaction. Ratio of two dominant ER channels i.e. σ_{3n} to σ_{2n} (solid squares) in 1st reaction and σ_{4n} to σ_{3n} (hollow squares) in 2nd reaction at different beam energies are shown in (c) and (d) respectively. Lines are calculations from Statistical model (see text for details).

6.1.3 Statistical model analysis

Statistical Model (SM) calculations were performed using the code PACE2 [15] with default potential parameters to study the relative contributions of different ER channels and estimate the contributions from missing channels. For energies below the Coulomb barrier,

the SM calculations were carried out by feeding the ℓ -distribution obtained from coupled channel calculations. The results of PACE2 calculations for the ratio of σ_{3n} to σ_{2n} for ${}^7\text{Li}+{}^{144}\text{Sm}$ and σ_{4n} to σ_{3n} for ${}^7\text{Li}+{}^{152}\text{Sm}$ are shown in Fig. 6.3(c) and (d) using level density parameters (ρ) equal to $A/9$ (dashed line), $A/10$ (dash-dot line) and $A/11$ (solid line). The calculation with $\rho=A/11$ provide a good description of the present experimental data for ER as well as their ratios. The combined cross-sections of two dominating channels i.e., $\sigma_{2n}+\sigma_{3n}$ in ${}^7\text{Li}+{}^{144}\text{Sm}$ reaction and $\sigma_{3n}+\sigma_{4n}$ in ${}^7\text{Li}+{}^{152}\text{Sm}$ reaction were calculated at each energy using the same parameters in PACE2 for all energies. The cross section for independent ER has been tabulated in Table 6.1 and Table 6.2 for ${}^7\text{Li}+{}^{144/152}\text{Sm}$ system. The contributions from the missing channels were accounted from the SM calculations and added to the dominating channels to obtain the experimental complete fusion cross section $\sigma_{\text{fus}}^{\text{expt}}$ which are Tabulated in Table 6.3 and shown in Fig. 6.4. The errors in $\sigma_{\text{fus}}^{\text{expt}}$ includes the experimental errors in ERs as well as the uncertainty in the SM calculations. Further, to check the consistency in SM results for different channels, $\sigma_{\text{fus}}^{\text{expt}}$ was given as input to PACE2 and its output for dominating ERs ($\sigma_{2n,3n}$ for ${}^7\text{Li}+{}^{144}\text{Sm}$ and $\sigma_{3n,4n}$ for ${}^7\text{Li}+{}^{152}\text{Sm}$) channels using different level densities $A/9$, $A/10$ and $A/11$ are performed and with level density of $A/11$ (solid lines) it is found to be in reasonable agreement with the data. Experimental CF excitation functions for the two reactions ${}^7\text{Li}+{}^{144,152}\text{Sm}$ are plotted in Fig. 6.4. It can be observed that at energies near and below the barrier the CF cross sections for ${}^7\text{Li}+{}^{152}\text{Sm}$ (open circles) are much higher than those of ${}^7\text{Li}+{}^{144}\text{Sm}$ (filled circles). The projectile being the same, this enhancement in CF cross section is certainly due to the deformed ${}^{152}\text{Sm}$ target compared to the spherical ${}^{144}\text{Sm}$ target involving ${}^6\text{Li}$ projectile and above targets [10]. Next we compared the CF cross sections involving same target but two different projectiles (${}^6,{}^7\text{Li}$) with different breakup threshold as shown in Fig. 6.4(b) and (c). It was observed that the CF cross sections for ${}^7\text{Li}$ induced reactions at above-barrier energies are larger than those for ${}^6\text{Li}$. It can be concluded that the breakup threshold for ${}^6\text{Li}$ being less than ${}^7\text{Li}$, the loss of incident flux is more for the reactions induced by the former compared to the latter. Thus the CF cross sections for the former are more suppressed due to breakup and this observation is consistent with the systematics made in our earlier paper [9].

Table6.1: different ER cross sections (2n channel¹⁴⁹Tb, 3n channel¹⁴⁸Tb) for ⁷Li+¹⁴⁴Sm reaction.

E _{lab} (MeV)	2n (¹⁴⁹ Tb) (mb)	error(mb)	3n (¹⁴⁸ Tb) (mb)	error(mb)
22.00	0.80	0.20	-	-
23.00	4.00	1.00	-	-
24.00	10.00	1.41	1.31	0.50
25.00	21.37	3.16	7.00	1.02
26.00	31.40	4.12	24.50	2.82
27.00	43.00	3.60	53.03	5.65
28.00	45.00	5.20	98.85	6.00
29.00	41.50	4.12	155.26	7.07
30.00	32.00	4.12	215.84	11.66
32.00	18.00	2.23	331.00	11.53
34.00	9.00	1.41	410.00	10.77
36.00	4.20	1.42	430.80	20.22
38.00	1.80	0.20	382.20	20.09
40.00	-	-	281.00	20.22

Table6.2: different ER cross sections (3n channel¹⁵⁶Tb, 4n channel¹⁵⁵Tb) for ⁷Li+¹⁵²Sm reaction.

E _{lab} (MeV)	3n (¹⁵⁶ Tb) (mb)	error(mb)	4n(¹⁵⁵ Tb) (mb)	error(mb)
20.00	0.18	0.07	-	-
21.00	0.88	0.24	-	-
22.00	3.62	0.40	-	-
23.00	10.33	1.20	-	-
24.00	29.43	1.10	-	-
25.00	60.98	1.06	-	-
26.00	102.19	2.20	-	-
27.00	137.45	0.70	20.00	2.79

28.00	165.00	0.90	45.00	3.75
29.00	205.40	1.00	80.00	5.71
30.00	204.00	4.00	138.00	5.49
32.00	180.00	1.78	281.00	8.56
34.00	143.00	3.00	460.00	10.26
36.00	85.00	3.00	588.00	9.19
38.00	58.00	2.00	669.00	10.06
40.00	39.00	1.00	668.43	9.93

Table 6.3: Measured complete fusion cross sections for ${}^7\text{Li}+{}^{144}\text{Sm}$ & ${}^7\text{Li}+{}^{152}\text{Sm}$ systems.

$E_{c.m.}(\text{MeV})$ ${}^7\text{Li}+{}^{144}\text{Sm}$	$\sigma_{CF}(\text{mb})$	Error(mb)	$E_{c.m.}(\text{MeV})$ ${}^7\text{Li}+{}^{152}\text{Sm}$	$\sigma_{CF}(\text{mb})$	error(mb)
20.98	0.85	0.21	19.11	0.25	0.10
21.93	4.72	1.18	20.07	1.10	0.30
22.88	13.65	1.81	21.03	4.10	0.50
23.84	35.60	4.17	21.98	11.20	1.30
24.79	70.33	6.29	22.94	31.00	1.20
25.74	120.49	8.41	23.89	63.20	1.50
26.70	180.46	10.00	24.85	107.00	2.00
27.65	245.45	10.21	25.81	164.00	3.00
28.60	310.65	15.50	26.76	218.00	4.00
30.51	445.53	15.00	27.72	295.00	6.00
32.42	550.74	14.27	28.67	353.00	7.00
34.33	640.30	29.84	30.59	475.00	9.00
36.23	750.01	39.26	32.50	620.00	11.00
38.14	803.77	57.84	34.41	696.00	10.00
-	-	-	36.32	779.00	11.00
-	-	-	38.23	850.00	12.00

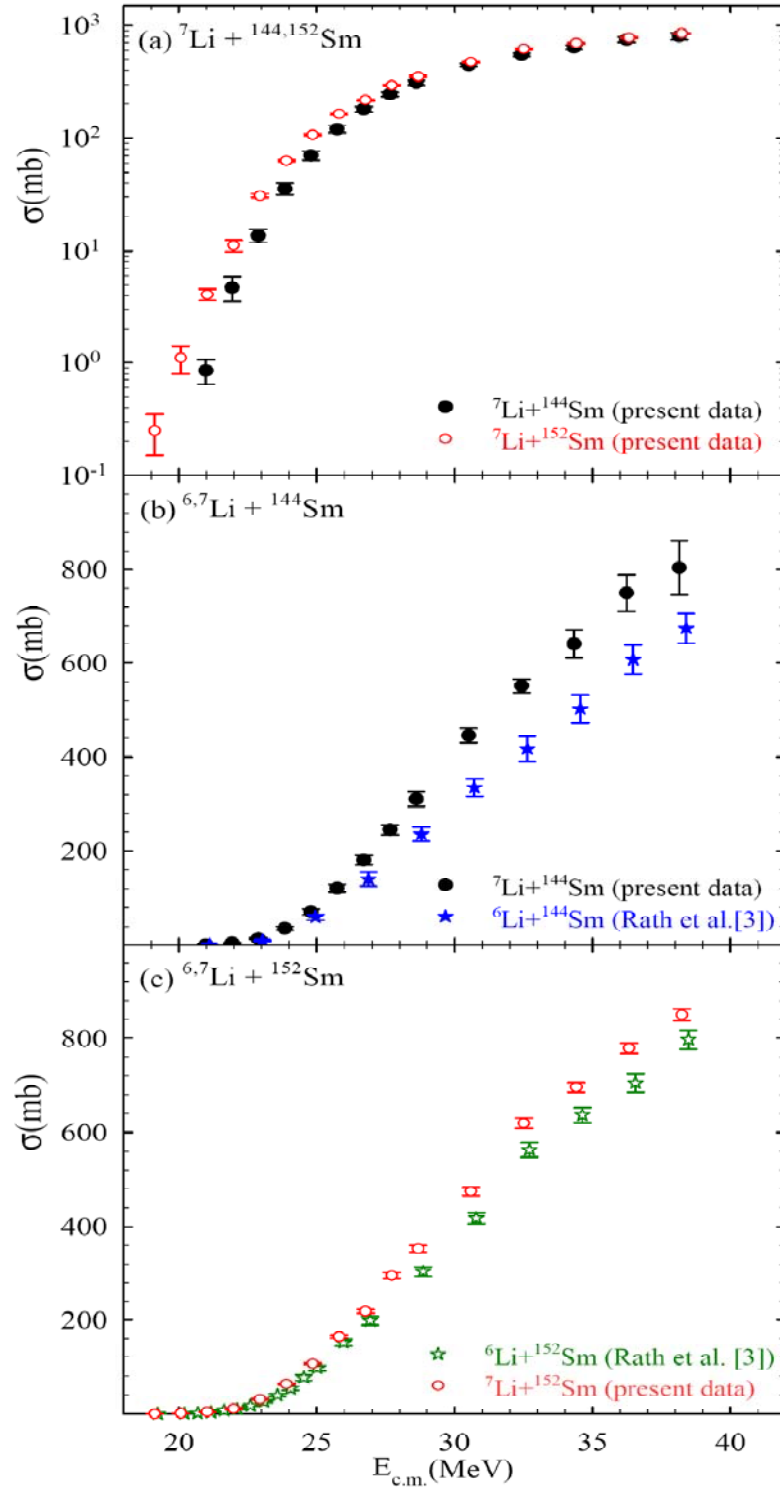


Fig 6.4: (a) Measured complete fusion cross sections for ${}^7\text{Li} + {}^{144}\text{Sm}$ (filled circles) and ${}^7\text{Li} + {}^{152}\text{Sm}$ (open circles). (b) Comparison of CF cross sections involving different projectiles i.e., ${}^6\text{Li}$ (filled stars) and ${}^7\text{Li}$ (filled circles) but same target (${}^{144}\text{Sm}$), showing the effect of projectile breakup threshold. (c) Same as (b) but involving a different target (${}^{152}\text{Sm}$).

6.1.4 Barrier distribution and CC analysis

Barrier distributions were calculated by the formula “ $d^2(\sigma_{\text{fus}}E_{\text{c.m.}})/dE_{\text{c.m.}}^2$ ” using the measured excitation functions for complete fusion σ_{fus} as a function of $E_{\text{c.m.}}$ for the above two reactions. Experimental fusion cross section for ${}^7\text{Li}+{}^{144}\text{Sm}$ and ${}^7\text{Li}+{}^{152}\text{Sm}$ reactions are shown in Fig. 6.5(a) and (b) respectively and they are represented by filled and hollow circles. Corresponding barrier distributions are shown in Fig. 6.5(c) and (d). The average fusion barriers obtained from the experimental barrier distributions are found to be $V_{\text{B}}=24.9 \pm 0.3\text{MeV}$ and $24.5\pm 0.3\text{ MeV}$ for ${}^7\text{Li}+{}^{144,152}\text{Sm}$ respectively. The value of V_{B} was obtained following the procedure adopted in Ref. [16]. Coupled-channels calculations using CCFULL code [17] are performed with the potential parameters that reproduced the average experimental fusion barriers. Potential parameters used for the coupled-channels (CC) calculations and corresponding uncoupled barrier heights V_{B} and radii R_{B} and curvatures $\sim\hbar\omega$, derived for the present systems, are given in Table 6.4. The full couplings included the coupling of the projectile ground state ($3/2^-$) and first excited state ($1/2^-$, 0.4776 MeV) with β_{00} (β_2 for the ground state reorientation) = 1.189, β_{01} (β_2 for the transition between the ground and the first excited states) = β_{11} (β_2 for the reorientation of the 1st excited state) = 1.24. Regarding target couplings, the vibrational state (3^- , $\beta_2=0.23$, $E_x=1.81$ MeV) was included for ${}^{144}\text{Sm}$. The effect of 2^+ ($\beta_2=0.11$, $E_x=1.61$ MeV) of ${}^{144}\text{Sm}$ was found to be less important compared to 3^- state. In the second reaction, since ${}^{152}\text{Sm}$ is a deformed nucleus in its ground state, both quadrupole (2^+ , 0.122 MeV) and hexadecapole (4^+) rotational states with deformation parameters $\beta_2=0.26$ and $\beta_4 = 0.05$ are coupled. Coupling to the breakup channel was not included. It was observed that the calculated values of CF with full couplings are higher than the measured ones at above barrier energies, and they are under predicted at sub-barrier energies. It was also observed that at sub-barrier energies, the calculated fusion cross-sections with only target couplings as well as with target+projectile couplings (dashed lines) are enhanced compared to the uncoupled values (dash-dot-dot line). However, at above-barrier energies, the calculated values of CF with or without full couplings are higher than the measured ones. Since the effect of

coupling on fusion at energies above the barrier is negligible, these calculations are independent of the number of channels that are coupled. Interestingly, the calculated CF cross sections for ${}^7\text{Li}+{}^{144,152}\text{Sm}$ when normalized by 0.76 and 0.75 respectively reproduce the experimental fusion as well as barrier distribution data at higher energies very well. Thus, one can conclude that the CF cross sections in this region for the above two reactions are suppressed by $\sim 24\pm 4\%$ and $25\pm 4\%$ respectively compared to the ones predicted by CCFULL calculations. The uncertainty of $\pm 4\%$ in suppression factor was estimated from the uncertainties in V_B and σ_F . Thus the suppression factors for the two reactions are found

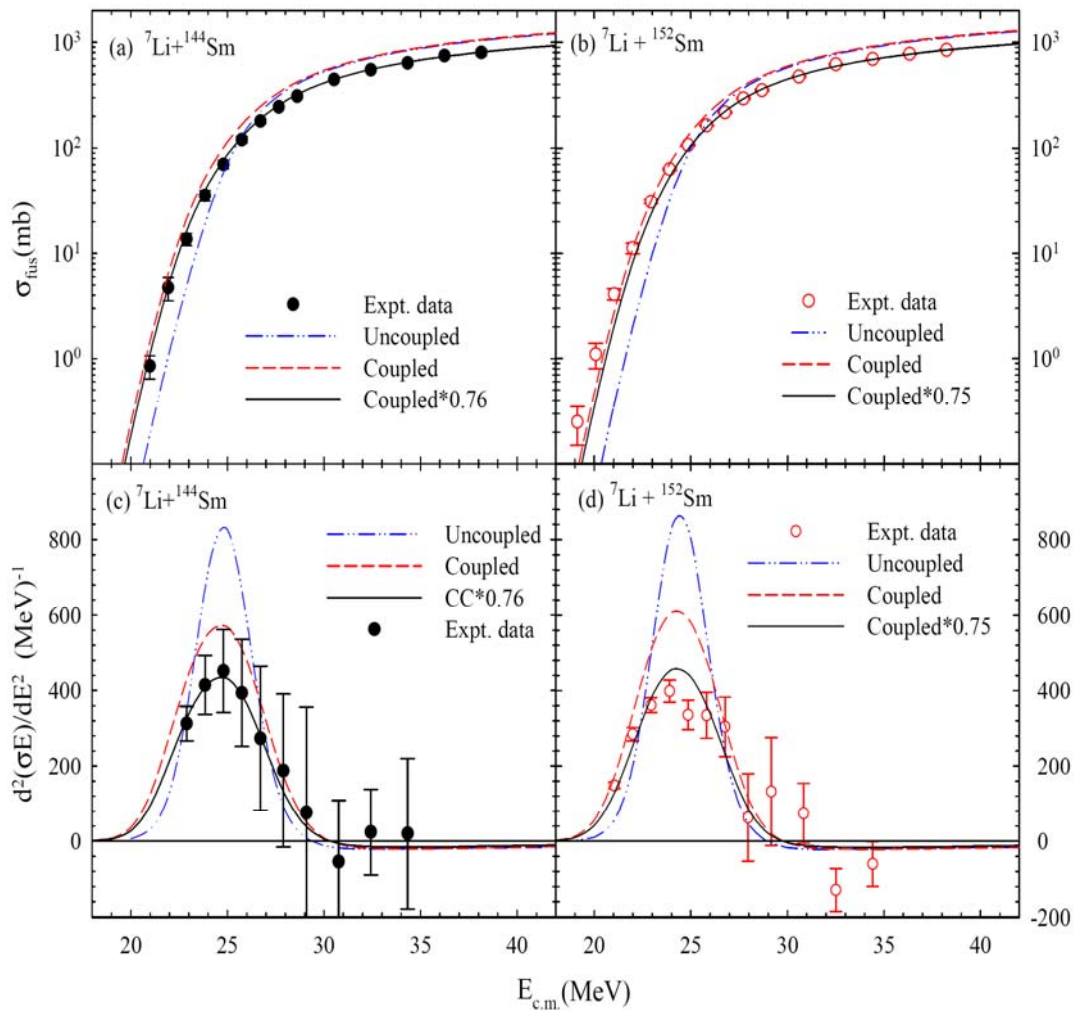


Fig. 6.5: (a,b) Measured complete fusion cross-sections for ${}^7\text{Li}+{}^{144}\text{Sm}$ (filled circles) and ${}^7\text{Li}+{}^{152}\text{Sm}$ (open circles) and (c,d) their corresponding barrier distributions. Dash-dot-dot and dashed lines represent the results of coupled-channels calculations for no-coupling case and with full couplings respectively. Solid lines are obtained by normalizing the coupled results by 0.75 and 0.76 for ${}^7\text{Li}+{}^{144,152}\text{Sm}$ reactions respectively.

Table 6.4: Parameters for CC potential used in CCFULL Calculations along with barrier parameters V_B , R_B and $\hbar\omega$

System	V_0 (MeV)	r_0 (fm)	a (fm)	V_B (MeV)	R_B (fm)	$\hbar\omega$ (MeV)
${}^7\text{Li}+{}^{144}\text{Sm}$	141.0	1.02	0.63	24.9	10.08	4.71
${}^7\text{Li}+{}^{152}\text{Sm}$	150.0	1.02	0.63	24.54	10.24	4.64

to be similar but smaller than the ones involving ${}^6\text{Li}$ as a projectile (i.e. ${}^6\text{Li}+{}^{144};{}^{152}\text{Sm}$, where the suppression factors were $\pm 32\%$ and 28% respectively [9,10]). These observations are consistent with the systematics made in our earlier work based on projectile breakup threshold and target atomic number [9]. It also shows that the CF at sub-barrier energies is enhanced due to both target deformation as well as projectile excitation. However, the calculated CF for ${}^7\text{Li}+{}^{152}\text{Sm}$ is still under-predicted compared to the experimental data. Similar observation was also made for ${}^6\text{Li}+{}^{152}\text{Sm}$ reaction [10]. This may imply that, at sub-barrier energies, there is coherence in the effects of projectile break up and target deformation.

6.1.5 Fusion cross sections using proximity potential

The measured CF cross sections data for the present systems were compared to those predicted using the ‘‘Proximity potentials’’ [18,19]. These potentials are parameterized from the existing fusion data in the literature for many systems involving mostly the tightly bound projectiles. Fusion barrier parameters, i.e., barrier height and barrier radius, can be obtained by adding the Coulomb potential with the proximity potentials as done by Dutt *et al.*[20] and they can be used to predict the fusion cross section. The original version of this potential(Proximity 1977) was described by J. Blocki *et al.* [18], which was later modified and renamed as ‘‘Proximity1988’’ by W. Reisdorf [19] and then to incorporate more refined mass formula of Moller and Nix [21,22]. Myers and Swiatecki [23], using their concept of droplet model, further updated the values of nuclear radii and nuclear surface

tension coefficients in the latest version of the above potential and named as ‘‘Proximity 2000’’. In the present work, fusion cross sections are calculated using the updated version ‘2000’ of proximity potential. Using the corresponding expressions for the fusion barrier parameters for ${}^7\text{Li}+{}^{144}\text{Sm}$ (${}^7\text{Li}+{}^{152}\text{Sm}$) reaction, the barrier height ‘ V_B ’, barrier radius ‘ R_B ’ and barrier curvature ‘ $\sim\hbar\omega$ ’ were calculated and listed in Table 6.5. The above parameters were used in the simplified Wong’s formula (which assumes the potential barrier to be of parabolic shape) to calculate the fusion cross sections using the wong expression. Fusion cross sections thus obtained using the proximity potential (version 2000) are shown in Fig. 6.6 (a) and (b) as dashed lines. It can be observed that they over estimate the experimental data at above barrier energies. To reproduce the experimental data, the calculated cross sections for both ${}^7\text{Li}+{}^{144}\text{Sm}$ as well as ${}^7\text{Li}+{}^{152}\text{Sm}$ reactions channel and leading to the suppression of complete fusion cross section using ‘Proximity 2000’ potential and required to be normalized by a factor of 0.78 and the results are represented by solid lines. This implies that the experimental CF for both the reactions at above barrier energies is suppressed by $\sim 22\%$ compared to the theoretical predictions using the Proximity potential. This is consistent with our earlier conclusions on CF suppression factors which were obtained by comparing the data with the predictions from the coupled-channels calculations using CCFULL. These observations confirm that the projectile breakup is playing a crucial role in reducing the flux from the entrance.

Table 6.5: Fusion barrier parameters V_B , R_B and $\hbar\omega$ obtained from Proximity potential.

System	V_B (MeV)	R_B (fm)	$\hbar\omega$ (MeV)
${}^7\text{Li}+{}^{144}\text{Sm}$	24.96	9.95	4.52
${}^7\text{Li}+{}^{152}\text{Sm}$	24.73	10.06	4.46

6.1.6 Systematics on suppression factor

To find the dependence of CF suppression factors on projectile breakup threshold and target charge, a systematic comparison was made for several reactions, including the

present data, involving weakly bound projectiles with $\alpha + x$ structures and different breakup threshold energy 'E_{th}' for the breakup of the projectiles into α and x . Fig. 6.7 shows the plot of the suppression factor '1-F_{CF}' (where F_{CF} is complete fusion fraction) as a function

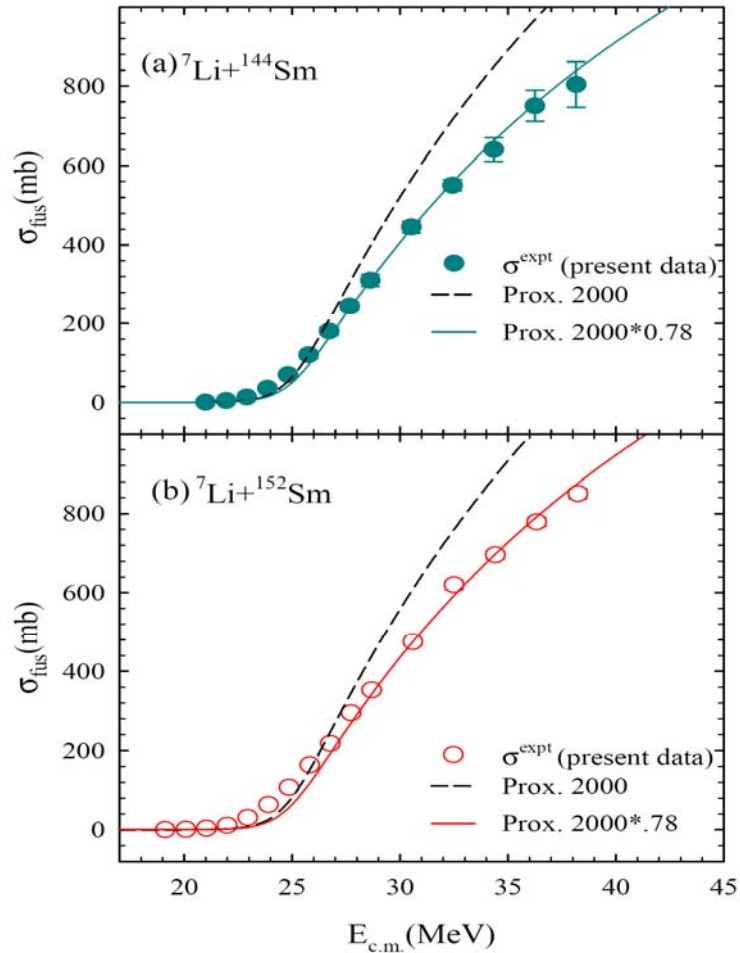


Fig 6.6: Fusion cross sections calculated for (a) ${}^7\text{Li}+{}^{144}\text{Sm}$ and (b) ${}^7\text{Li}+{}^{152}\text{Sm}$ reactions by wong's model using proximity potentials "Proximity 2000" are represented by dashed lines. The above cross sections multiplied by a factor of 0.78 and are represented by solid lines. Filled and hollow circles correspond to the measured CF data for ${}^7\text{Li}+{}^{144,152}\text{Sm}$ reactions respectively.

of (a) the product of charges of the projectile and the target 'ZpZt' and (b) projectile breakup threshold energy. The figure shows the suppression factors for the reactions involving (i) ${}^6\text{Li}$ with ${}^{144}\text{Sm}$ [9], ${}^{152}\text{Sm}$ [10], ${}^{208}\text{Pb}$ [24] and ${}^{209}\text{Bi}$ as targets, (ii) ${}^7\text{Li}$ with ${}^{144}\text{Sm}$ (present data), ${}^{152}\text{Sm}$ (present data), ${}^{159}\text{Tb}$ [9], ${}^{165}\text{Ho}$ [25] and ${}^{209}\text{Bi}$ [24], (iii) ${}^9\text{Be}$ with ${}^{89}\text{Y}$ [13], ${}^{124}\text{Sn}$ [12], ${}^{208}\text{Pb}$ [24] and ${}^{209}\text{Bi}$ [24], (iv) ${}^{10}\text{B}$ with ${}^{159}\text{Tb}$ [9] and ${}^{209}\text{Bi}$ [24], and (v) ${}^{11}\text{B}$

with ^{209}Bi [11]. The symbols represent the experimental data corresponding to different reactions as mentioned in the Figure, while a line represents the average value of suppression factors of the reactions involving a particular projectile e.g., ^6Li (solid line), ^7Li (dash-dot line), ^9Be (dashed line), ^{10}B (dash-dot-dot line) and ^{11}B (dotted line). It can be

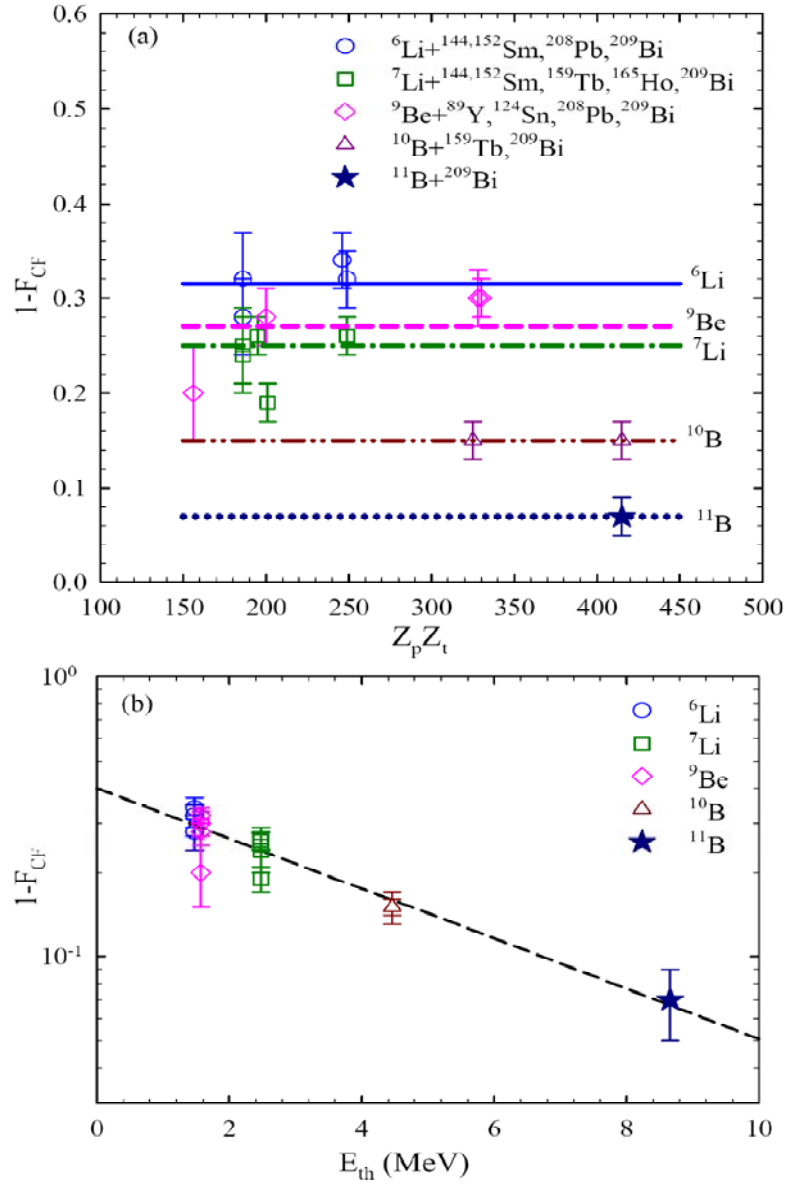


Fig.6.7: Suppression factor ($1-F_{CF}$) as a function of (a) the product of the charges of projectile and target (b) projectile breakup threshold for several reactions involving $^{6,7}\text{Li}$, ^9Be , $^{10,11}\text{B}$ projectiles including the present data. Dashed line is a guide to the eye.

observed from Fig.6.7(a) that the average value of the suppression factors for the reactions involving a particular projectile has a dependence on breakup threshold. This aspect has been brought out clearly in Fig. 6.7(b) where it can be seen that there is a smooth fall in the average suppression factor with the increase of E_{th} . However, it should be noted that for a particular projectile the suppression factor is not totally independent of target charge. For example, in case of ${}^9\text{Be}$ induced reactions, the suppression factor increases with target charge number. For other projectiles, the above dependence is not clear. To obtain a generalized behavior one needs to have data for a large number of reactions.

6.1.7 Summary

Complete fusion (CF) excitation functions for ${}^7\text{Li}+{}^{144,152}\text{Sm}$ reactions have been measured at energies near and above the Coulomb barrier. Activation technique was used to determine the cross sections of 2n- 3n- and 4n evaporation channels, which were the most dominating channels of decay of the compound nucleus formed by the complete fusion process in the measured energy range. Statistical model calculations were performed using PACE2 to estimate the relative contributions of other residue channels in order to determine the experimental cross sections for the complete fusion. Comparison of two reactions show that CF cross sections for ${}^7\text{Li}+{}^{152}\text{Sm}$ at sub-barrier energies are much enhanced compared to ${}^7\text{Li}+{}^{144}\text{Sm}$ but they are similar at above barrier energies. CF cross sections for the present reactions at above barrier energies were found to be slightly higher compared to the reactions with the same targets using ${}^6\text{Li}$ as projectile [9,10]. Fusion barrier distributions were derived from the measured fusion data and the average experimental barriers were obtained and used as constraints in the coupled channels calculations using CCFULL. CC results for both the reactions show an enhancement in fusion at energies below the barrier and suppression above the barrier compared to the predictions given by the single barrier penetration model. Coupling to the target and projectile excitation enhances the fusion cross sections at sub barrier energies and they get closer to the experimental data. However, the effect of coupling on fusion at energies above the barrier was negligible. Therefore it may imply that the measured CF cross sections at

above barrier energies are suppressed for the present reactions as compared to CCFULL calculations with or without any couplings. Fusion cross sections were also calculated by the Wong model using the fusion barrier parameters obtained from the parameterized proximity potentials (version 'Proximity2000'). A comparison with the measured CF data shows that the predictions at above barrier energies are much higher which are consistent with the CCFULL calculations. From these two comparisons it was found that the experimental CF data for ${}^7\text{Li}+{}^{144,152}\text{Sm}$ reactions at above barrier energies are suppressed by $\sim 24\pm 4\%$ compared to the theoretical predictions. The above suppression may be ascribed to the low breakup threshold energy of ${}^7\text{Li}$ which allows it to breakup prior to fusion. A systematic comparison of the CF suppression factors for different reactions involving weakly bound projectiles including present data shows that the suppression increases with the decrease of projectile breakup threshold. However, the dependence of suppression factor on target charge is not very clear. It demands more data on different reactions involving a particular projectile with a range of targets varying from light, medium to heavy mass nuclei.

Refernces

- [1] C. H. Dasso, S. Landowne, and A. Winther, Nucl. Phys.A405, 381 (1983)
- [2] M. Dasgupta *et al.*, Ann. Rev. Nucl. Part. Sc. 48, 401 (1998)
- [3] M. S. Hussein *et.al.*, Phys.Rev. C 46, 377 (1992)
- [4] N. Takigawa *et.al.*, Phys. Rev. C 47,R2470 (1993)
- [5] C. H. Dasso *et al.*, Nucl. Phys. A405, 381(1983)
- [6] C. Beck *et al.*, Phys. Rev. C 67, 054602 (2003)
- [7] R. Anjos *et al.*, Phys. Lett. B 534, 45 (2002)
- [8] A. Mukherjee *et al.*, Phys. Lett. B636, 91 (2006)
- [9] P.K. Rath *et al.*, Phys. Rev. C 79 (2009) R051601
- [10] P. K. Rath *et al.*, Nucl. Phys. A874, 14 (2012)
- [11] M. Dasgupta *et al.*, Nucl. Phys. A 834, 147c (2010)
- [12] V.V. Parkar *et al.*,Phys. Rev. C 82 (2010) 054601
- [13] C.S. Palshetkar *et al.*, Phys. Rev. C 82 (2010) 044608
- [14] J. Lubian *et al.*, Phys. Rev. C 64, 027601 (2001)
- [15] A. Gavron, Phys. Rev. C 21, 230 (1980)
- [16] R. Kossakowski *et al.*, Phys. Rev. C 32, 1612 (1985)
- [17] I. Tserruya *et al.*, Phys. Rev. Lett. 60, 14 (1988)
- [18] J. Blocki *et al.*, Ann. Phys. (NY) 105, 427 (1977)
- [19] W. Reisdorf, J. Phys. G: Nucl. Part. Phys. 20, 1297 (1994)
- [20] I. Dutt, R.K. Puri, Phys. Rev. C 81 , 064608 (2010)
- [21] P. Moller, J.R. Nix, Nucl. Phys. A 361, 117 (1981)
- [22] P. Moller *et al.*, At. Data Nucl. Data Tables 59, 185 (1995)
- [23] W. Myers and W. Swiatecki, Phys. Rev. C 62, 044610 (2000)
- [24] M. Dasgupta *et al.*, Phys. Rev. C 70, 024606 (2004)
- [25] V. Tripathi *et al.*, Phys. Rev. Lett. 88, 172701 (2002)

Chapter 7

This chapter closes with the summary and conclusions of the work carried out in the present investigation along with the future perspectives.

(A) Summary and Conclusions

In the present thesis, we have studied the reaction mechanism involving weakly bound ${}^6\text{Li}$ and ${}^7\text{Li}$ projectiles and medium mass nuclei ${}^{144}\text{Sm}$ (spherical) and ${}^{152}\text{Sm}$ (deformed) as a targets. The motivation for present work was stimulated from the rapid developments of radioactive ion beam (RIB) facilities in the recent years. Presently, the availability radioactive ion beam is not intense and good quality and there is a need to develop accelerator technology to improve the reliability of these beams. In the mean time, one can use the weakly/loosely bound stable beam such as ${}^6\text{Li}$, ${}^7\text{Li}$ and ${}^9\text{Be}$ for the study of breakup of these nuclei using different targets in the mass region varying from low to heavy nuclei. This will provide a strong basis for studies involving radioactive ion beam (RIB). Apart from that in comparison with strongly bound stable nuclei, the knowledge about the reaction mechanism of these weakly bound is limited. Keeping in view the reaction mechanism using weakly bound projectile we have investigated following points;

- (i) Complete fusion suppression involving loosely bound projectile.
- (ii) Effect of target deformation in the presence of projectile breakup
- (iii) Effect of projectile breakup threshold in complete fusion.

The experimental procedure for all the measurements was same. All the measurements on fusion were done at BARC-TIFR Pelletron accelerator facility, Mumbai, and the target thickness measurements were done using the above facility as well as the FOTIA facility at BARC, Mumbai. An activation analysis technique was used to determine the cross sections.

(i) Complete fusion suppression involving loosely bound projectile

In the first measurement, we chose the spherical ${}^{144}\text{Sm}$ target and ${}^6\text{Li}$ projectile. The complete fusion excitation function for ${}^6\text{Li} + {}^{144}\text{Sm}$ system was measured at energies near

and above the Coulomb barrier ($E_{\text{lab}}=20-40$ MeV). An activation technique was used to determine the cross sections of $2n$ and $3n$ evaporation channels, which were the most dominating channels of decay of the compound nucleus formed by the complete fusion process in the measured energy range. Statistical model calculations were performed using PACE2 to estimate the relative contributions of other residue channels in order to determine the experimental cross sections for the complete fusion. Coupled-channel calculations using CCFULL shows an enhancement in fusion at energies below the Coulomb barrier as compared to the predictions given by the single barrier penetration model. However, the experimental results suggest that there is an overall suppression of the fusion cross section, particularly at energies above the barrier, for the present reaction as compared to CCFULL calculations with or without full couplings. A comparison of the results for the present system with other systems involving strongly bound stable projectiles such as $^{12}\text{C} + ^{141}\text{Pr}$ and $^{20}\text{Ne} + ^{133}\text{Cs}$ forming similar compound nuclei, clearly shows that fusion cross sections for the present system are systematically lower. From these two comparisons, fusion suppression was estimated to be $32 \pm 5\%$. This suppression may be ascribed to the low breakup threshold energy of ^6Li , which allows it to break up prior to fusion. A similar procedure was applied to reanalyze the fusion data from the literature for $^7\text{Li} + ^{165}\text{Ho}$ and $^7\text{Li} + ^{159}\text{Tb}$, and it was found that the cross sections are suppressed by about 18% and 26% compared to those with $^{12}\text{C} + ^{160}\text{Gd}$ and $^4\text{He} + ^{162}\text{Dy}$ systems, respectively, forming the same compound nuclei. A systematic comparison of fusion excitation functions for several reactions involving loosely bound stable projectiles shows that the suppression in fusion is a common phenomenon, and it increases with (i) the increase in the target atomic number Z_T and (ii) the decrease of the projectile breakup threshold E_{th} . To obtain an empirical expression for the suppression as a function of Z_T and E_{th} , the fusion data for a large number of reactions involving loosely bound projectiles is necessary.

(ii) Effect of target deformation in the presence of projectile breakup.

The second experiment was to understand the role of target deformation versus projectile breakup. So a deformed isotope of ^ASm i.e., ^{152}Sm was used as a target in place of the spherical ^{144}Sm . The complete fusion cross sections for $^6\text{Li} + ^{152}\text{Sm}$ reaction were measured

at energies near and above the Coulomb barrier. The decay of the compound nucleus formed by the complete fusion process was dominated by neutron evaporation channels. Combined ER cross sections for 2n, 3n, 4n and 5n contribute to more than 97% of CF for most of the beam energies. ER cross sections were measured by recoil catcher technique followed by off-line gamma-ray spectrometry. Statistical model calculations were performed using PACE to quantitatively understand the ER cross sections, and estimate the contribution from the missing channels so as to obtain the experimental complete fusion cross sections. A comparison of the experimental data with ${}^6\text{Li}+{}^{144}\text{Sm}$ showed that at above-barrier energies the CF cross sections are comparable but at sub-barrier energies they are largely enhanced for the present system. This implies that the effect of target deformation on sub-barrier fusion, i.e., enhancement is independent of whether the projectile is weakly or strongly bound. Coupled-channels calculations using CCFULL were performed to understand the measured CF data. At sub-barrier energies, the coupling of target deformation shows enhancement in CF cross sections and explain the data. However, at above-barrier energies there is a suppression of $28\pm 4\%$ in the CF data compared to the CC calculations. The low energy threshold of the projectile seems to allow it to break up prior to fusion, leading to loss of flux from the entrance channel. It can therefore be concluded that the complete fusion cross section at energies above the barrier is suppressed due to projectile breakup. Thus the effects of both the target deformation as well as the projectile breakup are present, and their influence on each other seems to be negligible. CF cross sections for the present system at above-barrier energies are found to be smaller by a factor of $\sim 28\text{--}32\%$ than those calculated by Wong's formula using proximity potential, which is consistent with the above conclusion on fusion suppression. Comparison with the other systems involving strongly bound stable projectiles such as ${}^{12}\text{C}+{}^{141}\text{Pr}$ and ${}^{20}\text{Ne}+{}^{133}\text{Cs}$ forming similar compound nucleus also shows that CF cross-sections for the present system at above-barrier energies are systematically lower compared to those with strongly bound projectiles, which further supports the above mentioned suppression. Since the CF cross sections at sub-barrier energies are slightly higher than those predicted by CC calculations, it may be assumed that the net effect of breakup (i.e., suppression due to loss of flux plus enhancement due to breakup coupling) is a small enhancement in fusion at this region. CDCC calculations with projectile breakup channels

reveal that the dynamic polarization potential generated due to breakup coupling is repulsive which leads to reduction in absorption cross section. Fusion cross sections obtained by both the cumulative absorption and BPM methods are found to be smaller compared to the ones with no breakup coupling, supporting the above conclusions on the effect of projectile breakup. Present experimental data provide important input to the future realistic models of fusion with weakly bound projectiles to predict both qualitative and quantitative effects of projectile breakup at energies below as well as above Coulomb barrier energies, and how these effects get modified in the presence of large target deformation specially at sub-barrier energies where the deformation plays a significant role.

(iii) Effect of projectile breakup threshold in complete fusion.

In order to have a complete picture on the projectile and target dependences, the effects of projectile breakup threshold on fusion cross section have also been investigated. To do this another weakly bound nuclide i.e., ${}^7\text{Li}$ was chosen in place of ${}^6\text{Li}$. Since the projectile ${}^7\text{Li}$ breaks up into α and t with a higher breakup threshold energy (2.478 MeV) than ${}^6\text{Li} \rightarrow \alpha + d$ breakup (1.478 MeV), it is expected that the complete fusion (CF) suppression factor for ${}^7\text{Li}$ induced reactions would be less compared to that of ${}^6\text{Li}$. Thus, the complete fusion cross sections for two more reactions involving ${}^7\text{Li}$ as a projectile and the same targets as earlier (i.e. ${}^{144,152}\text{Sm}$) were measured. These results are compared with our earlier measurements to test the systematics on the suppression factor and its dependence on breakup threshold. It was found that the CF suppression in both ${}^7\text{Li} + {}^{144,152}\text{Sm}$ reactions are same (~26 %) but smaller than that of ${}^6\text{Li} + {}^{144,152}\text{Sm}$ reactions (~30%). For a particular target, it was observed that the CF cross sections at sub-barrier energies are same for the reactions involving both the projectiles. However, at above barrier energies the CF is larger for ${}^7\text{Li}$ than that of ${}^6\text{Li}$ induced reactions. Since the effect of inelastic or transfer couplings at high energies are negligible, it implies that due to larger breakup threshold of the former, the loss of incident flux by breakup is lower, and hence there is less suppression in CF. However, at sub-barrier energies, the CF is enhanced by both target as well as projectile excitations and possibly by breakup too.

In summary, the work described in the thesis contains a systematic study of fusion cross sections involving weakly bound projectiles like ${}^6\text{Li}$ and ${}^7\text{Li}$ with two Sm isotopes; one

spherical and another deformed. In this study following physical aspects have been investigated. It describes the results and conclusions on the effect of (i) breakup of a weakly bound projectile, (ii) target deformation and (iii) projectile breakup threshold on the complete fusion cross section. It has been observed that complete fusion cross section for all the systems (${}^6,7\text{Li}+{}^{144,152}\text{Sm}$) that we have measured are suppressed compared to those predicted by the coupled-channels calculations as well as those for the reactions involving strongly bound projectiles but forming similar compound nuclei. The suppression factor for ${}^6\text{Li}$ and ${}^7\text{Li}$ induced reactions are found to be $\sim 30\%$ and $\sim 26\%$ respectively. A systematics on suppression factor for the above systems along with other systems found in literature shows that the suppression increases with the decrease in breakup threshold of the projectile and increase in target Z . It was also observed that the effect of target deformation and the projectile deformation on fusion co-exist.

(B) Future perspectives

With the advent of radioactive ion beam (RIB) facilities around the world more and more weakly bound projectiles will be available for nuclear reaction studies. The knowledge acquired from the studies involving weakly bound stable projectiles from the present thesis work will be very useful to predict and compare the results of the reactions that are planned or studied using the present and upcoming RIB facilities respectively. For a proper prediction we need more and more experimental data even with the same weakly bound projectiles but different targets with good accuracy. At sub-barrier energy region where the fusion cross sections are very low, it is a real experimental challenge to measure the cross sections with high accuracy. Measurement of fusion cross sections at deep sub barrier energies is another challenge. There are a few measurements which showed that the effect of coupled channels alone cannot explain the experimental data on $\sigma_{\text{fus}}^{\text{expt}}$. The low energy fusion cross sections are very important in the context of nuclear astrophysics. A slight change in the slope of the fusion excitation function can have disastrous effect on the extrapolation of the fusion cross section to the low energies near the Gamow peak where astrophysical reactions take place. Another field where the knowledge of present thesis work will be very helpful is the formation and decay of super heavy nuclei. The study of

Chapter 7: Summary, conclusion

reaction mechanisms involving radioactive ion beams to form super heavy nuclei would be very interesting. The observation of complete fusion suppression in the reactions involving weakly bound projectiles would imply that the probability of super heavy element formation will be highly suppressed.

The future plan is to (i) measure the fusion cross sections at deep sub-barrier energy region involving both strongly as well as weakly bound projectiles (ii) measure the fusion and direct reaction cross sections involving radioactive ion beams and understand the effect of breakup coupling on the measured cross sections (iii) study the reactions which are of nuclear astrophysical interest and (iv) study the reactions that form the super heavy elements.